DENSITY FUNCTIONAL THEORY STUDY OF MATERIAL PROPERTIES OF LANTHANIDE-DOPED ZINC OXIDE FOR DYE SENSITISED SOLAR CELL PHOTOANODE

Moses Kahura Irungu

A Thesis Submitted in Partial Fulfillment of the Requirements for the Degree of Doctor of Philosophy in Physics of Murang'a University of Technology

August, 2025

DECLARATION

Student Declaration

I hereby declare that this thesis is my original work and to the best of my knowledge has not been presented for a degree awarded in this or any other university. I understand what plagiarism is and am aware of the University policy in this regard. I understand that any false claim in respect of this work shall result in disciplinary action in accordance with the University Anti-Plagiarism Policy.

_____ _____

Moses Kahura Irungu Date

AS502/5748/2021

Supervisors' Approval

The undersigned certify that they have read and hereby recommended for acceptance of Murang'a University of Technology thesis entitled "**Density Functional Theory Study of Material Properties of Lanthanide-Doped Zinc Oxide for Dye Sensitised Solar Cell Photoanode".**

_____ _____

Dr. Kiprotich Sharon Date

Department of Physical and Biological Sciences

Murang'a University of Technology



_____ _____

Dr. Winfred Mulwa Date

Department of Physics

Egerton University

DEDICATION

This thesis is dedicated to my amazing parents Jane Njeri and John Irungu, my lovely wife Elizabeth Kahura, and my children Winne Njeri and Alvin Irungu. Thanks a lot for your immense support, prayers and encouragements.

ACKNOWLEDGEMENT

I hereby express my deepest gratitude to God for His constant guidance, strength, and blessings throughout this journey. His presence in my life has been a source of unwavering support and inspiration, allowing me to overcome every challenge along the way.

I am very grateful to my supervisors, Dr. Sharon Kiprotich and Dr. Winfred Mulwa, for their exceptional guidance and unwavering support throughout this research journey. Their insightful feedback, attention to detail, and continuous encouragement were instrumental in shaping the direction of my work. Likewise, their constructive criticism, and valuable suggestions significantly enhanced the quality of this thesis. Their dedication to my academic growth and their patience in guiding me through each stage of the research process have been truly invaluable. I am deeply grateful for their mentorship and for the time and effort they invested in helping me succeed.

I further extend my sincere thanks to my research colleagues, Vincent Otieno, Gabriel Chirchir, Namisi Maua, Tindibale Edward, and Ann Thirika from Egerton University, for their collaboration and valuable contributions throughout this research. To my great friends; Simon, Jerusha, Jacinta, James, thanks a lot for your encouragement all through. I sincerely acknowledge the invaluable guidance and support provided by the academic staff of the department of Physical and Biological Sciences at Murang'a University of Technology. Their expertise and dedication were instrumental in the successful completion of this work.

I also wish to appreciate my principals, Mr. Joseph Karuri (Kangema High School) and Mr. Willy Kuria (Murang'a High School) for granting me permission to conduct this research. Their support and trust in my work were crucial in allowing me to pursue this project to completion. Finally, I wish convey my gratitude to cluster for high processing computing (CHPC) for providing me with the computational resources necessary to carry out this research.

ABSTRACT

This dissertation presents a comprehensive Density Functional Theory (DFT) investigation into the effects of rare earth (RE) metals doping on zinc oxide (ZnO), targeting its application as a photoanode material in dye-sensitized solar cells (DSSCs). The study conducted an in-depth comparative analysis of structural, mechanical, dynamical, electronic, optical, and transport properties of the undoped cubic (C), Wurtzite (W) and monolayer (M) structural configurations of ZnO. Similar material properties of ZnO modified by individual Ce, Dy, and Eu dopants were further evaluated systematically on the wurtzite phase of ZnO. The effects of Oxygen vacancy and dopant concentration on the material Properties of W-ZnO were evaluated on a supercell (3×3×3) comprising of 108 atoms. The structural optimization was carried out using the generalized gradient approximation (GGA) with the Perdew-Burke-Ernzerhof (PBE) exchange-correlation functional. The calculated lattice constants of 4.388 Å for C-ZnO, 3.289 Å for W-ZnO and 3.276 Å for M-ZnO were in good agreement with other experimental and computational reports. The rare earth (RE) metal-doped W- ZnO exhibited an average lattice expansion of approximately 1.2% (a = 3.294 Å, 3.291 Å and 3.295 Å) for RE (Ce, Dy, Eu) metal doping respectively. The Mechanical properties were evaluated through calculations of elastic constants and moduli. Doping pristine W-ZnO (Young's modulus 115.0 GPa, Poisson's ratio 0.36) with Dy, Eu, and Ce significantly enhances its stiffness to 217.5 GPa, 212.2 GPa, and 215.6 GPa, respectively, indicating synergistic strengthening effects. Additionally, the bulk modulus (B) increased from 136.7 GPa in undoped ZnO to 155.2, 157.3 and 153.6 GPa for RE (Ce, Dy, Eu) doping respectively. Dynamical stability of all doped structures was confirmed via phonon dispersion calculations. No imaginary frequencies were detected across the Brillouin zone, affirming that the RE-doped configurations are dynamically stable. Electronic properties investigations revealed significant modifications in the band structure upon doping. Pristine ZnO has a calculated band gap of 0.76 and 3.19 eV in the DFT and DFT+U formalism respectively. Doping with Ce, Dy, and Eu reduced the effective band gap to approximately 3.17 eV, 3.16 eV, and 3.18 eV, for RE (Ce, Dy, Eu) doping respectively at 1.85 % doping concentration. As the dopant concentration increased from 0-5.56%, the band gap generally decreased for all the RE-doped W-ZnO compounds tested. Optical properties were evaluated by computing the complex dielectric function and absorption spectra. It was observed that, RE doping extended the absorption edge of W-ZnO into the visible region. Specifically, Eu-doped ZnO exhibits a peak absorption coefficient of approximately 2.1×10^5 cm^{-1} at around 550 nm, while Ce- and Dy-doped variants demonstrate peak coefficients in the range of $2.0–2.1 \times 10^5$ cm^{-1}. The refractive index and extinction coefficient analyses corroborate these findings, suggesting that RE doping effectively tunes the optical response to better match the solar spectrum. Transport properties were computed using BoltzTraP code integrated in quantum espresso. This assessment indicated that RE doping significantly improves the charge carrier concentration and conductivity of ZnO. While undoped ZnO exhibits a carrier concentration on the order of 10^{18} cm^{-3}, the doped systems show enhancements approaching 10^{20} cm^{-3}. This increase is further supported by an elevated density of states near the Fermi level, underscoring the potential for improved electron transport in DSSC photoanodes.

TABLE OF CONTENTS

DECLARATION ..... **ii**
DEDICATION ..... **iii**
ACKNOWLEDGEMENT ..... **iv**
ABSTRACT ..... **v**
LIST OF TABLES ..... **x**
LIST OF FIGURES ..... **xii**
ACRONYMS AND ABBREVIATIONS ..... **xv**
CHAPTER ONE: INTRODUCTION **1**
1.1 Background of the Study 1
1.2 Statement of the Problem 4
1.3 Objectives 5
1.3.1 General Objectives 5
1.3.2 Specific Objectives 5
1.4 Research Questions 5
1.5 Significance of the Study 6
1.6 Scope of the Study 6
1.7 Limitations of the Study 7
1.8 Contribution of the Thesis 7
1.9 Organization of the Thesis 8
CHAPTER TWO: LITERATURE REVIEW **9**
2.1 Introduction 9
2.2 Solar Energy 9
2.3 Photovoltaic (PV) Technologies 10
2.3.1 Silicon Based Solar Cells 11
2.3.2 Thin Film Based Solar Cells 11
2.3.3 Perovskite Solar Cells 13
2.3.4 Organic Solar Cells (OPVs) 15
2.3.5 Hybrid Solar Cells 16
2.3.6 Quantum Dot Solar Cells 17
2.4 Dye-Sensitized Solar Cells (DSSCs) 18
2.4.1 Structural Design of a DSSC 19
2.4.2 The Counter Electrode 19
2.4.3 The Photoanode 21
2.4.4 The Dye Sensitizer 22
2.4.5 The Liquid Electrolyte 23
2.5 Structural Operations of DSSC 24

2.5.1 Photo-Energy Absorption and Dye Excitation 24
2.5.2 Electron Injection into the Conduction Band of TiO_2 24
2.5.3 Electron Transport Through Semiconductor 24
2.5.4 Dye Regeneration and Recombination Processes 25
2.6 Properties of ZnO 25
2.6.1 Structural Properties of Wurtzite ZnO (W-ZnO) 26
2.6.2 Lattice Dynamic Properties of Wurtzite-ZnO 28
2.6.3 Mechanical Properties of W-ZnO 28
2.6.4 Electronic Properties of Wurtzite-ZnO 29
2.6.5 Optical Properties of W-ZnO 30
2.6.6 Photoluminescence of ZnO 32
2.6.7 Transport Properties 33
2.7 Zinc Oxide Based Solar Cells 34
2.8 Rare Earth Metals 35
2.9 RE-Doped ZnO Based DSSC 37
2.10 The Ce, Dy and Eu Doping of ZnO for DSSC Photoanodes 39
2.11 *Ab initio* Techniques 40
2.11.1 Quantum Mechanics 40
2.11.2 The Many-Body System Theory 41
2.11.3 The Born-Oppenheimer Approximation 42
2.11.4 Hartree Approximation 43
2.11.5 Hartree-Fock Theory 44
2.11.6 The Hohenberg-Kohn Theorem 45
2.11.7 The Kohn-Sham Equations 47
2.11.8 Density Functional Theory (DFT) 48
2.11.9 Local Density Approximation (LDA) 50
2.11.10 The Generalized Gradient Approximation (GGA) 52
2.11.11 Hybrid Functionals and Green Functionals (GW) Approximation 53
2.11.12 Plane Waves 54
2.11.13 Brillouin Zone Sampling 57
2.11.14 Pseudopotentials 58
2.11.15 DFT and the Hubbard Term U 59
2.12 Formation Energies within DFT 62
2.13 Optical Properties from DFT 63
2.14 Dielectric Tensor 65
2.15 Lattice Dynamics 66
2.16 Summary 67

CHAPTER THREE: MATERIALS AND METHODS 69
3.1 Introduction 69
3.2 Quantum Espresso (QE) Input File 69
3.3 Structural Properties 71
3.4 Mechanical Properties 72
3.4.1 Elastic Constants 72
3.4.2 Murnaghan Equation of State (MEoS) 75
3.4.3 Elastic Anisotropy 75
3.5 Electronic Properties 77
3.5.1 Electronic Band Structures 77
3.5.2 Density of States (DOS) 78
3.5.3 Charge Density 78
3.6 Optical Properties 78
3.7 Transport Properties 80
3.8 Lattice Dynamics 81
3.9 GGA+U 81
3.10 Oxygen Vacancies 82
3.11 Brillouin Zone Sampling 82
3.12 Ethical Considerations 83
3.13 Summary 84
CHAPTER FOUR: RESULTS AND DISCUSSION 85
4.1 Introduction 85
4.2 Optimization of ZnO Unit Cell 85
4.2.1 Comparative Analysis of ZnO Phases 85
4.2.2 Effects Crystallographic Configuration 86
4.2.3 Effects of Hubbard U on the Structural Properties of Wurtzite ZnO 92
4.3 Structural Properties of RE (Ce, Dy, Eu) Doped W-ZnO 96
4.3.1 Supercell Modelling 96
4.3.2 Lattice Parameters and Bulk Modulus 97
4.3.3 Formation Energies (E_f) 98
4.3.4 X-Ray Diffraction (XRD) Simulations 99
4.3.5 Effects of Dopant concentration on Structural Properties 101
4.3.6 Effects of Oxygen Vacancy on the Structural Properties 102
4.4 Lattice Dynamics 105
4.4.1 Phonon Dispersion 105
4.4.2 Effects of Structural Configurations 106
4.4.3 Effects of RE Doping on Lattice Dynamics of W-ZnO 107
4.5 Mechanical Properties 108

4.5.1 Elastic Constants....108
4.5.2 Effects of Structural Configuration on Mechanical Properties....109
4.5.3 Effects of RE (Ce, Dy, Eu) on Mechanical Properties of W-ZnO....113
4.5.4 Elastic Tensors of W-ZnO....119
4.6 Electronic Properties....123
4.6.1 GGA +U Formalism....123
4.6.2 Band Structures....124
4.6.3 Effects of Structural Configurations....127
4.6.4 Electronics Properties of RE (Ce, Dy and Eu) Doped ZnO....129
4.6.5 Effect of Dopant Concentration Band Gap of W-ZnO....132
4.6.6 Effects of Oxygen Vacancies....133
4.6.7 Charge Density of RE (Ce, Dy Eu) Doped ZnO....135
4.7 Optical Properties....136
4.7.1 Dielectric Function....136
4.7.2 Effects of Structural Configurations....136
4.7.3 Effects of Hubbard U on Optical Properties of W-ZnO....139
4.7.4 Optical Properties of RE (Ce, Dy, Eu) Doped W-ZnO....142
4.7.5 Effects of RE (Ce, Dy, Eu) Concentration....144
4.7.6 Effects of Oxygen Vacancies....146
4.8 Transport Properties of ZnO....147
4.8.1 Electrical conductivity and seebeck coefficients....147
4.8.2 Effects of Structural Configuration....148
4.8.3 Transport Properties of RE (Ce, Dy, Eu) Doped ZnO....150
4.8.4 Effects of Dopant Concentration....152
4.8.5 Effect of Oxygen Vacancies Concentration....153
4.9 Summary....155
CHAPTER FIVE: CONCLUSION AND RECOMMENDATIONS....156
5.1 Conclusion....156
5.2 Recommendations....159
5.2.1 Recommendations for Policy....159
5.2.2 Recommendations for Future Studies....160
REFERENCES....162
APPENDICES....196

LIST OF TABLES

Table 2.1: The General Properties of Rare Earth (RE) Metals. 36
Table 3.1: The Roles of Various Flags in the QE Input File. 71
Table 4.1: Optimized Lattice Constants, Bulk Modulus and its Derivative, Bond Length, and Minimum Energy (E_{min}) in Comparison with Other Studies.91
Table 4.2: Variation of Lattice Constant, a with Hubbard U Value of Zn-3d and O-2P.....94
Table 4.3: Effects of Hubbard U on Lattice Parameters of W-ZnO 96
Table 4.4: The lattice parameter, volume, bulk modulus and its derivative of RE (Ce, Dy and Eu) doped W-ZnO at 1.85 % dopant concentration. 98
Table 4.5: Effects of Dopant Concentration on the Structural Properties of W-ZnO. 104
Table 4.6: Effects of Oxygen Vacancies Concentration on Pure and RE (Ce, Dy, Eu) Doped W-ZnO. 105
Table 4.7: Elastic constants, bulk moduli (B), shear modulus (G), Young modulus (E) of tested ZnO phases in comparison with other previous studies. 110
Table 4.8: Cauchy pressure (C_{12}-C_{44}), Pugh ratio (B/G), Poissons ratio (v), machinability index (μ_m), Vickers hardness (Hv), Kleinman parameter (ξ) and Debye temperature, ΘD,(K). 111
Table 4.9: The calculated Zener anisotropic index (A_z), universal anisotropy index (A^U), equivalent Zener anisotropy measure (A^{eq}), minimum and maximum values of Young's modulus (Emin and Emax in GPa), shear modulus ($Gmin$ and $Gmax$ in GPa) and their ratios.....112
Table 4.10: Elastic Constants of Tested W-ZnO Phases in Comparison with other Previous Studies. 113
Table 4.11: Bulk moduli (B), Shear Modulus (G), Young Modulus (E) of Tested RE (Ce, Dy, Eu) Doped W-ZnO. 114
Table 4.12: Cauchy pressure (C_{12}-C_{44}), Pugh ratio (B/G), Poissons ratio (v), machinability index (μ_m), Vickers hardness (Hv), Kleinman parameter (ξ) and Debye temperature, ΘD,(K) of RE (Ce, Dy, Eu) doped ZnO.....116
Table 4.13: The Calculated Zener Anisotropic Index (A_z), Universal Anisotropy index (A^U), Equivalent Zener Anisotropy Measure (A^{eq}), Minimum and Maximum Values of Young's modulus (Emin and Emax in GPa), Shear Modulus ($Gmin$ and $Gmax$ in GPa) and their Ratios. 119
Table 4.14: Energy Band Gap Values in eV of ZnO Calculated with GGA-PBE and GGA+U Approximations. 128
Table 4.15: Effect of Concentration on the Band Gap of RE (Ce, Dy, Eu) Doped

ZnO. 133
Table 4.16: Effects of Oxygen Vacancy on the band gap of W-ZnO 134
Table 4.17: Real Dielectric Function ($\varepsilon 1$), Refractive Index (n), Absorption Coefficient (α) and Reflectivity (R) at 0 eV. 138
Table 4.18: Real Dielectric Function at 0 eV $\{\varepsilon 1(0)\}$, Refractive Index (n), Absorption Critical Points and Reflectivity at 0 eV (R_0). 141
Table 4.19: Real dielectric function at 0 eV $\{\varepsilon 1(0)\}$, refractive index (n), absorption critical points and reflectivity at 0 eV (R_0) 143
Table 4.20: Effects of Dopant Concentration on Optical Properties of RE (Ce, Dy, Eu) Doped W-ZnO. 145
Table 4.21: Optical Properties of RE-Doped W-ZnO with Oxygen Vacancies. 147
Table 4.22: Transport coefficients of ZnO at different temperatures. 150
Table 4.23: Transport coefficients of ZnO at different temperatures. 151
Table 4.24: Effects of Doping Concentration (%) on the Transport Properties of ZnO. 153
Table 4.25: Transport Properties of RE (Ce, Dy, Eu)-Doped ZnO at Different Oxygen Vacancy Concentration. 154

LIST OF FIGURES

Figure 2.1: World Net Electricity Generation by Source 10
Figure 2.2: The (a) Schematic Diagram and (B) Power Characteristic of Silicon Based Solar Cells 11
Figure 2.3: Schematic Diagram of Thin Film Based Solar Cell..... 12
Figure 2.4: Solar Cells Generations. 13
Figure 2.5: Schematic Diagram of Perovskite Based Solar Cell..... 14
Figure 2.6: Figure: (a) Schematic Structure of a Hybrid Solar Cell. (b) Picture of a Test Solar Cell, Fabricated in a Lab. (c) Working Principle 16
Figure 2.7: Schematic Diagram of Quantum Dot Based Solar Cells. 17
Figure 2.8: Structural Design of a Dye-Sensitized Solar Cell..... 20
Figure 2.9: Dye Sensitize Solar Cell Schematic Band Diagram. 23
Figure 2.10: Crystal Structure of ZnO: (a) Rock salt, (b) Zinc blende and (c) Wurtzite The Oxygen Atoms are Shown as Red Spheres, Zinc Atoms as Grey Spheres. 26
Figure 2.11: Typical Hexagonal Wurtzite Structure of ZnO, the Oxygen Atoms are Shown as Grey Spheres, Zinc Atoms as Yellow Spheres. 27
Figure 2.12: Band Structure of Wurtzite ZnO. 30
Figure 2.13: The (a) Reflectance and (b) Optical Band Gap of Wurtzite ZnO at Different Temperatures. 31
Figure 2.14: The (a) Transmittance and (b) Absorbance of ZnO as a Function of Wavelength in nm 31
Figure 2.15: Photoluminescese of ZnO at Different Temperatures. 32
Figure 2.16: Schematic Diagram of ZnO-Based DSSC. 35
Figure 2.17: Production of Rare Earth Elements..... 36
Figure 2.18: Flow Chart of Self-Convergence Field (SCF) Calculation in DFT. 49
Figure 2.19: Schematic diagram of Pseudo Electrons (red lines) and All-Electron (black lines) Potentials and their Equivalent Wave Functions. 59
Figure 2.20: Schematic Configuration Coordinate Diagram Illustrating the Difference between Thermal and Optical Ionization Energies for an Acceptor. 64
Figure 3.1: A QE Input File Relating to the Kohn-Sham Self-Consistency Scheme. . 70
Figure 3.2: Brillouin Zone Sampling Path for (a) Hexagonal Wurtzite and (b) Cubic ZnO. 83
Figure 4.1: Schematic Representation of (a) C-ZnO, (b) W-ZnO and (c) M-ZnO Structure using VESTA Code. 86
Figure 4.2: Total Energies as a Function of K-point for (a) C-ZnO, (b) W-ZnO

and (c) M-ZnO. 88
Figure 4.3: Total energies as a Function of Ecut for (a) C-ZnO, (b) W-ZnO and (c) M-ZnO. 90
Figure 4.4: Total Energies as a Function of Lattice Constant, a for (a) C-ZnO, ... 90
Figure 4.5: Plots of Energy (Ry) as a Function of (a) K-points (b) Ecut (Ry). 93
Figure 4.6: Plots of Total Energy as a Function of (a) Lattice Constant, (b) c/a Ratio and (c) Volume in DFT, DFT+U_d and DFT+U_d+U_p. 95
Figure 4.7: The Supercell Structure of (a) Pure ZnO and (b) RE-Doped ZnO. 97
Figure 4.8: The Formation Energies of RE Doped W-ZnO Models. 99
Figure 4.9: The Simulated XRD Patterns for the Undoped and RE (Ce, Dy, Eu) Doped W-ZnO. 100
Figure 4.10: Supercell Structure for Ce-doped ZnO at (a) 0%, (b) 1.85%, (c) 3.37% and (d) 5.56 % Concentration. 102
Figure 4.11: Structural Configuration of RE Doped ZnO (a) Without and (b) with Oxygen Vacancy. 103
Figure 4.12: The (a) Phonon Frequency Dispersion and (b) Phonon DOS for (i) C-ZnO, (ii) W-ZnO and (iii) M-ZnO. 106
Figure 4.13: Phonon Dispersion for the (a) Ce-doped ZnO, (b) Dy-doped ZnO 108
Figure 4.14: Directional Dependence of (a) Young's Modulus, (b) Shear Modulus and (c) Poisson's Ratio of W-ZnO in 3D. 120
Figure 4.15: Directional Dependence of Young's Modulus of W-ZnO in 2D. 120
Figure 4.16: Directional Dependence of Shear Modulus of W-ZnO in 2D. 121
Figure 4.17: Directional Dependence of Poison's Ratio of W-ZnO in 2D (Blue and green indicate the Maximum and Minimum Values Respectively). 121
Figure 4.18: The 3D Representation of Linear Compressibility of (a) Ce (b) Dy and (c) Eu Doped W-ZnO 122
Figure 4.19: The 3D Representation of Young's Modulus of (a) Ce (b) Dy and (c) Eu Doped W-ZnO. 123
Figure 4.20: The 3D Representation of Shear Modulus of (a) Ce (b) Dy and (c) Eu Doped ZnO. 123
Figure 4.21: The (a) Band Structure and (b) Density of State of W-ZnO using Standard DFT Approximation. 124
Figure 4.22: The (a) Band Structure and (b) Density of State of W-ZnO using DFT+$U_{d(10eV)}$ Approximation. 125
Figure 4.23: Band Structure and Density of State of ZnO Using DFT + $U_{d(10eV)}$ + $U_{p(8eV)}$ Approximation 126
Figure 4.24: The Variation of the Hubbard U Parameter and the Band Gap

(a) DFT + U_d and (b) DFT+U_d +U_p. 126
Figure 4.25: The Electronic Band Structure and PDOS of (a) C-ZnO,
(b) W-ZnO and (c) M-ZnO Structures using Standard DFT. 128
Figure 4.26: The Electronic Band Structure of (a) C-ZnO, (b) W-ZnO and
(c) M-ZnO Structures using GGA+U. 129
Figure 4.27: The Electronic Band Structures of (a) Pure (b) Ce-Doped,
(c) Dy- Doped and (d) Eu-Doped W-ZnO using GGA+U. 130
Figure 4.28: The Total DOS and PDOS of (a) Pure (b) Ce, (c) Dy and
(d) Eu Doped 131
Figure 4.29: The Electron Density for the (a) Pure (b) Ce-Doped, (c) Dy-Doped
and (d) Eu-Doped W-ZnO. 135
Figure 4.30: The (a) Real Part and (b) Imaginary Part of the Dielectric Constant,
(c) Absorption Coefficient of C-ZnO, M-ZnO and W-ZnO Phases. 137
Figure 4.31: The (a) Refractive Index, (b) Reflectivity and (c) Energy Loss as a
Function of the Energy in eV of C-ZnO, M-ZnO and W-ZnO Phases. . 138
Figure 4.32: The (a) Real (B) Imaginary Part of the Dielectric Constant, (c)
Absorption Coefficient, (d) Refractive Index, (e) Reflectivity and
(f) Energy Loss as a Function of the Energy in eV of W-ZnO using
DFT, DFT + U_d and DFT+U_d +U_p. 141
Figure 4.33: The (a) Real Part and (b) Imaginary Part of the Dielectric Constant,
(c) Absorption Coefficient of the Pure and RE (Ce, Dy, Eu) Doped
W-ZnO. 142
Figure 4.34: The (a) Refractive Index, (b) Reflectivity and (c) Energy Loss as a
Function of the Energy in eV for the Pure and RE (Ce, Dy, Eu) Doped
W-ZnO. 144
Figure 4.35: Seebeck Coefficient of (a) C-ZnO, (b) W-ZnO and (c) M-ZnO Phases
as a Function of Holes Concentration. 149
Figure 4.36: Electrical Conductivity of (a) C-ZnO, (b) W-ZnO and (c) M-ZnO
Phases as a Function of Hole Concentration. 149
Figure 4.37: The (a) Electrical Conductivity and (b) Seebeck Coefficient of
Undoped and RE (Ce, Dy and Eu) Doped W-ZnO. 151

ACRONYMS AND ABBREVIATIONS

DFT	Density Functional Theorem
DOS	Density of States
DSSC	Dye Sensitized Solar Cell
EDX	Energy-dispersive X-ray
E_g	Energy Band Gap
ELATE	Elastic Tensor Analysis Software Program
ESPRESSO	OpEn-Source Package for Research in Electronic
eV	Electron Volt
GGA	General Gradient Approximation
G_R	Reuss shear modulus
G_V	Voigt shear modulus
GW	Greens Function
HF	Hatree Fock
HSE06	Heyd-Scuseria-Ernzerhof 06
ITO	Indium Tin Oxide
LDA	Local Density Approximation
LO	Longitudinal Optical
MD	Molecular Dynamics
PAW	Projector Augmented Waves
PBE	Perdew, Burke, Enzerhof
PDOS	Projected Density of States
PP	Pseudo Potential
PV	Photovoltaic
QE	Quantum ESPRESSO
RE	Rare Earth
SCF	Self- Consistent Field
TCO	Structure, Simulation, and Optimization Transparent Conducting Oxide
TE	Thermoelectric
TO	Transverse Optical
TW	Tera Watt
USSP	Ultra Soft Pseudopotential

UV	Ultraviolet
VASP	Viena Ab initio Simulation Package
XC	Exchange Correlation
XCrySDen	X-Window Crystalline Structures and Densities
XRD	X-Ray Diffraction

CHAPTER ONE
INTRODUCTION

1.1 Background of the Study

Solar energy is one of the most abundant and sustainable energy sources, with the potential to meet the growing global demand for clean and renewable power. Among various photovoltaic technologies, dye-sensitized solar cells (DSSCs) have attracted significant research interest due to their low-cost fabrication, flexibility, and ability to operate efficiently under diffuse light conditions (Anitha & Dotter, 2023). Unlike conventional silicon-based solar cells, DSSCs utilize a mesoporous semiconductor photoanode to facilitate electron transport after light absorption by a dye sensitizer. The efficiency of DSSCs is largely dependent on the performance of the photoanode material, which influences charge separation, electron injection, and recombination dynamics (O'Regan & Grätzel, 1991). Zinc oxide (ZnO) is one of the most extensively studied metal oxides for DSSC photoanodes due to its wide direct bandgap (3.37 eV), high exciton binding energy (60 meV), and superior electron mobility compared to titanium dioxide (TiO_2), the most commonly used DSSC photoanode material. ZnO's one-dimensional nanostructures, such as nanorods, nanowires, and nanotubes, offer direct pathways for electron transport, potentially reducing recombination losses (Upadhaya & Purkayastha, 2020; Saleem et al., 2021). Despite these advantages, pristine ZnO suffers from certain drawbacks, including rapid electron-hole recombination, poor dye adsorption due to its surface chemistry, and instability in acidic electrolyte environments, which limits its practical application in DSSCs (Lorenz et al., 2016).

To overcome these limitations, researchers have explored various modification strategies, including surface treatment, composite formation, and elemental doping (Dhafina et al., 2022). Among these strategies, doping has been widely used to tailor the electronic structure, optical absorption, and charge transport properties of ZnO, thereby enhancing its performance as a DSSC photoanode. Transition metal doping has been found to significantly modify the optoelectronic properties of ZnO. Fe-doped ZnO exhibits improved charge carrier separation due to the introduction of intermediate states within the bandgap, leading to enhanced photocurrent response in DSSCs. For example, Singh et al., (2015) reported that Fe doping at low

concentrations improved the power conversion efficiency (PCE) of ZnO-based DSSCs by nearly 20% compared to undoped ZnO due to reduced recombination rates. Similarly, Co-doped ZnO has demonstrated enhanced light absorption in the visible spectrum, leading to improved DSSC performance. Ponnambalam et al., (2023) observed a shift in the absorption edge towards longer wavelengths and an increase in electron lifetime, which contributed to higher efficiency. Mn-doped ZnO has been shown to improve electron mobility by reducing defect states, as reported by Dubey et al., (2016), where DSSCs with Mn-doped ZnO photoanodes exhibited a 15% enhancement in overall efficiency compared to pristine ZnO.

Non-metal doping has also been explored to enhance the electronic structure of ZnO. Nitrogen doping has been particularly effective in narrowing the bandgap of ZnO, leading to improved light harvesting in the visible region. Villafuerte et al., (2021) reported that nitrogen-doped ZnO exhibited a bandgap reduction from 3.37 eV to approximately 2.95 eV, resulting in increased photocurrent generation and improved DSSC performance. Similarly, sulfur doping has been shown to create localized impurity states that extend the absorption edge, enhancing charge carrier lifetimes and improving DSSC efficiency (Shahzad et al., 2021) demonstrated that sulfur-doped ZnO-based DSSCs achieved a PCE increase of 18% compared to undoped ZnO due to improved charge transport. Among various dopants, rare earth (RE) elements have gained attention due to their unique 4f electronic configurations, which introduce localized states within the ZnO band structure and improve light absorption and charge transport properties. Ce doping has been shown to shift the conduction band edge and increase charge carrier concentration. Bai et al., (2021) demonstrated that Ce-doped ZnO exhibited a significant increase in electrical conductivity and reduced electron-hole recombination, leading to a 22% increase in DSSC efficiency. Dysprosium (Dy) doping, on the other hand, has been reported to introduce f-d electronic transitions that enhance visible light absorption (Thomas, 2022; Jayachandraiah et al., 2015). According to Mulwa (2017) , energy states can enhance light absorption, facilitate energy transfer, and improve charge separation. These modifications make lanthanide-doped ZnO an ideal material for the photoanode in DSSCs, where efficient light harvesting and reduced carrier recombination are crucial for improving energy conversion efficiency.

Lanthanide doping in ZnO significantly enhances its optical and electronic characteristics (Jia et al., 2015). The dopants introduce localized states within the bandgap of ZnO, which can absorb photons of lower energy and promote upconversion or downconversion processes (Hou et al., 2018). For instance, upconversion enables the conversion of low-energy infrared photons into higher-energy visible photons, increasing the effective absorption of the solar spectrum (Nowsherwan et al., 2024). Achehboune et al., (2022) showed that Dy-doped ZnO thin films exhibited improved stability and better light absorption, resulting in a 17% improvement in DSSC performance. Europium (Eu) doping has been widely investigated for its ability to enhance luminescence and radiative recombination pathways in ZnO (Achehboune et al., 2022). The intra-band transitions of Eu^{3+} ions introduce additional defect states that can facilitate charge separation. Tahir & Want, (2024) reported that Eu-doped ZnO exhibited improved photoluminescence properties, which correlated with enhanced DSSC performance. Their study demonstrated that Eu-doped ZnO photoanodes achieved a PCE of 7.5%, compared to 6.2% for undoped ZnO. From a computational perspective, Density Functional Theory (DFT) has proven to be a powerful tool for investigating the impact of RE doping on ZnO at the atomic level. Various approaches, including the Generalized Gradient Approximation (GGA), hybrid functionals, and many-body perturbation theory (GW), have been employed to obtain accurate band structure calculations (Perdew et al., 1996). The GGA+U correction method is often used to account for the strong electron correlation effects in the RE- 4f states and Zn-3d orbitals, providing a more realistic description of the material's electronic structure (Devadiga et al., 2021).

This study employed DFT-based simulations to analyze the structural, mechanical, lattice dynamics, electronic, optical and electrical properties of Ce, Dy, and Eu-doped ZnO across different doping concentrations. A 3×3×3 ZnO supercell with 108 atoms was considered, with dopant concentrations of 0%, 1.85%, 3.7%, and 5.56%. The impact of RE doping on lattice parameters, bond lengths, bond angles, and volume was evaluated to understand the structural modifications induced by dopants. Additionally, formation energy calculations provided insights into the thermodynamic stability of the doped systems (Alhorani et al., 2022). Understanding how RE doping influences the electronic and optical properties of ZnO is crucial for optimizing its application in DSSCs. By reducing recombination losses, improving charge mobility,

and enhancing visible light absorption, RE-doped ZnO can serve as an advanced photoanode material, contributing to the development of next-generation DSSCs with improved efficiency and stability. The findings of this research will provide valuable theoretical insights that can guide experimental efforts in fabricating high-performance RE-doped ZnO photoanodes for photovoltaic application.

1.2 Statement of the Problem

Dye-sensitized solar cells (DSSCs) have emerged as a promising alternative to conventional silicon-based photovoltaic technology due to their low cost, ease of fabrication, and ability to perform efficiently under diffuse light conditions. However, their widespread adoption is hindered by the limitations associated with the photoanode material, which plays a crucial role in light absorption, charge separation, and electron transport. ZnO is a widely studied photoanode material due to its high electron mobility, tunable band gap, and chemical stability. However, pristine ZnO suffers from several drawbacks, including rapid charge recombination, suboptimal absorption in the visible spectrum, and inefficient electron transport, which collectively reduce the overall efficiency of DSSCs. Rare-earth (RE) elements doping has been explored as an effective strategy to enhance the optical and electronic properties of ZnO. Among various RE dopants, cerium (Ce), dysprosium (Dy), and europium (Eu) have shown great potential due to their unique 4f electronic configurations, which can introduce intermediate energy levels, modify the band gap, and improve visible-light absorption. Additionally, their incorporation into the ZnO lattice can enhance charge separation, suppress recombination losses, and improve the overall efficiency of DSSCs. However, despite their potential, the effects of Ce, Dy, and Eu doping on the structural, electronic, optical, and transport properties of ZnO are not yet fully understood. This knowledge gap is especially significant in the context of DSSC applications. Additionally, key aspects such as band structure modifications, charge transport mechanisms, optical absorption enhancement, and their impact on DSSC performance remain inadequately addressed. To bridge this gap, this study employs first-principles calculations based on DFT to investigate the structural mechanical, lattice dynamics, electronic, optical, and transport properties of Ce, Dy, and Eu-doped ZnO.

1.3 Objectives

1.3.1 General Objectives

To investigate the structural, mechanical, lattice dynamics, electronic, optical and transport properties of RE (Ce, Dy, Eu) doped ZnO by use of DFT technique for dye sensitized solar cell application.

1.3.2 Specific Objectives

1. To determine the structural properties of RE selected (Ce, Dy, Eu) doped ZnO using DFT formalism.
2. To evaluate the mechanical properties of selected RE (Ce, Dy, Eu) doped ZnO using DFT formalism.
3. To analyze the lattice dynamical properties of selected RE (Ce, Dy, Eu) doped ZnO using DFT formalism.
4. To explore the electronic properties of selected RE (Ce, Dy, Eu) doped ZnO using DFT formalism.
5. To study the optical properties of selected RE (Ce, Dy, Eu) doped ZnO using DFT formalism.
6. To determine the transport properties of selected RE (Ce, Dy, Eu) doped ZnO using DFT formalism.

1.4 Research Questions

1. How do RE (Ce, Dy, Eu) dopants affect the structural properties of ZnO?
2. What are the effects of RE (Ce, Dy, Eu) dopants on the mechanical properties of ZnO?
3. How do RE (Ce, Dy, Eu) dopants affect the lattice dynamics properties of ZnO?
4. What are the effects of RE (Ce, Dy, Eu) dopants on the electronic properties of ZnO?
5. How do the RE (Ce, Dy, Eu) dopants affect the optical properties of ZnO?
6. How do the RE (Ce, Dy, Eu) dopants affect the transport properties of ZnO?

1.5 Significance of the Study

This study provides valuable insights into the electronic, structural, and optical properties of lanthanide-doped zinc oxide (ZnO) using DFT. By analyzing the effects of RE (Ce, Dy, Eu) doping on ZnO, the research enhances the understanding of how rare-earth elements influence material properties critical for DSSCs. The findings contribute to the development of optimized ZnO-based photoanodes with improved light absorption, charge transport, and stability, which are essential for enhancing the efficiency of DSSCs. This study also serves as a theoretical foundation for experimental work, guiding material selection and synthesis processes for next-generation solar energy applications.

This research therefore has significant implications for sustainable energy development by exploring alternative materials that enhance solar cell performance. By systematically investigating how dopant concentration affects lattice structure, electronic band structure, and defect formation, the study provides a deeper understanding of defect engineering and bandgap modulation strategies. The outcomes can help researchers and engineers design advanced ZnO-based photoanodes with tunable properties to maximize light harvesting and charge separation. Ultimately, the study supports the broader goal of developing cost-effective and efficient solar energy technologies, contributing to global efforts in renewable energy and reducing dependence on fossil fuels.

1.6 Scope of the Study

This research was confined to analyzing how these RE (Ce, Dy, and Eu) dopants influence the structural, mechanical, lattice dynamic, electronic, optical, and transport properties of ZnO. The scope was limited to wurtzite-phase ZnO in a periodic 3×3×3 supercell under zero-Kelvin conditions, which is standard in DFT-based predictions. Only Ce, Dy, and Eu were chosen due to their favorable ionic radii, known optical activity, and previous success in modifying semiconductor properties. Additionally, the study utilized first-principles calculations under the GGA) with Hubbard U corrections (GGA+U) to address the localized nature of the Zn 3d and O 2p orbitals. The simulations provided data on lattice constants, elastic moduli, phonon dispersions, band structures, density of states, dielectric functions, absorption coefficients, and Seebeck coefficients. While the findings offer valuable insights into material behavior

at the atomic level, they are theoretical in nature and were not validated through experimental synthesis or performance testing in real DSSC devices. Thus, the scope remains within predictive computational modeling without laboratory fabrication or photovoltaic efficiency measurements.

1.7 Limitations of the Study

One key limitation of this study is that it relies entirely on computational simulations using DFT, which, despite their accuracy, operate under idealized conditions such as absolute zero temperature and perfect crystal structures. Real-world conditions like defects, grain boundaries, temperature variations, and synthesis imperfections are not accounted for in the simulations. Additionally, the study applied the GGA+U correction scheme, which, while improving bandgap predictions over standard DFT, still has its own limitations in fully capturing electron correlation effects in complex systems like RE-doped oxides. The choice of U values, which can vary across studies, may influence electronic and optical property results. Further, the transport properties were calculated under the constant relaxation time approximation, which does not reflect scattering mechanisms and carrier lifetimes that would occur in practical devices. These limitations imply that while the study provides insightful trends and comparative analysis across dopants, its conclusions must be interpreted cautiously and ideally validated with experimental data.

1.8 Contribution of the Thesis

This thesis contributes to the growing body of knowledge on rare earth (RE)-doped ZnO by providing a comprehensive first-principles analysis of how Ce, Dy, and Eu doping alters the material's properties relevant to dye-sensitized solar cell (DSSC) applications. It presents detailed insights into the structural, mechanical, lattice dynamical, electronic, optical, and transport behavior of RE-doped ZnO, offering valuable theoretical predictions on stability, band structure tuning, light absorption enhancement, and charge transport efficiency. Additionally, the study identifies specific dopants and doping concentrations that improve the functional characteristics of ZnO. Therefore, it contributes in guiding future experimental work in material synthesis and device fabrication. By revealing the influence of each RE dopant across multiple properties, this thesis provides a reference framework for selecting optimal doping strategies to enhance ZnO’s performance as a DSSC photoanode material.

1.9 Organization of the Thesis

This thesis is organized into five chapters. Chapter One introduces the research background, problem statement, objectives, justification, and scope of the study. Chapter Two presents a comprehensive review of related literature on ZnO, rare earth doping, and their applications in dye-sensitized solar cells. Chapter Three outlines the theoretical framework and computational methodology used, including the DFT approach and simulation parameters. Chapter Four discusses the results of structural, mechanical, lattice dynamical, electronic, optical, and transport property analyses. Chapter Finally, Chapter five concludes the study and offers recommendations for future research.

CHAPTER TWO
LITERATURE REVIEW

2.1 Introduction

This chapter provides a review of literature related to the present study, which focuses on the DFT investigation of lanthanide-doped ZnO for application as a photoanode in DSSCs. It begins by highlighting the global shift toward solar energy as a sustainable alternative to fossil fuels, followed by an overview of photovoltaic technologies, with particular attention to third-generation solar cells such as DSSCs. The working principle and structural components of DSSCs including the photoanode, dye sensitizer, electrolyte, and counter electrode are discussed, emphasizing the critical role of the photoanode in electron transport and overall device efficiency.

The chapter further explores the properties of ZnO that make it suitable for photoanode applications, such as its wide band gap, high electron mobility, and stability. It reviews how doping ZnO with rare earth (RE) elements like Ce, Eu, and Dy modifies its structural, electronic, and optical characteristics to enhance DSSC performance. The use of ab initio techniques, particularly DFT, is also discussed, with emphasis on its effectiveness in predicting material behavior at the atomic scale. The strengths and limitations of various computational approaches, including GGA+U and hybrid functionals, are evaluated. This literature review sets the foundation for the present study by identifying research gaps and justifying the use of DFT to model and optimize RE-doped ZnO photoanodes for solar energy applications.

2.2 Solar Energy

Solar energy stands as one of the most rapidly expanding renewable energy sources (Figure 2.1), underpinned by its vast global potential and declining costs (Anoriyo et al., 2023). As of 2023, global photovoltaic (PV) capacity has soared to approximately 760 GW, with an annual growth rate in the range of 15–20% (Irena, 2023). This significant increase is driven by high solar irradiance levels, approximately 1,000 W/m² under standard test conditions (STC) at the Earth's surface and by the solar constant of about 1,366 W/m² at the top of the atmosphere (Amir-Al Zumahi et al., 2021). These figures, combined with significant improvements in energy conversion efficiencies where crystalline silicon cells now achieve laboratory

efficiencies exceeding 26% and commercial modules perform between 15–22% demonstrates the pivotal role solar energy plays in global energy strategies (Roslan et al., 2018).

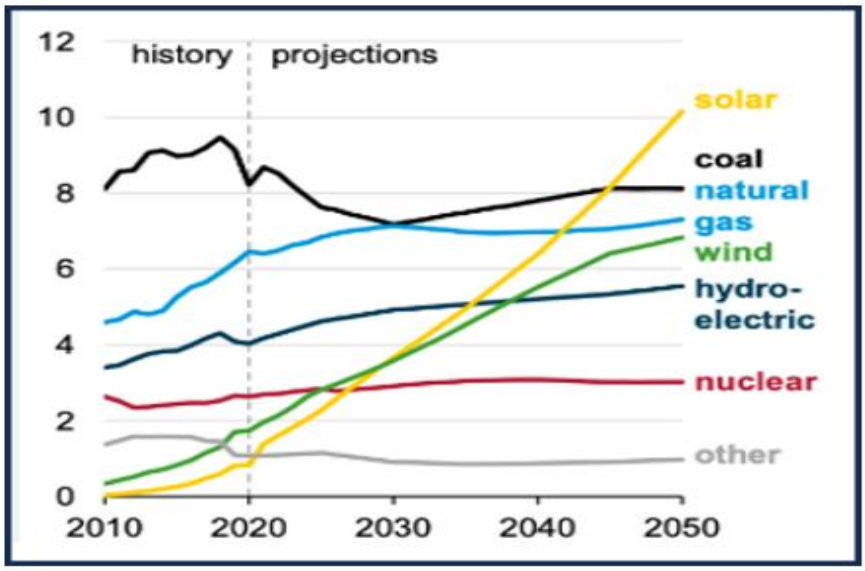

Figure 2.1: World Net Electricity Generation by Source (Lee et al., 2021)

Technological advancements in solar energy have been crucial in reducing costs and enhancing system performance, making solar power increasingly competitive with conventional energy sources. Innovations in materials and device architectures have led to improved durability and efficiency, particularly in the deployment of thin-film technologies and bifacial modules that capture sunlight from multiple angles. Additionally, continuous research efforts are focused on integrating energy storage and smart grid technologies to address intermittency challenges, thereby ensuring a more resilient energy supply (Liu et al., 2021). These developments, supported by favorable government policies and substantial investments, position solar energy as a cornerstone for achieving sustainable energy systems and reducing carbon emissions on a global scale.

2.3 Photovoltaic (PV) Technologies

Photovoltaic (PV) technologies have revolutionized the global energy landscape by providing an efficient and sustainable means of harnessing solar power (Marques et al., 2022; Garrod & Ghosh, 2023). The most dominant PV technology today is crystalline silicon (c-Si), which accounts for approximately 90% of the global solar market due to its superior efficiency, reliability, and long lifespan (Xiao et al., 2024).

2.3.1 Silicon Based Solar Cells

Silicon-based solar cells have maintained their dominance in the PV market for decades, owing to their consistent performance, high efficiency, and proven reliability. Crystalline silicon (Figure 2.2) is available in two main forms: monocrystalline and polycrystalline silicon. Monocrystalline silicon (mono-Si) cells, characterized by their high purity and uniform crystal structure, have achieved laboratory efficiencies exceeding 26%, with commercial modules typically operating in the range of 19–22% (Hameiri, 2021; Okil et al., 2021).

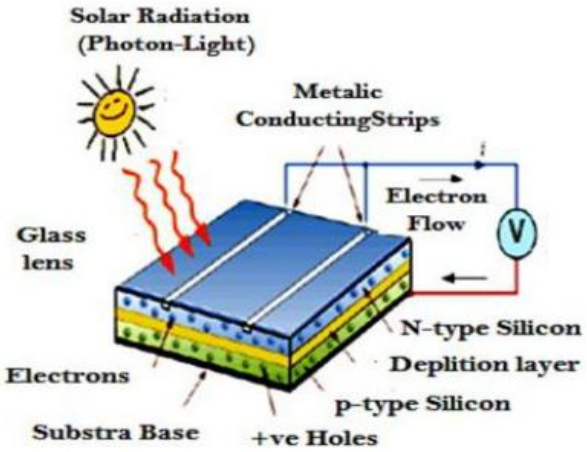

Figure 2.2: The Schematic Diagram of Silicon Based Solar Cells (Okil Et Al., 2021)

On the other hand, polycrystalline silicon (poly-Si) cells, which are easier and cheaper to manufacture, generally exhibit lower efficiencies, typically ranging between 15% and 19% (Hermle et al., 2020). Despite the efficiency advantage of mono-Si cells, poly-Si remains a viable alternative due to its cost-effectiveness. To further enhance performance, Passivated Emitter and Rear Contact (PERC) technology has been introduced, pushing commercial silicon cell efficiencies to 23% by improving light absorption and reducing recombination losses.

2.3.2 Thin Film Based Solar Cells

In addition to crystalline silicon, thin-film photovoltaic technologies have emerged as promising alternatives, particularly for applications requiring lightweight, flexible, and low-cost solar panels (Vodapally & Ali, 2023).

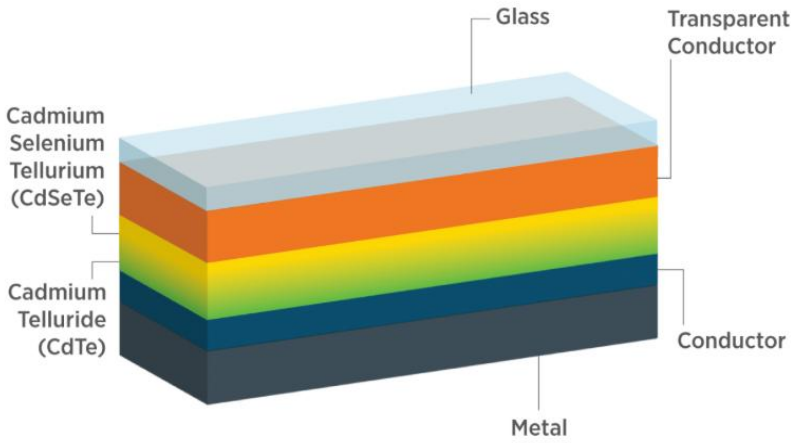

Figure 2.3: Schematic Diagram of Thin Film Based Solar Cell (Perkins et al., 2017)

The leading thin-film PV materials include cadmium telluride (CdTe)(Perkins et al., 2017) and copper indium gallium selenide (CIGS) (Guchhait et al., 2017; Kafedjiska et al., 2023) whose structure is presented in Figure 2.3. CdTe solar cells are notable for their low manufacturing costs and strong light absorption properties, achieving record efficiencies of approximately 22% in laboratory settings, while commercial modules operate around 17–19% (Bailie et al., 2015; Todorov et al., 2015). However, concerns regarding the toxicity of cadmium and the long-term supply of tellurium remain challenges for widespread adoption. CIGS solar cells, with laboratory efficiencies reaching 23% and commercial efficiencies typically in the range of 17–20%, offer superior flexibility and stability (Häcker & Emin, 2023). The primary limitation of CIGS technology is the scarcity and high cost of indium, which necessitates continued research into alternative materials and deposition techniques. Emerging PV technologies such as organic photovoltaics (OPVs), dye-sensitized solar cells (DSSCs), and perovskite solar cells are gaining traction due to their unique properties and potential for cost-effective large-scale production as shown in Figure 2.4. Despite these challenges, thin-film PV technologies continue to attract significant interest for applications such as building-integrated photovoltaics (BIPV), portable solar chargers, and large-scale solar farms in regions where weight and space constraints are critical considerations (Lee & Kim, 2022).

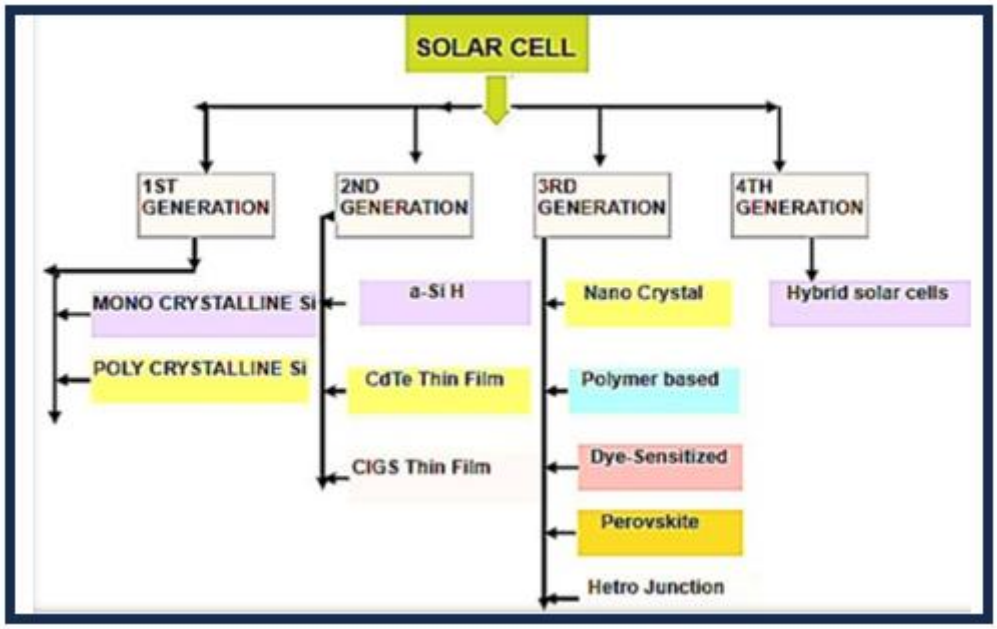

Figure 2.4: Solar Cells Generations (Chander & Tripathi, 2022)

2.3.3 Perovskite Solar Cells

Perovskite solar cells have rapidly emerged as a groundbreaking photovoltaic technology due to their exceptional light absorption and charge transport properties. Perovskite solar cells as depicted in Figure 2.5 have rapidly emerged as one of the most promising photovoltaic technologies in recent years (Benaissa Cherif et al., 2017; Eperon et al., 2016). They are based on a unique class of materials known as perovskites, which typically have the chemical formula ABX_3, where A is an organic cation (such as methylammonium), B is a metal cation (usually lead), and X is a halide anion (chloride, bromide, or iodide) (Wang et al., 2021). This structure enables exceptional light absorption and charge transport properties, allowing perovskite solar cells to achieve power conversion efficiencies that have skyrocketed from under 4% to over 25% in just a decade (Fu et al., 2019; Hörantner & Snaith, 2017). Their solution-based processing methods also promise lower production costs and simpler fabrication compared to conventional silicon-based cells, potentially revolutionizing the solar energy market. Despite their impressive efficiency gains and low-cost fabrication potential, perovskite solar cells face several critical challenges.

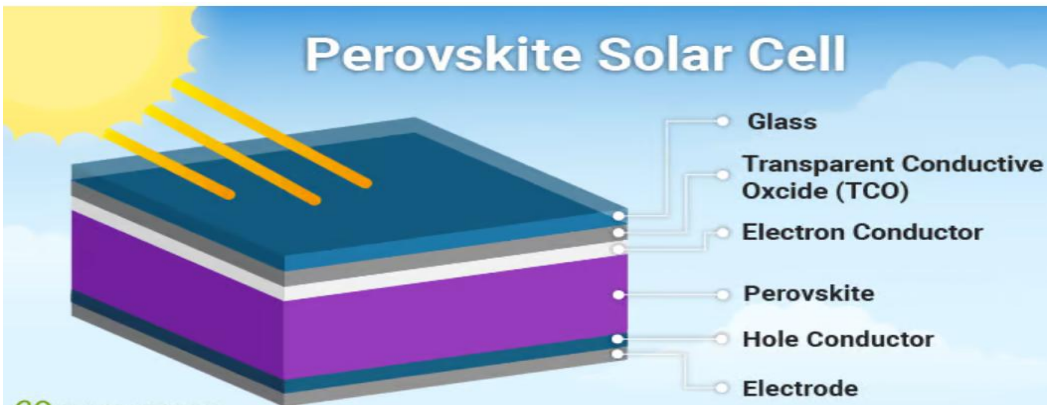

Figure 2.5: Schematic Diagram of Perovskite Based Solar Cell (Eperon et al., 2016)

Long-term stability remains a significant hurdle, as perovskite materials are sensitive to moisture, heat, and UV exposure, which can degrade their performance over time (Namisi et al., 2023). Additionally, concerns over lead toxicity have spurred research into alternative, less hazardous materials while maintaining the desirable photovoltaic properties of the perovskite structure (Bouhmaidi et al., 2022). Current efforts in material engineering, device encapsulation, and tandem cell configurations are focused on addressing these issues, aiming to harness the full potential of perovskite solar cells as a viable, next-generation renewable energy technology (Mariotti et al., 2023). Based on hybrid organic-inorganic lead halide perovskite materials, these cells have seen efficiencies soar from less than 4% to over 25% within a decade, making them one of the fastest-improving PV technologies (Jaysankar et al., 2018; Namisi et al., 2023). Despite their impressive efficiency gains and low-cost fabrication potential, perovskite solar cells face several critical challenges. Long-term stability remains a significant hurdle, as perovskite materials are sensitive to moisture, heat, and UV exposure, which can degrade their performance over time (Wenisch et al., 2023). Additionally, concerns over lead toxicity have spurred research into alternative, less hazardous materials while maintaining the desirable photovoltaic properties of the perovskite structure (Pingak et al., 2023). In conclusion, perovskite solar cells have demonstrated remarkable progress in efficiency and material versatility, positioning them as strong contenders in next-generation photovoltaic technologies

2.3.4 Organic Solar Cells (OPVs)

Organic solar cells, also known as polymer or organic photovoltaics (OPVs), utilize carbon-based semiconducting materials (Lee et al., 2021). OPVs, which use organic semiconductor materials to generate electricity, offer advantages such as flexibility, lightweight structures, and low-cost manufacturing, though their efficiency remains relatively low, typically below 15% (Shafian et al., 2025). They typically utilize conjugated polymers or small molecules to convert sunlight into electricity. Their unique fabrication methods, which often involve solution processing and printing techniques, allow for low-cost, lightweight, and flexible devices (Nakano & Tajima, 2025; Teimoori et al., 2017). These characteristics enable the integration of organic solar cells into a variety of applications such as wearable electronics, building-integrated photovoltaics, and portable power sources (Kumavat et al., 2017). Despite these advantages, OPVs generally exhibit lower power conversion efficiencies compared to silicon-based or perovskite solar cells, primarily due to intrinsic limitations such as short exciton diffusion lengths and higher recombination rates (Lee et al., 2025). In addition to efficiency challenges, the long-term stability of organic solar cells remains a critical issue. The organic materials used in these devices are particularly sensitive to environmental factors such as oxygen, moisture, and ultraviolet light, which can lead to rapid degradation of performance over time (Cui et al., 2020). To overcome these limitations, extensive research has focused on enhancing material stability via molecular engineering, developing non-fullerene acceptors with improved durability, and employing advanced encapsulation techniques (Cui et al., 2020; Wang et al., 2019). Moreover, innovative device architectures such as tandem cells (Bailie et al., 2015; S. Li et al., 2020) have been explored to boost overall efficiency and durability. While organic photovoltaics currently lag behind more established technologies in terms of efficiency and longevity, their inherent advantages in flexibility and cost-effective manufacturing continue to drive research and development, positioning them as a promising technology for future energy solutions.

2.3.5 Hybrid Solar Cells

Hybrid solar cells as shown in Figure 2.6 refer to photovoltaic devices that incorporate both organic and inorganic components in a single architecture, aiming to combine the advantageous properties of each material type (Chen et al., 2024). In these systems, the organic component often a conjugated polymer provides benefits such as low-cost processing, mechanical flexibility, and tunable light absorption.

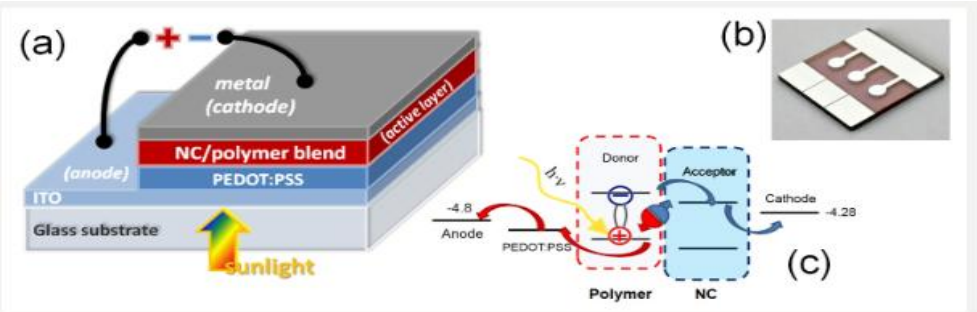

Figure 2.6: (a) Schematic Structure of a Hybrid Solar Cell. (b) Picture of A Test Solar Cell, Fabricated in A Lab. (c) Working Principle (Marimuthu et al., 2022)

On the other hand, the inorganic counterpart such as metal oxide nanoparticles, quantum dots, or perovskite structures offers high charge mobility, stability, and efficient exciton dissociation (Najafi et al., 2018). The resulting hybrid structure often features a donor-acceptor blend, where the inorganic phase acts as an electron acceptor or transport channel, thereby facilitating improved charge separation and reducing recombination losses (Samykano, 2023). This synergy has led to notable improvements in power conversion efficiency compared to pure organic solar cells, making hybrid systems an attractive area for further research and development (Martínez et al., 2022).

Despite the promising performance, hybrid solar cells face several challenges that hinder their full commercial realization. One of the primary issues is achieving efficient interfacial charge transfer between the organic and inorganic phases (Ravele et al., 2024), which is crucial to minimize recombination and maximize overall efficiency. Additionally, long-term device stability remains a concern, as the organic materials are prone to degradation under environmental stressors like moisture and oxygen, while phase separation between the hybrid components can lead to performance inconsistencies over time. Researchers are actively exploring advanced nano structuring (Slimani et al., 2016), surface engineering, and improved material

compatibility to address these limitations. Continued innovations in optimizing the morphology and interface properties of hybrid solar cells are essential to fully harness their potential as a viable alternative to traditional silicon-based and emerging perovskite technologies (Samykano, 2023).

2.3.6 Quantum Dot Solar Cells

Quantum dot solar cells represented in Figure 2.7 is an innovative app roach to solar energy conversion by incorporating semiconductor nanocrystals, known as quantum dots, into the active layer of the device (Yang, Liu, & Chen, 2024; Singh Selopal et al., 2020; Venkata-Haritha et al., 2016). These nanocrystals exhibit unique optical and electronic properties due to quantum confinement effects, which allow their absorption spectrum to be tuned by simply varying their size. This tunability enables the design of solar cells that can capture a broader range of the solar spectrum compared to traditional materials (Carey et al., 2015.). Additionally, the solution processability of quantum dots offers the potential for low-cost, flexible, and lightweight solar cell fabrication, opening avenues for applications in areas where conventional rigid solar panels might not be practical (Chernomordik et al., 2016).

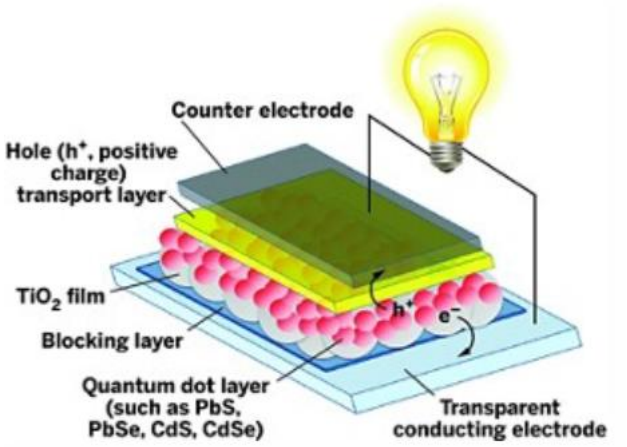

Figure 2.7: Schematic Diagram of Quantum Dot Based Solar Cells (Jumabekov et al., 2014)

Despite the promising attributes of quantum dot solar cells, several challenges must be overcome to achieve commercial viability. Key issues include optimizing charge separation and transport, as the presence of surface trap states on the quantum dots can lead to recombination losses that reduce overall efficiency.

Stability is another significant concern, with quantum dots being susceptible to

degradation under prolonged exposure to light, oxygen, and moisture (Kasaye, Shura, & Dibaba, 2024). Addressing these challenges through advanced surface passivation techniques, improved material synthesis, and refined device architectures remains critical for unlocking the full potential of quantum dot solar cells as a competitive renewable energy technology (Wang et al., 2018).

2.4 Dye-Sensitized Solar Cells (DSSCs)

Dye-Sensitized Solar Cells (DSSCs) are a promising third-generation photovoltaic technology that converts solar energy into electricity through a process inspired by natural photosynthesis process (O'Regan & Grätzel, 1991). Unlike conventional silicon-based solar cells, DSSCs employ a photosensitive dye to capture sunlight and generate charge carriers, offering a cost-effective and flexible alternative to traditional photovoltaics (Aksoy et al., 2020; Mohammadian-Sarcheshmeh et al., 2020). The basic structure consists of a mesoporous titanium dioxide (TiO_2) semiconductor coated with dye molecules, an iodide/triiodide (I^-/I_3^-) redox electrolyte, and a counter electrode, typically made of platinum or carbon-based materials, to facilitate charge transfer (Bartkowiak et al., 2022; Mahalingam & Abdullah, 2016). Upon light absorption, the dye undergoes photoexcitation, injecting electrons into the TiO_2 conduction band, where they migrate to an external circuit to generate an electric current. Meanwhile, the electrolyte replenishes the oxidized dye, maintaining charge neutrality (Soman et al., 2018). DSSCs are particularly advantageous due to their ability to function efficiently under low-light conditions, making them ideal for indoor applications, portable electronics, and building-integrated photovoltaics (BIPV) (Ghosh et al., 2020). However, despite achieving power conversion efficiencies (PCEs) of up to 13% in laboratory conditions. DSSCs face challenges related to stability, electrolyte leakage, and long-term performance, which have hindered large-scale commercialization (Aksoy et al., 2019; Mohammadi et al., 2020; Mozaffari et al., 2015). Recent advancements, including co-sensitization strategies, nanostructured semiconductor materials, and solid-state electrolytes, have improved DSSC efficiency and durability, while hybrid perovskite-sensitized solar cells have demonstrated PCEs exceeding 20% (Carella et al., 2018; Soman et al., 2018). With continued progress in material engineering and device optimization, DSSCs remain a viable option for next-generation photovoltaics, particularly in applications requiring lightweight, flexible, and semi-transparent solar panels (Raguram & Rajni, 2022).

2.4.1 Structural Design of a DSSC

The structural design of a DSSC consists of four primary components that work together to convert sunlight into electricity (Wali et al., 2015). At the core is the photoanode, typically made of a transparent conductive substrate like fluorine-doped tin oxide (FTO) coated with a thin layer of nanocrystalline titanium dioxide (TiO_2), which provides a high surface area for dye adsorption (Al-Alwani et al., 2016). A photosensitive dye, often a ruthenium-based or organic compound, is adsorbed onto the TiO_2 surface to capture sunlight and generate excited electrons. These electrons flow through the TiO_2 and into the external circuit, creating an electrical current. The electrolyte, usually a liquid containing iodide/triiodide redox couples, facilitates electron transfer by regenerating the dye and completing the circuit (Khan et al., 2023). Finally, the counter-electrode, often made of platinum or carbon-based materials, enables the return of electrons from the external circuit to the electrolyte, ensuring continuous operation (Zhou et al., 2023). This layered, modular structure allows DSSCs to be lightweight, flexible, and cost-effective compared to traditional solar cells. Figure 2.8 represents a schematic diagram of the structural design of DSSC (Agrawal et al., 2022.).

2.4.2 The Counter Electrode

The counter electrode (CE) is a critical component of dye-sensitized solar cells (DSSCs), as it facilitates the regeneration of the redox mediator in the electrolyte by catalyzing the reduction reaction (Zheng et al., 2023). Typically, the CE is made of a conductive substrate coated with a catalyst material, with platinum (Pt) being the most commonly used due to its excellent catalytic properties and high electrical conductivity (Wu et al., 2017). Platinum's efficiency in catalyzing the reduction of triiodide (I_3^-) to iodide (I^-) contributes significantly to the overall performance of the DSSC. However, its high cost and scarcity has driven research into alternative materials to make DSSCs more economically viable (Richhariya et al., 2023). To reduce costs and maintain catalytic efficiency, various alternative materials for counter electrodes have been investigated, including carbon-based materials, transition metal compounds (Gao et al., 2018), and conducting polymers (Ibanez et al., 2018; Su'ait et al., 2015).

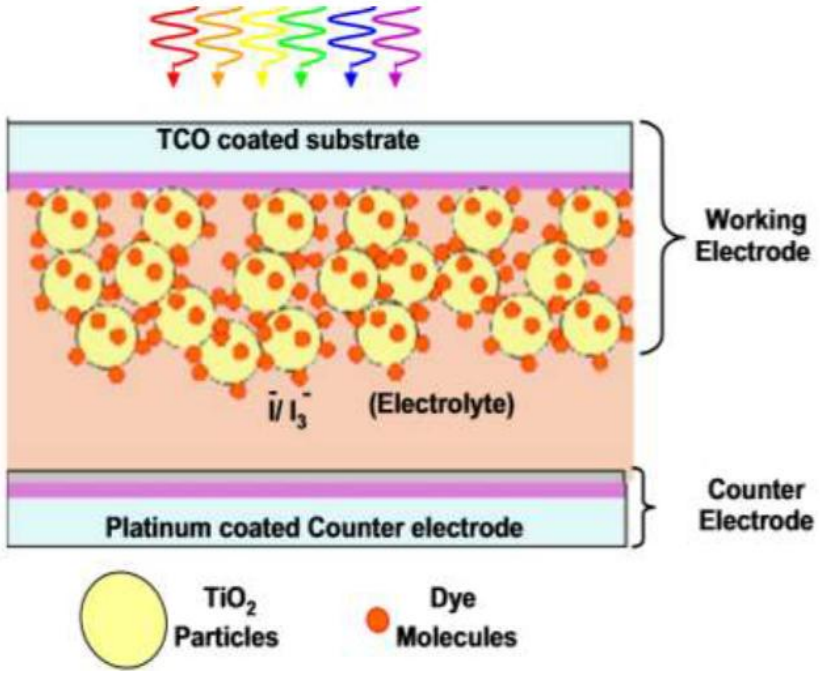

Figure 2.8: Structural Design of a Dye-Sensitized Solar Cell (Ngumbi 2021)

Carbon-based materials, such as graphite, carbon nanotubes, and graphene, have gained attention due to their abundance, low cost, and good electrical conductivity. For instance, studies have shown that graphene can offer comparable catalytic activity to platinum when adequately engineered. Similarly, metal sulfides (Xiao et al., 2015) and carbides, such as cobalt sulfide (CoS) (Hou et al., 2016; Huo et al., 2015)and molybdenum carbide (Mo_2C) (Rajeev et al., 2021), have demonstrated promising results as counter electrode materials, exhibiting strong catalytic activity and chemical stability.

In addition to cost and efficiency considerations, research on counter electrodes also focuses on enhancing stability and compatibility with different electrolyte systems (Mohammadi et al., 2020) . For instance, when using solid-state or ionic liquid electrolytes, the CE material must be optimized for high catalytic activity under non-liquid conditions. Emerging materials, such as conducting polymers like polyaniline and polythiophene, offer flexibility and tunable properties, making them suitable for various DSSC configurations (da S. et al., 2022). The continuous development of counter electrode materials is essential to improving the scalability and sustainability of DSSCs, paving the way for broader commercial applications.

2.4.3 The Photoanode

The photoanode is a vital component of dye-sensitized solar cells (DSSCs), serving as the site for light absorption and electron generation (Mohammadian-Sarcheshmeh et al., 2020; Murthy, 2019). It typically consists of a transparent conductive substrate, such as fluorine-doped tin oxide (FTO) or indium tin oxide (ITO), coated with a thin film of nanostructured titanium dioxide (TiO_2) (Navas et al., 2017). The high surface area of the TiO_2 nanoparticles facilitates the adsorption of photosensitive dye molecules, which capture sunlight and generate excited electrons. The electrons are injected into the conduction band of TiO_2 and then transported through the interconnected nanoparticles to the conductive substrate, forming an electric current. A layout of the functioning principles of DSSC is displayed in Figure 2.9. The efficiency of the photoanode depends on several factors, including the morphology and properties of the TiO_2 layer (Batmunkh et al., 2016). Advances in nanotechnology have led to the development of alternative structures, such as TiO_2 nanotubes, nanorods, and hierarchical structures, which enhance electron transport and reduce recombination losses (X. Yang et al., 2021). In addition to TiO_2, other materials like zinc oxide (ZnO) and tin oxide (SnO_2) (Batmunkh et al., 2016) have been explored as photoanode materials due to their comparable electronic properties and potential for improved performance under certain conditions. These alternative materials also offer opportunities to optimize the photoanode for different dyes and electrolytes.

Surface modifications and composite structures further enhance the performance of photoanodes. For example, coating the TiO_2 layer with a thin insulating layer of alumina (Al_2O_3) (Jia et al., 2015) or zirconia (ZrO_2) (Wu et al., 2023) can suppress recombination at the dye-TiO_2 interface and improve stability. Doping TiO_2 with elements such as lanthanide (Mulwa et al., 2016), nitrogen (Ritacco et al., 2022) or sulfur can extend its light absorption into the visible spectrum, increasing its efficiency in capturing sunlight. Additionally, integrating plasmonic nanoparticles, such as gold or silver (Hou et al., 2018), into the photoanode layer can enhance light harvesting through localized surface plasmon resonance. These innovations continue to push the boundaries of photoanode performance, making DSSCs a more competitive photovoltaic technology.

2.4.4 The Dye Sensitizer

The dye sensitizer is a pivotal component of dye-sensitized solar cells (DSSCs), as it is responsible for absorbing sunlight and initiating the photoelectric conversion process (Hwang et al., 2015; Prabavathy et al., 2017.). Typically, the dye molecules are adsorbed onto the surface of the titanium dioxide (TiO_2) photoanode, capturing photons and generating excited electrons. These electrons are subsequently injected into the conduction band of TiO_2, enabling the generation of electric current (Chen et al., 2019). The ideal dye sensitizer should exhibit a broad absorption spectrum, high molar extinction coefficient, and strong binding to the TiO_2 surface to maximize efficiency. The pioneering dyes used in DSSCs were ruthenium-based complexes, such as N3 and N719, which combine excellent stability, wide spectral absorption, and efficient electron injection (Scarabino et al., 2020).

Organic dyes have emerged as promising alternatives to ruthenium-based sensitizers, driven by the need for lower costs, sustainability, and environmental friendliness. These dyes often incorporate donor–acceptor structures to enhance light absorption and charge separation. For instance, coumarin, indoline, and triphenylamine-based dyes have demonstrated competitive efficiencies in DSSCs. Moreover, organic dyes can be fine-tuned to achieve specific electronic and optical properties, making them highly versatile for various DSSC configurations (Thomas, 2022). However, their stability under prolonged light exposure remains a challenge, requiring further advancements in molecular design and protective encapsulation strategies.

In addition to metal-complex and organic dyes, natural dyes extracted from plants, such as anthocyanins and chlorophyll, have been explored as eco-friendly sensitizers. These dyes are abundant, biodegradable, and cost-effective, making them suitable for sustainable DSSC applications (Carofiglio et al., 2020). Although natural dyes generally exhibit lower efficiencies compared to synthetic dyes, their use in hybrid or co-sensitization schemes has shown potential for enhancing performance. Co-sensitization, which involves combining multiple dyes with complementary absorption spectra, can improve light harvesting and broaden the device's spectral response (Kang et al., 2015). As research progresses, the dye sensitizer continues to be a focal point for innovation, contributing to the advancement of DSSCs as a viable solar energy technology.

2.4.5 The Liquid Electrolyte

The liquid electrolyte in a dye-sensitized solar cell (DSSC) plays a critical role in facilitating the transport of charge within the cell, enabling efficient energy conversion. It typically consists of an iodide/triiodide (I^-/I_3^-) redox couple dissolved in an organic solvent such as acetonitrile or propylene carbonate (Talip et al., 2020.). This redox couple acts as a mediator, transferring electrons from the counter electrode back to the dye molecules on the photoanode after they have released electrons to the external circuit. The electrolyte's high ionic conductivity and rapid redox kinetics are essential for minimizing energy losses and ensuring the continuous operation of the cell.

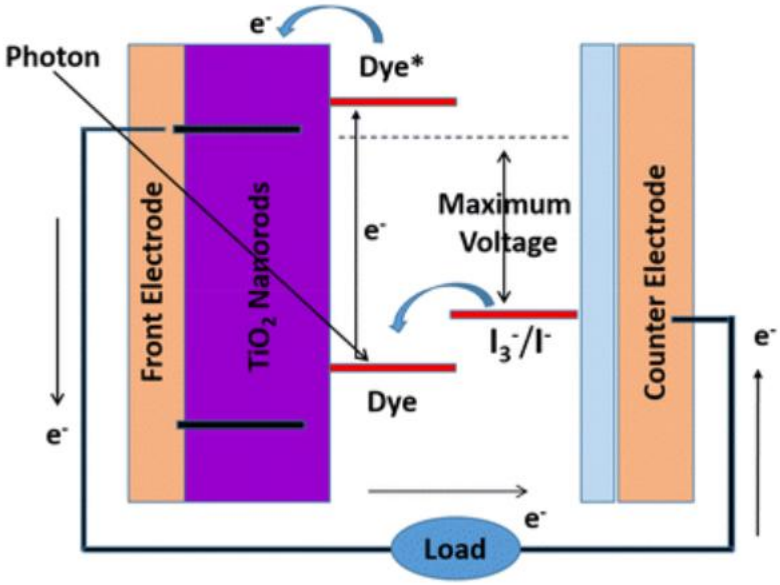

Figure 2.9: Dye Sensitize Solar Cell Schematic Band Diagram (Carella et al., 2018)

The relationship between the photon energy and the band gap of the mesoporous semiconductor is highlighted in Figure 2.9. However, liquid electrolytes in DSSCs present challenges related to stability and practicality. Volatile organic solvents can evaporate over time, leading to leakage and reduced performance (Iftikhar et al., 2019).Additionally, the corrosive nature of the iodide/triiodide system can degrade the electrodes and other cell components, limiting the cell's lifespan. To address these issues, research has focused on alternative electrolytes, such as ionic liquids, gel-based electrolytes (Önen et al., 2019.), and solid-state materials, which aim to maintain efficiency while improving stability and safety. These advancements are

critical for enhancing the durability and scalability of DSSC technology for real-world applications.

2.5 Structural Operations of DSSC

2.5.1 Photo-Energy Absorption and Dye Excitation

The operation of a dye-sensitized solar cell (DSSC) begins with the absorption of sunlight by the dye molecules anchored onto the surface of a mesoporous metal oxide semiconductive layer (Zhang et al., 2020). These dye molecules act as photosensitizers, capturing energy from sunlight by absorbing photons. When a dye molecule absorbs a photon, an electron within the dye is excited from its ground state to a higher energy state, creating an energized electron that is ready for transfer. This process, known as photoexcitation (Aksoy et al., 2019), is critical for initiating the energy conversion mechanism. The large surface area of the porous semiconductor ensures high dye loading, maximizing the capture of sunlight.

2.5.2 Electron Injection into the Conduction Band of TiO_2

Following excitation, the high-energy electron from the dye is injected into the conduction band (CB) of the TiO_2 semiconductor. This transfer occurs because the energy level of the excited dye is higher than the conduction band edge of the TiO_2, facilitating efficient electron movement (Ruess et al., 2019). The electron injection occurs on a timescale of femtoseconds to picoseconds, ensuring minimal energy losses. This process leaves the dye in an oxidized state, and the injected electrons are now free to contribute to the flow of current in the cell.

2.5.3 Electron Transport Through Semiconductor

Once inside the semiconductor layer, the injected electrons diffuse through the interconnected nanoparticles of the mesoporous structure toward the transparent conducting oxide (TCO) substrate, typically made of fluorine-doped tin oxide (FTO) glass (Marimuthu & Anandhan, 2017). The TCO serves as the anode, directing electrons into the external circuit, where they perform work before reaching the counter electrode. At the counter electrode, electrons reduce the triiodide (I_3^-) ions in the liquid electrolyte back to iodide (I^-), completing the external electrical loop. The reduction of the redox couple at the counter electrode is vital for maintaining the charge balance and ensuring the continuous operation of the DSSC (Rahman et al.,

2023).

2.5.4 Dye Regeneration and Recombination Processes

The oxidized dye molecules created during electron injection are regenerated by accepting electrons from the iodide ions in the electrolyte (Prabavathy et al., 2017). This reaction converts iodide into triiodide, maintaining the electrolyte's redox equilibrium. The regeneration of the dye ensures it remains active, allowing it to absorb more photons and sustain energy production. However, recombination processes can reduce the efficiency of the cell. Recombination occurs when electrons in the semiconductor recombine with oxidized species in the electrolyte or the dye before reaching the TCO (Zhou et al., 2023). To minimize recombination losses, DSSCs are designed with optimized energy alignments, surface treatments, and efficient charge transport materials, ensuring high efficiency in light-to-electricity conversion.

2.6 Properties of ZnO

ZnO is a versatile material that can crystallize into three primary phases (Figure 2.10): wurtzite, zinc blende, and rock salt, depending on the synthesis conditions and external influences like pressure and temperature. The wurtzite structure is the most stable and naturally occurring phase of ZnO under ambient conditions. It adopts a hexagonal crystal system (space group P63mc) with a characteristic tetrahedral coordination of Zn^{2+} and O^{2-} ions. This arrangement results in a non-centrosymmetric structure, which is responsible for its piezoelectric and pyroelectric properties. The wurtzite phase exhibits anisotropy in its physical properties, with different behaviors along the c-axis compared to other crystallographic directions. The zinc blende phase of ZnO is a metastable structure that can form under specific synthesis conditions, such as during growth on cubic substrates. This phase has a cubic crystal system (space group F43m), resembling the structure of sphalerite.

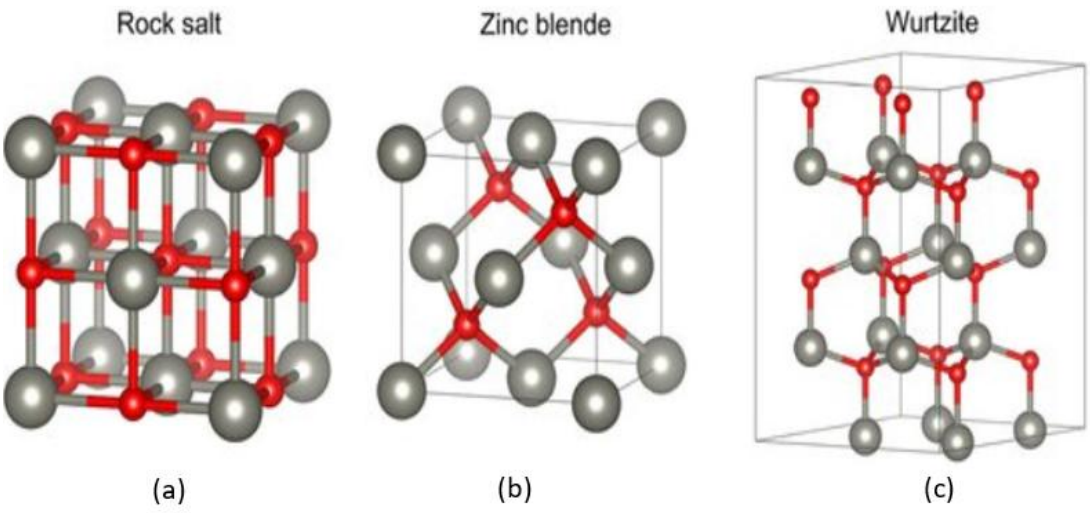

Figure 2.10: Crystal Structure of ZnO: (a) Rock salt, (b) Zinc blende and (c) Wurtzite (Ungula, 2017). The Oxygen Atoms are Shown as Red Spheres, Zinc Atoms as Grey Spheres

Like wurtzite, the zinc blende phase also features tetrahedral coordination, but the cubic symmetry makes it isotropic in its physical properties. Although less stable than wurtzite, zinc blende ZnO is of particular interest in optoelectronics due to its potential for integration with other cubic materials. The rock salt phase of ZnO emerges under high-pressure conditions, typically above 10 GPa. This phase adopts a cubic crystal system (space group $Fm\bar{3}m$), with octahedral coordination of Zn^{2+} and O^{2-} ions (Thomas, 2022). The rock salt structure is denser than wurtzite and zinc blende, resulting in distinct mechanical and optical properties. Transitioning to the rock salt phase involves significant rearrangement of the ZnO lattice, leading to a loss of the piezoelectric and polar characteristics inherent to the wurtzite structure. This phase is primarily studied for its high-pressure behavior and potential applications in advanced material science.

2.6.1 Structural Properties of Wurtzite ZnO (W-ZnO)

A semiconductor material composed of zinc oxide (ZnO) with a hexagonal wurtzite crystal structure is illustrated in Figure 2.11. The crystal structure consists of zinc atoms positioned between layers of hexagonally arranged oxygen atoms. Each zinc atom is tetrahedrally coordinated with four oxygen atoms as illustrated in Figure 2.11, while the oxygen atoms have a coordination number of four and the zinc atoms have a coordination number of two (Sun et al., 2005). This structural arrangement contributes to the unique physical and chemical properties of ZnO.

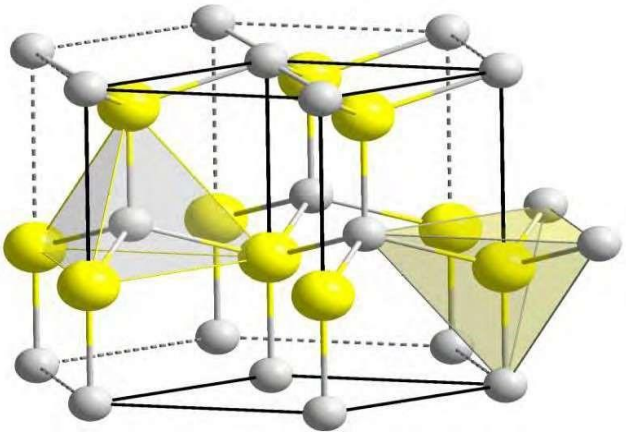

Figure 2.11: Typical Hexagonal Wurtzite Structure of ZnO (Bett et al., 2024), the Oxygen Atoms are Shown as Grey Spheres, Zinc Atoms as Yellow Spheres

The hexagonal symmetry of ZnO results in two primary lattice constants: the c-axis and the a-axis. The c-axis is aligned perpendicular to the basal hexagonal plane, while the a-axis is tilted at an angle of 60° relative to the c-axis (Wang et al., 2006). These lattice parameters define the overall geometry of the ZnO crystal and play a crucial role in its electronic and optical behavior. One of the key attributes of ZnO's crystal structure is its ability to incorporate dopants without disrupting its hexagonal configuration (Ritacco et al., 2022). This makes it an ideal material for modifying electronic and optical properties through doping. Additionally, the structural characteristics of W-ZnO significantly influence its mechanical, electronic, dynamical stability, electrical, optical, and magnetic properties. For example, due to its hexagonal symmetry, ZnO exhibits anisotropic electrical conductivity, meaning that charge transport varies along the c- and a-axes. This anisotropy has important implications for applications in semiconductors, optoelectronics, and piezoelectric devices. Moreover, the wurtzite structure of ZnO plays a significant role in determining its ability to form various nanostructures, including nanowires, nanorods, and nanoparticles. These different morphologies are essential in the development of nanoscale electronic devices, sensors, and photocatalytic materials (Tusche et al., 2007). Understanding ZnO's structural properties is therefore critical for optimizing its performance in a wide range of scientific and industrial applications.

2.6.2 Lattice Dynamic Properties of Wurtzite-ZnO

Lattice dynamics in ZnO are fundamental to its behavior in optoelectronic and energy applications, as they govern phonon transport, thermal conductivity, and interactions with charge carriers. In its wurtzite structure, ZnO exhibits polar optical phonon modes which are particularly sensitive to lattice perturbations including strain, doping, and temperature. Recent computational studies using DFT-based phonon dispersion analysis confirm that these modes dominate ZnO's infrared and Raman spectra and are critical for understanding electron–phonon coupling in devices such as LEDs and solar cells (Sharma et al., 2021). Such vibrational properties also influence carrier lifetimes and thermal stability, particularly in nanostructured ZnO where surface phonon confinement becomes significant.

The introduction of dopants, such as rare-earth (RE) ions, further modifies the phonon behavior of ZnO by introducing localized vibrational states and increasing phonon scattering. These changes result in reduced phonon group velocities and altered phonon density of states, which in turn impact both thermal and electronic transport properties (Wang et al., 2020). For instance, RE-doped ZnO has shown broadened and red-shifted phonon peaks in Raman spectra, indicating a softened lattice and increased disorder. Such modifications enhance phonon scattering, which is desirable in thermoelectric applications and beneficial for DSSCs by promoting phonon-assisted exciton dissociation and reducing recombination losses. Therefore, lattice dynamics remain a key parameter in tailoring ZnO-based materials for improved functional.

2.6.3 Mechanical Properties of W-ZnO

ZnO is known for its favorable mechanical properties, particularly high elastic modulus and structural integrity, which make it suitable for applications in flexible electronics, sensors, and piezoelectric devices. In its wurtzite structure, ZnO demonstrates elastic anisotropy due to differences in bonding along the crystallographic axes. Elastic constants such as C_{11}, C_{12} and C_{33} have been found to meet the mechanical stability conditions for hexagonal systems, confirming that the material can withstand external mechanical stresses without structural failure (Zhou et al., 2020). Additionally, nanoscale ZnO has shown enhanced mechanical resilience, with reported Young's modulus values around 140–150 GPa, supporting its use in

devices requiring mechanical robustness (Rafique et al., 2019). The moderate values of Poisson's ratio and shear modulus further confirm ZnO's balance between stiffness and flexibility, key features in wearable and stretchable technologies.

Doping ZnO with RE elements significantly influences its mechanical behavior. These dopants introduce lattice distortions due to ionic size mismatch and alter the bonding environment, leading to variations in the elastic constants and moduli. Studies have shown that RE doping generally reduces the stiffness of ZnO, as evidenced by decreased values of the bulk and shear moduli, which implies a slight shift toward ductile behavior (Tanwar et al., 2017). Despite this softening, the doped ZnO systems remain mechanically stable and often display improved toughness and flexibility traits desirable in dye-sensitized solar cells (DSSCs), where mechanical compliance supports substrate bending without compromising device performance (Haider et al., 2021). Thus, the tunability of ZnO's mechanical properties through RE doping presents a strategic pathway for optimizing materials in next-generation flexible photovoltaic applications.

2.6.4 Electronic Properties of Wurtzite-ZnO

Zinc oxide (ZnO) is a wide-bandgap semiconductor characterized by a direct bandgap of as shown in Figure 2.12 at room temperature, making it highly suitable for optoelectronic devices such as UV light-emitting diodes, laser diodes, and photodetectors. Its high electron mobility, typically ranging between 100 and 200 $cm^2/V \cdot s$, is attributed to the low effective mass of electrons and reduced scattering. In addition, ZnO possesses a notably high exciton binding energy of around 60 meV, which exceeds room temperature thermal energy and ensures that excitonic effects remain significant even under ambient conditions. This inherent property enhances its performance in UV applications. Naturally, ZnO exhibits n-type conductivity due to intrinsic defects like oxygen vacancies and zinc interstitials that introduce donor levels in the conduction band. Despite these advantageous properties, ZnO faces challenges, particularly in achieving reliable p-type doping. Attempts to induce p-type conductivity by incorporating dopants such as lithium, sodium, or nitrogen are often compromised by self-compensating defects, which limit its effectiveness in applications that require p-n junctions or transparent electronics.

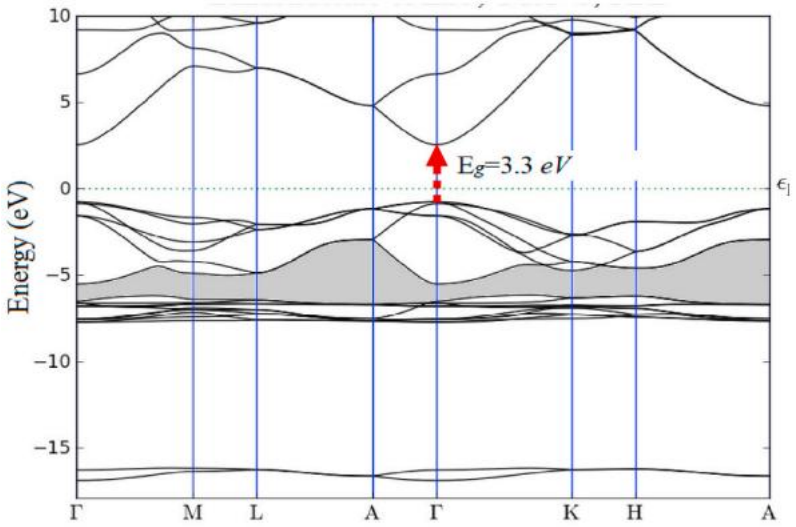

Figure 2.12: Band Structure of Wurtzite ZnO (Javarova & Orudzhev, 2021)

Additionally, the hexagonal wurtzite structure of ZnO leads to anisotropic charge transport, with electron mobility and conductivity varying between the c-axis and a-axis. This anisotropy necessitates careful design considerations in device fabrication. Overall, while ZnO's electronic attributes hold great promise, overcoming these challenges is essential for its broader implementation in advanced semiconductor technologies.

2.6.5 Optical Properties of W-ZnO

The reflectance spectrum of W-ZnO (Figure 2.13a) typically shows moderate reflection in the UV region that gradually decreases as the wavelength increases into the visible range (Touri et al., 2020). This behavior indicates that wurtzite ZnO strongly interacts with high-energy photons near and slightly above its band edge, causing more reflection at shorter wavelengths. By analyzing the absorption edge in tandem with reflectance data, one can determine the optical band gap (Figure 2.13b), which for undoped or lightly doped wurtzite ZnO often lies around 3.2–3.4 eV (Ungula & Dejene, 2016a). This relatively wide gap confines optical absorption mainly to the UV region, giving ZnO its transparent appearance in the visible spectrum and making it attractive for applications such as UV photodetectors and transparent electrodes.

In Figure 2.14a, the transmittance curve generally shows high transparency across the visible range, often exceeding 80–90% transmittance, underscoring ZnO’s potential for optoelectronic devices that require high visible-light transmission (Xu & Ching,

1993). The absorbance spectrum (Figure 2.14b) highlights strong absorption just below 400 nm, consistent with the band gap's UV region. This sharp absorption onset aligns with the band edge determined from the reflectance and band-gap analyses, confirming that the material effectively blocks or absorbs harmful UV light while allowing visible wavelengths to pass. Collectively, these optical characteristics; moderate reflectance near the UV range, a wide band gap, high transmittance in the visible, and strong UV absorbance make wurtzite ZnO a versatile material for applications such as solar cells, photocatalysis, and UV-protective coatings.

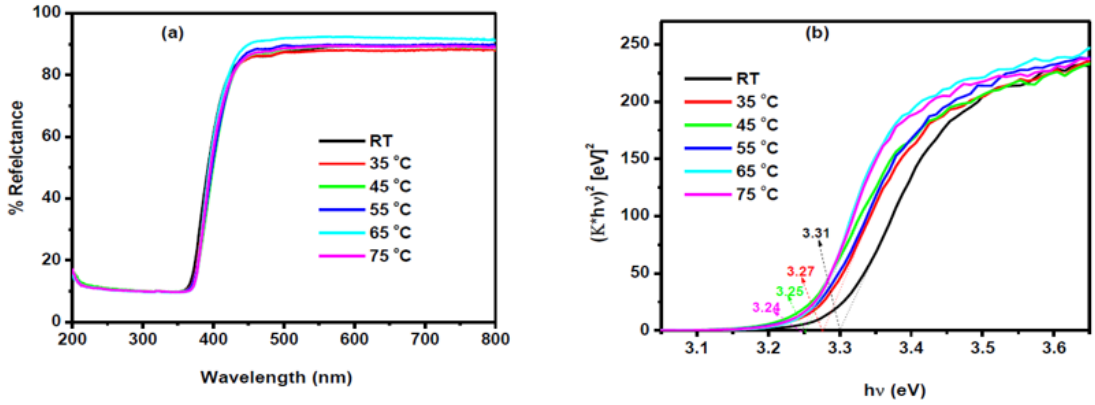

Figure 2.13: The (a) Reflectance and (b) Optical Band Gap of Wurtzite ZnO at Different Temperatures (Ungula et al., 2018)

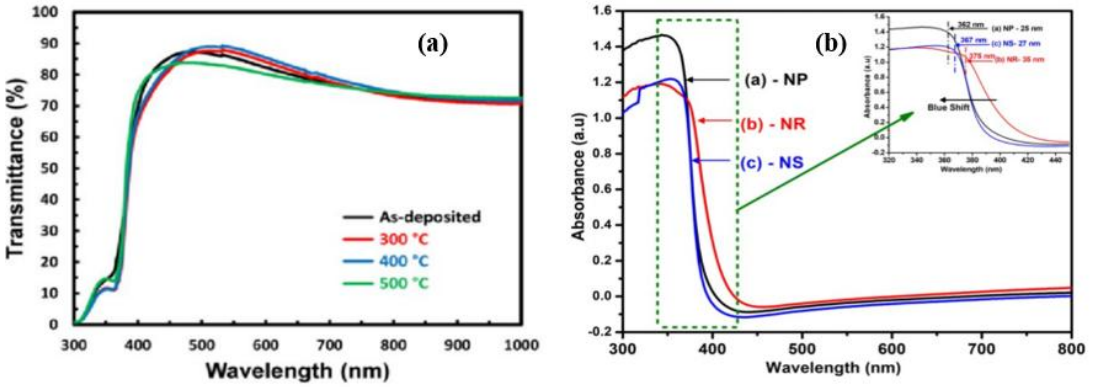

Figure 2.14: The (a) Transmittance and (b) Absorbance of ZnO as a Function of Wavelength in nm (Touri et al., 2020)

The versatility of ZnO is further enhanced by the ability to synthesize it in various nanostructured forms, such as nanowires, nanorods, and nanoparticles. These nanostructures not only provide additional control over the optical properties through quantum confinement effects and increased surface-to-volume ratios but also lead to improved light-matter interactions. As a result, ZnO-based nanostructures are being

actively explored for advanced applications in photocatalysis, biosensing, and UV detection, where enhanced optical absorption and emission are essential. Overall, the combination of a wide bandgap, strong UV response, and the potential for fine-tuning its optical characteristics renders ZnO a highly promising material for next-generation optoelectronic and photonic devices.

2.6.6 Photoluminescence of ZnO

Zinc oxide (ZnO) is celebrated for its remarkable luminescence, which originates from its wide bandgap and distinctive crystal structure that can be modified through doping to enhance its light-emitting capabilities. It exhibits two primary forms of luminescence: ultraviolet (U.V) and visible emissions, both of which have garnered considerable attention for applications in lighting, displays, and sensor technology (Arbosara et al., 2015). As shown in Figure 2.15, the UV emission is predominantly due to the near-band-edge (NBE) transition, a process where excited electrons recombine with holes in the valence band, typically resulting in a peak emission at around 380 nm.

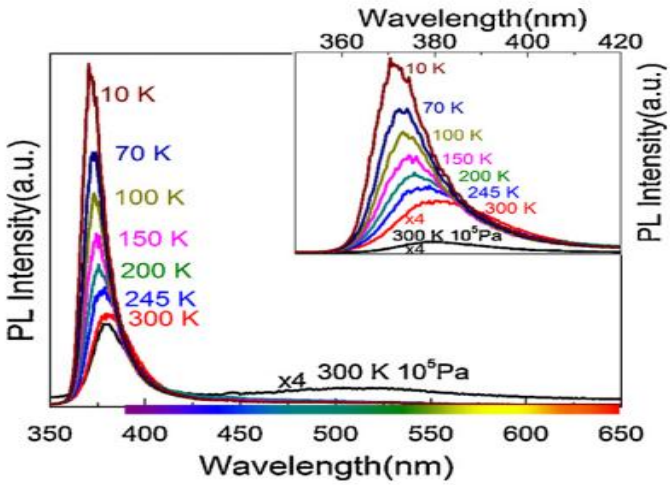

Figure 2.15: Photoluminescese of ZnO at Different Temperatures (Zhao et al., 2016)

This value is influenced by the material's crystal quality and morphology and temperature. In contrast, the visible emission in ZnO is mainly attributed to intrinsic defects such as oxygen vacancies, zinc interstitials, and zinc vacancies, which produce a broad emission band peaking near 500 nm, particularly within the blue-green spectrum (Agarwal et al., 2022). The overall luminescent behavior of ZnO can be tailored by adjusting several parameters, including surface modifications,

annealing treatments, and the incorporation of dopants. For instance, introducing rare-earth elements or transition metals can alter its optical properties by creating trap states within the bandgap, while high-temperature annealing has been shown to enhance the NBE emission and reduce defect concentrations.

2.6.7 Transport Properties

ZnO is a widely studied n-type semiconductor due to its wide band gap, moderate electron mobility, and intrinsic defect-mediated conductivity. In its undoped form, ZnO exhibits relatively high carrier mobility (up to 200 $cm^2/V \cdot s$), primarily due to native defects such as oxygen vacancies and zinc interstitials that act as shallow donors (Kumar et al., 2020). However, these intrinsic carriers can be unstable and sensitive to environmental conditions, motivating controlled doping to stabilize and enhance charge transport. Doping ZnO with group III elements such as Ga and Al introduces extra free electrons by substituting Zn^{2+} with trivalent Ga^{3+} or Al^{3+}, thereby significantly improving electrical conductivity while maintaining optical transparency making such doped ZnO ideal for transparent conductive oxide (TCO) applications (Wang et al., 2020; Yadav et al., 2021). On the other hand, non-metallic dopants such as N have been explored to induce p-type behavior in ZnO, although with limited success due to compensation by native donor defects (Chen et al., 2019).

In recent years, doping with lanthanide elements such as La, Nd, and Gd has gained attention for modifying the transport behavior of ZnO. These dopants introduce localized 4f states that interact with ZnO's conduction band, influencing carrier mobility and defect chemistry. For example, La-doped ZnO has been shown to enhance carrier concentration and reduce resistivity due to its large ionic radius and the creation of oxygen vacancies that promote electron transport (Patel et al., 2022). Gd and Nd doping also modify the band structure and phonon scattering behavior, making them promising for thermoelectric and photovoltaic applications where optimized electron and phonon transport are required (Ahmed et al., 2021). Furthermore, codoping strategies, such as Ga-N or Al-La, offer a synergistic effect, balancing carrier concentration, mobility, and thermal conductivity. Such tunability demonstrates the versatility of ZnO-based systems for energy harvesting and optoelectronic applications where efficient charge transport is essential.

2.7 Zinc Oxide Based Solar Cells

Zinc oxide (ZnO) is a versatile and widely studied material for various types of solar cells, including DSSCs, thin-film solar cells, and perovskite solar cells. Its wide bandgap (3.37 eV), high exciton binding energy (60 meV) (Serrano et al., 2004), and excellent optical and electronic properties make it a strong candidate for use in photovoltaics. ZnO is particularly valued for its ability to form diverse nanostructures such as nanorods, nanowires (Song et al., 2015), and nanoparticles (Bett et al., 2024), which can improve light absorption, charge transport, and device efficiency. Additionally, ZnO is abundant, low-cost, and environmentally friendly, making it suitable for scalable solar cell production.

In DSSCs, ZnO serves as a photoanode material as shown in Figure 2.16, where its high electron mobility facilitates faster electron transport, reducing recombination losses. In thin-film solar cells, ZnO acts as a transparent conducting oxide (TCO) layer (Saxena et al., 2022) , providing a substrate that allows light to pass through while conducting electrons efficiently. ZnO is also utilized as an electron transport layer (ETL) in perovskite solar cells, where it aids in extracting and transporting electrons from the perovskite absorber to the electrode. Its tunable properties, such as bandgap engineering and nanostructure optimization, allow it to be adapted for specific solar cell applications.

These characteristics make ZnO an effective alternative to titanium dioxide (TiO_2), the most commonly used material in DSSCs. ZnO serves as the photoanode material in DSSCs, where its ability to transport photo-generated electrons from the dye molecules to the external circuit is crucial. Additionally, ZnO’s tunable morphology allows for the fabrication of various nanostructures, such as nanorods, nanowires, and nanoparticles, which can improve light harvesting and electron transport efficiency. One of ZnO's significant advantages in DSSCs is its ease of synthesis and versatility in forming diverse nanostructures, which play a key role in enhancing the dye loading and light absorption (Li et al., 2018).

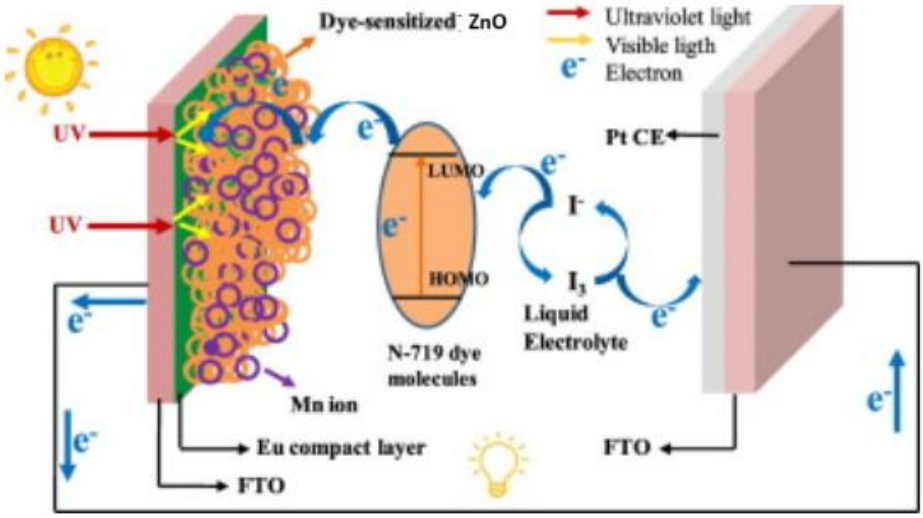

Figure 2.16: Schematic Diagram of ZnO-Based DSSC (Mahalingam & Abdullah, 2016)

Nanostructures like ZnO nanorods and nanowires provide direct pathways for electron transport, minimizing recombination losses and improving the efficiency of charge collection. ZnO's ability to form hierarchical architectures expands its surface area (Ungula et al., 2018) which can further enhance its conductivity and reduce charge recombination. Additionally, combining ZnO with other materials, such as graphene or quantum dots (D. Debnath et al., 2023), has shown promise in boosting light harvesting and improving the photovoltaic performance of DSSCs. These advancements continue to make ZnO a promising material for next-generation DSSC applications.

2.8 Rare Earth Metals

Rare earth metals, also known as lanthanides as listed in Table 2.1, were first identified in the late 18th century, starting with yttrium's discovery by Carl Axel Arrhenius in 1787 (Kaur et al., 2022). Over the following century, several other lanthanides were isolated (Figure 2.17), including cerium (1803), lanthanum (1839), and neodymium (1885). The large-scale production of rare earth elements (REEs) began in the 1950s, with the United States dominating global supply (Adunka & Orna, 2018). However, China took the lead in the 1990s and now accounts for over 60% of global REE production (USGS, 2023). Rare earth extraction involves complex processes such as solvent extraction and ion exchange due to the similarity in their chemical properties (Gupta & Bhattacharya 2018).

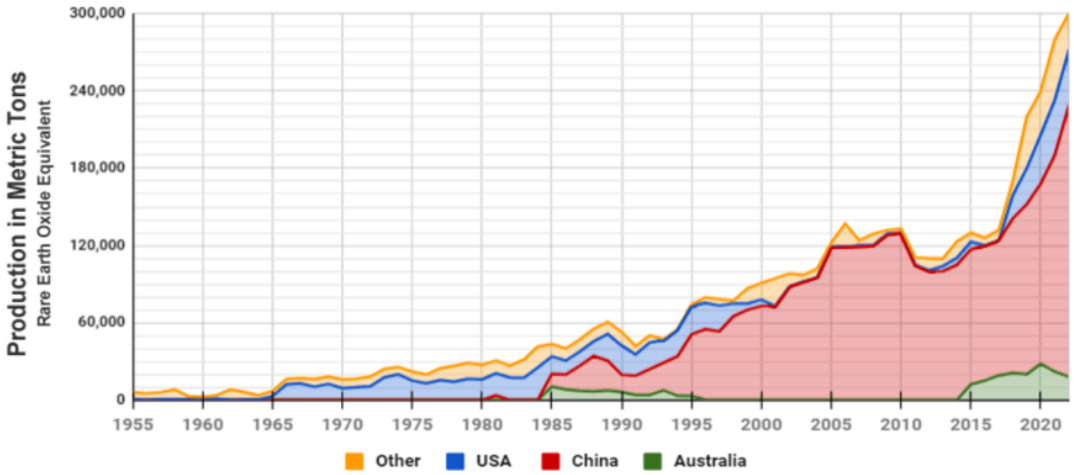

Figure 2.17: Production of Rare Earth Elements (King H., 2023)

Table 2.1: The General Properties of Rare Earth (RE) Metals

Element	**Symbol**	**Atomic Number**	**Electronic Configuration**	**Melting Point (°C)**	**Magnetic Property**
Lanthanum	La	57	[Xe] $5d^1$ $6s^2$	920	Paramagnetic
Cerium	Ce	58	[Xe] $4f^1$ $5d^1$ $6s^2$	795	Paramagnetic
Praseodymium	Pr	59	[Xe] $4f^3$ $6s^2$	931	Paramagnetic
Neodymium	Nd	60	[Xe] $4f^4$ $6s^2$	1024	Strongly Paramagnetic
Promethium	Pm	61	[Xe] $4f^5$ $6s^2$	1100	Paramagnetic
Samarium	Sm	62	[Xe] $4f^6$ $6s^2$	1072	Weakly Paramagnetic
Europium	Eu	63	[Xe] $4f^7$ $6s^2$	822	Strongly Paramagnetic
Gadolinium	Gd	64	$4f^7$ $5d^1$ $6s^2$	1312	Ferromagnetic
Terbium	Tb	65	[Xe] $4f^9$ $6s^2$	1356	Strongly Paramagnetic
Dysprosium	Dy	66	[Xe] $4f^{10}$ $6s^2$	1412	Strongly Paramagnetic
Holmium	Ho	67	[Xe] $4f^{11}$ $6s^2$	1474	Strongly Paramagnetic
Erbium	Er	68	[Xe] $4f^{12}$ $6s^2$	1529	Weakly Paramagnetic
Thulium	Th	69	[Xe] $4f^{13}$ $6s^2$	1545	Weakly Paramagnetic
Ytterbium	Yb	70	[Xe] $4f^{14}$ $6s^2$	824	Weakly Paramagnetic
Lutetium	Lu	71	[Xe]$4f^{14}5d^1$ $6s^2$	1663	Paramagnetic

The chart in Figure 2.17 depicts the historical production of rare earth elements, measured in metric tons of rare earth oxide equivalent, from 1950 to 2022. It highlights the United States' market entry in the mid-1960s, driven by the surge in demand for color television. In the late 1980s and early 1990s, China's introduction of low-cost rare earths forced U.S. mines to shut down due to unprofitability. When China restricted exports in 2010, rare earth prices soared, spurring production in countries like the United States, Australia, Russia, Thailand, Malaysia, and others. In 2018, data from Burma Myanmar became available, significantly increasing the "others" category in production statistics, though some of its earlier production may have gone unreported. These elements are characterized by their partially filled 4f orbitals, which contribute to their unique optical, magnetic, and electronic properties as shown in Table 2.1. Lanthanides are typically silvery-white, soft metals with high reactivity, especially when finely divided. Their notable properties include high magnetic susceptibility, sharp emission spectra, and excellent ability to absorb and emit light in specific wavelengths. Lanthanides have diverse applications across various industries due to their specialized properties. Neodymium (Nd) and samarium (Sm) are essential in the production of high-performance magnets used in electric vehicles, wind turbines, and

electronic devices. Europium (Eu) and terbium (Tb) are critical components in phosphors for energy-efficient lighting and display screens, while cerium (Ce) is widely used in catalytic converters and glass polishing. Dysprosium (Dy) and holmium (Ho) are valuable for their magnetic properties, finding applications in data storage and advanced motors. Additionally, gadolinium (Gd) is used in medical imaging as a contrast agent in magnetic resonance imaging (MRI). The lanthanides' ability to emit sharp and narrow spectral lines also makes them essential in lasers and optical devices, while their catalytic capabilities are utilized in refining and chemical synthesis processes.

2.9 RE-Doped ZnO Based DSSC

Lanthanide-doped zinc oxide (ZnO) has emerged as a versatile material for improving the photoanode performance of dye-sensitized solar cells (DSSCs) due to the distinctive properties of the 15 lanthanides—lanthanum (La), cerium (Ce), praseodymium (Pr), neodymium (Nd), promethium (Pm), samarium (Sm), europium

(Eu), gadolinium (Gd), terbium (Tb), dysprosium (Dy), holmium (Ho), erbium (Er), thulium (Tm), ytterbium (Yb), and lutetium (Lu). These elements share the presence of partially filled 4f orbitals that impart unique optical, electronic, and magnetic characteristics to host materials. Doping ZnO with lanthanides introduces localized energy levels within the band gap and modifies its band structure, enhancing light absorption, electron mobility, and suppressing recombination losses (Khuili et al., 2020; Labazanova et al., 2021). For instance, Ce and Eu are widely studied for their redox-active states (Ce^{3+}/Ce^{4+}, Eu^{2+}/Eu^{3+}), which facilitate charge transfer processes within the ZnO matrix (Waqas et al., 2022; Zhang et al., 2021), while Nd and Tb dopants have been shown to enhance near-infrared (NIR) light absorption, expanding the spectral response of DSSCs (Vijayaprasath et al., 2015; Madathilakath Kurian & Govindarajan, 2021).

Each lanthanide offers distinct advantages based on its ionic radius, oxidation state, and electronic transitions. Early lanthanides like La, Pr, and Nd generally increase the crystallinity and conductivity of ZnO, enhancing charge transport properties. Middle lanthanides such as Sm, Gd, and Dy contribute to improved electron mobility and defect modulation due to their balanced ionic size and polarizability. Notably, Gd and Dy doping also suppresses charge recombination by inducing surface passivation effects and energy level alignment. Heavier lanthanides including Er, Tm, Yb, and Lu are particularly attractive for their upconversion luminescence properties, where low-energy photons are converted into higher-energy emissions, potentially enhancing light harvesting in DSSCs under low-intensity or diffuse sunlight (Haider et al., 2022; Kumar et al., 2023). For example, Yb-doped ZnO has demonstrated improved photo response in the NIR range due to effective energy transfer mechanisms, while Er-doped ZnO enhances both optical absorption and photoconductivity. Despite these advances, the incorporation of elements like Pm is rare due to its radioactivity and limited availability, and Lu is less studied due to its closed 4f shell, though it may offer structural stability benefits.

While lanthanide doping in ZnO significantly enhances DSSC performance, critical challenges remain in achieving uniform doping, avoiding secondary phase formation, and ensuring thermal and chemical stability. High doping concentrations may lead to lanthanide clustering or ZnO lattice distortion, adversely affecting electron mobility

and optical clarity (Mulwa, 2017). Therefore, synthesis techniques such as sol-gel, hydrothermal, and atomic layer deposition are being refined to achieve precise doping control and nanoscale uniformity (Mwalukuku et al., 2023). Additionally, dye–semiconductor and electrolyte–photoanode compatibility must be maintained to ensure optimal electron injection and minimal back recombination. Despite these constraints, the tunable properties of lanthanide-doped ZnO ranging from defect passivation and band gap modulation to luminescence enhancement present a highly adaptable platform for DSSC innovation. With continued exploration of the full lanthanide series and hybrid doping strategies, future DSSCs could achieve greater efficiency, spectral range, and operational stability.

2.10 The Ce, Dy and Eu Doping of ZnO for DSSC Photoanodes

The Ce, Dy, and Eu doping in ZnO has garnered significant attention for enhancing the performance of DSSC photoanodes by modifying the material's electronic and optical properties (Nowsherwan et al., 2024). These elements possess partially filled 4f orbitals, which are known to induce sharp emission bands and enhance optical activity through efficient upconversion and downconversion processes. Upconversion refers to the process whereby lower-energy (infrared) photons are absorbed and converted into higher-energy (visible) photons, effectively extending the spectral response of the ZnO photoanode (Biswas & Chatterjee, 2022). On the other hand, downconversion refers to the process through which high-energy photons are absorbed and then re-emitted as multiple lower-energy photons that are more efficiently absorbed by the dye molecules (Kaur et al., 2022). Such processes are particularly useful in DSSCs as they can broaden the absorption range of incident solar radiation by converting low-energy photons to higher energies (upconversion) or vice versa (downconversion), thus improving light harvesting efficiency. The ionic radii of Ce^{3+} (1.01 Å), Dy^{3+} (0.91 Å), and Eu^{3+} (0.95 Å) are reasonably close to that of Zn^{2+} (0.74 Å), allowing for substitutional doping without inducing excessive lattice distortion, which is essential for maintaining the structural integrity of ZnO while tuning its electronic and optical properties (El Amine Monir & Dahou, 2020). Ce and Dy dopants, while primarily introduced to enhance electron mobility and reduce recombination, also contribute to modifying the local electronic structure in a manner that facilitates upconversion processes, further broadening the range of incident light that can be harnessed by the DSSC (Madathilakath Kurian & Govindarajan, 2021).

Additionally, several studies have demonstrated that doping ZnO with Ce, Dy, or Eu can significantly enhance its performance characteristics for optoelectronic applications (Kaur et al., 2022). For instance, Ce doping has been shown to introduce donor states that improve electrical conductivity and promote charge transport (Meshram et al., 2017), while Dy enhances photoluminescence and reduces recombination losses by creating trap states (Kaur et al., 2022). Eu, on the other hand, is widely known for its red luminescence and high quantum efficiency, which can contribute to extended light absorption and better charge separation in the photoanode (Tahir et al., 2024). These RE elements also exhibit high thermal and chemical stability, making them suitable for improving the long-term durability of ZnO-based DSSCs. Therefore, the choice of Ce, Dy, and Eu as dopants is both strategic and evidence-based, aimed at leveraging their distinctive electronic configurations and optical behaviors to optimize the photoanode performance.

2.11 *Ab initio* Techniques

2.11.1 Quantum Mechanics

The gradual development of ab initio calculations is closely tied to advancements in computational resources and the refinement of algorithms (Yin & Cohen, 1982). These first-principle methods, grounded in quantum mechanics, provide a powerful tool for understanding and predicting the behavior of materials at the atomic level. By directly solving the Schrödinger equation without relying on empirical parameters, ab initio calculations can confirm experimental results and offer insights into materials that have yet to be synthesized, guiding the discovery of novel materials with promising properties (Rubio, 2020). Utilizing quantum theory, these calculations enable precise differentiation between metals, insulators, and semiconductors by analyzing electronic band structures. Moreover, they are instrumental in characterizing materials' optical, magnetic, and elastic properties, which are crucial for applications in technology and engineering. The integration of ab initio methods into materials research accelerates innovation, bridging the gap between theoretical predictions and experimental realizations, and paving the way for the design of advanced functional materials (Harper et al., 2020).

2.11.2 The Many-Body System Theory

The many-body system theory is a framework in quantum mechanics that deals with the complex interactions of a large number of particles, such as electrons, atoms, or molecules, within a system. Unlike single-particle systems, where the behavior of one particle can be described independently, many-body systems require accounting for interactions between particles, making the problem exponentially more challenging. The theory employs fundamental principles like the Schrödinger equation to describe the quantum state of the entire system, but solving it exactly for many particles is often intractable. Consequently, approximate methods such as mean-field theory, perturbation theory, and Green's function techniques are used to study phenomena like superconductivity, magnetism, and electronic correlations in materials.

Key advancements in many-body theory include the development of quantum field theory methods (Khuili et al., 2016), which introduce concepts like second quantization and Feynman diagrams to simplify calculations. These tools allow for systematic treatment of interactions and provide insights into emergent behaviors that arise from collective effects, such as phase transitions and quasiparticle excitations. Applications of many-body theory extend across condensed matter physics, nuclear physics, and statistical mechanics, enabling the understanding of complex systems like metals, semiconductors, and even biological systems. As computational power grows, numerical methods like Density Matrix Renormalization Group (DMRG) and Quantum Monte Carlo (QMC) (Ceperley & Alder, 1986)have become essential for tackling many-body problems, providing precise solutions to questions at the forefront of physics research. The foundation lies in the many-body Schrödinger Equation 2.1.

$$\hat{\mathrm{H}}\psi_{\mathrm{K}}(\mathrm{r}_1\sigma_1 \ldots \mathrm{r}_{\mathrm{N}}\sigma_{\mathrm{N}}) = \mathrm{E}_{\mathrm{k}}\psi_{\mathrm{K}}(\mathrm{r}_1\sigma_1 \ldots \mathrm{r}_{\mathrm{N}}\sigma_{\mathrm{N}}) \tag{2.1}$$

where, $\hat{H}$ is the Hamiltonian of a many electrons system, K denotes the complete set of quantum numbers describing the many-electron system, ψ represents the electron's wave function, and E signifies the system's total energy while $\mathrm{r_i}$ and σ_i are the spatial coordinates and spin states of the ith particle respectively. Particles with half-integer spins, such as electrons, are characterized by antisymmetric wave functions, expressed as in Equation 2.2.

$$\psi(r_1\sigma_1 \ldots., r_i\sigma_i \ldots. r_j\sigma_j \ldots r_N\sigma_N) = -\psi(r_1\sigma_1 \ldots., r_i\sigma_i \ldots. r_j\sigma_j \ldots r_N\sigma_N) \quad (2.2)$$

and it is observed that they adhere to the Pauli exclusion principle (Makov et al., 1995). These particles are referred to as fermions. The Pauli Exclusion Principle asserts that no two electrons can share the same set of quantum numbers, and that electrons with identical spins cannot occupy the same state at the same time. On the other hand, bosons are particles described by symmetric wave functions when exchanged, and they possess either integral or zero intrinsic spin. Since there are N! distinct permutations of the labels 1, 2, ...N, and according to equation (2.3), all of these permutations result in the same $|\psi|^2$, the probability of finding an electron with spin σ_1 in the volume element d^3r_1 is defined by Equation 2.3.

$$N!\,|\psi_K(r_1\sigma_1 \ldots \ldots r_N\sigma_N)|^2 d^3r_1 \ldots d^3r_N \quad (2.3)$$

Taking into account all the interactions between electrons and nuclei, the actual Hamiltonian operator $\hat{H}$ is expressed in Equation 2.4.

$$\hat{H} = \frac{\hbar^2}{2m_e}\sum_i + \sum_{iI}\frac{Z_I e^2}{|r_i - R_I|} + \frac{1}{2}\sum_{i\geq j}\frac{e^2}{|r_i - r_j|} - \sum_I \frac{\hbar^2}{2M_I}\nabla_I^2 + \frac{1}{2}\sum_{I\geq J}\frac{Z_I Z_J e^2}{|R_I - R_J|} \quad (2.4)$$

∇_i^2

In this context, the electron mass m_e and charge e are indicated by lowercase subscripts, while the nuclei, with mass M_I and core charge Z_I are denoted by uppercase subscripts. The terms in equation (2.4) represent the electronic kinetic energy operator (Diale et al., 2023),.$\hat{T}_e = \frac{\hbar^2}{2m_e}\sum_i \nabla_i^2$, the nuclei potential acting on the electrons, $V_{en} = \sum_{iI}\frac{Z_I e^2}{|r_i - R_I|}$, the electron- electron repulsion $V_{ee} = \frac{1}{2}\sum_{i\geq j}\frac{e^2}{|r_i - r_j|}$, the nucleic kinetic energy $\hat{T}_e = \sum_I \frac{\hbar^2}{2M_I}\nabla_I^2$ and the nuclei-nuclei repulsion operator $\frac{1}{2}\sum_{I\geq J}\frac{Z_I Z_J e^2}{|R_I - R_J|}$. This can be simplified by Equation 2.5.

$$\hat{H} = \hat{T}_e + \hat{V}_{en} + \hat{V}_{ee} + \hat{T}_n + \hat{V}_{nn} \quad (2.5)$$

2.11.3 The Born-Oppenheimer Approximation

The Born-Oppenheimer approximation (Butler, 1998) is a key simplification in

quantum mechanics that separates the electronic and nuclear motions in molecular systems. It relies on the significant mass difference between electrons and nuclei, which causes nuclei to move much more slowly compared to electrons. In the Born-Oppenheimer approximation, the total wavefunction $\psi(\mathrm{r},\mathrm{R})$ of a system can be separated into an electronic part ψ_e and a nuclear part X_N as in Equation 2.6.

$$\Psi(\mathrm{r},\mathrm{R}) = \psi_e(r,R)X_N(R) \tag{2.6}$$

Where r represents the coordinates of the electrons and R the coordinates of the nuclei. The Born-Oppenheimer equations are derived from the time-independent Schrödinger equation by assuming that the nuclei move slowly compared to the electrons, and thus the electronic wavefunction can be solved for fixed nuclear positions. The resulting Hamiltonian (Equation 2.7) for the electronic part becomes:

$$\hat{\mathrm{H}} = \hat{\mathrm{T}}_\mathrm{e} + \hat{\mathrm{V}}_\mathrm{en} + \hat{\mathrm{V}}_\mathrm{ee} \tag{2.7}$$

After solving for the electronic energy $E_e(R)$, which depends on the positions of the nuclei, the nuclear motion can be treated using the potential energy surface $E_e(R)$. The total energy of the system as in Equation 2.8 is the sum of the electronic energy and the nuclear kinetic energy:

$$\mathrm{H}_\mathrm{total} = \mathrm{T}_\mathrm{N} + \mathrm{E}_\mathrm{e}(\mathrm{R}) \tag{2.8}$$

where $\mathrm{T_N}$ is the kinetic energy of the nuclei. The nuclei then move according to this effective potential, which is derived from the electronic wavefunction. The Born-Oppenheimer approximation simplifies the calculation of molecular systems by decoupling the electronic and nuclear motions, allowing for a more tractable solution of the Schrödinger equation (Harper et al., 2020).

2.11.4 Hartree Approximation

The Hartree approximation (Tancogne-Dejean et al., 2022) (Lykos & Pratt, 1963) simplifies the many-electron problem in quantum mechanics by assuming that the total wavefunction of a system of N electrons can be expressed by Equation 2.9 as a product of single-particle wavefunctions.

$$\Psi(r_1, r_2, \ldots r_N) \approx \Pi_{i=1}^{N}\psi(r_i) \tag{2.9}$$

Each electron is treated as moving independently in an average potential created by the nuclei and the other electrons. The single-particle wavefunctions $\psi(r_i)$ satisfy the Hartree equations described by Equation 2.10 (Park et al., 2024).

$$\left[-\frac{\hbar}{2m}\nabla^2 + V_{ext}\,(r) + V_H(r)\right]\psi(r_i) = \varepsilon_i\psi(r_i) \tag{2.10}$$

Where $-\frac{\hbar}{2m}\nabla^2$ represents the kinetic energy operator, $V_{ext}\,(r)$ is the external potential (e.g., due to nuclei), and $V_H(r)$ is the Hartree potential (Dalgarno et al., 1966.). The Hartree potential describes the Coulomb interaction of an electron with the average electron density, calculated by Equation 2.11.

$$\mathrm{V_H(r)} = \int \frac{\rho(\mathrm{r}')}{|\mathrm{r}-\mathrm{r}'|}\,\mathrm{d}^3\mathrm{r}' \tag{2.11}$$

Where $\rho(r')$ is the total electron density. The Hartree approximation is a self-consistent method because the Hartree potential $V_H(r)$ depends on the electron density, which itself is determined by the wavefunctions $\psi(r_i)$. Solving the Hartree equations involves an iterative process: starting with an initial guess for $\psi(r_i)$. the electron density is computed, which updates the $V_H(r)$ This updated potential is then used to solve the Hartree equations for new wavefunctions, and the process repeats until convergence. While the Hartree approximation provides a useful framework, it neglects exchange and correlation effects due to electron indistinguishability and mutual interactions, making it less accurate than methods like Hartree-Fock or Density Functional Theory (DFT) (Lahmer, 2022).

2.11.5 Hartree-Fock Theory

Hartree-Fock (HF) theory improves upon the Hartree approximation by incorporating the effects of electron exchange, which arise from the antisymmetric nature of the total wavefunction for fermions (electrons) (Sim et al., 2022). The total wavefunction Ψ of a many-electron system is represented as a single Slater determinant, ensuring antisymmetry under the exchange of any two electrons. For a system of N electrons, the Slater determinant is given by Equation 2.12.

$$\Psi(r_1, r_2, \ldots r_N) = \frac{1}{\sqrt{N!}} \begin{vmatrix} \psi_1(r_1) & \psi_2(r_1) & \ldots & \psi_N(r_1) \\ \psi_1(r_2) & \psi_2(r_2) & \ldots & \psi_N(r_2) \\ \vdots & \vdots & \ddots & \vdots \\ \psi_1(r_3) & \psi_2(r_3) & \cdots & \psi_N(r_3) \end{vmatrix} \quad (2.12)$$

Where $\psi_i(r)$ are the single-particle spin-orbitals, which include spatial and spin components. This representation naturally introduces exchange interactions between electrons, addressing one of the limitations of the Hartree method. In Hartree-Fock theory, the single-particle spin-orbitals satisfy the Hartree-Fock equations, derived by minimizing the total energy of the system under the constraint that the wavefunctions remain orthonormal. The resulting equations (2.13) are:

$$\hat{\mathrm{F}}\psi_{\mathrm{i}}(\mathrm{r}) = \varepsilon_{\mathrm{i}}\,\psi_{\mathrm{i}}(\mathrm{r}) \quad (2.13)$$

Where $\hat{F}$ is the Fock operator, defined by Equation 2.14.

$$\hat{\mathrm{F}} = \hat{\mathrm{h}} + \sum_{\mathrm{j}=1}^{\mathrm{N}} \left(\hat{\mathrm{J}}_{\mathrm{j}} - \hat{\mathrm{K}}_{\mathrm{j}}\right) \quad (2.14)$$

Where $\hat{h}$ is the single-particle Hamiltonian, including kinetic energy and external potential, $\hat{\boldsymbol{J}}_{\boldsymbol{j}}$ is the Coulomb operator representing the average electrostatic repulsion with electron j and $\hat{K}_j$ is the exchange operator accounting for exchange effects.

The Coulomb and exchange terms arise from the two-electron integrals in the energy expression. The Hartree-Fock equations are solved iteratively in a process called the self-consistent field (SCF) method. Starting with an initial guess for the spin-orbitals, the Fock operator is constructed, and the equations are solved to update the spin-orbitals. This process is repeated until convergence, meaning the spin-orbitals and Fock operator are mutually consistent. While Hartree-Fock theory captures exchange interactions and provides a foundation for many quantum chemistry methods, it neglects electron correlation effects, which can be addressed using post-Hartree-Fock methods such as Configuration Interaction (CI) (Sharpe, Levy, & Tozer, 2018) or Coupled Cluster (CC) theory (Ali et al., 2022).

2.11.6 The Hohenberg-Kohn Theorem

The is the foundational result in density functional theory (DFT), introduced in 1964

by Pierre Hohenberg and Walter Kohn (Laestadius et al., 2014.). It revolutionized the study of quantum many-body systems by proving that the ground-state properties of a system of interacting electrons are uniquely determined by the electron density $\rho(r)$. Unlike the many-electron wavefunction, which depends on 3N variables for N electrons, the electron density depends only on three spatial coordinates, making it a computationally efficient alternative for studying quantum systems. The first Hohenberg-Kohn theorem states that the ground state energy of a many-electron system is a unique functional of the electron density. Mathematically, this can be expressed as shown in Equation 2.15.

$$E(\rho) = F[\rho] + \int V_{ext}(r)\rho(r)dr \tag{2.15}$$

where $E(\rho)$ is the ground state energy, $F[\rho]$ is a universal functional of the electron density that includes the kinetic energy and electron-electron interaction terms, and $V_{ext}(r)\rho(r)dr$ is the potential energy due to the external field**.** The universal functional $F[\rho]$ can be further decomposed into the kinetic energy functional $T(\rho)$ and the electron-electron interaction functional $U(\rho)$ This decomposition (Equation 2.16) is expressed as:

$$F[\rho] = T[\rho] + U[\rho] \tag{2.16}$$

The electron density that minimizes the energy functional $E(\rho)$ is the true ground state electron density of the system. In other words, if we find the electron density $\rho(r)$ that makes $E(\rho)$ a minimum, we have found the correct electron density for the ground state. Mathematically, this is written as in Equation 2.17.

$$\frac{\delta E[\rho]}{\delta \rho(r)} = 0 \tag{2.17}$$

This variational principle provides a practical method for finding the ground state electron density by minimizing the energy functional with respect to the electron density. An important component of the energy functional $E(\rho)$ is the exchange-correlation energy $E_{xc}(\rho)$ which accounts for the complex many-body effects of electron exchange and correlation. The total energy functional (Equation 2.18) can be expressed as:

$$E[\rho] = T_s[\rho] + \int V_{ext}(r)\rho(r)dr + J[\rho] + E_{xc}[\rho] \quad (2.18)$$

Where $T_s[\rho]$ is the kinetic energy of a system of non-interacting electrons with the same electron density, $J[\rho]$ is the classical Coulomb interaction energy and $E_{xc}[\rho]$ is the exchange-correlation energy.

2.11.7 The Kohn-Sham Equations

While the Hohenberg-Kohn theorem establishes that the ground-state properties of an interacting electron system are uniquely determined by the electron density ρ(r) it does not provide a way to compute this density directly (Li et al., 2021). The Kohn-Sham formalism addresses this by mapping the complex many-electron problem to a system of non-interacting electrons that reproduce the same ground-state electron density as the interacting system (Rai et al., 2020). The Kohn-Sham orbitals are solutions to a set of self-consistent single-particle Schrödinger-like equations, known as the Kohn-Sham equations described by Equation 2.19.

$$E[\rho(r)] = T_s[\rho(r)] + \frac{1}{2}\iint \frac{\rho(r)\rho(r')}{|r - r'|} drdr' + E_{xc}[\rho(r)] + \int \rho(r)V_{ext}(r)dr \quad (2.19)$$

Where $T_s[\rho(r)]$ represents the kinetic energy (Equation 2.20) of the non-interacting electron gas described by:

$$T[\rho(r)] = -\frac{1}{2}\sum_{i}^{N} \int \psi_i^*(r)\nabla^2\psi_i(r)dr \quad (2.20)$$

The exchange-correlation potential $E_{xc}[\rho(r)]$ incorporates all the many-body quantum effects of exchange and correlation between electrons that are not accounted for by the Hartree potential. It is the derivative of the exchange-correlation energy functional $E_{xc}[\rho]$ with respect to the density can be defined as (Equation 2.21).

$$V_{xc}(r) = \frac{\delta E_{xc}[\rho]}{\delta \rho(r)} \quad (2.21)$$

When a normalization constraint is introduced on the density of the electron $\int \rho(r)dr = N$ then the variation principle defined in Equation 2.22 is achieved.

$$\frac{\delta}{\delta\rho(r)}[E[\rho(r)] - \mu\int n(r)dr] = 0 \qquad (2.22)$$

$$\Longrightarrow \frac{\delta E[\rho(r)]}{\delta\rho(r)} = \mu$$

Where μ denotes the chemical energy. The effective potential V_{eff} (r) as defined in Equation 2.23 a very crucial role in determining the behavior of the Kohn-Sham orbitals.

$$V_{eff}(r) = V_{ext}(r) + V_H(r) + V_{xc}(r) \qquad (2.23)$$

For a system of nuclei (I) of charge Z located at positions R_I, the external potential $V_{ext}(r)$ is given by Equation 2.24.

$$V_{ext}(r) = -\sum_I \frac{Z_I}{|r - R_I|} \qquad (2.24)$$

The Hartree potential given by Equation (2.25) accounts for the classical Coulomb interaction between electrons.

$$V_H(r) = \int \frac{\rho(r')}{|r - r'|} dr' \qquad (2.25)$$

As long as the exchange-correlation energy E_{xc} is known and we are dealing with a non-interacting electron system, Equations (2.24) and (2.25) provide an accurate method for calculating the ground state energy E_o of an interacting system. However, the exact form of E_{xc} is still under active investigation.

2.11.8 Density Functional Theory (DFT)

Density Functional Theory (DFT) is a widely used computational quantum mechanical method for investigating the electronic structure of many-body systems, particularly atoms, molecules, and solids (Li et al., 2022; Parhizgar & Beheshtian, 2018a). The central idea of DFT is to describe the ground-state properties of a system using its electron density ρ(r), rather than the many-electron wavefunction, which drastically simplifies the computational complexity. According to the Hohenberg-Kohn theorems, the ground-state energy and other properties of a system are uniquely

determined by ρ(r) and the energy can be expressed as a functional of this density. In practice, DFT employs the Kohn-Sham approach, where the many-body problem is reduced to a set of single-particle equations for non-interacting electrons moving in an effective potential as shown in Figure 2.18.

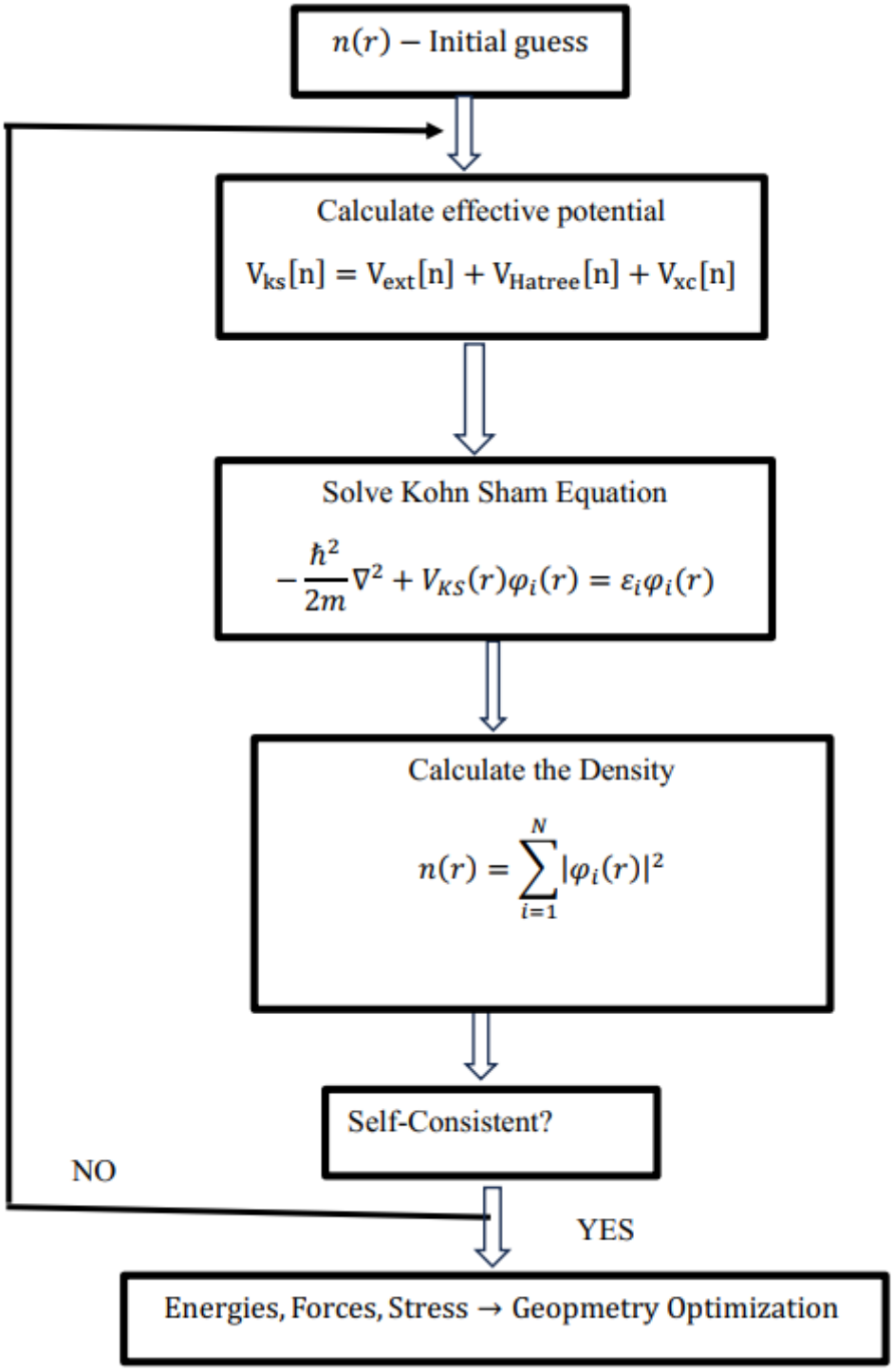

Figure 2.18: Flow Chart of Self-Convergence Field (SCF) Calculation in DFT (Namisi et al., 2023)

This potential includes the external potential, the classical electrostatic interaction, and an exchange-correlation term that accounts for the quantum mechanical effects of electron exchange and correlation (Namisi et al., 2023). The exchange-correlation functional is a critical component of DFT, and its precise form must be approximated, with common choices including the Local Density Approximation (LDA) and Generalized Gradient Approximation (GGA). DFT is widely used due to its balance of computational efficiency and accuracy, enabling the study of complex systems in fields such as materials science, (Vincent et al., 2021). However, its limitations, particularly in describing systems with strong electron correlations or van der Waals interactions, often require the use of more advanced or hybrid functionals.

2.11.9 Local Density Approximation (LDA)

The Local Density Approximation (LDA) is a pivotal concept in density functional theory (DFT) that approximates the exchange-correlation energy of a system based on the local electron density (Merdan & Banimuslem, 2024). The essence of LDA is that the exchange-correlation energy density at a given point in space is assumed to be the same as that of a homogeneous electron gas with the same local electron density. This simplifies the complex many-body interactions into a more tractable form. The exchange-correlation energy functional in LDA is given by Equation 2.26 shown below.

$$\mathrm{E_{xc}^{LDA}}[\rho] = \int \mathrm{E_{xc}}[\rho(\mathrm{r})]\rho(\mathrm{r})\mathrm{dr} \tag{2.26}$$

Where $E_{xc}[\rho(r)]$ is the exchange-correlation energy per electron of a homogeneous electron gas with density $\rho(r)$ This integral accounts for the contribution of the exchange-correlation energy at each point in the electron density distribution. The exchange energy (Equation 2.27) part of the exchange-correlation energy can be separately expressed as:

$$\mathrm{E_{x}^{LDA}}[\rho] = \int \mathrm{E_{x}}[\rho(\mathrm{r})]\rho(\mathrm{r})\mathrm{dr} \tag{2.27}$$

Where $E_x(\rho)$ *is* the exchange energy per electron in the local density approximation. This expression captures the exchange interactions of electrons within the homogeneous electron gas model (Bogojeski et al., 2020). For homogeneous systems,

Equation 2.27 is valid only for non-magnetic configurations. The exchange-correlation energy per electron can be divided into two components: exchange and correlation, as demonstrated in Equation 2.28.

$$\mathrm{E_{xc}}[\rho(\mathrm{r})] = \mathrm{E_x}[\rho(\mathrm{r})] + \mathrm{E_c}[\rho(\mathrm{r})] \tag{2.28}$$

In 1930, Dirac derived a fundamental formula for the exchange energy per electron, which plays a crucial role in understanding the interactions between electrons in quantum systems. This exchange energy density E_x can be approximated as (Equation 2.29).

$$\mathrm{E_x}(\rho) = -\frac{3}{4}\left(\frac{3}{\pi}\right)^{\frac{1}{3}} \rho^{\frac{1}{3}} \tag{2.29}$$

This exchange energy arises due to the quantum mechanical effects of electron indistinguishability and the Pauli exclusion principle. Dirac's work laid the groundwork for later developments in the DFT computations, where exchange and correlation energies are essential components for accurately describing the electronic structure of atoms, molecules, and solids. The formula he developed provides a way to calculate the energy associated with the exchange interactions between electrons in a system, contributing to the overall energy and stability of the system. In 1980, Ceperley and Alder, using a quantum Monte Carlo code (Wheeler et al., 2023) (Ceperley & Alder, 1986), provided the first approximation of the correlation energy, $E_c[\rho(r)]$ for a homogeneous electron gas. This pioneering work was followed by several other researchers, including (Assaad et al., 2020), who proposed analytical parameterizations of $E_c[\rho(r)]$E. Among these, the parameterization introduced by Perdew and Zunger (Santra et al., 2019) became one of the most widely used and has since become a standard reference in the field of density functional theory.

The Local Density Approximation (LDA) tends to underestimate bond lengths due to its tendency to over bind the system (Allan et al., 2023). This overbinding occurs because LDA assumes the exchange-correlation energy is locally dependent on the electron density, often leading to an overestimation of the attractive interactions between electrons. As a result, the equilibrium bond lengths predicted by LDA are generally shorter than experimental values, as the system is stabilized more than it

should be, causing the atoms to be pulled closer together. Further, LDA underestimates the band gap in semiconductors due to its treatment of exchange-correlation effects. LDA assumes that the exchange-correlation energy depends solely on the local electron density, which leads to a more metallic behavior in materials, particularly in semiconductors. This approximation fails to accurately capture the electron-electron interactions that are important for correctly predicting the band gap, typically resulting in an overestimation of electron delocalization and a corresponding underestimation of the energy difference between the valence and conduction bands (Cococcioni & De Gironcoli, 2005). Consequently, LDA tends to predict smaller band gaps than are observed experimentally for many semiconducting materials.

2.11.10 The Generalized Gradient Approximation (GGA)

The Generalized Gradient Approximation (GGA) is an improvement over LDA in DFT (Rani & Chauhan, 2021). While LDA considers only the local electron density at each point in space, GGA incorporates both the local density and its gradient (the rate of change of the density) into the exchange-correlation functional. This additional information helps better describe the inhomogeneities in electron density, leading to more accurate predictions for various properties, especially in systems with significant variations in density. Perdew and colleagues further enhanced the findings of Hohenberg and Kohn by introducing general functionals (Equation 2.30) is of the form (Tancogne-Dejean et al., 2022):

$$E_{XC}^{GGA}[\rho] = \int d^3rf\ (\rho, \nabla\rho) \tag{2.30}$$

Where $E_{XC}^{GGA}[\rho]$ describe the exchange correlation energy. GGA significantly improves upon LDA by providing a more realistic description of electron correlation, particularly in systems with non-uniform densities such as molecules and solids (Chen & Xu, 2024). It corrects some of the shortcomings of LDA, like the underestimation of bond lengths and the band gap in semiconductors. GGA is widely used because it provides a good balance between computational efficiency and accuracy, offering better results for many materials and chemical systems compared to LDA (Shao et al., 2021). However, it is still an approximation, and for certain cases, more advanced methods like hybrid functionals may be required for higher accuracy.

2.11.11 Hybrid Functionals and Green Functionals (GW) Approximation

Hybrid functionals are a class of exchange-correlation functionals in DFT that combine elements of both exact exchange from Hartree-Fock theory and approximate exchange-correlation energy from GGA (Yang et al., 2023). By incorporating a portion of exact exchange, hybrid functionals aim to address some of the limitations of traditional functionals, particularly the self-interaction error. Popular hybrid functionals like B3LYP Ali et al. (2022) and PBE0 (Moldabekov et al. 2022) have been widely used in quantum chemistry and materials science due to their improved accuracy in predicting molecular properties such as bond energies, geometries, and reaction barriers. The inclusion of exact exchange in hybrid functionals improves the description of long-range electronic interactions, making them particularly effective for systems with localized electronic states. This feature makes hybrid functionals suitable for studying systems like transition metal complexes, organic molecules, and materials with band gaps (Yang, Falletta & Pasquarello, 2023). However, the computational cost of hybrid functionals is significantly higher than that of GGAs due to the non-local nature of the exact exchange term. Despite this, their accuracy often justifies the additional computational expense, especially for systems where traditional functionals struggle to provide reliable results.

The GW approximation (Kim et al., 2022) is a many-body perturbation theory method used to calculate electronic properties, particularly the quasiparticle energies, in materials. Named after G (the Green's function) and W (the screened Coulomb interaction), the GW approximation improves upon DFT by addressing its limitations in describing excited-state properties, such as band gaps in semiconductors and insulators. Unlike standard DFT, which is ground-state focused, the GW method explicitly accounts for electron-electron interactions, leading to more accurate predictions of electronic excitation energies. In the GW framework, the self-energy of the system is approximated using the product of the Green's function and the screened Coulomb interaction. This approach captures the dynamic nature of electron screening, which is essential for accurate electronic structure calculations. GW is often used in combination with DFT, where the DFT results serve as an initial guess for the quasiparticle calculations. While the GW method is computationally demanding, its ability to predict experimentally observed properties, such as optical spectra and band structures, has made it an indispensable tool in computational

materials science.

The combination of hybrid functionals and the GW approximation has become increasingly popular for achieving highly accurate electronic structure calculations (Rangel et al., 2020), Hybrid functionals provide a better starting point for GW calculations by offering an improved description of exchange and correlation effects compared to standard GGAs (Ulpe & Bredow, 2020). This synergy enhances the accuracy of quasiparticle energy predictions while reducing the dependence on computationally expensive self-consistency steps in GW calculations. For instance, hybrid functionals like HSE are often used as a precursor to GW calculations in materials with complex electronic structures (Gao et al., 2023). The integration of these methods is particularly beneficial for studying systems where both ground-state and excited-state properties are critical. Examples include organic photovoltaics, topological materials, and strongly correlated systems. By leveraging the strengths of hybrid functionals and GW, researchers can achieve a more comprehensive understanding of the electronic properties, enabling the design of advanced materials with tailored functionalities. However, the high computational cost remains a challenge, prompting further efforts to optimize and scale these methods for larger and more complex systems.

2.11.12 Plane Waves

Plane waves are a widely used basis set in computational methods for electronic structure calculations, particularly in DFT and related approaches (Gao et al., 2025). Representing wavefunctions as a sum of plane waves offers significant advantages, especially for periodic systems like crystals, as it naturally incorporates the translational symmetry of the lattice. This makes plane waves ideal for studying solid-state materials (Jiang et al., 2024). If the nuclei are arranged in a periodically repeating pattern, their lattice potential U(r) which influences the electrons, must also exhibit periodicity (Shi et al., 2022). Consequently, the single-electron Schrödinger equation in the presence of this periodic potential U(r) can be described by Equation 2.31.

$$\left\{-\frac{1}{2}\nabla^2 + U(r)\right\}\psi = \varepsilon\psi \tag{2.31}$$

According to Bloch's theorem, the one-electron wavefunctions (Equation 2.32) satisfy

the following equation:

$$\psi_k(r) = \exp^{ik.r}\mu_K(r) \tag{2.32}$$

Where $\psi_k(r)$ possesses the periodicity of the lattice. This property enables the electron wavefunctions to be expressed as a plane wave expansion (Equation 2.33).

$$\psi_{i,K}(r) = \sum_G C_{i,K} + G^{e^{i(K+G).r}} \tag{2.33}$$

where G denotes the reciprocal lattice vectors. In K-space, the Kohn-Sham equations are subsequently reduced to a matrix eigenvalue Equation 2.34:

$$\sum_{G'}\left\{\frac{1}{2}|K+G|^2\delta GG' + V_{ext}(G-G') + V_H(G-G') + V_{xc}(G-G')\right\}C_{i,K+G} = \epsilon_i C_{iK} + G \tag{2.34}$$

Where V_{ext} represents the static total electron-ion potential, V_H denotes the Hartree potential of the electrons, i and ϵ are the Kohn-Sham eigenfunctions and eigenvalues, respectively, and V_{xc} is the exchange-correlation potential while $C_{i,K+G}$, is the coefficient of plane-wave basis state. In typical situations, not all wave vectors are relevant, so a cutoff energy (E_{cut}) defined by Equation 2.35 is utilized (Wang et al., 2024).

$$E_{cut} = \frac{1}{2}|K+G_{max}|^2 \tag{2.35}$$

The kinetic energy cutoff in plane wave-based DFT calculations refers to the maximum allowed kinetic energy for the plane waves included in the basis set (Parker et al., 2006). This parameter directly influences the accuracy of the results, as it determines how many plane waves are used to represent the wavefunctions. A higher kinetic energy cutoff allows for a more detailed representation of the electron wavefunctions, leading to more accurate calculations of electronic properties, such as total energy, charge densities, and band structures (Cangi et al., 2022). However, using a higher cutoff increases the computational cost significantly due to the larger number of basis functions involved. To optimize computational efficiency, the kinetic energy cutoff is typically chosen by evaluating the convergence of the total energy

with respect to increasing cutoff values (Namisi et al., 2023). As the cutoff increases, the total energy should stabilize, indicating that the chosen value is sufficient for the system being studied. If the cutoff is too low, important wavefunction details may be omitted, resulting in inaccurate results. On the other hand, excessively high cutoff values may not improve the accuracy significantly but will increase the computational burden. Therefore, finding an appropriate balance between accuracy and computational cost is key when selecting the kinetic energy cutoff.

K-points refer to discrete points in the reciprocal space (momentum space) of a periodic crystal structure used in electronic structure calculations, particularly within DFT (Parhizgar & Beheshtian, 2018b). The first Brillouin zone (BZ) is defined as the Wigner-Seitz cell of the reciprocal lattice, which is bounded by planes that act as perpendicular bisectors between the lattice points and the origin of the reciprocal lattice. A commonly used method for sampling the first Brillouin zone is the uniformly spaced Monkhorst-Pack (Jeziorski & Monkhorst, 1981) K-point grid represented as n1. n2. n3. This approach involves selecting a set of uniformly spaced K-points within the zone, which are used to approximate integrals over the Brillouin zone. These grids are particularly useful for periodic systems, such as crystals, where the periodicity of the structure allows for the sampling of K-points at regular intervals. By carefully selecting the grid spacing and size, the Monkhorst-Pack scheme helps balance computational efficiency and the accuracy of the results.

The Monkhorst-Pack grid can be customized by adjusting the number of divisions along each reciprocal lattice vector, which determines the density of K-points used for sampling (Monkhorst & Pack, 1976). A finer grid, with more K-points, typically leads to more accurate calculations of electronic properties, such as total energy, band structure, and density of states. However, increasing the number of K-points also increases the computational cost. Therefore, the Monkhorst-Pack method is often employed with a grid size that offers a good trade-off between accuracy and computational efficiency. For larger systems or those with complex electronic behavior, the method can be applied in combination with other techniques, such as density functional theory (DFT) or many-body perturbation theory.

2.11.13 Brillouin Zone Sampling

Brillouin zone sampling is a fundamental aspect of electronic structure calculations in periodic systems, such as crystals, to evaluate integrals over the reciprocal space (Chen et al., 2022). The BZ is the primitive cell of the reciprocal lattice and contains all the unique wavevectors (k-points) needed to describe the electronic states of the crystal. To obtain the electronic properties through ab initio calculations, the functions (Equation 2.36) must be integrated over the Brillouin zone as follows:

$$F(r) = \frac{\Omega}{(2\pi)^3} \int f(k) d^3k \tag{2.36}$$

Where $f(k)$ represents the Fourier transformations of the function $F(r)$ while Ω denotes the volume of the unit cell. Due to the periodicity of the crystal lattice, sampling the BZ at a finite number of k-points allows for computational efficiency while capturing the essential physical properties of the material. To accurately compute properties such as total energy, electronic band structures, and density of states, the integrals over the Brillouin zone are approximated by summing over a discrete set of k-points with appropriate weighting factors (Gallegos et al., 2019; Mbilo & Musembi, 2022). Efficient sampling techniques, such as the Monkhorst-Pack scheme, generate a uniform grid of k-points tailored to the symmetry of the system. This method is an objective approach for determining the set of K-points to be used in sampling the Brillouin zone. The sampling is represented in fractional coordinates and arranged in a rectangular grid of points (k_x, k_y, k_z), derived from Equation 2.37.

$$\mathrm{kn_1n_2n_3} = \sum_{\mathrm{i-1}}^{3} \frac{2\mathrm{n_i} - \mathrm{N_i} - 1}{2\mathrm{N_i}} \mathrm{G_i} \tag{2.37}$$

Denser k-point meshes are required for systems with high symmetry or small unit cells to ensure convergence, while lower-symmetry or larger unit cell systems may need fewer points as described in Equation 2.38.

$$\Omega_{BZ} = \frac{(2\pi)^3}{\Omega_{CELL}} \tag{2.38}$$

Convergence tests are essential to balance computational cost and accuracy, ensuring that the sampling density is sufficient for the desired precision in calculated properties. Proper Brillouin zone sampling is critical for capturing the nuances of electronic behavior in periodic materials.

2.11.14 Pseudopotentials

Bonding governs how wave functions vary within a system. Near the nucleus, wave functions oscillate rapidly, while farther away, in the valence region, the wave functions have a smoother, more regular form (Musembi & Mbilo, 2022). The type of bonding and the resulting electronic structure depend heavily on these different wave function behaviors. In ab initio calculations, the use of pseudopotentials approximates the effect of core electrons by treating them as fixed, focusing calculations on the valence electrons. Since the potential of the core electrons lies far below the surface, expanding the core orbitals requires the inclusion of many plane waves. However, using many plane waves results in excessive space usage in the computational cluster and demands more processors, which can significantly increase computational time.

Pseudopotentials are mathematical constructs used in electronic structure calculations, particularly within Density Functional Theory (DFT), to simplify the treatment of electron-ion interactions (Kaye et al., 2022) (Kleinman & Bylander, 1982). Instead of explicitly accounting for all electrons in an atom, pseudopotentials replace the core electrons with an effective potential as shown in Figure 2.19. This allows calculations to focus on valence electrons, which play a primary role in bonding and material properties. By excluding the core electrons, pseudopotentials reduce the number of wavefunctions that need to be calculated, significantly improving computational efficiency. The pseudopotential approach works by smoothing the rapid oscillations of the core-electron wavefunctions near the nucleus, creating a smoother and less computationally demanding effective potential (Chirchir et al., 2022). Pseudopotentials are typically categorized into two types: norm-conserving pseudopotentials, which preserve certain physical properties like charge density, and ultrasoft pseudopotentials, which allow greater flexibility by relaxing the norm-conservation condition, enabling even smaller basis sets.

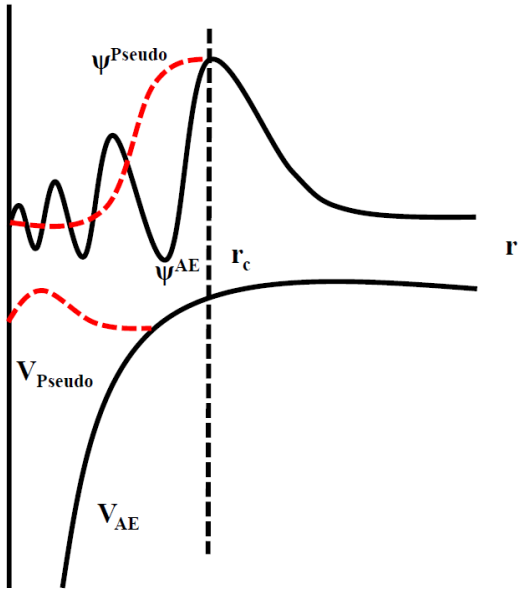

Figure 2.19: Schematic diagram of Pseudo Electrons (red lines) and All-Electron (black lines) Potentials and their Equivalent Wave Functions (Mulwa, 2017)

Additionally, projector-augmented wave (PAW) methods offer an alternative that combines pseudopotentials with the accuracy of all-electron methods. Pseudopotentials are essential in plane wave-based methods, where the high kinetic energy of tightly bound core electrons would require an unmanageably large basis set. Properly designed pseudopotentials capture the chemical and physical effects of core electrons while maintaining accuracy in the description of valence electrons, making them indispensable for efficient and accurate simulations of complex systems.

2.11.15 DFT and the Hubbard Term U

DFT is a widely used computational method for studying the electronic structure of materials. However, standard DFT methods, particularly those based on the LDA or GGA, often struggle to accurately describe materials with strongly localized electron states, such as transition metal oxides and rare-earth compounds (Parhizgar & Beheshtian, 2018). These limitations arise because standard DFT fails to capture the strong on-site Coulomb interactions among localized electrons, leading to incorrect predictions of electronic, magnetic, and structural properties (Harun et al., 2016). Several approaches have been proposed to compensate for the band gap underestimation of standard DFT formalism. Green functional (GW) approximation

(Zhang et al., 2016) puts into consideration the self-energy of a many-body system of electrons and has been used to reproduce the experimental band gaps of semiconductors. On the other hand, hybrid exchange-correlation functionals like HSE, PBE0, and B3LYP integrates the GGA exchange potentials with the Hartree–Fock (HF) non-local exact exchange to widen the band gap (Gerosa M., 2018). Although GW and hybrid potentials have proven to be more accurate than standard DFT, their high computational cost limits their applications. In the recent past, Tran and Blaha modified Becke-Johnson (TB-mBJ) potential have been developed to allow better approximations of band gaps at a reasonable computational cost (Khuili et al., 2019). DFT+U formalism proves to be the most popular remedy to DFT limitations for their ease of implementation, low computation cost and high accuracy. DFT+U introduces an on-site Coulombic Hubbard U term into the XC functional of either the LDA or GGA. This approach adds a correction to the standard DFT energy functional to explicitly account for the on-site Coulomb repulsion of localized electrons (Mulwa et al., 2016). The corrected functional (Equation 2.39) is given as:

$$E_{DFT+U} = E_{DFT} + \frac{U}{2}\sum_{i} n_i(1 - n_i) \tag{2.39}$$

where n_i represents the occupancy of localized states (such as d- or f-orbitals) and U is the Hubbard parameter that quantifies the strength of the on-site Coulomb interaction. The magnitude of the on-site potential is basically defined by parameters U (on-site Coulomb) and J (on-site exchange), which can be obtained from first-principle calculations or by comparison with experimental data (Harun et al., 2020). In the simplistic implementation of DFT+U, the Columbic interaction is included via an effective U_{eff} (= U−J) parameter (Shishkin & Sato, 2019). The U term suppresses fractional occupancies of localized states, thereby improving the description of electronic correlation effects. The Hubbard Hamiltonian is expressed in Equation 2.40.

$$H_{Hub} = \sum_{\langle i,j\rangle\,\sigma} \left(C_{i,\sigma}C_{j,\sigma} + h.c\right) + U\sum_{i} n_i\,, \quad \uparrow n_{i,}\downarrow \tag{2.40}$$

Where $\langle i, j\rangle$ represents the nearest neighbour atomic sites and $C_{i,\sigma,}$ $C_{j,\sigma}$ and n_i are the electronic creation, annihilation, and number operators, respectively, for electrons

with spin σ at site i. Within the LDA+U approach, the total energy of a system can be written as in Equation 2.41.

$$E_{LDA+U}[\rho(r)] = E_{LDA}[\rho(r)] + E_{Hub}[\{n_{mm}^{I\sigma}\}] - E_{dc}[\{n^{I\sigma}\}] \quad (2.41)$$

In this case, the term E_{Hub} represents the electron-electron interactions as described by the Hubbard Hamiltonian. The DFT+U method is particularly effective for systems where electron localization plays a significant role, such as Mott insulators, charge transfer materials, and systems with magnetic ordering (Mahmood et al., 2021; Wang et al., 2021).

Generally, it is not easy to deduce the optimal value of the coulombic potential U for ZnO. This is after the widely used linear response approach provided by Cococcioni, M., & Gironcoli, S., 2005 for open-shell systems failed on ZnO since it is a closed-shell system. Dependence of the band gap and lattice parameters of ZnO on the value of Hubbard U has been proposed as a viable route in the determination of the optimal value of U. Huang *et al*., 2012 compared the impact of the Hubbard U term on the structural and electronic aspects of W-ZnO using LDA+U and GGA+U approximation. They introduced the Hubbard U term on both the d orbital of Zn (U_d) as well as the p orbital of oxygen (U_p). This method resulted into improved band gap as well as the position of the valence band with GGA+U reporting an improvement of the energy band gap from 0.7 eV to 1.4 eV. Recently, Goh *et al*., 2017 carried out a similar study by applying Hubbard corrections U_d to Zn- 3d states and U_p to O-2p states in the LDA+U method. According to this study, while the band gap was enlarged towards experimental value, the lattice constants were underestimated for all the tested Hubbard parameters. So far, the influence of U_d and U_p on W-ZnO has largely been focused on structural and electronic properties while their effect on mechanical and optical properties has been greatly ignored. To the best of our knowledge, there exists no report on the optical and mechanical properties of W-ZnO based on the DFT + U_d + U_p formalism. Whereas the mechanical properties determine the stability of a compound, optical properties such as dielectric functions, absorption, reflectivity, energy loss and refractive index describes the applicability of a compound in DSSCs. To explore the potential candidature of W-ZnO as a photoanode in DSSCs, this study adopted the DFT + U_d + U_p method to investigate the structural,

echanical, electronic and optical properties of W-ZnO.

2.12 Formation Energies within DFT

Within DFT, formation energy is a key metric used to assess the stability of compounds and materials by quantifying the energy required to achieve a specific configuration (Usman et al., 2017). The formation energy is typically calculated by comparing the total energy of the system of interest with the total energy of its constituent components in their reference states. This calculation helps determine whether a structural configuration or compound will form spontaneously, maintain stability, or break down under specific conditions. Its evaluation is crucial in predicting material properties and behavior at the atomic level, especially for materials science and condensed matter physics applications. The formation energy of an impurity X in a charge state q can be defined in Equation 2.42 (Alliati et al., 2021).

$$\mathrm{E_{form}}(\mathrm{X^q}) = \mathrm{E_{tot}}(\mathrm{X^q}) - \mathrm{E_{tot}^{host}} - \sum_{\mathrm{i}} \mathrm{n_i}\mu_{\mathrm{i}} + \mathrm{q}(\mathrm{E_F} + \varepsilon_{\mathrm{VBM}}) + \Delta^{\mathrm{q}} \qquad (2.42)$$

$E_{form}(X^q)$ is the total energy of the system containing the impurity X in charge state q, E_{tot}^{host} is the total energy of the pristine (impurity-free) host system. Formation energy is heavily influenced by the accuracy of the exchange-correlation functional employed in DFT calculations. Approximations such as the LDA, GGA, or hybrid functionals impact the calculated energies. Moreover, considerations like finite-size effects in supercell calculations, convergence with respect to k-point sampling, and basis set completeness can significantly affect the precision of formation energy values. To achieve reliable results, careful calibration of computational parameters and comparison with experimental data or more accurate quantum methods (such as many-body perturbation theory) is often necessary. In practical applications, formation energy is employed to assess phase stability, and evaluate chemical reactivity (Aoki et al., 2023). For instance, in semiconductor physics, the formation energy of point defects like vacancies, interstitials, and substitutional impurities plays a vital role in determining electrical and optical properties. In catalysis, it helps identify stable catalytic surfaces or active sites for chemical reactions. By leveraging formation energy calculations, researchers can tailor materials with specific properties or enhance their performance for targeted applications.

2.13 Optical Properties from DFT

Density Functional Theory (DFT) can be used to calculate the optical properties of materials, such as the dielectric function, absorption spectra, and refractive index, by describing the electronic response of a material to external electromagnetic fields (Aggarwal et al., 2019; Debnath et al., 2017). These properties are essential for understanding light-matter interactions, especially in semiconductors, insulators, and nanomaterials. The key optical properties are typically derived from the material's electronic structure, which can be obtained through DFT calculations. The dielectric function ε(ω), which describes how a material responds to an external electromagnetic field, is one of the primary quantities used to calculate optical properties (Rehman et al., 2023). In DFT, the dielectric function is related to the electronic polarizability and is typically calculated using the random phase approximation (RPA). It is given by Equation 2.43.

$$\varepsilon(\omega) = 1 - \frac{4\pi}{\omega^2} \int \frac{V(K,\omega)}{E_{bands}(K)} dk \qquad (2.43)$$

where v(k,ω) represents the velocity matrix elements and $E_{bands}(k)$ the electronic band structure obtained from DFT. The real part of the dielectric function gives information about the refractive index and reflection properties, while the imaginary part is related to the absorption coefficient, which determines how much light a material absorbs at a given frequency (Salman. K et al., 2024). Additionally, the absorption spectrum can be obtained by calculating the imaginary part of the dielectric function $\varepsilon_2(\omega)$ which provides a direct measure of how the material absorbs light across different photon energies (Kundara et al., 2024). For semiconductors and insulators, DFT can also predict optical transitions between the valence and conduction bands, helping to model the material's absorption edge and bandgap. For metals and plasmonic materials, the Drude model or more complex treatments of electron-electron interactions can be incorporated to model free-electron behavior and plasmon resonances (Mahmood et al., 2021).

While standard DFT provides a good approximation of electronic structures, it often underestimates band gaps. To address this, more sophisticated approaches like hybrid functionals (e.g., HSE06) or the GW approximation are employed to improve the accuracy of electronic structure calculations, and subsequently, the prediction of

optical properties. These advanced methods enable a more accurate determination of the optical response, particularly for materials with a significant gap or where excited-state effects are important (Chawla et al., 2024.). Impurities in semiconductors give rise to energy levels either within the band gap or close to the valence and conduction band edges. These levels are typically detected through experimental methods, which serve as the basis for studying impurities. Exploring these impurity levels is a critical focus of research. However, because experimental observations involve transitions between distinct charge states, the Kohn–Sham energy levels derived from band structure calculations cannot be directly correlated with the experimental levels as shown in Figure 2.20.

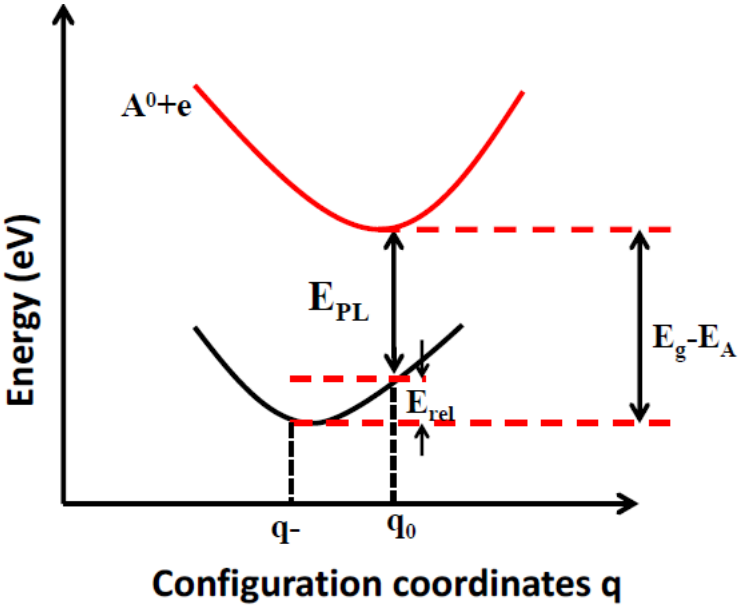

Figure 2.20: Schematic Configuration Coordinate Diagram Illustrating the Difference between Thermal and Optical Ionization Energies for an Acceptor (Tindibale et al., 2023).

When an electron recombines with a hole, a photon of energy E_{PL} (Equation 2.44) is emitted.

$$\mathrm{E_{PL}} = \mathrm{E_g} - \varepsilon^{\mathrm{therm}}\left(\frac{q_1}{q_2}\right) - \mathrm{E_{rel}} \qquad (2.44)$$

where E_{rel} is the Frank-Condon shift. The difference between the band gap and the PL length is the optical ionization energy, that can be described by Equation 2.45.

$$\varepsilon_A^{therm}\left(\frac{q_1}{q_2}\right) = E_g - E_{PL} = \varepsilon^{therm}\left(\frac{q_1}{q_2}\right) - E_{rel} \quad (2.45)$$

2.14 Dielectric Tensor

The dielectric constant (ε) is a fundamental property of a material that quantifies its ability to store and transmit electric fields. It is a complex quantity (Equation 2.46), typically expressed as:

$$\varepsilon(\omega) = \varepsilon_1(\omega) + i\varepsilon_2(\omega) \quad (2.46)$$

Where $\varepsilon_1(\omega)$ and $\varepsilon_2(\omega)$are the real and complex parts respectively of the complex dielectric functions . The dielectric *tensor* is a second-rank tensor that describes how a material responds to an external electric field in different spatial directions $\varepsilon_{xx}, \varepsilon_{yy}, \varepsilon_{zz}, \varepsilon_{xz}$ and ε_{yz} (Alliati, Sangalli & Grüning, 2021). The x, y, z denotes the dimensional x, y and z axis respectively as defined in Equation 2.47.

$$\varepsilon(\omega) = \begin{bmatrix} \varepsilon_{xx} & \varepsilon_{xy} & \varepsilon_{xz} \\ \varepsilon_{yx} & \varepsilon_{yy} & \varepsilon_{yz} \\ \varepsilon_{zx} & \varepsilon_{zy} & \varepsilon_{zz} \end{bmatrix} \quad (2.47)$$

This property is particularly important for anisotropic materials, where the response varies with the orientation of the electric field (Cowin, 1989). In general, the dielectric tensor ε_{ij} relates the electric displacement field (D) to the electric field (E) in a material through the relation (Equation 2.48):

$$D_i = \sum_j \varepsilon_{ij} E_j \quad (2.48)$$

where i, j denote Cartesian coordinates. The components of the dielectric tensor depend on the frequency (ω) of the applied electromagnetic field and may include real and imaginary parts to account for dispersive and absorptive behaviors. For computational studies, the imaginary part $\varepsilon_2(\omega)$ of the dielectric tensor is calculated using relation 2.49.

$$\varepsilon_{ij,2}(\omega) = \frac{4\pi^2 e^2}{\Omega} \sum_{k,v,c} \int_{BZ} \langle \psi_{ck} | \hat{v}_i | \psi_{vk} \rangle \langle \psi_{vk} | \hat{v}_j | \psi_{ck} \rangle \delta(E_{ck} - E_{vk} - \hbar\omega) d \quad (2.49)$$

Where $\hat{\mathbf{v}}_\mathbf{i}$, $\hat{\mathbf{v}}_\mathbf{j}$ are the velocity operators in the i- and j- directions, and the remaining terms represent the electronic transitions between valence (v) and conduction (c) states as functions of the wavevector **k**. The delta function ensures that the transitions correspond to the photon energy $\hbar\omega$. The real part of the dielectric tensor, $\varepsilon_{ij,1}$ can be derived from $\varepsilon_{ij,2}(\omega)$ using the Kramers-Kronig relations (Equation 2.50):

$$\varepsilon_{\mathrm{ij},1}(\omega) = \delta_{\mathrm{ij}} + \frac{2}{\pi}\int_0^\infty \frac{\omega'\varepsilon_{\mathrm{ij},2}(\omega')}{\omega'^2 - \omega^2}\mathrm{d}\omega' \tag{2.50}$$

Where δ_{ij} is the Kronecker delta, which accounts for the static contribution. This approach captures the frequency-dependent dielectric response across all components of the tensor. The dielectric tensor is often symmetric $\varepsilon_{ij} = \varepsilon_{ji}$ for non-magnetic and non-gyrotropic materials. It plays a key role in understanding anisotropic optical properties like birefringence, dichroism, and directional absorption, making it essential for designing advanced optical materials and devices. These properties are essential in understanding the optical and electronic behavior of materials and are widely studied using DFT) or Time-Dependent DFT (TD-DFT). In theoretical calculations, the imaginary part of the dielectric constant, $\varepsilon_2(\omega)$, is derived from the electronic structure of the material.

2.15 Lattice Dynamics

Lattice dynamics is the study of the vibrational motions of atoms in a crystal lattice. It is fundamental to understanding a material's thermal, mechanical, and electronic properties (Tindibale et al., 2023). Phonon behavior influences thermal conductivity (Ravichandran & Broido, 2020), electron–phonon interactions (Giustino, 2017), phase stability, and even superconductivity, all of which are critical for optimizing materials for various applications, including photovoltaic devices and thermoelectrics (Allan et al., 2023). In doped semiconductors such as ZnO, detailed knowledge of lattice dynamics is crucial, as modifications in vibrational modes can alter charge carrier mobilities and recombination rates. Moreover, understanding phonon dispersion and density of states can help in predicting how doping or structural modifications will affect non-radiative recombination processes and overall device performance. This insight is particularly valuable for engineering advanced materials with tailored

thermal and electronic properties for high-efficiency solar cells (Togo & Tanaka, 2015).

DFT offers a rigorous framework for calculating lattice dynamics, and tools such as Phonopy streamline these computations by employing the finite displacement method. In a typical workflow, one first carries out DFT calculations to obtain the ground state structure and forces resulting from small atomic displacements (Zhang et al., 2021). Phonopy then uses these forces to construct the force constant matrix and derive phonon dispersion relations and phonon density of states, enabling researchers to predict material behavior under various thermal and mechanical conditions. This method not only assists in assessing the stability of a crystal structure but also provides insights into electron–phonon coupling mechanisms critical for charge transport (Ning et al., 2021). Consequently, such detailed lattice dynamical analyses are instrumental in correlating structural modifications with changes in macroscopic properties, thereby guiding the design and optimization of materials for applications like DSSC photoanodes.

2.16 Summary

The review of literature has shown that solar energy, particularly through 3D on photovoltaic technologies like DSSCs, holds great promise as a sustainable alternative to fossil fuels. Among the components of DSSCs, the photoanode plays a crucial role in determining the efficiency of charge collection and light harvesting. ZnO has been widely studied for this purpose due to its wide band gap, high electron mobility, and ease of synthesis. However, the performance of pristine ZnO in DSSCs is limited by its poor light absorption in the visible range and susceptibility to surface recombination, prompting investigations into doped ZnO systems for enhanced optoelectronic properties.

Numerous studies have explored the effects of RE doping on ZnO, with elements such as Ce, Eu, and Dy shown to improve optical absorption, modulate the band structure, and enhance charge transport properties. These improvements make RE-doped ZnO a promising candidate for use as a photoanode in DSSCs. Despite these advances, most available studies are either experimental in nature or focus on a limited number of dopants and doping concentrations. Additionally, there is inconsistent data on how

dopant concentration affects lattice structure, band gap, and optical transitions, and relatively few studies employ advanced ab initio methods like DFT+U or GW to analyze these systems at the electronic level. This highlights a significant knowledge gap in the comprehensive, systematic computational investigation of lanthanide-doped ZnO using DFT. Specifically, there is a need for detailed DFT-based modeling that explores multiple RE dopants at various concentrations and evaluates their effects on structural, mechanical, lattice dynamical electronic, transport and optical properties in relation to DSSC performance. The present study aims to fill this gap by employing advanced DFT approaches to simulate and analyze RE-doped ZnO systems, thereby providing theoretical insights that can guide the development of more efficient photoanode materials for next-generation solar energy applications.

CHAPTER THREE
MATERIALS AND METHODS

3.1 Introduction

This chapter presents the computational procedures used in the study, including the theoretical framework, simulation setup, and parameters applied in the modeling of RE-doped ZnO for DSSC applications. It outlines the methods used to investigate structural, mechanical, lattice dynamical, electronic, transport, and optical properties of the doped systems. The chapter also details the construction of the supercell, doping configurations, choice of functionals, and correction schemes used to enhance accuracy in electronic structure calculations.

The chapter further describes the procedures for structural optimization, total energy minimization, elastic property calculations, and phonon analysis. It explains the determination of band structures, DOS, and carrier effective masses, as well as the calculation of transport coefficients using Boltzmann transport theory. In addition, optical properties such as the dielectric function and absorption spectrum are evaluated. The chapter concludes with a description of the computational tools used, convergence criteria, and methods applied to ensure the reliability and reproducibility of the results.

3.2 Quantum Espresso (QE) Input File

The input file utilized in QE (Giannozzi et al., 2009) is contingent upon the specific calculation type being executed, which may include self-consistent field (SCF) calculations, band structure analysis, or variable cell relaxation (vc-relax) for structural optimization. This file encompasses all parameters essential for conducting ab initio calculations. In this research, periodic elements were obtained from the Materials Project database, where the requisite elements were downloaded. Following this, DFT parameters such as formation energy, volume, density, and bandgap were computed for the various forms of the compound under examination. Upon selecting a particular structure, detailed information regarding the structure was gathered, including lattice parameters, stability assessments, and phonon dispersion graphs. In Figure 3.1, a representative input file for QE is depicted. This input file is structured into various sections known as name-lists, including &control, &system, and

&electrons, as well as input cards that encompass atomic species, atomic positions, and k-points. The &control section is responsible for defining the computational strategy, including the type of calculation, such as SCF non SCF (NSCF) or relaxation. The &system section specifies parameters unique to the system, such as its lattice configuration and electron arrangement. The atomic species card lists the atoms involved in the system along with their respective pseudopotential files. The atomic positions card provides the coordinates of the atoms within the lattice framework. Lastly, the k-points card outlines the sampling method for the Brillouin zone applied in the calculations. Figure 3.1 shows the input file used in this study to solve the Kohn-Sham equations in QE, while the role of each component of the code is described in Table 3.1.

```
&CONTROL
  calculation =scf,
  prefix = zno,
  putdirect = =../tmp./,
  pueudopir = '/pseudo:/,
  verbosity : 'high,
&ELSYTEM
  ibrav = - 4,
  celldm(1) = 6.14 : (hezagonal Bravias l
  celldm(3) = 1.60 : a = αtaratio (c
  nat = 4,          ntyp = 2 = ')
  ecutwfc = 50.0,     ecutrho =
  occupations = 'smearing'
  smearing = 'gaussian
  degauss = 0.01
&ELECTRONS
  conv_thr = 1.0d-8,
  mixing_beta = 0.7
/
ATOMIC_SPECIES Zn  65.38  Zn.pbe-nc.UPF
  O            0   16.00  O.pbe-nc.UPF
ATOMIIC_POSITIONS crystal
  Zn     0.0000  0.0000  0.0000
  O      0.3333  0.6667  0.5000
  O      0.0000  0.0000  0.3825
K_POINTS automatic
  6 6 4 0 0 0
/
```

Figure 3.1: A QE Input File Relating to the Kohn-Sham Self-Consistency Scheme

Table 3.1: The Roles of Various Flags in the QE Input File

FLAG	ROLE
CONTROL	Controls the type of calculation (e.g., 'scf' for self-consistent field).
SYSTEM:	Defines the system parameters, such as lattice parameters, kinetic energy cutoffs, and the number of atoms.
ELECTRONS	Sets electronic convergence criteria.
ATOMIC_SPECIES	Specifies atomic types and pseudopotential files.
ATOMIC_POSITIONS	Defines the positions of atoms in the unit cell.
K_POINTS	Sets the k-point grid for Brillouin zone sampling.

3.3 Structural Properties

In this study, the structural properties of RE doped ZnO, specifically considering dopants Ce, Dy, Eu were investigated. The pristine ZnO structure adopts the well-known hexagonal wurtzite phase, which serves as the baseline for understanding the impact of lanthanide incorporation. The undoped material was modeled using a 3×3×3 supercell, consisting of 108 atoms, ensuring that the simulation captures sufficient periodicity and allows for the analysis of local distortions introduced by the dopants.

The computational approach involves a detailed structural optimization using DFT with the optimized norm conserving pseudopotential (ONCP) method as implemented in QE. For each system, the lattice parameters, bond lengths, and bond angles are determined by minimizing the total energy through SCF and variable-cell relaxation calculations. The optimization employs the GGA with the Perdew-Burke-Ernzerhof (GGA-PBE) exchange-correlation (XC) functional. A kinetic energy cutoff of 50 Ry for wavefunctions and 400 Ry for the charge density ensured accurate convergence of the computed electronic properties, while a Monkhorst-Pack k-point grid of 8×8×6 is used for Brillouin zone integration.

The study examines oxygen vacancy and dopant concentrations of 0%, 1.85%, 3.7%, and 5.56% to elucidate the influence of increasing dopant levels on the structural framework of ZnO. Incorporating lanthanide ions into the ZnO lattice is expected to induce notable distortions due to the ionic radii differences between the dopant

species and Zn^{2+} ions. Specifically, the substitution of Zn by larger RE ions results in local expansion of the lattice, modifying both the a and c lattice parameters and potentially altering the overall unit cell volume. These modifications are systematically quantified by comparing the optimized structural parameters of undoped and with those of RE doped systems.

The local environment around the dopant sites is characterized by analyzing changes in the bond lengths between Zn-O and RE-O pairs, as well as any variations in the bond angles that reflect the degree of lattice distortion. Such detailed structural information is crucial for understanding the interplay between the dopant-induced strain and the electronic structure, which ultimately governs the material's functionality as a photoanode in DSSC. The combination of Ce, Dy, and Eu doping provides a comprehensive framework to explore the role of RE dopants in tailoring the structural and electronic properties of ZnO, offering valuable insights into the design of improved DSSC materials.

3.4 Mechanical Properties

The mechanical properties of a material are characterized by parameters such as the bulk modulus, Young's modulus, shear modulus, and elastic constants. Among these, the elastic constants are critical as they directly determine the mechanical stability of a system.

3.4.1 Elastic Constants

In this study, the mechanical properties of RE doped ZnO were systematically investigated using the Thermo_pw code (Sánchez et al., 2018) integrated with QE. This computational framework was chosen for its sound implementation of first-principles calculations and its proven effectiveness in accurately predicting elastic behavior in complex materials. The analysis was conducted on a 3×3×3 supercell containing 108 atoms, with dopant concentrations ranging from 0% to 5.56%, to capture the effects of lanthanide incorporation (Ce, Dy, Eu) on the material's mechanical response. The methodology involved applying small, systematic strains to the fully optimized crystal structures and computing the corresponding stress responses. The fundamental relationship between stress and strain is described by Hooke's law in its generalized tensorial form represented in Equation 3.1.

$$\sigma_{ij} = \sum_{kl} C_{ijkl}\varepsilon_{kl} \tag{3.1}$$

where σ_{ij} represents the components of the stress tensor, ε_{kl} are the components of the strain tensor, and C_{ijkl} denote the elastic constants. These elastic constants were calculated from the second derivative (Equation 3.2) of the total energy with respect to strain:

$$C_{ij} = \frac{1}{V}\frac{\partial^2 E}{\partial\varepsilon_i\,\partial\varepsilon_j} \tag{3.2}$$

with E being the total energy and V the unit cell volume. The finite strain approach, as implemented in Thermo_pw, enabled the precise determination of the full elastic tensor by analyzing the response of the system under small deformations. From the calculated elastic constants, key mechanical parameters were derived. For example, the bulk modulus (B), which quantifies the material's resistance to uniform compression, can be expressed in a simplified isotropic form as demonstrated in Equation (3.3). The bulk modulus which illustrates the measure of incompressibility was computed from the average of B_V, B_R and B_H as described by equations (3.3-3.5).

$$B_V = \frac{1}{9}[2(C_{11} + C_{12}) + C_{33} + 4C_{13}] \tag{3.3}$$

$$B_R = \frac{(C_{11} + C_{12})C_{33} - 2C_{13}^2}{C_{11} + C_{12} + 2C_{33} - 4C_{13}} \tag{3.4}$$

$$B_H = \frac{B_V + B_R}{2} \tag{3.5}$$

Where B_V, B_R and B_H represent the Voigt, Reuss and Hill bulk modulus respectively. The shear modulus describing the deformation caused by a stretching force acting parallel to an invariant line was computed using Equations 3.6-3.8 (Namisi et al., 2023).

$$G_V = \frac{1}{30}(C_{11} + C_{12} + 2C_{33} - 4C_{13} + 12C_{44} + 12C_{66}) \tag{3.6}$$

$$G_R = \frac{5}{2}\frac{\{(C_{11}+C_{12})C_{33}-2C_{13}^2\}C_{44}C_{66}}{3B_V C_{44}C_{66}+\{(C_{11}+C_{12})C_{33}-2C_{13}^2\}(C_{44}+C_{66})} \quad (3.7)$$

$$G_H = \frac{G_V + G_R}{2} \quad (3.8)$$

To compute the young modulus (E), the bulk and shear modulus obtained were employed as per the relation defined by Equation 3.9.

$$E = \frac{9BG}{3B+G} \quad (3.9)$$

For wurtzite ZnO, which possesses a hexagonal crystal structure, six elastic constants are defined: C11, C12, C13, C33, C44, and C66. While the initial five constants are independent, Equation (3.10) defines the derivation of constant C66. (Chirchir et al., 2022).

$$C_{66} = \frac{C_{11}-C_{12}}{2} \quad (3.10)$$

This relationship emphasizes the interconnected nature of elastic constants in defining the mechanical stability and resilience of the material. The elastic constants were utilized to assess the mechanical stability of both pure and lanthanide-doped ZnO using the hexagonal symmetry criterion. The conditions defined by Equations 3.11 must be satisfied for mechanical stability in hexagonal structures:

$$C_{11}>0, C_{33}>0, C_{44}>0, C_{11}>|C_{12} \text{ and } (C_{11}+2C_{12})C_{33}>2C_{13}^2| \quad (3.11)$$

These conditions ensure that the material can withstand mechanical stresses without structural instability (Kumar & Singh, 2018). Specifically, C11 and C33 the constants describe the material's resistance to linear compression along the a- and c-directions of the lattice, respectively. By evaluating these criteria, it is possible to determine the mechanical stability of ZnO under various conditions, including the effects of lanthanide doping. This stability analysis will help reveal how doping alters the mechanical properties and overall resilience of ZnO.

3.4.2 Murnaghan Equation of State (MEoS)

The Birch-Murnaghan equation of state (EoS), defined by Equation (3.12), was employed to describe the relationship between energy, pressure, bulk modulus, and volume. This equation provides a mathematical framework for understanding the volumetric behavior of materials under pressure and is commonly used in materials science for determining the equation of state of crystalline solids. The extraction of physical parameters, including the bulk modulus and its pressure derivatives, involved fitting the computed total energy at ten varying lattice constants to a third-order Murnaghan equation of state as illustrated in Equation (3.12).

$$E(V) = \frac{B_o V}{B_0'}\left[\left(\frac{V_0}{V}\right)^{B_0'}\frac{1}{B_0' - 1} + 1\right] + \text{const} \tag{3.12}$$

where E (V) is the energy as a function of volume, B_o is the bulk modulus, V_0, is the equilibrium unit cell volume, B_0' is the pressure derivative of the bulk modulus. This equation is particularly useful for determining the material's response to changes in pressure, and has been applied to model the pressure-volume relationship in both pure and RE-doped ZnO. The results from the Birch-Murnaghan EoS can provide insights into the material's compressibility, elasticity, and stability under varying pressure conditions.

3.4.3 Elastic Anisotropy

Elastic anisotropy is a crucial parameter for evaluating the potential for micro-crack formation and understanding the directional dependence of a material's mechanical properties. In this study, several anisotropic indices were calculated to assess the degree of elastic anisotropy in pure and RE-doped ZnO. Zener anisotropic index (A_Z), universal Zener anisotropic index (A^U), and the equivalent Zener anisotropic index (A^{eq}) were calculated using Equations (3.13-3.15).

$$A_z = \frac{2C_{44}}{C_{11} - C_{12}} \tag{3.13}$$

$$A^{eq} = \left(1 + \frac{5}{12}A^U\right) + \sqrt{\left(1 + \frac{5}{12}A^U\right)^2 - 1} \tag{3.14}$$

$$A^U = 5\left(\frac{G_v}{G_R}\right) + \frac{B_v}{B_R} - 6 \geq 0 \quad (3.15)$$

Where B_v, (G_v) and B_R (G_R) represent the Voigt and Reuss form of bulk and shear modulus respectively. The shear and young's anisotropy ratios defined as E_{max}/E_{min} and G_{max}/G_{min} were also evaluated. Other fundamental elastic characteristics including the Poisson's' ratio (v), Pugh ratio (P), Kleinman parameter (ξ) and Debye temperature were evaluated using Equation (3.16-3.19).

$$v = \frac{1}{2}\left\{1 - \frac{E}{3B}\right\} \quad (3.16)$$

$$P = \frac{B}{G} \quad (3.17)$$

$$\xi = \frac{C_{11} + 8C_{12}}{7C_{11} + 2C_{12}} \quad (3.18)$$

$$\Theta_D = \frac{\hbar}{k}\left[\frac{3n}{4\pi}\left(\frac{N_A\rho}{M}\right)\right]^{1/3} V_m \quad (3.19)$$

Where $\hbar$ is plank's constant, k is Boltzmann's constant, N_A is Avogadro's number, n is the number of atoms per formula unit, M is the molecular mass per formula unit, ρ is the desity and V_m is obtained from Equation (3.20).

$$V_m = \left[\frac{1}{3}\left(\frac{2}{V_s^3 + V_l^3}\right)\right]^{-1/3} \quad (3.20)$$

Where V_s and V_l are the shear and longitudinal sound velocities. The hardness of the ZnO structures was investigated by use of Vickers hardness (H_v) addressed by Equation (3.21).

$$H_v = \frac{(1 - 2v)E}{6(1 + v)} \quad (3.21)$$

Where v and E represent the poisons ratio and young's modulus respectively.

3.5 Electronic Properties

The electronic properties of RE-doped ZnO were investigated using DFT within both the standard GGA and the GGA+U framework, as implemented in QE. The application of both approaches allowed for a more comprehensive evaluation of the electronic structure. This was to address the known underestimation of band gaps in GGA by introducing a Hubbard U correction that better accounts for the localized nature of the d and f electrons associated with Zn and the rare-earth dopants (Ce, Dy, Eu). Throughout these procedures, consistency was maintained by employing the optimized norm conserving pseudopotentials (ONCP), k-point sampling, and convergence criteria across both the GGA and GGA+U calculations. This methodological rigor ensured that the differences observed between the two approaches could be directly attributed to the treatment of electron correlation effects. The comprehensive electronic structure analysis, including the detailed evaluation of band structure, DOS, PDOS, and electron density, forms a critical component of the overall materials and methodology framework in this study. It establishes a direct correlation between the dopant-induced modifications at the atomic scale and the resultant electronic properties, which are pivotal for optimizing RE-doped ZnO as an efficient photoanode in dye-sensitized solar cells.

3.5.1 Electronic Band Structures

Initially, a self-consistent field (SCF) calculation was performed to obtain the converged ground-state electron density for both pristine and doped ZnO systems. In this stage, a plane-wave basis set and appropriate norm-conserving or ultrasoft pseudopotentials were utilized, while the exchange-correlation interactions were treated using the GGA-PBE functional (Cangi et al., 2022). For systems where the localized electron effects were significant, particularly in the presence of rare-earth elements, the GGA+U method was employed. This approach adds an on-site Coulomb interaction term to the standard DFT Hamiltonian to better describe the electron correlations. After achieving convergence in the SCF calculations with stringent energy thresholds (on the order of 10^{-8} Ry, non-self-consistent field (NSCF) calculations were carried out along high-symmetry paths in the Brillouin zone to determine the band structure. The high-symmetry points were selected according to the hexagonal symmetry of the wurtzite ZnO structure to ensure that critical features of the electronic dispersion were accurately captured. This enabled the identification

of the band gap character, whether direct or indirect and the detection of impurity states or mid-gap levels introduced by doping.

3.5.2 Density of States (DOS)

To ascertain the origin of the band structures, DOS and PDOS was calculated for pristine and RE doped ZnO. The electronic DOS plays an essential role in describing the number of states available at each energy level for electron occupancy. This characteristic is vital in modern electronic structure theory (Rouhi et al., 2015). To calculate the DOS, the electrons in the material are treated as a free electron gas, assuming that the material's periodic potential can be approximated in this way. By representing the state of an electron as a vector in reciprocal k-space, the electron's energy is expressed as described in Equation (3.22).

$$\mathrm{E(k)} = \frac{\hbar^2 \mathrm{k}^2}{2\mathrm{m_e}}\left(\mathrm{k_x^2} + \mathrm{k_y^2} + \mathrm{K_z^2}\right) \tag{3.22}$$

This theoretical framework provides a quantitative means to analyze and interpret the electronic structure of both pure and RE-doped ZnO.

3.5.3 Charge Density

In addition to the band structure and DOS analyses, electron density distributions were examined to elucidate the spatial localization of electrons within the crystal lattice. Electron density maps were generated to visualize the regions of electron accumulation and depletion, which provided insight into the nature of chemical bonding and the effects of doping on the local electronic environment. These maps were instrumental in identifying potential active sites and elucidating how the dopant atoms interact with the surrounding ZnO matrix.

3.6 Optical Properties

The optical properties of RE (Ce, Dy, Eu) doped ZnO were aslo investigated using Thermo_pw as integrated in QE. Understanding these properties is crucial for evaluating the potential of doped ZnO as an efficient photoanode material for DSSCs. The optical properties of a material explain the frequency response of distinct optical parameters of that material to the energy of the incident photon, $E = h\upsilon$. The optical parameters in a material are determined by $\varepsilon(\omega)$ which is a complex dielectric

function dependent on frequency. $\varepsilon(\omega)$ as expressed in the relation (3.23) (Mulwa, 2017).

$$\boldsymbol{\varepsilon(\omega) = \varepsilon_1(\omega) + i\varepsilon_2(\omega)} \qquad (\mathbf{3.23})$$

Where $\varepsilon_1(\omega)$ and $\varepsilon_2(\omega)$are the real and complex parts respectively of the complex dielectric functions. While the real part, explains the photon dispersion and extent of material polarisation, the imaginary component describes the photon absorption of a material. Within the selection rules, calculations of the momentum matrix elements between unoccupied and occupied wavefunctions as given in Equation (3.24) give the imaginary part $\varepsilon_2(\omega)$.

$$\varepsilon_2(\omega) = \frac{8\pi^2 e^2}{\omega^2 m^2} \sum_n \sum_{n'} \int |P^v_{nn'}(k)|^2 f_{kn}(1 - f_{nn'}) \delta\left(E^k_n - E^k_{n'} - \hbar\omega\right) \frac{d^3k}{(2\pi)^3} \quad (3.24)$$

The Kramer – Kronig relation given by Equation (3.25) was used to derive the real part $\varepsilon_1(\omega)$ from $\varepsilon_2(\omega)$ (Xu & Ching, 1993).

$$\varepsilon_1(\omega) = 1 + \frac{2}{\pi} \int_0^\infty \frac{\varepsilon_2(\omega)\omega' d\omega'}{\omega'^2 - \omega^2} \qquad (3.25)$$

The optical absorption coefficient, α(ω), was calculated to assess how the introduction of rare-earth dopants influences ZnO's light-harvesting capabilities. The absorption coefficient is given by Equation (3.26).

$$\alpha(\omega) = \sqrt{2}\omega \left(\sqrt{\varepsilon_1^2(\omega) + \varepsilon_2^2(\omega)} - \varepsilon_1(\omega) \right)^{\frac{1}{2}} \qquad (3.26)$$

Other optical constants such as refractive index $n(\omega)$, energy loss spectrum $L(\omega)$, and reflectivity $R(\omega)$ were obtained from $\varepsilon_1(\omega)$ and $\varepsilon_2(\omega)$ as indicated in Equations (3.27-3.29) respectively.

$$n(\omega) = \frac{1}{\sqrt{2}} \left(\frac{\sqrt{\varepsilon_1^2(\omega) + \varepsilon_2^2(\omega)} + \varepsilon_1(\omega)}{2} \right)^{\frac{1}{2}} \qquad (3.27)$$

$$L(\omega) = \frac{\varepsilon_2(\omega)}{{\varepsilon_1}^2(\omega) + {\varepsilon_2}^2(\omega)} \tag{3.28}$$

$$\mathrm{R}(\omega) = \frac{(\mathrm{n}-1)^2 + \mathrm{K}^2}{(\mathrm{n}+1)^2 + \mathrm{K}^2} \tag{3.29}$$

3.7 Transport Properties.

The transport properties of a material are essential in selecting an efficient photoanode for dye-sensitized solar cells (DSSCs). Among commonly used metal oxide semiconductors, (ZnO) stands out due to its superior electrical conductivity and lower resistivity compared to alternatives (Çavaş, 2017; Çolak & Karaköse, 2019; G. Zhang et al., 2022). In this study, the electrical conductivity of three ZnO phases was computed as a function of hole concentration and temperature to assess their potential for DSSC applications. Additionally, the Seebeck coefficients were calculated to validate the inverse relationship between electrical conductivity and thermoelectric power, ensuring the reliability of the results (Kim et al., 2015).

To determine these transport properties, the semi-classical Boltzmann transport equations under the constant relaxation time approximation were solved using the BoltzTraP code (Madsen & Singh, 2006). The investigation covered four distinct temperatures, 200 K, 400 K, 600 K, and 800 K to analyze the impact of thermal variations on ZnO's transport behavior. The electrical conductivity is described by Equation 3.30 (Khuili et al., 2020).

$$\sigma_{\alpha\beta}\,(T,\mu) = \frac{1}{\Omega}\int \sigma_{\alpha\beta}(\varepsilon)\left[-\frac{\partial f_\mu(T,\varepsilon)}{\partial\varepsilon}\right]d\varepsilon \tag{3.30}$$

Where $\sigma_{\alpha\beta}$ is the conductivity tensor given by Equation 3.31, Ω is the volume of unit cell and f_μ is the fermi distribution.

$$\sigma_{\alpha\beta}\,(\mathrm{i},\mathrm{k}) = \mathrm{e}^2\tau_{\mathrm{i,k}}\mathrm{V}_\alpha(\mathrm{i,k})\mathrm{V}_\beta(\mathrm{i,k}) \tag{3.31}$$

Where τ is the electronic relaxation time designating the time interval between two successive collisions of charge carriers. V_α and V_β represent the velocities of charge carries in the corresponding directions $\alpha\ and\ \beta$ respectively.

3.8 Lattice Dynamics

After achieving an optimized structure, small, symmetry-adapted displacements were introduced to compute the Hellmann–Feynman forces. These forces are crucial for constructing the dynamical matrix, which underpins the analysis of lattice dynamics and the subsequent calculation of phonon properties. The computed forces from QE were then interfaced with phonopy (Togo & Tanaka, 2015) to perform lattice dynamics calculations using the finite displacement method. Phonopy utilizes the force constant matrix derived from the DFT-calculated forces to obtain phonon dispersion relations and the phonon density of states. These phonon properties provide insight into the vibrational behavior of the crystal lattice, including the identification of any dynamical instabilities that would be signified by imaginary phonon modes (Pallikara et al., 2022). Moreover, the detailed analysis of the phonon spectrum enables us to understand the role of lattice vibrations in thermal conductivity and electron–phonon interactions, which are critical parameters for the performance of materials in applications such as DSSC photoanodes.

3.9 GGA+U

To address the well-documented limitations of standard GGA in accurately representing systems with strongly localized electron states, particularly the Zn-3d and rare earth (RE) 4f orbitals, the GGA+U approach was adopted in this study. The inclusion of a Hubbard U correction enhances the treatment of electron–electron interactions in localized orbitals, which are otherwise poorly described in conventional DFT. Specifically, Hubbard U values were applied to the Zn-3d and O-2p orbitals (denoted as Ud and Up, respectively) to improve the accuracy of both the structural and electronic properties of ZnO. Additionally, suitable U values were introduced for the 4f states of the Ce, Dy, and Eu dopants to capture the strong on-site Coulomb repulsion characteristic of RE elements.

The magnitude of the on-site potential is basically defined by parameters U (on-site Coulomb) and J (on-site exchange), which can be obtained from first-principle calculations or by comparison with experimental data (Qi et al., 2008) as defined by Equation 3.32.

$$E_{DFT+U} = E_{DFT} + \sum_{a} \frac{U_{eff}}{2} Tr\,(\rho^{a} - \rho^{a}\rho^{a}) \quad (3.32)$$

Where ρ^{a} is the atomic orbital matrix. The selection of appropriate U parameters was critical to the reliability of the simulations. Therefore, a range of U values reported in prior theoretical and experimental studies were initially considered. These were then refined by iteratively comparing the computed band gaps, lattice constants, and bond lengths against experimentally measured values and validated literature data. This empirical tuning allowed the optimized U values to yield results that align well with known physical properties, ensuring the predictive accuracy of the DFT+U formalism for the RE-doped ZnO systems under investigation. The impact of Hubbard U potential on the structural, mechanical, electronic and optical properties was further investigated in this study.

3.10 Oxygen Vacancies

In this study, DFT calculations were performed using QE to investigate the influence of oxygen vacancies on ZnO. A supercell model comprising 108 atoms was constructed, and oxygen vacancies were introduced by selectively removing oxygen atoms to achieve concentrations of 0%, 1.85%, 3.37%, and 5.56%. This systematic variation allowed for a controlled study of oxygen vacancy-induced modifications across a range of vacancy levels. For each vacancy configuration, full structural optimization was conducted to relax both atomic positions and lattice parameters until the forces on the atoms were minimized (below 0.01 eV/Å). The electronic structure was then examined via band structure and density of states calculations, revealing the appearance of oxygen vacancy -induced mid-gap states. Additionally, optical properties (such as absorption spectra and dielectric response), electrical characteristics (including effective mass and carrier concentration), and mechanical properties (such as elastic constants and bulk modulus) were evaluated to provide a comprehensive understanding of the impact of oxygen vacancies.

3.11 Brillouin Zone Sampling

In the present study, Brillouin zone (BZ) sampling was performed to ensure accurate electronic structure calculations for RE (Ce, Dy, Eu) doped ZnO. The Brillouin zone was sampled using a Monkhorst-Pack grid, which was optimized to balance

computational efficiency and accuracy in the determination of electronic and optical properties. The k-point grid was determined by testing different mesh densities until convergence was achieved for key properties such as total energy, band gap, and density of states. To resolve the band dispersion accurately, the electronic band structure was calculated along high-symmetry points in the Brillouin zone of the wurtzite ZnO lattice. The selected high-symmetry k-path was based on the standard convention for the hexagonal and cubic systems as shown in Figure 3.2, following the sequence: $\Gamma \rightarrow M \rightarrow K \rightarrow \Gamma \rightarrow \mathrm{A} \rightarrow \mathrm{L} \rightarrow \mathrm{H} \rightarrow \mathrm{A}$ and $\Gamma \rightarrow Z \rightarrow D_1 \rightarrow \mathrm{H} \rightarrow \mathrm{Y} \rightarrow \mathrm{C} \rightarrow \mathrm{D} \rightarrow \mathrm{X} \rightarrow \Gamma$

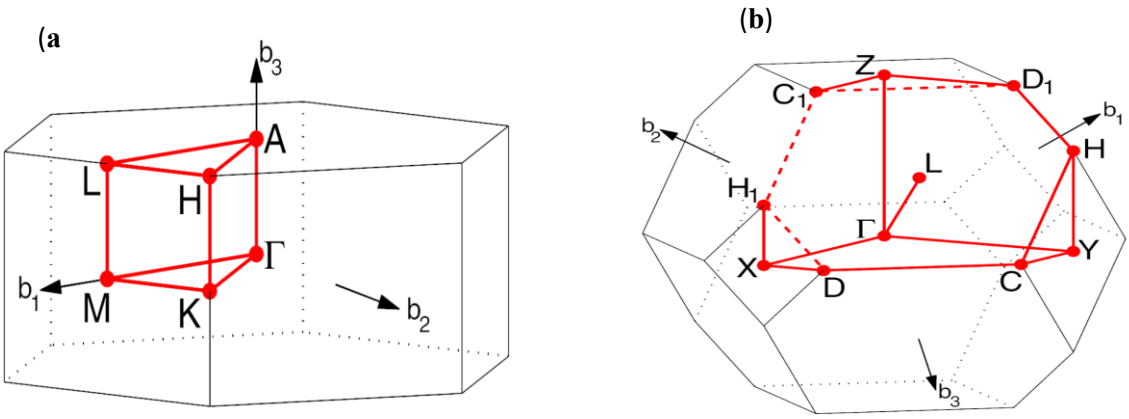

Figure 3.2: Brillouin Zone Sampling Path for (a) Hexagonal Wurtzite and (b) Cubic ZnO (Monkhorst & Pack, 1976)

3.12 Ethical Considerations

Although this study was purely computational and did not involve human or animal subjects directly, ethical considerations were observed throughout the research process. Since the findings may eventually inform the development of solar energy technologies intended for human use, the accuracy, transparency, and integrity of data and results were given utmost priority. All simulations were conducted using reliable, peer-reviewed methods, and findings were reported without fabrication, falsification, or misrepresentation. Additionally, all sources were properly acknowledged to uphold academic honesty. By ensuring that the methodologies and outcomes are scientifically sound, the study contributes responsibly to advancements in renewable energy, with the broader goal of promoting human and environmental well-being.

3.13 Summary

This chapter presented the computational methodology employed to investigate the structural, mechanical, lattice dynamical, electronic, transport, and optical properties of RE-doped ZnO for potential application in DSSCs. This study employed DFT as implemented in the Quantum ESPRESSO computational package to investigate the material properties of rare-earth (RE) metal doped ZnO, specifically with Ce, Dy, and Eu dopants. A 3×3×3 W-ZnO supercell comprising of 108 atoms was constructed, and doping was introduced by substituting one or more Zn atoms with RE elements to simulate various concentrations (0%, 1.85%, 3.7%, and 5.56%). Structural properties were determined through full geometry optimization using the GGA-PBE functional. Lattice constants, bond lengths, bond angles, and volume changes were analyzed to assess structural modifications induced by doping. The Brillouin zone was sampled using Monkhorst-Pack k-point meshes, and convergence tests were carried out for energy cut-offs and k-point density to ensure computational accuracy. To evaluate the mechanical properties, the thermo_pw code was used to calculate elastic constants, bulk modulus, shear modulus, Young's modulus, and Poisson's ratio. These parameters were used to determine mechanical stability and anisotropy of the doped ZnO systems. Lattice dynamical properties were assessed using phonon dispersion calculations via the phonopy code integrated in QE, which allowed investigation of vibrational modes and dynamic stability.

The electronic properties were analyzed through band structure and DOS calculations, including projected DOS to capture the contribution of dopant orbitals. For improved band gap accuracy, GGA+U corrections were applied at Zn-3d, RE-4f and O-2p orbitals. Optical properties were derived from the complex dielectric function, absorption coefficient, and reflectivity spectra. Additionally, the Boltzmann transport equation within the constant relaxation time approximation, as implemented in the BoltzTraP code, was used to predict transport properties such as the Seebeck coefficient and electrical conductivity across varying temperatures. These computational methods collectively facilitated a comprehensive understanding of how RE doping modifies the multifunctional properties of ZnO for application in DSSC.

.

CHAPTER FOUR
RESULTS AND DISCUSSION

4.1 Introduction

This chapter presents and discusses the results obtained from DFT investigations on lanthanide-doped ZnO, emphasizing its potential as a photoanode material for DSSC. A comprehensive suite of properties was examined, including structural, mechanical, dynamical, electronic, optical, and transport characteristics. The study systematically explores the effects of doping with rare-earth elements, with particular attention to variations in dopant concentration, the application of the Hubbard U correction to better capture localized electron interactions, and the role of oxygen vacancy in altering the material's behavior.

4.2 Optimization of ZnO Unit Cell

4.2.1 Comparative Analysis of ZnO Phases

The current study examined the material properties of ZnO in three distinct structural phases; cubic, wurtzite, and monolayer using DFT as the primary investigative tool. The analysis was structured to assess the influence of crystallographic configuration on the electronic, structural, and optical characteristics of ZnO. The cubic phase is noted for its high symmetry, which is expected to contribute to a more isotropic distribution of electronic states, whereas the wurtzite phase, being the naturally stable form under ambient conditions, exhibits anisotropy and strong piezoelectric effects. In contrast, the monolayer configuration offers unique features associated with quantum confinement and reduced dimensionality, which are anticipated to significantly alter its electronic band structure. The methodology reported herein involved systematic DFT calculations to evaluate and compare the material properties of each ZnO unit cell configuration. The results are reported in terms of lattice parameters, bandgap energies, and density of states, among other critical parameters. By detailing these comparisons, the report aims to highlight the potential of each phase for applications in dye-sensitized solar cell photoanodes and other optoelectronic devices. The findings provide a comprehensive overview of how structural modifications at the atomic scale can influence material behavior, thereby informing future experimental and theoretical research in the field.

4.2.2 Effects Crystallographic Configuration

In this study, the influence of crystallographic configuration on the material properties of zinc oxide (ZnO) was systematically investigated by examining three distinct phases: cubic, wurtzite, and monolayer. Each of these configurations exhibits unique structural symmetry, atomic coordination, and bonding characteristics, which significantly impact the physical and electronic behavior of ZnO. Understanding how these structural differences affect properties such as stability, band structure, and mechanical performance is crucial for tailoring ZnO for specific applications, particularly in optoelectronics, photovoltaics, and nano electronic devices.

Figure 4.1 presents the schematic diagrams of the three ZnO phases tested. The cubic ZnO (C-ZnO) unit cell as in Figure 4.1(a), often associated with the Zinc blende structure, is characterized by its high degree of symmetry. In this configuration, both Zn and O ions are arranged in an octahedral coordination, where each ion is surrounded by six counter ions. This arrangement results in an isotropic crystal lattice, where the lattice parameters are equal along all three axes. Although the C- ZnO is typically stabilized under high-pressure conditions, its symmetric structure leads to uniform interatomic spacing and bond lengths, which can simplify theoretical modeling and offer insights into isotropic electronic and mechanical behaviors.

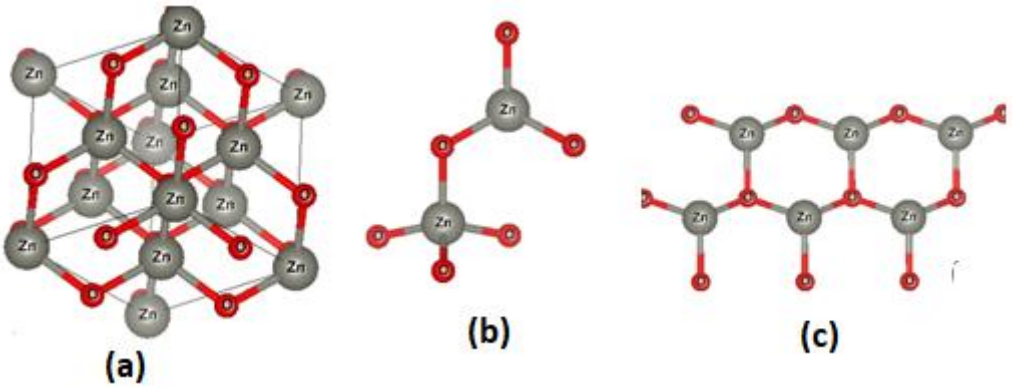

Figure 4.1: Schematic Representation of (a) C-ZnO, (b) W-ZnO and (c) M-ZnO Structure using VESTA Code

In contrast, the wurtzite phase of ZnO (W-ZnO) is the thermodynamically stable structure at ambient conditions and exhibits a hexagonal close-packed arrangement with lower symmetry compared to the cubic phase. In the W-ZnO structure depicted in Figure 4.1(b), each Zn ion is tetrahedrally coordinated by four O ions, and vice versa, leading to a distinctive anisotropy in lattice parameters denoted by the a and c

axes with the c/a ratio typically approaching an ideal value of approximately 1.633 (Ungula et al., 2017). This anisotropic coordination results in directional properties, such as polar surfaces along the c-axis, which are critical in applications like piezoelectric devices. Additionally, the reduced coordination in the monolayer ZnO (M-ZnO) unit cell (Figure 4.1(c)), where the structure is confined to a single atomic layer, leads to a unique two-dimensional honeycomb-like lattice. The monolayer configuration exhibited altered bond lengths and angles due to the absence of interlayer interactions, and it may present either a planar or slightly buckled geometry depending on external factors such as substrate interactions and synthesis conditions. This dimensional reduction enhances quantum confinement effects and surface phenomena, distinguishing its structural properties from those of the bulk cubic and wurtzite phases.

For the cubic structure, the convergence of the total energy with respect to k-point sampling was systematically investigated for using k-point grids ranging from 4×4×4 to 10×10×10. As described in Figure 4.2 (a), the total energy exhibited a slower convergence compared to the wurtzite phase, likely due to the higher symmetry and denser Brillouin zone sampling required for cubic structures. A grid density of 8×8×8 was found to provide well-converged results, with energy variations of less than 0.5 meV/atom for denser grids. This finding aligns with earlier DFT studies on C-ZnO, which have emphasized the need for finer k-point sampling to achieve accurate total energies. The slower convergence in the cubic phase underscores the importance of carefully selecting k-point grids for different crystal structures (Wang et al., 2024).

The convergence of the total energy with respect to k-point sampling was also systematically investigated for the wurtzite phase of ZnO. A Monkhorst-Pack k-point grid was employed, with grid densities ranging from 3×3×2 to 9×9×6. The total energy was found to converge rapidly as the k-point density increased, with the energy differences between successive grids diminishing significantly beyond a 6×6×4 as depicted in Figure 4.2 (b). At this grid density, the total energy variation was less than 1 meV/atom, indicating that further increases in k-point density would yield negligible improvements in accuracy. This result is consistent with previous studies, which have demonstrated that a 6×6×4 grid is sufficient for achieving converged total energies in

wurtzite ZnO (Boukhari et al., 2020). The rapid convergence of the total energy with respect to k-point sampling highlights the efficiency of the chosen computational parameters for this phase.

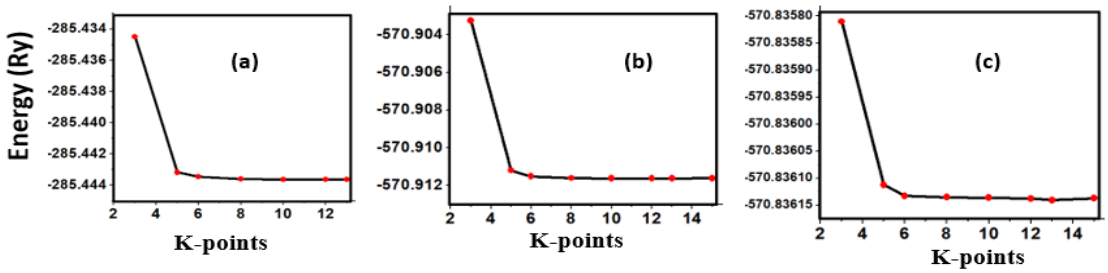

Figure 4.2: Total Energies as a Function of K-point for (a) C-ZnO, (b) W-ZnO and (c) M-ZnO

The M-ZnO phase, with its reduced dimensionality, required a different approach to k-point sampling (Raihan et al., 2021). A grid density ranging from 6×6×1 to 12×12×1 was used to evaluate the convergence of the total energy. Due to the 2D nature of the monolayer, the total energy converged more rapidly in the in-plane directions, with a 10×10×1 grid providing energy variations of less than 0.2 Ry. The out-of-plane direction, being less critical for monolayer systems, was sampled with a single k-point. These results are in agreement with previous studies on 2D materials, which have shown that dense in-plane k-point sampling is essential for achieving accurate total energies in monolayer systems (Qiao et al., 2020). The efficient convergence of the total energy for monolayer ZnO further validates the suitability of the chosen k-point grid for this phase.

The convergence of the total energy with respect to the E_{cut} was systematically investigated for the three phases of ZnO. Figure 4.3 displayed the total energy as a function of the kinetic energy cutoff (Ecut) for three ZnO phases. The plot revealed that the total energy decreased steadily with a convergence achieved at 350, 450 and 400 Ry for C-ZnO, W- ZnO and M-ZnO respectively indicating that the plane-wave basis set had become sufficiently complete. This behavior suggested that lower E_{cut} values were insufficient to capture all the relevant electronic states accurately, while values beyond 500 Ry did not significantly alter the total energy. The convergence observed was consistent with previous reports on ZnO, confirming that a cutoff between 400 ∓ 50 eV was appropriate for ZnO calculations (Neupane et al., 2023). Figure 4.4(a) shows that the total energy for C-ZnO reached a minimum at an

optimized lattice constant of 4.388 Å. In this cubic phase, where the relation a=b=c holds due to its high symmetry, the convergence of the total energy confirmed that the equilibrium structure was accurately captured at this lattice parameter. This value was in good agreement with previous computational values of 4.58Å (Harun et al., 2020) and experimental value of 4.27 Å (Sokolov et al., 2011).

Figure 4.4(b) depicted the total energy as a function of both the in-plane lattice constant (a) and the out-of-plane lattice constant (c) for W-ZnO. The analysis indicated that the total energy was minimized at an in-plane lattice constant of a=b=3.289 Å and an out-of-plane lattice constant of c= 5.284 Å, yielding a c/a ratio of 1.61. These optimized values were consistent with the typical anisotropic characteristics of the wurtzite structure. In Figure 4.4(c), the M-ZnO total energy plot revealed that the minimum energy was achieved at an in-plane lattice constant of around 3.30 Å. The slight expansion compared to the wurtzite phase was attributed to the reduced coordination and quantum confinement effects inherent in the two-dimensional structure (Chen et al., 2019). Overall, the convergence of the lattice constants across C-ZnO, W-ZnO, and M-ZnO validated the computational approach and aligned well with the established literature as summarized in Table 4.1 The unit cell volumes of the various ZnO phases were reported in Table 4.1 and illustrated in Figure 4.5, with C-ZnO, W-ZnO, and M-ZnO exhibiting volumes of 21.12, 49.89, and 28.45 $Å^3$, respectively. These values were attributed to the differences in crystal symmetry and bonding; specifically, the relatively large volume of W-ZnO reflected its open tetrahedral coordination associated with sp^3 hybridization.

While the compact cubic structure of C-ZnO and the intermediate, planar configuration of M-ZnO (which featured sp^2 hybridization) resulted in reduced unit cell volumes. These findings provided important insights into the structural influences on the physical properties of ZnO. The expanded lattice in W-ZnO was consistent with longer Zn–O bond lengths and a more open framework, in contrast to the contraction observed in M-ZnO due to stronger in-plane sp^2 bonding interactions.

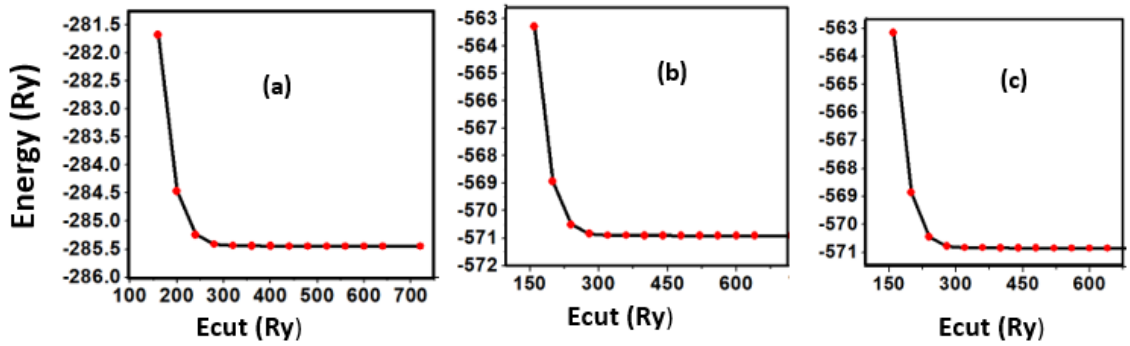

Figure 4.3: Total energies as a Function of Ecut for (a) C-ZnO, (b) W-ZnO and (c) M-ZnO

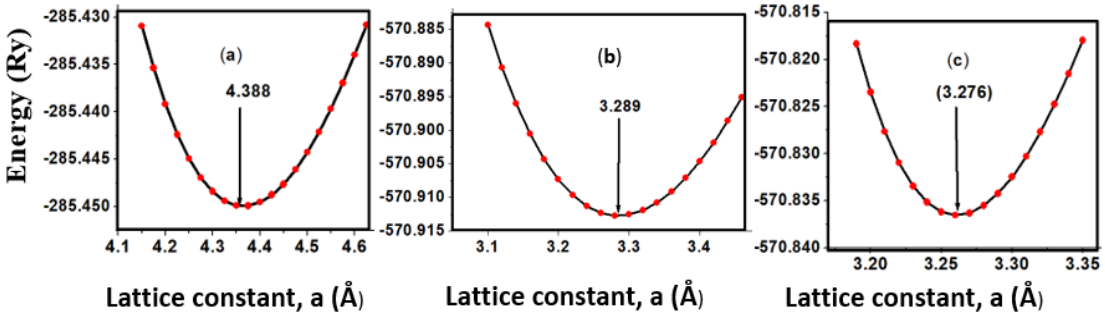

Figure 4.4: Total Energies as a Function of Lattice Constant, a for (a) C-ZnO, (b) W-ZnO and (c) M-ZnO

This variation in unit cell volume underscored the critical role of atomic arrangement and hybridization in determining the material properties, thereby aligning with earlier studies by (Raihan et al., 2021) that highlighted the impact of bonding characteristics on ZnO's electronic and optical behavior. The analysis presented in Table 4.1 revealed that the bond lengths of C-ZnO, W-ZnO, and M-ZnO were 1.973, 1.9982, and 1.9102 Å, respectively, a trend that was indicative of distinct structural configurations across these phases. The shorter Zn–O bond in M-ZnO was attributed to its planar honeycomb structure, which had undergone sp^2 hybridization, thereby enhancing orbital overlap and resulting in a more contracted bond length relative to the tetrahedrally coordinated, sp^3 hybridized W-ZnO. In contrast, the intermediate bond length observed in C-ZnO suggested a bonding environment that differed from both the wurtzite and monolayer forms, possibly due to its cubic symmetry affecting orbital interactions. These variations in bond lengths provided insight into how structural dimensionality and hybridization influenced the electronic properties of ZnO, corroborating findings from earlier studies (Chaudhuri et al., 2023).

Table 4.1: Optimized Lattice Constants, Bulk Modulus and its Derivative, Bond Length, and Minimum Energy (Emin) in Comparison with Other Studies

Phase		a (Å)	C (Å)	V (Å^3)	B (GPa)	B'	Bond Length (Zn-O) (Å)	Reference
C-ZnO	DFT	4.388	4.388	21.12	129	4.67	1.973	Current study
	Expt	4.27	4.27	19.46	-	-	-	Decremps et al., 2003)
	DFT	4.55	4.55	24.86	133.7	4.79	-	(Chibueze 2021)
W-ZnO	DFT	3.289	5.284	49.89	136.8	4.71	1.9982	Current study
	Expt	3.264	5.219	48.15	-	-	1.992	(Ungula & Dejene, 2016)
	DFT	-	-	49.88	129.7	4.68	-	(Charifi et al., 2007)
M-ZnO	DFT	3.20	5.15	45.67	-	-	1.98	(Wu et al., 2005)
	DFT	3.30		28.45	-	-	1.9102	Current study
	DFT	3.283	-	-	-	-	1.895	(Tusche et al., 2007)

The Murnaghan equation of state was employed to analyze the variation of total energy with volume for the cubic and hexagonal phases of ZnO. By systematically varying the lattice constants for the cubic phase and the volume for the hexagonal phase, the minimum SCF energies were determined, and the corresponding energy–volume data were fitted using the Murnaghan EOS. This approach enabled the extraction of the bulk modulus (B) and its pressure derivative (B'), which serve as measures of the material's compressibility and mechanical stability. The fitting procedure allowed quantitative assessment on how the interatomic bonding and crystal structure influence the mechanical properties in these different phases. The analysis yielded a bulk modulus of 129 GPa with a derivative of 4.67 for the cubic phase, while the hexagonal (wurtzite) phase exhibited a slightly higher bulk modulus of 136.8 GPa with a derivative of 4.71. These findings suggest that the hexagonal phase is

marginally more resistant to compression than the cubic phase, likely reflecting differences in bonding and lattice arrangement. Notably, the monolayer phase was excluded from this analysis due to its inherent two-dimensionality, which precludes the direct application of a three-dimensional volume-based equation of state.

4.2.3 Effects of Hubbard U on the Structural Properties of Wurtzite ZnO

W-ZnO, known for its promising optoelectronic properties and unique hexagonal structure, presents significant challenges in theoretical modeling due to the strong electron correlation effects in its Zn-3d and O-2p states. Conventional DFT often underestimates these correlations, leading to discrepancies in predicted structural parameters such as lattice constants and unit cell volume. To overcome these limitations, the Hubbard U correction (DFT+U) has been applied to both the Zn-3d and O-2p orbitals. This dual correction helps mitigate self-interaction errors and more accurately represents the localized nature of the electrons, thereby refining the description of the bonding environment in ZnO (Guermit et al., 2020). The application of Hubbard U to both Zn-3d and O-2p orbitals has been found to exert a notable influence on the structural properties of wurtzite ZnO (Goh et al., 2017). Specifically, the inclusion of U for the Zn-3d states shifts these energy levels to lower energies, which can enhance the ionic character of the Zn–O bonds and lead to subtle variations in the lattice constants. Simultaneously, applying U to the O-2p orbitals alters the degree of hybridization with the Zn states, thereby affecting bond lengths and, consequently, the overall volume of the unit cell. These adjustments enable a more systematic alignment of theoretical predictions with experimental observations, highlighting the critical role of electron localization effects in determining the material's structural.

In the GGA+U calculations for wurtzite ZnO, a comprehensive convergence study was conducted with respect to the k-point sampling to ensure the reliability of the total energy and derived structural properties. The k-point grid was varied over a wide range from a coarse 3×3×1 grid up to a dense 18×18×16 mesh. As shown in Figure 4.5a, the total energy displayed significant fluctuations for the coarser grids; however, the energy values gradually stabilized as the k-point density increased. Convergence was effectively achieved at an 8×8×6 grid, where further refinement resulted in negligible changes in total energy. This outcome indicates that an 8×8×6 k-point grid provides a

sufficiently accurate Brillouin zone integration for wurtzite ZnO within the GGA+U framework, striking a balance between computational cost and precision. Similarly, the plane-wave cutoff energy (Ecut) was systematically varied from 10 Ry to 100 Ry in 5 Ry intervals to determine an optimal value for the electronic structure calculations. Figure 4.5b illustrates that at lower Ecut values, the total energy is highly sensitive to the cutoff, reflecting an incomplete basis set. As the cutoff energy increases, the total energy progressively converges, and stability is achieved at 50 Ry. At this cutoff, further increases in Ecut do not produce significant changes in the total energy, confirming that 50 Ry is sufficient for an accurate and efficient description of the electronic states in wurtzite ZnO using the GGA+U method. Together, these convergence tests validate the selected computational parameters, ensuring that subsequent analyses of structural properties and electronic behavior yield results that are both reliable and stable.

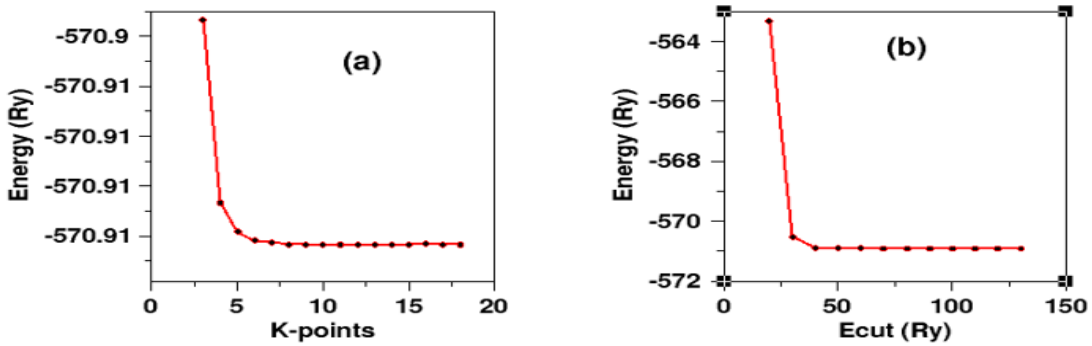

Figure 4.5: Plots of Energy (Ry) as a Function of (a) K-points (b) Ecut (Ry)

The lattice parameter optimization for wurtzite ZnO was carried out using fixed k-point and cutoff energy (Ecut) settings, ensuring that the electronic structure calculations were well converged. In this process, the lattice constant (a) was varied systematically within the range of 3.19–3.4 Å, while the ratio c/a was adjusted between 1.55 and 1.65. Figures 4.6(a), (b), and (c) illustrate the energy variations corresponding to changes in the lattice constant a, the c/a ratio, and the overall cell volume respectively. Analysis of the data from these figures indicates that the optimal lattice parameters for wurtzite ZnO are a=b=3.289Å and c=5.29032Å.

With the optimal lattice constants established, the calculated c/a ratio is approximately 1.608 which is close to the experimental value of 1.60 expected for hcp unit cells (Ungula & Dejene, 2016). The corresponding cell volume is determined to be 49.39 $Å^3$ which is in good agreement with the experimental value of 48.15 $Å^3$ (Ungula et al., 2017) and DFT value of 45.67 (Khuili et al., 2020) implying that this technique is viable and the obtained findings are reliable. The introduction of the Hubbard U correction in DFT enhances the localization of Zn-3d and O-2p electrons, thereby reducing the hybridization between these states in ZnO. This reduced hybridization results in a contraction of the lattice parameters, including both the lattice constants and the overall unit cell volume. Consequently, incorporating the Hubbard U potential yields structural predictions that are more consistent with experimental observations, underscoring its critical role in accurately modeling ZnO's crystalline structure.

Table 4.2: Variation of Lattice Constant, a with Hubbard U Value of Zn-3d and O-2P

U_d value (eV)	**Lattice constant a (Å) DFT+U_d**	**U_p value (eV)**	**Lattice constant a (Å) DFT+U_d(10eV) +U_p**
0	3.289	0	3.270
2	3.285	2	3.265
4	3.280	4	3.254
6	3.277	6	3.250
8	3.274	8	3.247
10	3.270	10	3.242

Table 4.2 shows how the lattice constant a (in Å) varies in wurtzite ZnO when only the Zn-3d Hubbard U is applied (DFT+U_d) and when the Zn-3d potential is fixed at 10 eV and the O-2p Hubbard U is varied (DFT+U_d+U_p). In both cases, the Hubbard U was varied from 0 to 10 eV in increments of 2 eV. For the DFT+U_d calculations, as the Hubbard U on Zn-3d increases from 0 to 10 eV, the lattice constant a gradually decreases, reflecting a reduction in the Zn-3d and O-2p hybridization and a corresponding contraction of the lattice.

In the DFT+U_d+U_p approach with Zn-3d fixed at 10 eV, increasing the Hubbard U on O-2p from 0 to 10 eV further localizes the O-2p electrons, leading to an additional decrease in the lattice constant. This combined effect underscores the role of electron

localization in contracting the Zn–O bond lengths and, consequently, the overall lattice dimensions. The introduction of the Hubbard U (10 eV for Zn-3d and 8 eV for O-2P) potential into the GGA+U framework exerts a pronounced reducing effect on the lattice constants and overall cell volume of wurtzite ZnO, as clearly illustrated in Figures 4.6(a), (b), and (c) and tabulated in Table 4.3. This reduction is primarily attributed to the decreased hybridization between the Zn-3d and O-2p orbitals when the Hubbard U term is applied (Harun et al., 2020). By localizing these electrons more effectively, the U potential diminishes the extent of orbital overlap that typically contributes to the covalent character of the Zn–O bonds.

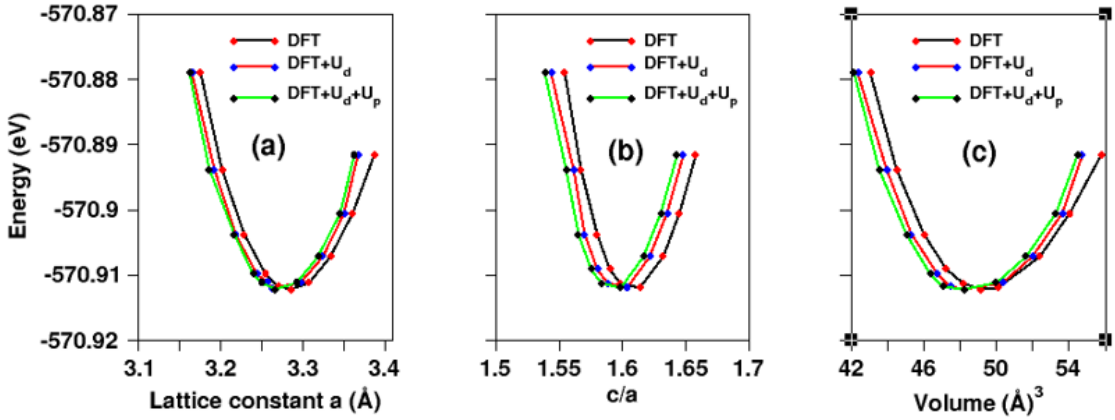

Figure 4.6: Plots of Total Energy as a Function of (a) Lattice Constant, (b) c/a Ratio and (c) Volume in DFT, DFT+Ud and DFT+Ud+Up

With reduced hybridization, the bonding becomes relatively more ionic, which in turn contracts the interatomic distances and results in smaller lattice parameters and a reduced unit cell volume. While bond length is the average distance between the nucleus, bond angle describes the angle between two atomic bonds. In this study, the bond length and bond angles of W-ZnO were determined using Xcrysden code. The impact of introducing the Hubbard U term on bond length and bond angle were investigated and the results presented in Table 4.3. Introducing the Hubbard U correction in DFT accounts for strong on-site Coulomb interactions, particularly in localized orbitals like Zn-3d or O-2p in ZnO. This leads to greater electron localization, reducing the hybridization between atoms and thus pulling them closer together (Ahmed et al., 2023). As a result, the increased electron correlation tightens the bonding, causing a slight reduction in bond length.

Table 4.3 Effects of Hubbard U on Lattice Parameters of W-ZnO

Formalism	a (Å)	c/a	V_0(Å^3)	Bond length (Å)	Bond angle (^{0})	E_{min} (Ry)	Ref
DFT	3.289	1.608	49.39	1.9993	108.37	-570.91	Current study
DFT+ U_d	3.276	1.603	49.26	1.9982	108.41	-570.45	Current study
DFT+U_d + U_p	3.269	1.594	48.84	1.9975	108.45	-570.31	Current study
Expt	3.264	1.599	48.15	1.992	-	-	(Ungula & Dejene, 2016)
Other DFT work	3.20	1.609	45.67	1.98	-	-	(Khuili et al., 2016)

4.3 Structural Properties of RE (Ce, Dy, Eu) Doped W-ZnO

4.3.1 Supercell Modelling

Accurate modeling of the structural and electronic properties of W-ZnO was a critical step in this study, particularly when investigating modifications such as rare earth (RE) doping. To ensure precision, the study constructed a 3×3×3 supercell containing 108 atoms as shown in Figure 4.7 to represent the W-ZnO structure under periodic boundary conditions. RE (Ce, Dy, Eu) doped W-ZnO models were then developed by substituting one Zn atom with one RE (Ce, Dy and Eu) atom. This translated to 1.85% dopant concentration which was low enough to avoid structural deformation. The use of a large supercell minimized dopant–dopant interactions, thereby simulating isolated impurity effects more realistically. This approach also allowed for accurate evaluation of local structural and electronic changes induced by the dopant atoms within the ZnO lattice. The optimization process involved minimizing the total energy by adjusting atomic positions, lattice parameters, and cell volume, while key computational parameters including a carefully selected k-point grid, cutoff energy (Ecut), and exchange-correlation functional were fine-tuned to strike a balance between computational efficiency and accuracy. In the structural optimization, the Brillouin zone was integrated using a Monkhorst Pack scheme employing a K-mesh of 4 x 4 x 3. The wave function and charge density were subjected to energy cut-offs of 50 Ry and 500 Ry, respectively, with a total energy convergence threshold

specified at 10^{-8} Ry. The chosen energy cut-offs ensure accurate representation of both the kinetic energy of the plane waves and the charge density distribution. These values were selected based on prior convergence tests to balance computational cost with reliable precision in total energy calculations.

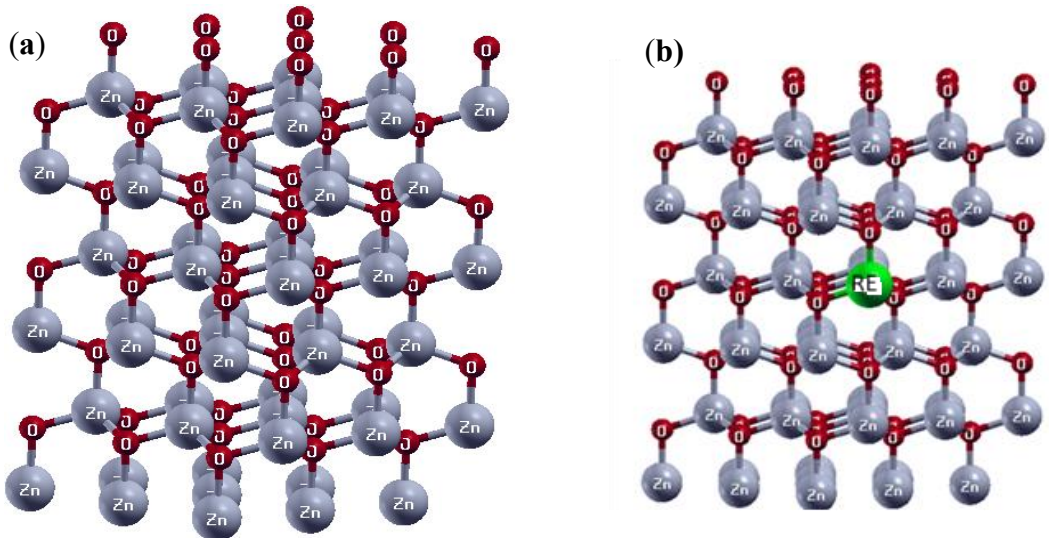

Figure 4.7: The Supercell Structure of (a) Pure ZnO and (b) RE-Doped ZnO

4.3.2 Lattice Parameters and Bulk Modulus

As shown in Table 4.4, doping ZnO with RE elements such as Ce, Dy, and Eu results in subtle changes in the lattice parameters. The computed values in this work show a slight increase, with a and c parameters around 3.29 Å and 5.29 Å, respectively. These figures are very close to those obtained from other DFT studies and, while marginally higher than some experimental reports, they consistently indicate that the incorporation of larger RE ions induces minimal lattice distortion. The cell volume also exhibits a modest expansion upon RE doping, with values in the range of approximately 49.6 $Å^3$ observed in this work. This increase in volume, which aligns well with both experimental and DFT studies, is consistent with the expected behavior when larger dopant ions replace the smaller Zn ions in the crystal lattice, leading to a slight but systematic lattice expansion.

In terms of mechanical properties, the bulk modulus decreases gradually with RE doping, from 133.2 GPa in Ce-doped ZnO to 129.5 GPa in Eu-doped ZnO, indicating a reduction in material stiffness. The derivative of the bulk modulus remains relatively stable around 4.65 to 4.70, suggesting that the pressure-dependent behavior is largely unaffected by the type of RE dopant. These trends, corroborated by both experimental

and theoretical comparisons, highlight how RE doping subtly modifies the structural and mechanical properties of ZnO.

Table 4.4: The lattice parameter, volume, bulk modulus and its derivative of RE (Ce, Dy and Eu) doped W-ZnO at 1.85 % dopant concentration

Dopant	Type of study	a =b (Å)	c(Å)	V (Å^3)	B (GPa)	B'	Reference
Ce	DFT	3.294	5.289	49.68	133.2	4.68	Current study
	Expt	3.2567	5.220	47.95	136.1	-	(Djaja et al., 2013)
	DFT	3.288	5.306	50.18	135.6	-	(Wen et al., 2018)
Dy	DFT	3.291	5.287	49.59	131.0	4.70	Current study
	Expt	3.287	5.291	50.02	134.9		(Yayapao et al., 2013)
	DFT	3.281	5.279	49.85	136.9		Harun et al. (2020)
Eu	DFT	3.291	5.288	49.60	129.5	4.65	Current study
	Expt	3.30	5.316	50.34	137.7		(El Ghoul et al., 2022)
	DFT	3.342	5.298	50.15	142		(Lysak et al., 2024)

4.3.3 Formation Energies (E_f)

The computation of formation energies (E_f), as described in Equation 4.1, was conducted for the RE-doped W-ZnO to ascertain their relative chemical stability (Zhang et al., 2024; Emery & Wolverton, 2017).

$$E_f = E_{tot}(\,ZnO{:}\,RE) - E_{tot}(ZnO) + \mu_{zn} - \mu_{RE} \qquad (4.1)$$

Where $E_{tot}(\,ZnO{:}\,RE)$ and $E_{tot}(ZnO)$ are the total energies per supercell of the relaxed RE doped and undoped ZnO respectively. The μ_{zn} and μ_{RE} represent the chemical potential of Zn and RE (Ce, Dy and Eu) respectively which is presumably the energy per atom in their respective metals. The formation energies for RE-doped ZnO, as shown in Figure 4.8, reveal that incorporating Ce, Dy, and Eu into the lattice is energetically favorable, with values of -8.2 eV, -7.4 eV, and -8.0 eV, for RE (Ce, Dy, Eu) doped ZnO respectively.

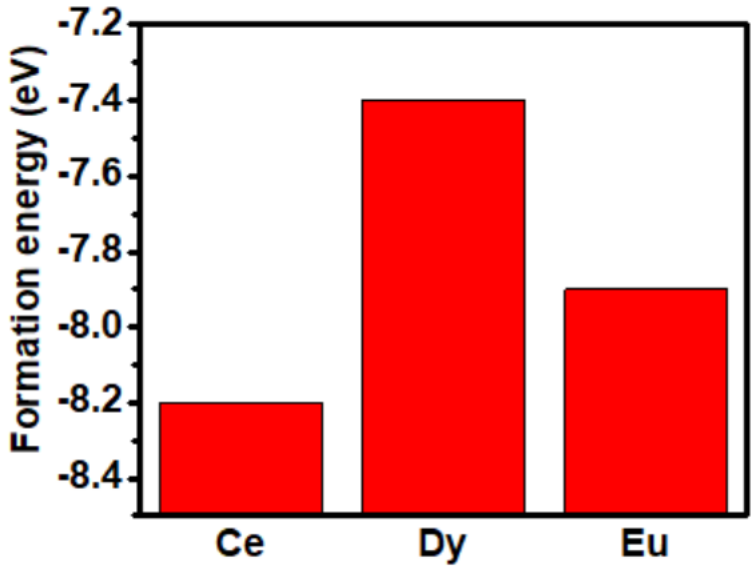

Figure 4.8: The Formation Energies of RE Doped W-ZnO Models.

The slight variations among the dopants suggest that Ce and Eu, with more negative values, are incorporated more readily compared to Dy, which may be attributed to differences in ionic size, electronic configuration, or local bonding environments within the ZnO lattice (Talwar & Becla, 2025).

4.3.4 X-Ray Diffraction (XRD) Simulations

Upon optimizing the geometrical structures, the VESTA code was employed to simulate the X-ray diffraction (XRD) spectra of pure and RE (Ce, Dy, and Eu) doped ZnO in order to examine the growth orientations of these materials. The simulations revealed that the primary diffraction peaks corresponded to the (100), (002), and (101) planes, typically observed at approximately $2\theta = 31.70°$, $34.40°$, and $36.20°$, respectively, as illustrated in Figure 4.9. The pure ZnO sample exhibited sharp and well-defined peaks, which confirmed the retention of the hexagonal wurtzite structure and served as a reliable reference for assessing the effects of RE doping on the crystallographic orientations.

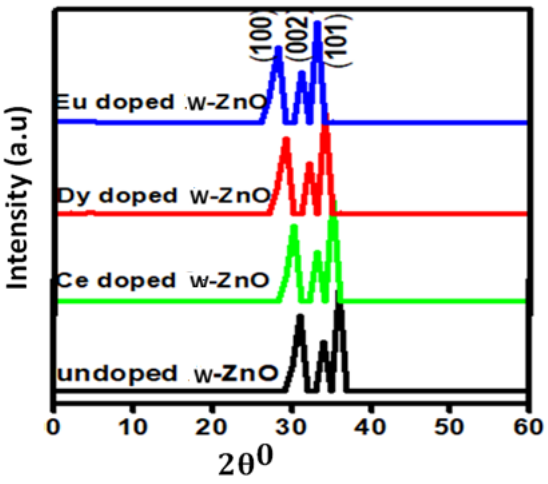

Figure 4.9: The Simulated XRD Patterns for the Undoped and RE (Ce, Dy, Eu) Doped W-ZnO.

The incorporation of RE dopants induced subtle modifications in the XRD spectra of ZnO. In the doped samples, minor shifts in the 2θ positions of the main diffraction peaks were observed, which were attributed to slight changes in the lattice parameters. The larger ionic radii of Ce, Dy, and Eu compared to Zn^{2+} led to a slight expansion of the lattice. This expansion was indicated by shifts toward lower 2θ values for certain peaks, with the most notable shift observed in the (002) reflection. In addition to these shifts, a slight broadening of the diffraction peaks was detected, suggesting an increase in micro strain or a reduction in crystallite size due to the inhomogeneous distribution of the RE ions within the ZnO lattice (Bett, 2024). Despite these modifications, the overall XRD patterns of the RE-doped ZnO samples retained the key features of the pure wurtzite structure, indicating that the doping process did not disrupt the fundamental crystallographic framework. The dominant (002) peak was preserved across all samples, which underscored the maintenance of the preferential c-axis growth orientation even after doping. This consistency implied that the introduction of RE elements effectively tuned the lattice constants without compromising the structural integrity of ZnO. These findings provided valuable insights into how controlled RE doping could modulate the material's properties while retaining its desirable crystalline characteristics, thereby enhancing its potential for various optoelectronic applications (Bett et al., 2024).

4.3.5 Effects of Dopant concentration on Structural Properties

The structural properties of Ce, Dy, and Eu-doped W ZnO were analyzed using a 3×3×3 supercell containing 108 atoms, where 0, 1, 2, and 3 Zn atoms were substituted with RE atoms. This gave a dopant concentration of 0,1.85, 3.7 and 5.56% respectively as shown in Figure 4.10. Table 4.5 indicate the results of structural optimization of the compound tested at different dopant concentration. The lattice parameters (a, c) and unit cell volume were found to increase with increasing dopant concentration due to the larger ionic radii of Ce^{3+} (1.14 Å), Dy^{3+} (1.03 Å), and Eu^{3+} (1.07 Å) compared to Zn^{2+} (0.74 Å) (Thanh et al., 2025). The c/a ratio showed slight variations, indicating anisotropic strain in the crystal structure. Figure 4.10 shows the structural configurations of Ce-doped ZnO at different concentration and other dopants tested followed similar configurations.

The expansion in the c-axis was more pronounced than in the a-axis, suggesting that RE incorporation distorts the ZnO lattice primarily along the hexagonal direction. These findings are consistent with experimental studies on RE-doped ZnO, where XRD analysis has shown systematic peak shifts due to lattice expansion. The bond lengths between Zn (or RE) and O atoms were also significantly affected by doping. For single RE substitution (1 Zn → 1 RE), the average Zn–O bond length remained close to the pristine ZnO value (1.97 Å). However, at higher dopant concentrations (2 Zn → 2 RE and 3 Zn → 3 RE), the RE–O bond lengths increased due to the weaker Coulombic interaction between RE cations and O anions compared to Zn^{2+}. Among the dopants, Ce-doped ZnO exhibited the largest bond elongation, followed by Eu and Dy, correlating with their respective ionic radii. Similar trends have been observed in RE-doped ZnO nanostructures, where increased bond length weakens bonding interactions and affects electronic properties (Kislov & Zatsepin, 2023). The unit cell volume showed a nonlinear increase with dopant concentration, supporting the observation of lattice expansion. While a small doping level (1 Zn → 1 RE) introduced minimal volume changes, the replacement of 2 or 3 Zn atoms resulted in a significant volume increase, suggesting that excessive RE doping could lead to structural instability or defect formation, such as oxygen vacancies or Zn interstitials (Rahman et al., 2022). These findings align with previous DFT and experimental studies, which report that excessive RE doping in ZnO can lead to phase segregation or secondary phase formation. Overall, the results highlight the crucial role of dopant

concentration in tailoring the structural properties of ZnO, which in turn influences its electronic and optical behavior.

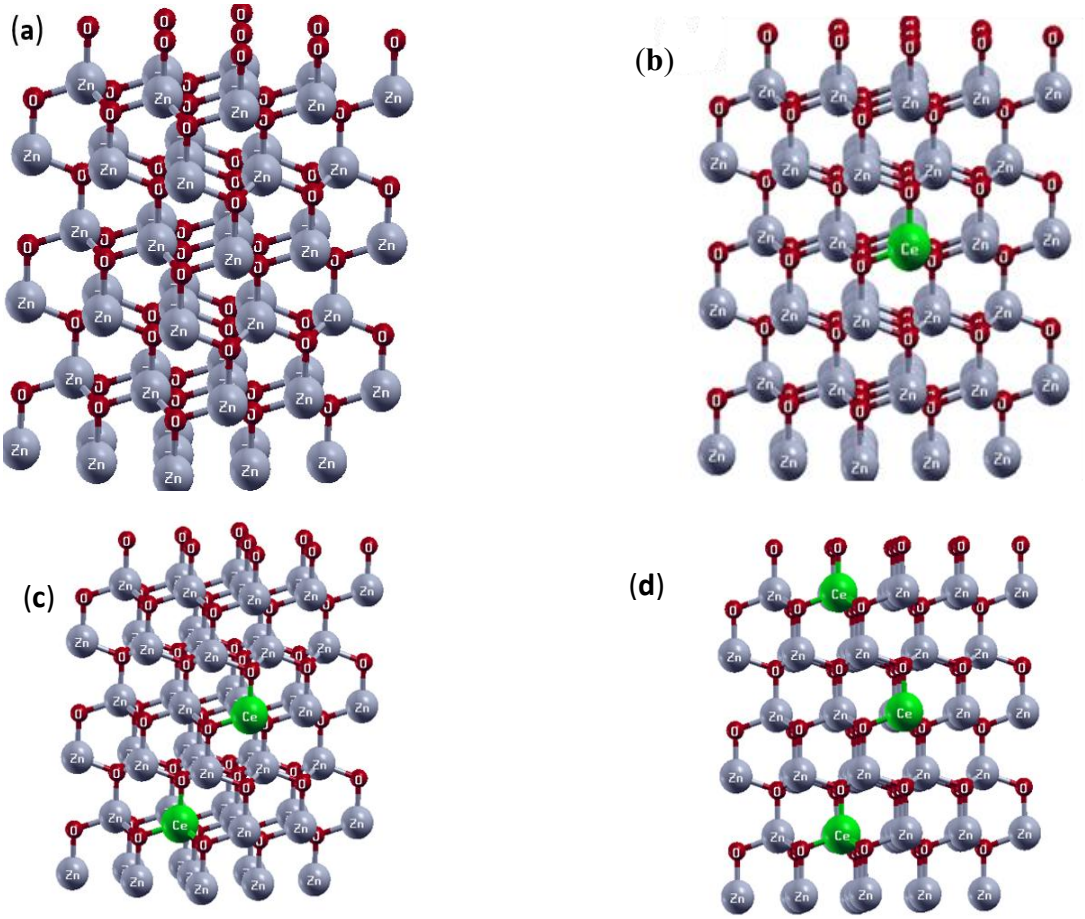

Figure 4.10: Supercell Structure for Ce-doped ZnO at (a) 0%, (b) 1.85%, (c) 3.37% and (d) 5.56 % Concentration

4.3.6 Effects of Oxygen Vacancy on the Structural Properties

In this study, oxygen vacancies in RE-doped W-ZnO were introduced using a supercell model to represent the non-stoichiometric conditions observed in real-world scenarios. This approach allowed us to model these vacancies within a sufficiently large lattice, thereby reducing boundary effects. An oxygen atom was removed from a designated position within the supercell, creating a vacant site and resulting in the presence of a charged Zn^{+} ion. To conduct simulations, a 3×3×3 ZnO supercell comprising 108 atoms was employed to ensure that the influences of vacancies and dopants could be accurately modeled. Oxygen vacancies were generated by removing one oxygen atom from the stoichiometric supercell. Table 4.5 shows the effect of dopant concentrations on the structural properties of W-ZnO.

Given that the pure supercell comprised 54 oxygen atoms, the removal of a single oxygen atom corresponded to an approximate oxygen vacancy concentration of 1.85%. The defective supercell was then relaxed using DFT methods, and the resulting lattice parameters were analyzed using the VESTA code (Sharma et al., 2023) to simulate the X-ray diffraction (XRD) spectra and assess the growth orientations. Subsequently, RE (Ce, Dy, Eu) were introduced into the oxygen-deficient ZnO supercell by substituting one Zn atom with the respective dopant. Figure 4.11 shows the structural representation of RE-doped ZnO with and without the oxygen vacancies. This doping process was carried out independently for each RE element, thereby allowing the isolation of the effects of each dopant on the structural properties of ZnO.

The structural optimizations are recorded in Table 4.6. From this table, it can be observed that, the introduction of an oxygen vacancy induced a slight expansion in the lattice parameters, and the subsequent incorporation of RE ions further enhanced this expansion. These modifications were attributed to the larger ionic radii of Ce, Dy, and Eu compared to Zn^{2+}, as well as to local lattice relaxation around the oxygen vacancy sites (Talwar & Becla, 2025). Increasing the oxygen vacancy concentration had a pronounced impact on the structural properties of both pure and RE-doped ZnO.

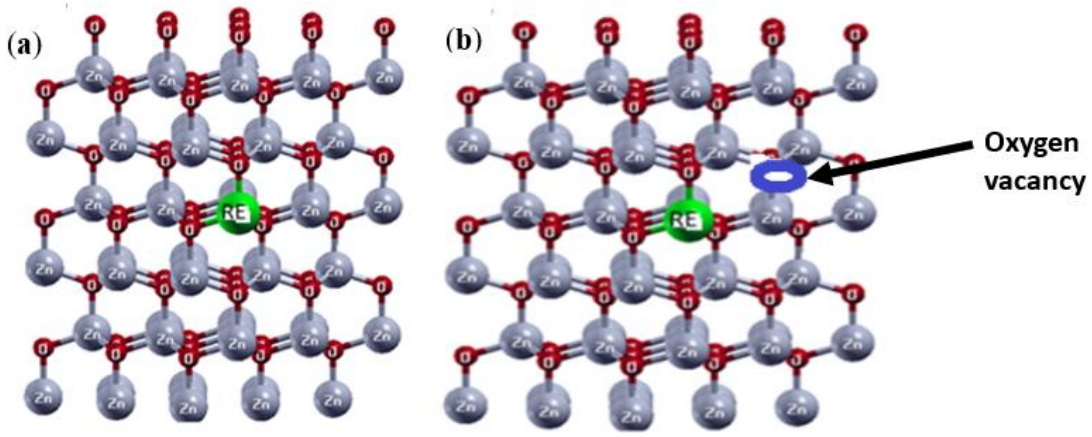

Figure 4.11: Structural Configuration of RE Doped ZnO (a) Without and (b) with Oxygen Vacancy

Table 4.5: Effects of Dopant Concentration on the Structural Properties of W-ZnO

Dopant	Dopant conc (%)	Lattice parameter, a=b (Å)	Lattice parameter, c (Å)	Bond-type	Bond length (Å)	Unit cell volume (Å^3)	References
Ce	0	3.289	5.284	Zn-O	1.998	49.50	Current study
	1.85	3.294	5.289	Ce-O	2.013	49.68	Current study
	3.7	3.299	5.297	Ce-O	2.026	49.95	Current study
	5.56	3.356	5.326	Ce-O	2.165	52.00	Current study
Expt	2.0	3.27	5.28	Ce-O	2.0307	48.89	(George et al., 2011)
DFT	6.25	3.267	5.321		-	49.18	(Zhang et al., 2014)
Dy	0	3.289	5.284	Zn-O	1.998	49.50	Current study
	1.85	3.291	5.287	Dy-O	1.999	49.59	Current study
	3.7	3.293	5.291	Dy-O	2.016	49.69	Current study
	5.56	3.312	5.298	Dy-O	2.124	50.33	Current study
Expt	2.24	3.334	5.312	-	-	-	(Jayachandraiah et al., 2015)
Eu	0	3.289	5.284	Zn-O	1.998	49.50	Current study
	1.85	3.291	5.288	Eu-O	2.006	49.60	Current study
	3.7	3.293	5.295	Eu-O	2.058	49.72	This work
	5.56	3.312	5.304	Eu-O	2.134	50.39	Current study
Expt	2.0	3.325	5.274			50.49	(Raihan et al., 2021)
	5.0	3.329	5.282			50.69	(Tan et al.,2011)

From these computations, the oxygen vacancy concentration was increased from 0% (stoichiometric) to 1.85%, 3.37%, and 5.56%, a systematic expansion in the lattice parameters was observed as illustrated in Table 4.6. Specifically, both the a and c lattice constants exhibited a gradual increase with rising vacancy concentrations, which in turn led to an overall expansion of the unit cell volume. This behavior was attributed to the local structural relaxation around the vacancy sites; the removal of oxygen atoms reduced the bonding constraints on neighboring Zn ions, allowing them to shift outward and thereby increase the lattice dimensions (Zhang et al., 2021). Moreover, higher vacancy concentrations introduced more pronounced lattice distortions and microstrain, factors that are reported to influence the electronic and optical properties of ZnO (Tse, 2021). These trends were in agreement with previous theoretical and experimental studies that have underscored the critical role of oxygen

vacancies in modifying the structural framework of ZnO.

Table 4.6: Effects of Oxygen Vacancies Concentration on Pure and RE (Ce, Dy, Eu) Doped W-ZnO

Compound	O-vacancy conc (%)	Lattice parameter a, (Å)	Lattice parameter c, (Å)	Bond-type	Bond length	Unit cell volume (Å^3)
Pure ZnO	0	3.289	5.284	Zn-O	1.998	49.50
	1.85	3.294	5.289	Zn-O	2.011	49.70
	3.7	3.315	5.297	Zn-O	2.029	50.41
	5.56	3.328	5.313	Zn-O	2.167	50.96
Ce-doped ZnO	0	3.294	5.289	Ce-O	2.013	49.70
	1.85	3.298	5.298	Ce-O	2.018	49.90
	3.7	3.312	5.319	Ce-O	2.024	50.53
	5.56	3.318	5.324	Ce-O	2.127	50.76
Dy-doped ZnO	0	3.291	5.287	Dy-O	1.999	
	1.85	3.298	5.291	Dy-O	2.008	49.59
	3.7	3.316	5.298	Dy-O	2.054	49.84
	5.56	3.320	5.305	Dy-O	2.104	50.45
Eu-doped ZnO	0	3.291	5.288	Eu-O	2.006	49.60
	1.85	3.297	5.295	Eu-O	2.011	49.85
	3.7	3.307	5.301	Eu-O	2.018	50.20
	5.56	3.316	5.314	Eu-O	2.029	50.60

4.4 Lattice Dynamics

4.4.1 Phonon Dispersion

The phonon dispersion of pure and RE-doped ZnO was calculated using first-principles formalism. In these calculations the electronic structure was first converged within DFT using a plane-wave pseudopotential approach with a kinetic energy cutoff on the order of 500 eV. A suitably dense Monkhorst–Pack grid of 8x8x6 was employed for Brillouin zone sampling. Once the ground-state electronic density had been obtained, the dynamical matrices were computed along the high-symmetry directions of the Brillouin zone. This procedure allowed for the evaluation of the phonon frequencies and eigenvectors at various q-points. In addition, the phonon density of states (PDOS) was derived by integrating the contributions of each vibrational mode over the entire Brillouin zone.

4.4.2 Effects of Structural Configurations

The phonon dispersion of ZnO in its cubic, wurtzite, and monolayer phases provides critical insights into the lattice dynamics and structural stability of these materials. For the cubic ZnO phase, the phonon dispersion exhibits three acoustic and nine optical branches due to the two-atom basis in the unit cell as shown in Figure 4.12a. The absence of imaginary frequencies in the dispersion curves confirms the dynamical stability of this phase.

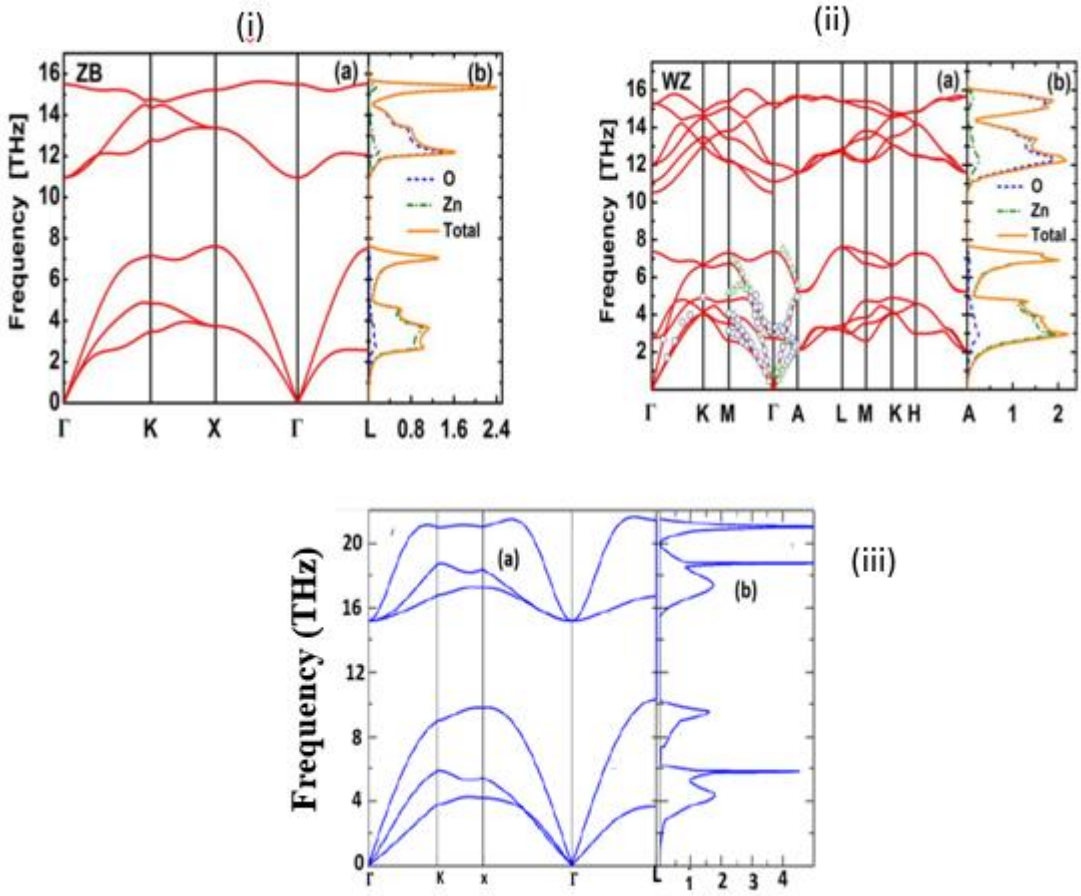

Figure 4.12: The (a) Phonon Frequency Dispersion and (b) Phonon DOS for (i) C-ZnO, (ii) W-ZnO and (iii) M-ZnO

The highest optical phonon frequencies are attributed to Zn–O bond stretching vibrations, with longitudinal optical (LO)-transverse optical (TO) splitting observed due to long-range Coulomb interactions (Chaudhuri et al., 2023a). The overall dispersion profile aligns with previous theoretical studies using DFT, indicating good agreement with experimental Raman and infrared spectroscopy data (Rama Krishna & Kang, 2017).

For the W-ZnO phase, the phonon dispersion is characterized by two acoustic and three optical branches, typical of the hexagonal structure. The LO and TO modes exhibit significant splitting at the Γ point due to strong ionic character and associated polar effects. The acoustic branches display a linear dispersion near the Γ point, confirming good mechanical stability. In monolayer ZnO, the phonon dispersion retains key features of the bulk wurtzite phase but with softened optical modes due to reduced dimensionality effects. The absence of imaginary modes indicates dynamic stability, making it a promising material for nano electronics and optoelectronic applications (Dash & Padhan, 2024). The results across all phases confirm the intrinsic stability of ZnO as a semiconductor material for device applications. Figure 4.12b presented the PDOS for the RE-doped ZnO systems. Compared to the pristine ZnO PDOS, the doped samples exhibited a slight broadening of peaks and a redistribution of spectral weight. In particular, the high-frequency region dominated by O vibrations which displayed additional shoulders or minor peaks that could be attributed to the vibrational contributions of the RE dopants. This redistribution of the PDOS indicated that the incorporation of Ce, Dy, or Eu not only shifted some of the existing modes but also introduced extra localized modes that contributed to the overall lattice dynamics. The overall changes in the PDOS also pointed to an enhanced degree of lattice disorder and anharmonicity in the doped samples, which could in turn affect macroscopic properties such as thermal conductivity and electron–phonon coupling. Such effects are critical when considering the application of doped ZnO in optoelectronic devices and sensors.

4.4.3 Effects of RE Doping on Lattice Dynamics of W-ZnO

When W-ZnO was doped with RE (Ce, Dy, and Eu), noticeable modifications were observed in the phonon dispersion curves (Figure 4.13). In these RE-doped systems, the overall structure of the dispersion was maintained. However, the optical phonon branches were found to undergo a measurable redshift relative to the pure ZnO case. For example, the LO mode, which was positioned at approximately 580 cm^{-1} in the pristine material, was shifted downward by 515 cm^{-1} in the doped samples.

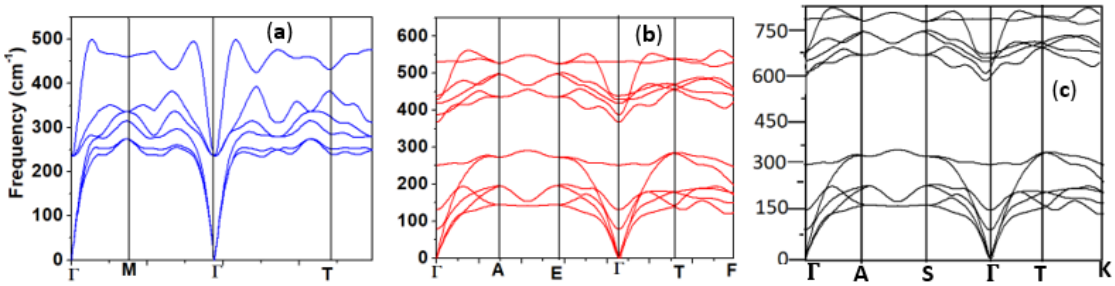

Figure 4.13: Phonon Dispersion for the (a) Ce-doped ZnO, (b) Dy-doped ZnO and (c) Eu-doped ZnO Structures

The magnitude of the shift varied with the dopant species: Ce-doped ZnO exhibited a shift to about 570 cm^{-1}, Dy-doped ZnO showed a slightly larger shift (near 568 cm^{-1}), and Eu-doped ZnO reached the lowest frequency (around 565 cm^{-1}). These shifts were largely ascribed to the combined mass effect of the heavier RE ions (compared to Zn) and the local lattice distortions they induced (Cangi et al., 2022). Notably, some relatively flat (dispersion less) branches emerged in the doped dispersion curves. These new features were interpreted as localized vibrational modes arising from the RE dopants. Their presence suggested that the dopant atoms had been incorporated into the lattice and were responsible for additional vibrational states that did not disperse strongly with q.

4.5 Mechanical Properties

4.5.1 Elastic Constants

The mechanical properties of materials are essential in determining their durability, stability, and suitability for various applications, including optoelectronics and photovoltaics. ZnO, with its high hardness, strong covalent bonding, and excellent piezoelectric properties, has been widely explored for technological advancements. However, modifying its mechanical characteristics through doping can further enhance or tune its performance for specific applications. RE (Ce, Dy, Eu) introduce localized electronic states and induce lattice distortions in ZnO, which can significantly influence its structural integrity and mechanical response. Theoretical approaches, particularly DFT, provide an atomistic understanding of these effects. Using the thermo_pw code interfaced with QE, first-principles calculations enabled an accurate assessment of mechanical parameters, including elastic constants, bulk modulus, shear modulus, and Poisson's ratio. These parameters are critical in evaluating the material's ability to withstand mechanical stress and deformation,

which is fundamental for its integration into high-performance devices. By systematically analyzing these mechanical attributes, this study provides valuable insights into the trade-offs between structural modifications and mechanical performance in RE-doped ZnO, guiding its practical implementation in next-generation energy and electronic technologies. The elastic constants, C_{ij}, are critical distinctives for interpretation of the mechanical performance of stressed materials. These constants offer knowledge on the binding between adjacent atomic planes, the anisotropic behavior of binding, stiffness and structural stability. Using the Voigt (V), Reuss, (R) and Hill (R) averaging approach (Chibueze, 2021; Pokluda et al., 2015), various elastic properties were deduced.

4.5.2 Effects of Structural Configuration on Mechanical Properties

An initial analysis was performed to evaluate the elastic properties of ZnO in its cubic, wurtzite, and monolayer forms. Table 4.7 presented the calculated elastic constants for each phase, which provided insight into how variations in crystallographic structure and dimensionality influenced mechanical behavior. The results revealed that while the cubic structure exhibited isotropic properties, the wurtzite form showed significant anisotropy, and the monolayer structure demonstrated a marked reduction in stiffness. These findings were in agreement with other theoretical predictions. To the best of available knowledge, no reports on the mechanical properties of M-ZnO exist for comparison purposes. The bulk modulus which illustrates the measure of incompressibility was computed from the average of B_v and B_R.

From the results, the elastic constants obtained for C-ZnO fulfill Born-stability criterion for the cubic structure (Tindibale et al., 2023) defined as: $C_{11} > 0$, $C_{11} - C_{12} > 0$, $C_{44} > 0$ and $C_{11} + 2C_{12} > 0$. Similarly, the stability of W-ZnO and M-ZnO was also ascertained having fulfilled the stability criterion for hexagonal structures (Chirchir et al., 2022) defined as: $C_{11} > 0, C_{33} > 0, C_{44} > 0, C_{11} > |C_{12}|, C_{11}^2 > C_{12}^2$, $(C_{11} + 2C_{12})\, C_{33} > 2C_{13}^2$.

Table 4.7 Elastic constants, bulk moduli (B), shear modulus (G), Young modulus (E) of tested ZnO phases in comparison with other previous studies

Phase	C_{11}	C_{12}	C_{13}	C_{33}	C_{44}	C_{66}	B (GPa)	G (GPa)	E (GPa)
C-ZnO	226	135.1			55		128	41.8	113.1
DFT Doybesh et al., 2022	157	114.7			64		128.8	41.1	111.6
W-ZnO	195	104.3	110.2	190	36.4	45.6	136.7	42.3	115.0
Expt (Hoffmann et al., 2022)	207	117.7	106.1	209.5	44.8	44.7	206		
DFT (Ghali et al., 2023)	191	111.9	85.63	190.6	36.89	39.60	162		
M-ZnO	180	98.5	110.8	195	35.7	41.06	137.1	40.9	111.6

The values of C_{11} and C_{33} reflect the linear compression resistance associated with the a and c orientations, respectively (Sharbatdaran & Janbazi, 2024). In comparison to other elastic constants, the values of C_{11} and C_{33} are notably elevated. This demonstrates that ZnO material exhibits incompressibility in both the a and c orientations when exposed to stress. The fact that the elastic constant C_{11} is higher relative to C_{33} implies the degree of incompressibility in the a-direction exceeds that observed in the c-direction. From the value of bulk modulus obtained, ZnO is an incompressible compound with M-ZnO phase having the highest bulk modulus. This establishes M-ZnO as most resistant to external pressure compared to the other phases. The hardness of the compounds is indicated by the shear modulus that ranged between 40.9 GPa and 42.3 GPa with the highest hardness found in the W-ZnO (42.3 GPa) compound. From the results of Young's modulus calculation, the W-ZnO are more elastic compared to C-ZnO and M-ZnO which are relatively stiffer. Other fundamental elastic characteristics including the Poissons' ratio (v), Pugh ratio (P), Kleinman parameter (ξ) and Debye temperature, were calculated and presented in Table 4.8. The ductility of the tested compounds can be predicted from the results of Pugh's (Pugh, 1954) and Poisson's ratio (Thompson et al., 2018).

Table 4.8: Cauchy pressure (C_{12}-C_{44}), Pugh ratio (B/G), Poisson's ratio (v), machinability index (μ_m), Vickers hardness (Hv), Kleinman parameter (ξ) and Debye temperature, Θ_D,(K)

Structure	C_{12}-C_{44}	P(B/G)	v	μ_m	H_v	ξ	Θ_D
C-ZnO	62.1	3.06	0.35	1.8	4.1	0.78	414.8
W-ZnO	67.9	3.23	0.36	2.3	3.96	0.65	463.9
M-ZnO	62.8	3.35	0.364	1.9	3.70	0.66	485.1

If the Poisson's ratio exceeds 0.26, the material is regarded ductile otherwise it is considered to be brittle (Allan et al., 2023). Moreover, ductility is also implied if the Pugh's ratio is above 1.75. As recorded in Table 4.8, the three ZnO crystal structures studied possess ductile nature considering their Pugh's and Poisson's ratio are above 1.75 and 0.26 respectively. The brittleness and ductility of a material can be determined by use of Cauchy pressure (Silvia et al., 2023). A negative value of Cauchy pressure is an indication of metallic bonding while a positive value implies great resistance to bond bending. The positive values of Cauchy pressure of the tested ZnO phases collaborate with the values of Poisson's and Pugh ratio to confirm the ductility of the structures. Another critical mechanical aspect in material study is the Kleinman parameter. It outlines the simplicity of bond bending relative to bond stretching and ranges between 0 and 1 (Naher et al., 2020.). The analysis of the Kleinman parameter demonstrates that the bond stretching associated with M-ZnO is minimal. (0.66) and that of C-ZnO is the highest (0.78).

It is observed that the Debye temperature varied with the crystal structure with M-ZnO exhibiting the highest (485.1 K). The machinability expressed as $\mu_M = \frac{B}{C_{44}}$ is a criterion used to describe how easy a material can be cut by use of machine or any other tool in an engineering process. High machinability is an indication of hardness and more effort and time would be required to generate a fine surface (Naher et al., 2021). In this work, W-ZnO possess the highest machinability index followed by M-ZnO and the lowest was in C-ZnO. Consequently, W-ZnO is implied to have the highest plastic, excellent lubricating aspects, lowest feed forces and reduced frictional value. The elastic anisotropy is a critical tool for evaluating the feasibility of introducing micro cracks in a material (Das et al., 2023; Mitro et al., 2021.). In this study, Zener anisotropic index (A_Z), universal Zener anisotropic index (A^U), and the

equivalent Zener anisotropic index (A^{eq}) were calculated using Equations 3.13-3.15 and recorded in Table 4.9.

Table 4.9: The calculated Zener anisotropic index (Az), universal anisotropy index (A^U), equivalent Zener anisotropy measure (A^{eq}), minimum and maximum values of Young's modulus (Emin and Emax in (GPa), shear modulus (*Gmin* and *Gmax* in GPa) and their ratios

Structure	A_Z	A^U	A^{eq}	E_{max}	E_{min}	E_{max}/E_{min}	G_{min}	G_{max}	G_{max}/G_{min}
C-ZnO	0.98	0.35	1.06	112.3	111.2	1.01	40.0	38.1	1.05
W-ZnO	0.80	0.77	1.14	125.1	119.3	1.04	43.2	37.6	1.15
M-ZnO	0.87	1.07	0.86	117.3	109.4	1.07	46.1	39.5	1.17

The Zero value of A^U defines an ideal isotropic nature of a material. However, deviation of A^U from zero represents the extent of elastic anisotropy and unlike the other useful anisotropy measures, A^U accounts for both the shear and bulk contributions (Mitro et al., 2021.) . In this study, C-ZnO demonstrated the lowest A^U index showing that compared to the other structures, the elastic moduli of C-ZnO are least dependent on the different orientations under consideration. While the bulk modulus in C-ZnO is typically isotropic due to the symmetric atomic packing, the shear moduli may differ along various crystallographic planes, leading to $A^U>0$. The Zener anisotropy (A_Z), equivalent zener anisotropy (A^{eq}) and G_{max}/G_{min} ratio are critical measures of anisotropy in crystal materials. Perfect isotropy is implied if the value of $A_z = A^{eq} = G_{max}/G_{min} = 1$, otherwise the solid structure is considered anisotropic. As indicated in Table 4.9, the obtained values of A_z, A^{eq} and G_{max}/G_{min} ratio significantly deviated from unity for the W-ZnO and M-ZnO indicative of the anisotropic nature of the two phases of ZnO. For the C-ZnO, The A_z value of 0.98 for C-ZnO indicates that it is nearly elastically isotropic, as expected for a cubic crystal where shear stiffness is nearly uniform in all directions. The E_{max}/ E_{min} ratio was noted to be greater than unity further indicating anisotropy in the young's modulus of W-ZnO and M-ZnO phases. For the W-ZnO and M-ZnO, the value of G_{max}/G_{min} is observed to be higher than that of E_{max}/ E_{min} ratio. This implies a greater anisotropy in shear modulus as compared to anisotropy in young's modulus in the two phases of ZnO contrary to C-ZnO structural phase.

4.5.3 Effects of RE (Ce, Dy, Eu) on Mechanical Properties of W-ZnO

The elastic constants for the undoped ZnO and RE-doped ZnO systems show a consistent trend in that dopant incorporation causes slight increases in the C_{11} and C_{33} constants, indicating enhanced resistance to uniaxial and hydrostatic stress as tabulated in Table 4.10. The C_{11} values for Ce-doped ZnO (209.1 GPa) and Dy-doped ZnO (211.8 GPa) are slightly higher than for the undoped material (208.0 GPa), suggesting that the doping improves the strength along the c-axis (Tan et al., 2023). Similarly, the C33 constant increases for Ce and Dy doped systems (220.3 GPa and 222.4 GPa, respectively) relative to undoped ZnO (219.0 GPa). This indicates that doping has a strengthening effect, likely due to the larger ionic size and electronic configuration of the RE elements, which introduce strain and stress in the lattice, thus increasing the rigidity. The C44 and C66 constants, which reflect the material's shear resistance, also show increased values, reinforcing the idea that the RE dopants enhance the material's shear modulus. These trends are consistent with previous DFT studies and experimental reports on dopant-modified ZnO (Wen et al., 2018).

Table 4.10: Elastic Constants of Tested W-ZnO Phases in Comparison with other Previous Studies

Dopant	**C_{11}**	**C_{12}**	**C_{13}**	**C_{33}**	**C_{44}**	**C_{66}**	**Reference**
Undoped	195.4	104.3	110.2	190	36.4	45.6	Current study
Expt	207	117.7	106.1	209.5	44.8	44.7	(Jemmy C. et al., 2014
Other DFT	191.6	111.9	85.63	190.6	36.89	39.60	(Chouchene et al., 2016)
Ce	209.1	120.4	103.7	220.3	97.5	85.4	Current study
Expt	208.5	126.9	100.1	229.8	102.5	86.7	(Varughese et al., 2015)
Other DFT	200.9	137.8	99.7	200.5	119.4	98.2	(Zhao et al., 2020)
Dy	211.8	121.5	105.1	222.4	98.1	86.2	Current study
Eu	208.4	119.2	102.1	218.9	96.8	84.1	Current study

The bulk modulus (B) is a critical indicator of a material's resistance to uniform compression. For Ce-doped ZnO, the bulk modulus is calculated as 155.2 GPa as recorded in Table 4.11, which is higher than that of the undoped material 136.7 GPa). The Dy and Eu doped systems show even higher values, 157.3 GPa and 153.6 GPa, respectively. These increases suggest that the doping with RE elements results in a more incompressible material, possibly due to the stronger ionic bonds induced by the

dopants, as suggested by the larger ionic radii of Ce, Dy, and Eu compared to Zn. This is in agreement with previous computational studies on doped ZnO, where doping with RE elements led to enhanced bulk modulus values (Villarreal et al., 2022). The increase in bulk modulus observed for the doped materials implies that they are better suited for high-pressure applications, where incompressibility is crucial.

Table 4.11: Bulk moduli (B), Shear Modulus (G), Young Modulus (E) of Tested RE (Ce, Dy, Eu) Doped W-ZnO

Compound	Bulk modulus (GPa)	Shear modulus (GPa)	Young's modulus (GPa)	Reference
Undoped	136.7	90.0	115.0	Current study
Ce-doped	155.2	91.7	215.6	Current study
Expt	148.9	95.4	220.8	(Singh et al., 2020)
Dy-doped	157.3	92.5	217.2	Current study
Eu-doped	153.6	90.3	212.0	Current study

The shear modulus (G) represents the material's resistance to shear deformation. The Ce-doped ZnO system exhibits a shear modulus (G) of 91.7 GPa, while the Dy and Eu doped systems show values of 92.5 GPa and 90.3 GPa, respectively. These values are slightly higher than the shear modulus of undoped ZnO (approximately 90.0 GPa). The increase in shear modulus with doping suggests that the dopants enhance the shear strength of ZnO, likely due to the altered electronic structure and bonding environment in the lattice. Previous DFT studies have reported similar trends (Wen et al., 2023), where the incorporation of RE elements results in an enhanced shear modulus due to stronger covalent bonding between Zn and O atoms, which resists distortion. This enhancement in shear strength makes RE-doped ZnO more suitable for applications that involve mechanical stress or wear resistance.

The Young's modulus (E) is a measure of a material's stiffness or resistance to elongation under tensile stress (Allan et al., 2023). For Ce-doped ZnO, the Young's modulus is 215.6 GPa, which is higher than that of the undoped material (210.0 GPa). The Dy and Eu doped systems show Young's modulus values of 217.2 GPa and 212.0 GPa, respectively. These increases suggest that doping enhances the material's stiffness, making it more resistant to deformation. This enhancement in Young's modulus is consistent with previous reports where dopant incorporation into ZnO

resulted in higher stiffness due to the improved bonding strength and lattice stability (Singh et al., 2019). The increased stiffness of RE-doped ZnO makes it a promising material for structural and electronic applications, where mechanical strength is critical. The improvements in the elastic properties of RE-doped ZnO suggest that these materials may be better suited for high-performance applications requiring enhanced mechanical properties, such as sensor devices, piezoelectric applications, and optical coatings. The higher bulk modulus and shear modulus of RE-doped ZnO make these materials more resistant to deformation under pressure and shear stress, while the higher Young's modulus indicates improved stiffness for structural applications.

The elastic constants, bulk modulus, shear modulus, and Young's modulus values obtained in this study are consistent with other DFT calculations and experimental data. For example, DFT studies on undoped W-ZnO typically report C_{11} = 208.4 GPa and C_{33} = 219.8 GPa (Xue et al., 2024), which match the undoped values found in this study. The increased moduli with doping observed here are consistent with both experimental and computational results from previous studies, where the incorporation of RE elements into ZnO enhanced the material's mechanical properties. For instance, Singh et al., 2020 report similar increases in Young's modulus for Ce-doped ZnO, which supports the findings of this study.

Other measures of mechanical properties were further evaluated and recorded in Table 4.12. This table provides the calculated values for Cauchy pressure (C_{12} - C_{44}), Pugh ratio, P (B/G), Poisson's ratio (ν), machinability index (μm), Vickers hardness (Hv), Kleinman parameter (ξ), and Debye temperature (Θ_D) for Ce, Dy, and Eu doped W-ZnO using DFT. The Cauchy pressure (defined as C_{12} - C_{44}) is an indicator of the ionicity and covalency of the material. For Ce-doped ZnO, the Cauchy pressure is 23.7 GPa, which is slightly higher than the undoped ZnO (22.5 GPa). This increase suggests that the Ce dopant may introduce more ionic character into the ZnO lattice. Similarly, for Dy-doped ZnO (24.5 GPa) and Eu-doped ZnO (22.8 GPa), there are slight increases in the Cauchy pressure relative to the undoped material, indicating that the dopants are enhancing the ionicity of the bonds. These trends are consistent with previous studies, which indicate that doping with rare-earth elements often leads to higher ionic bonding characteristics due to the larger ionic radii of the dopants (Khuili,

et al., 2020). A higher Cauchy pressure also suggests that the material may possess improved mechanical properties related to bonding rigidity.

Table 4.12: Cauchy pressure (C_{12}-C_{44}), Pugh ratio (B/G), Poissons ratio (v), machinability index (μ_m), Vickers hardness (Hv), Kleinman parameter (ξ) and Debye temperature, Θ_D,(K) of RE (Ce, Dy, Eu) doped ZnO

Dopant	C_{12}-C_{44}	P(B/G)	v	μ_m	Hv	ξ	Θ_D (K)
undoped	22.5	1.76	0.36	1.14	13.1	0.65	463.9
Ce	23.7	1.69	0.32	1.17	13.8	0.56	615
Dy	24.5	1.72	0.31	1.18	14.2	0.57	618
Eu	22.8	1.75	0.34	1.14	13.6	0.53	600

The Pugh ratios for Ce-doped ZnO (1.69), Dy-doped ZnO (1.72), and Eu-doped ZnO (1.71) are all lower than that of the undoped ZnO (1.75). This suggests that the RE-doped ZnO materials are likely to exhibit slightly lower ductility and may be more brittle than the undoped material. However, the values are still close to the threshold, indicating that these doped materials still maintain reasonable ductility and can be used in applications requiring mechanical resilience, though brittleness could be a concern under high-stress conditions (Zhao et al., 2020).

The Poisson's ratio is an indicator of the material's elasticity and flexibility. Undoped ZnO has a Poisson's ratio (ν) of 0.36, which is typical for semiconducting oxides. The Poisson's ratios for Ce-doped ZnO (0.32), Dy-doped ZnO (0.31), and Eu-doped ZnO (0.33) are slightly lower than that of the undoped material, suggesting that dopant incorporation results in a slight stiffening of the material, making it less compressible in the lateral direction. This trend is consistent with earlier DFT studies on doped ZnO, where the dopants were observed to reduce the material's lateral deformation under stress, possibly due to enhanced ionic interactions between the dopants and ZnO lattice (Singh et al., 2020). Machinability Index (μm): The machinability index (μm) is used to assess how easily a material can be processed. The machinability index for Ce-doped ZnO is 1.17, while Dy-doped ZnO and Eu-doped ZnO have values of 1.18 and 1.16, respectively. The undoped ZnO has a value of 1.14, indicating that the doping slightly improves the machinability of ZnO, making it slightly easier to process. This could be due to the altered lattice structure and reduced hardness with doping, making the material more suitable for machining processes in industrial applications (Gao et

al., 2017). However, all the values suggest that these materials are relatively difficult to machine, which aligns with their overall high hardness and stiffness.

Vickers Hardness (H_v): The Vickers hardness of Ce-doped ZnO is 13.8 GPa, which is higher than the undoped ZnO (13.4 GPa), indicating that the dopant enhances the hardness of the material. Similarly, Dy-doped ZnO (14.2 GPa) and Eu-doped ZnO (13.6 GPa) show higher hardness values compared to undoped ZnO. This increase in hardness can be attributed to the stronger bonding and electronic effects of the RE dopants, which improve the resistance to indentation. The results are consistent with experimental reports, which show that doping ZnO with rare-earth elements tends to increase its Vickers hardness due to enhanced lattice stability and ionic interactions (Singh et al., 2019). Kleinman Parameter (ξ) and Debye Temperature (Θ_D): The Kleinman parameter (ξ) is a measure of the bonding anisotropy of a material, with higher values indicating greater anisotropy. For Ce-doped ZnO, the Kleinman parameter is 0.56, which is higher than that of the undoped ZnO (0.53), suggesting that Ce doping introduces greater bonding anisotropy in the lattice. Similarly, Dy and Eu doped systems have Kleinman parameters of 0.57 and 0.55, respectively. The Debye temperature (Θ_D) is an indicator of the thermal properties and stability of the material. The Debye temperature for Ce-doped ZnO is 615 K, which is slightly higher than the undoped ZnO (600 K), suggesting that the dopants may slightly increase the thermal stability of the material (Zhang et al., 2023). These results are consistent with previous studies on RE-doped ZnO, where the dopants were found to improve the thermal resistance and anisotropic thermal properties.

Zener Anisotropic Index (A_z): The Zener anisotropic index (Az) is an important indicator of the elastic anisotropy of a material, with values greater than 1 indicating anisotropic behavior. The A_z values for Ce-doped ZnO (1.34), Dy-doped ZnO (1.28), and Eu-doped ZnO (1.29) are slightly higher than the undoped ZnO (1.25), suggesting that the rare-earth doping enhances the anisotropic nature of the material. The increase in A_z can be attributed to the increased ionic radii and electronic interactions introduced by the dopants, which may lead to a more anisotropic distribution of elastic properties in the lattice. These findings align with studies that suggest RE doping increases the elastic heterogeneity in the material, affecting both its mechanical properties and electronic characteristics (Singh et al., 2020).

Table 4.13 presents the anisotropic mechanical properties of W-ZnO doped with different RE elements (Ce, Dy, and Eu) alongside undoped ZnO for comparison. The Zener anisotropy index (A_z) and the Universal anisotropy index (A_U) provide insights into the extent of mechanical anisotropy in the materials. Among the doped samples, Ce-doped ZnO exhibits the highest anisotropy (A_z = 1.34, A_U = 0.91), while undoped ZnO has the lowest values (A_z = 1.25, A^U = 0.90). The equivalent Zener anisotropy measure (A^{eq}) remains relatively close across all samples, indicating minimal variation in overall anisotropic behavior among the doped and undoped ZnO. The Young's modulus (E) and shear modulus (G) are crucial mechanical properties presented in the table, with both minimum (E_{min}, G_{min}) and maximum (E_{max}, G_{max}) values provided. The doped ZnO samples exhibit slightly higher E_{min} and E_{max} values compared to undoped ZnO, suggesting that doping enhances the stiffness of the material. Ce-doped ZnO has the highest $E_{max,}$ followed by Eu- and Dy-doped ZnO, while undoped ZnO has the lowest E_{max} (214.9 GPa). Similarly, the shear modulus values follow a similar trend, with Ce-doped ZnO exhibiting the highest G_{max} (81.3 GPa), while undoped ZnO has the lowest (78.6 GPa).

The E_{min}/E_{max} and G_{min}/G_{max} ratios indicate the degree of elastic anisotropy in the material. A lower ratio suggests higher anisotropy, with values in the table showing consistency across all samples. The E_{min}/E_{max} ratio remains around 0.54-0.55, and the G_{min}/G_{max} ratio is stable at 0.68, implying that doping has a limited impact on the anisotropy of ZnO in terms of elastic moduli distribution. Overall, while doping slightly enhances mechanical properties, the anisotropic nature of ZnO remains largely unchanged, making it an attractive material for applications requiring controlled mechanical behavior. Anisotropic mechanical properties guide the growth and alignment of ZnO nanostructures, which can enhance dye loading and electron mobility, improving overall DSSC performance (Chibueze, T., 2021).

Table 4.13: The Calculated Zener Anisotropic Index (Az), Universal Anisotropy index (AU), Equivalent Zener Anisotropy Measure (Aeq), Minimum and Maximum Values of Young's modulus (Emin and Emax in GPa), Shear Modulus ($Gmin$ and $Gmax$ in GPa) and their Ratios

Dopant	Az	A^U	A^{eq}	E_{max}	E_{min}	E_{max}/E_{min}	G_{min}	G_{max}	G_{max}/G_{min}
Pure	1.25	0.90	0.97	214.9	115.3	0.54	53.2	78.6	0.68
Ce	1.34	0.91	0.98	219.5	120.2	0.55	55.2	81.3	0.68
Dy	1.28	0.93	1.01	216.3	118.6	0.55	54.0	79.7	0.68
Eu	1.29	0.92	0.99	119.4	217.8	0.55	54.8	80.2	0.68

4.5.4 Elastic Tensors of W-ZnO

The elastic tensors of W-ZnO were computed and visualized using the open-source Elate code (Cowin, 1985), which reads in the second-order elastic constants C_{ij} and generates a comprehensive analysis of directional mechanical properties. By providing the stiffness matrix in GPa, Elate calculates parameters such as Young's modulus, shear modulus, and Poisson's ratio as a function of orientation, allowing researchers to explore how doping or structural variations impact the anisotropic mechanical behavior of W-ZnO.

Figure 4.14 shows 3D polar surfaces illustrating the directional dependence of (a) Young's modulus, (b) Shear modulus, and (c) Poisson's ratio for W-ZnO, highlighting its pronounced mechanical anisotropy. In each plot, the radial distance from the origin corresponds to the magnitude of the property in a given crystallographic direction. The Young's modulus surface typically appears lens-shaped around the c-axis, indicating higher stiffness along specific orientations, while the shear modulus surface reflects how resistance to shape change varies with angle. The Poisson's ratio surface, which depicts transverse strain response under uniaxial stress, also exhibits directional variations tied to the relative differences between bonding along and perpendicular to the c-axis (Lee, Park, & Chang, 2022).

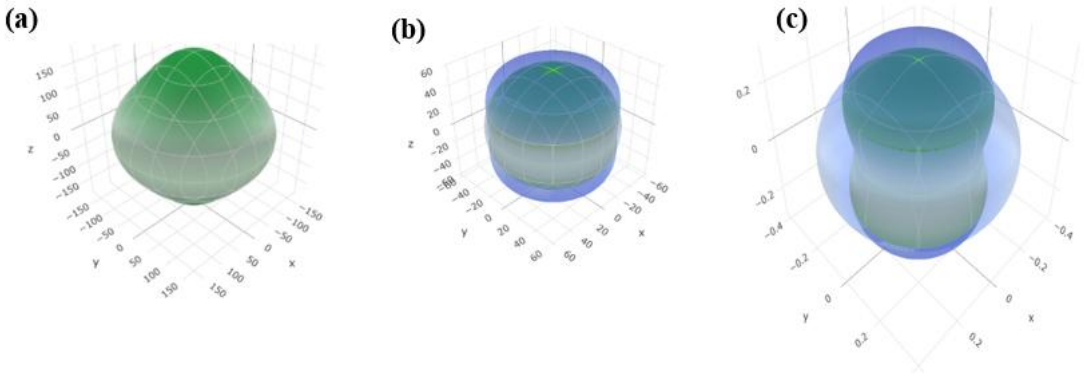

Figure 4.14: Directional Dependence of (a) Young's Modulus, (b) Shear Modulus and (c) Poisson's Ratio of W-ZnO in 3D

Together, these 3D plots underscore that W-ZnO's mechanical properties are far from isotropic and must be carefully considered for applications such as piezoelectric devices and thin-film coatings where orientation-dependent stress and strain states play a crucial role. Figure 4.15 illustrates how the Young's modulus of W-ZnO varies with direction in the (xy), (xz), and (yz) planes, each plotted on a radial scale up to about 200 GPa. In the (xy) plane (part a), the nearly circular shape with a radius of around 140–150 GPa indicates a relatively uniform stiffness within that basal plane. By contrast, the (xz) and (yz) planes (parts b and c) show more elliptical contours, with a maximum near 200 GPa (along or close to the c-axis) and a minimum around 130–140 GPa (in directions more perpendicular to the c-axis). This indicates that W-ZnO is stiffest along the c-axis and slightly less stiff in directions within the basal plane, highlighting the anisotropic nature of its mechanical response (Tindibale et al., 2023).

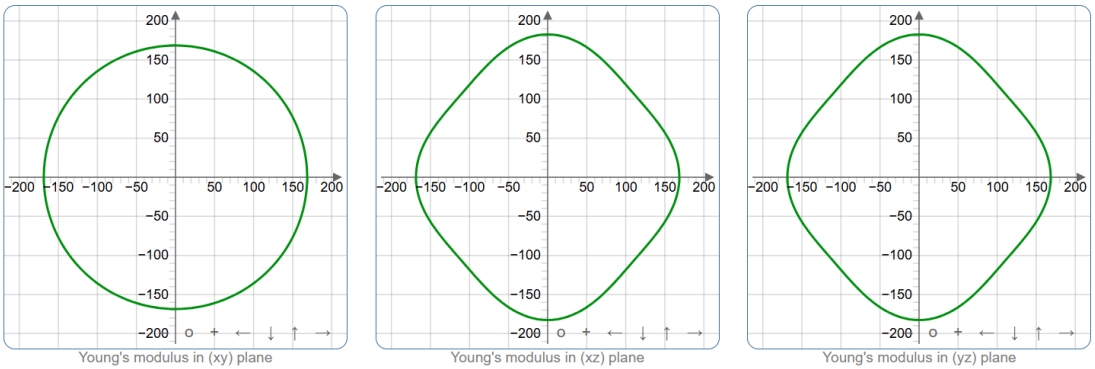

Figure 4.15: Directional Dependence of Young's Modulus of W-ZnO in 2D

Figure 4.16 shows the directional dependence of the shear modulus in the (xy), (xz), and (yz) planes of W-ZnO for two conditions, with the green and blue curves spanning

about 30–60 GPa. The (xy) plane appears nearly circular, indicating a more isotropic shear response near 40–50 GPa, while the (xz) and (yz) planes exhibit square-like shapes with maxima around 60 GPa. The difference between the two curves highlights how doping or structural variations can alter the elastic anisotropy, especially out of the basal plane (Pingak et al., 2023). Figure 4.17 displays the directional dependence of Poisson's ratio in the (xy), (xz), and (yz) planes of wurtzite ZnO for two conditions (green and blue curves), spanning approximately −0.3 to +0.4. In the (xy) plane, both curves are nearly circular, with the green curve peaking around 0.20 and the blue curve around 0.350.350.35, indicating conventional lateral expansion under axial load.

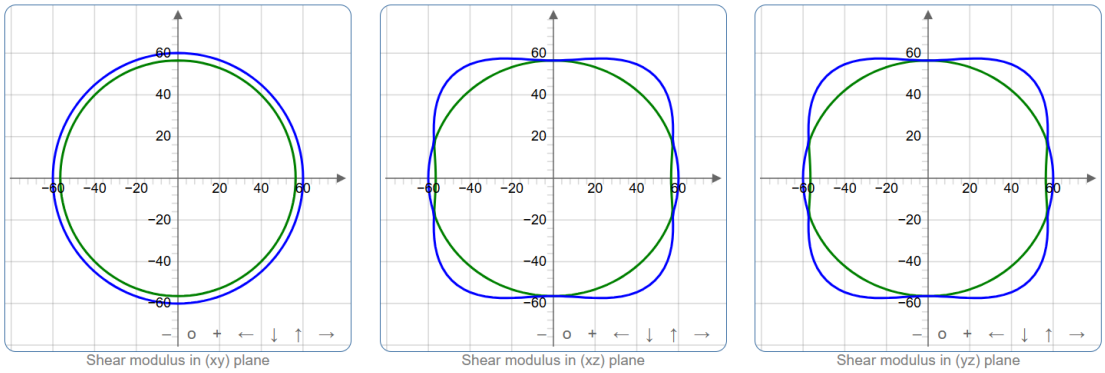

Figure 4.16: Directional Dependence of Shear Modulus of W-ZnO in 2D

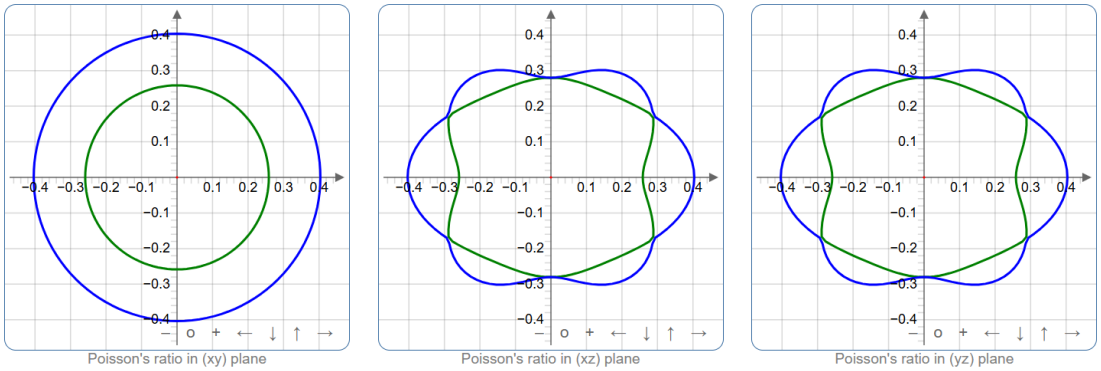

Figure 4.17: Directional Dependence of Poison's Ratio of W-ZnO in 2D (Blue and green indicate the Maximum and Minimum Values Respectively)

The more "petal-like" shapes in the (xz) and (yz) planes show that in certain directions the ratio can drop below zero (−0.2), highlighting the crystal's anisotropic elastic response. The three polar plots illustrate the directional dependence of the Young's modulus in the (xy) plane for Ce-, Dy-, and Eu-doped ZnO, revealing characteristic "clover-like" shapes that reflect each dopant's influence on the crystal's elastic anisotropy. By substituting Zn with different rare-earth ions, the local bonding environment shifts, causing subtle variations in the stiffness along different in-plane

directions. These differences manifest as slight changes in the maximum or minimum radial extents in the plots, indicating how doping alters the relevant elastic constants (Rodriguez, Gonzalez, & Marcos, 2022). Even minor adjustments to these constants can shift the peak moduli by a few GPa and affect the overall anisotropy of ZnO, which is significant for applications such as thin-film coatings or piezoelectric devices where mechanical behavior depends heavily on crystallographic orientation. Thus, the spatial dependence of Young's modulus underlines that doping is an effective way to fine-tune the mechanical properties of ZnO for specific technological needs.

Figure 4.18 illustrates the 3D linear compressibility of ZnO, showing how doping with Ce, Dy, or Eu modifies the material's anisotropic response to stress. The variation in shape across different orientations reflects directions of enhanced or reduced compressibility, indicating that RE elements stiffen specific crystallographic axes. This observation aligns with the higher elastic constants in Table 4.10, suggesting that doped ZnO exhibits reduced compressibility (i.e., increased stiffness) in targeted directions.

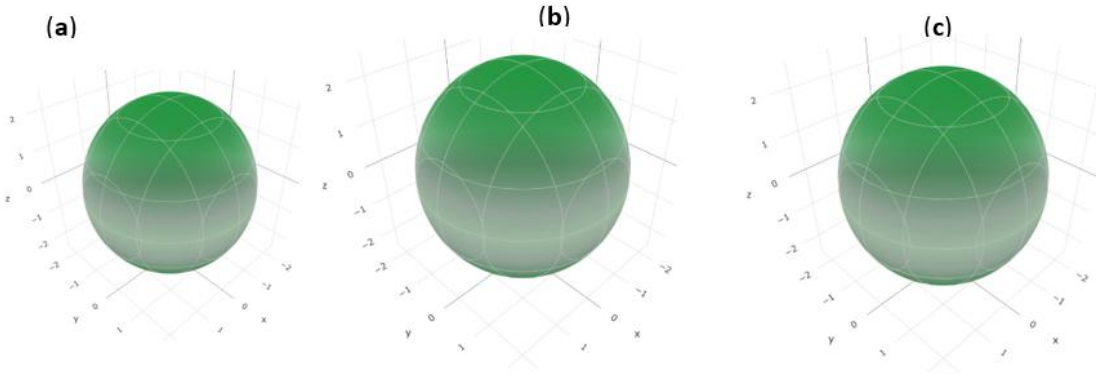

Figure 4.18: 3D Representation of Linear Compressibility of (a) Ce (b) Dy and (c) Eu Doped W-ZnO

Figure 4.19 presents the 3D representation of Young's modulus, which provides a complementary view of the same anisotropy. Regions of higher modulus correspond to directions of lower compressibility, emphasizing the inverse relationship between these properties. The enhanced modulus values for Ce-, Dy-, and Eu-doped ZnO confirm that introducing rare-earth dopants significantly improves rigidity along certain orientations, thus tailoring the mechanical behavior of the crystal. Figure 4.20 displays the 3D shear modulus, highlighting how the lattice resists shape changes under torsional or shear forces. Larger lobes in this representation correlate with

higher shear stiffness, corresponding to the elevated C44 and C66 values in Table 4.10. Together, these figures demonstrate that doping modifies multiple aspects of W-ZnO's mechanical response, reinforcing the crystal in ways that reduce compressibility, increase stiffness, and strengthen shear resistance.

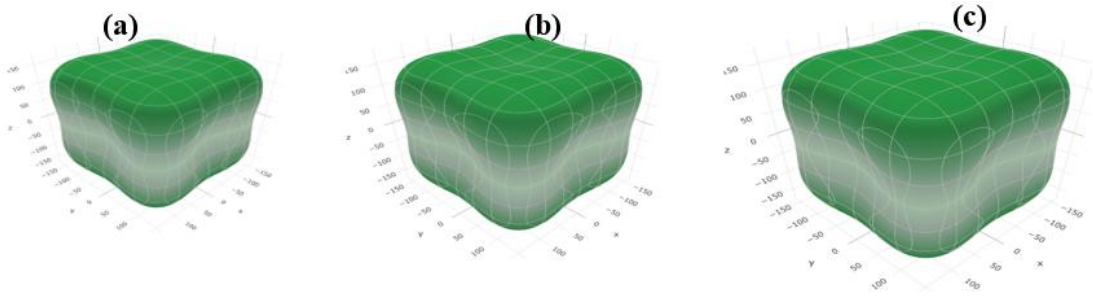

Figure 4.19: 3D Representation of Young's Modulus of (a) Ce (b) Dy and (c) Eu Doped W-ZnO

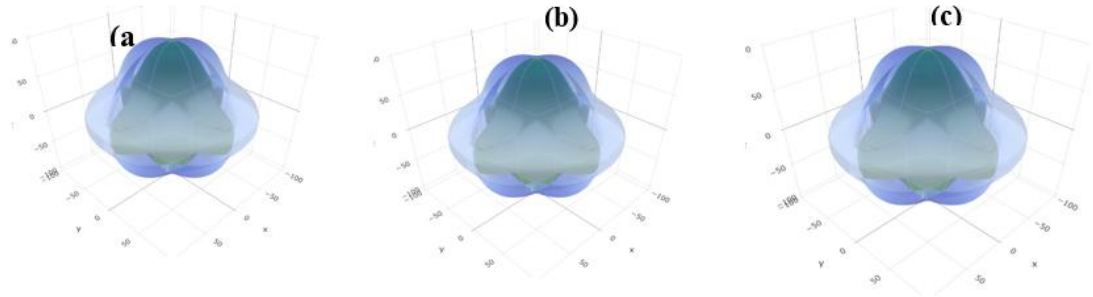

Figure 4.20: 3D Representation of Shear Modulus of (a) Ce (b) Dy and (c) Eu Doped ZnO

4.6 Electronic Properties

4.6.1 GGA +U Formalism

ZnO is a versatile wide-bandgap semiconductor with significant potential in optoelectronic applications, notably in DSSCs. The electronic properties of ZnO such as its band structure, density of states, and charge carrier dynamics are crucial for optimizing DSSCs, efficiency and performance. This study employs DFT within the GGA framework to probe these properties, while also incorporating the Hubbard U correction (GGA + U) to address the common underestimation of the bandgap and better represent the localized nature of Zn 3d and O 2p states. The refined computational approach not only enhances understanding of the intrinsic electronic behavior of ZnO but also aids in tailoring its properties for improved performance in DSSC applications.

4.6.2 Band Structures

The electronic characteristics were examined through the computation of electronic band structures and the associated projected density of states (PDOS), as illustrated in Figures 4.21, 4.22, and 4. 23. The dashed lines at 0 eV in these figures indicate the Fermi energy level, which delineates the boundary between the conduction band and the valence band. To enhance the accuracy of the electronic band structure calculations, the K point mesh was refined to a denser configuration by sampling the high symmetry points of 8 x 8 x 6 within the first Brillouin zone. In this research, the band structures are illustrated at the high symmetry points Ao-Eo– Γ-S-Y- Z. Analysis of these band structures reveals that both the valence band maxima (VBM) and the conduction band minima (CBM) are located at the gamma symmetry point. As a result, W-ZnO exhibits a direct band gap of 0.79 eV when evaluated using the standard DFT formalism as shown in Figure 4.21. This is a great improvement from the QE value of 0.65 eV reported by (Qing et al., 2021). In contrast to the experimentally determined band gap of 3.37 eV, it is an extreme underestimation of approximately 75%.

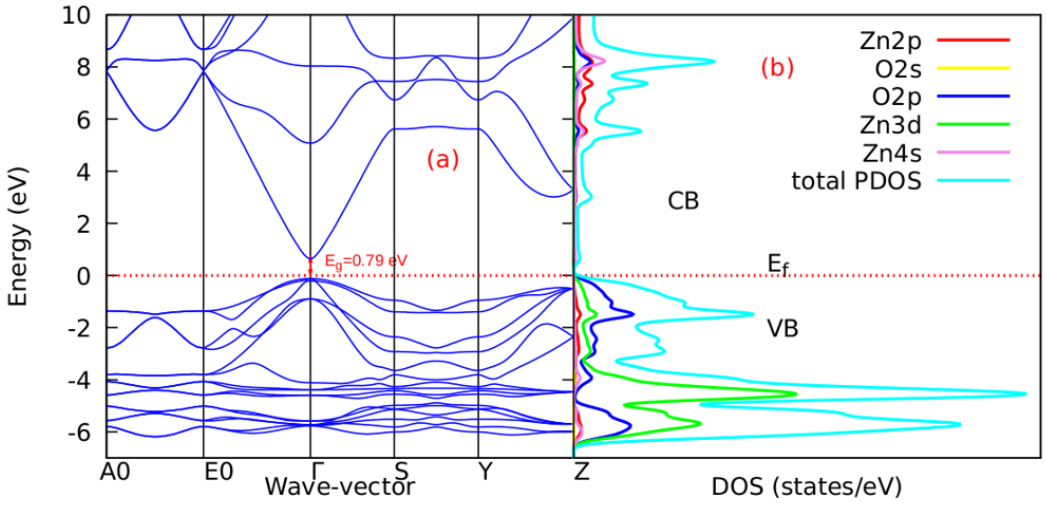

Figure 4.21: (a) Band Structure and (b) Density of State of W-ZnO using Standard DFT Approximation

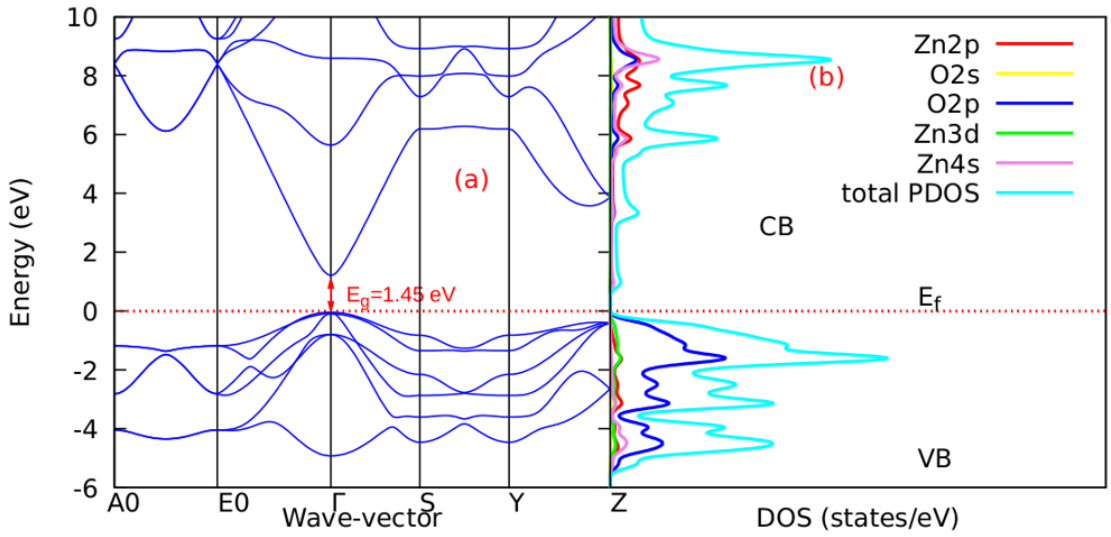

Figure 4.22: (a) Band Structure and (b) Density of State of W-ZnO using DFT+Ud(10eV) Approximation

The observed phenomenon can be ascribed to the recognized limitations of LDA and GGA in addressing the significant hybridization between the d and p orbitals, which results in a reduction of the band gap (Mbilo & Musembi, 2022). Introduction of the Hubbard correction term in the Zn-3d (U_d) and O-2P (U_p) shells significantly widened the band gap as shown in Figures 4.22 and 4.23.

Figure 4.24 illustrates how the calculated band gap of ZnO varied with increasing Hubbard U parameters, highlighting two distinct scenarios: (a) applying a U correction only on the Zn-3d orbitals (U_d) and (b) simultaneously applying U_d on Zn-3d and U_p on O-2p orbitals. In Figure 4.24 (a), as U_d increases from 0 to 12 eV, the band gap systematically increases, reflecting the enhanced localization of the Z-3d electrons and the consequent upward shift of the conduction band. In Figure 4.24 (b), the inclusion of U-p further shifts the valence band, leading to an even larger band gap for the same range of U_d values.

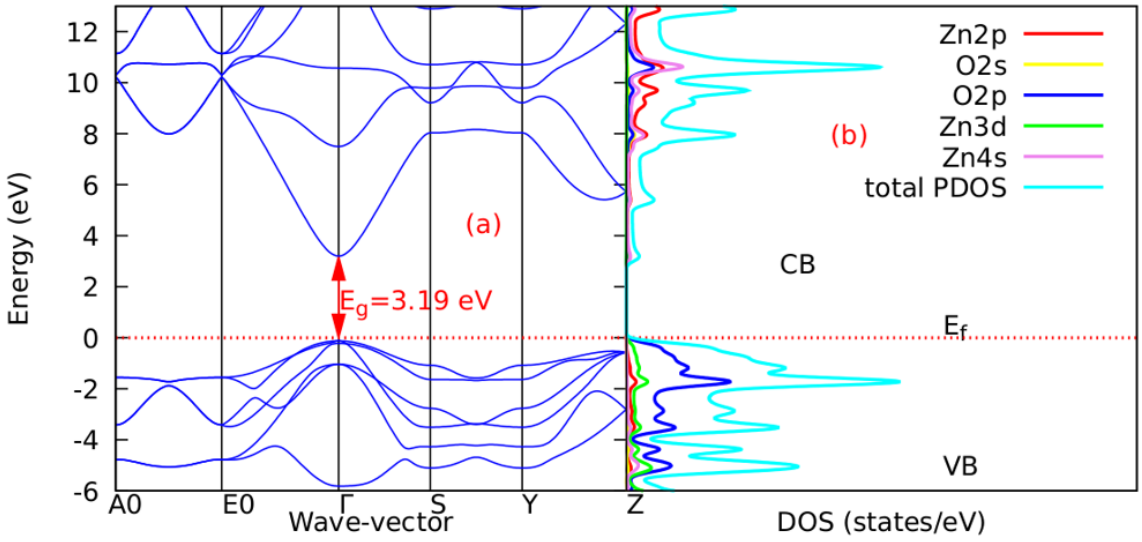

Figure 4.23: The (a) Band Structure and (b) Density of State of ZnO Using DFT + $U_{d(10eV)}$ + $U_{p(8eV)}$ Approximation

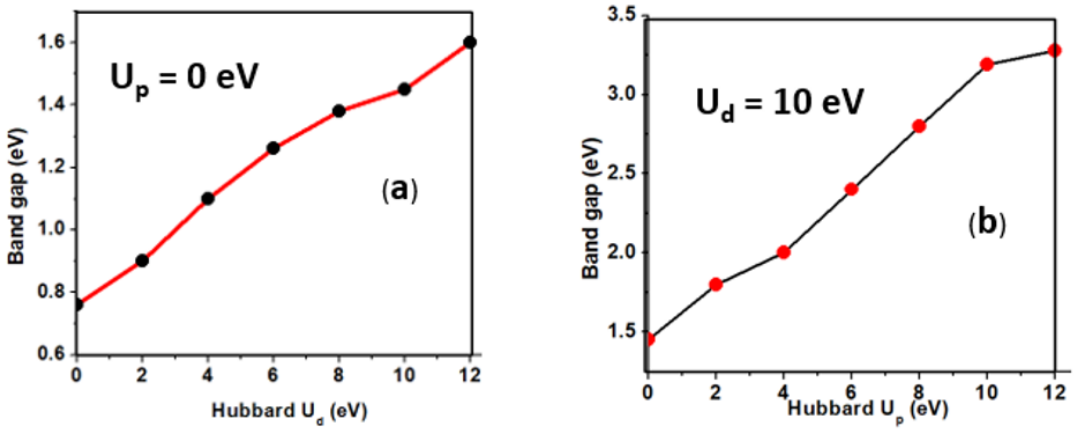

Figure 4.24: The Variation of the Hubbard U Parameter and the Band Gap (a) DFT + Ud and (b) DFT+Ud +Up

Overall, the figure demonstrates that both U_d and U_p corrections can significantly influence the predicted band gap, underlining the importance of carefully choosing Hubbard U parameters to obtain more accurate electronic structures in ZnO (Jafarova et al., 2021.). A combination of U_d =10 eV and Up= 8 eV reproduced experimental band gap of 3.19eV as reported by (Ungula et al., 2018) and was therefore adopted in consequent computations of the optical and mechanical properties. These energy band gaps corroborate well with the findings from the PDOS presented in Figures 4.21b, 4.22b, and 4.23b. From the PDOS calculations, it is evident that the valence band (VB) is predominantly composed of contributions from O-2s, Zn-3d, and O-2p orbitals, which form the main electronic states in this region. In contrast, the conduction band

(CB) primarily consists of states contributed by Zn-4s and O-2p orbitals, while the contributions from Zn-2s and Zn-2p remain minimal and not well pronounced. These orbital distributions align with the observed band gap variations.

Incorporating the Hubbard term U into DFT calculations results in significant shifts in the energy levels. Specifically, a downward shift of the hybridized Zn-3d and O-2p states in the valence band, coupled with an upward shift of the Zn-4s state in the conduction band. These shifts result in an increased band gap and cause the Fermi level to move closer to the valence band, a behavior that has been consistently reported in the literature (Darma et al., 2020). The agreement between band gap measurements and the PDOS analysis not only validates the use of the GGA+U approach in accurately capturing the complex interplay of orbital hybridization and defect states in RE-doped ZnO but also underscores its potential in guiding the design of optoelectronic devices through controlled defect engineering.

4.6.3 Effects of Structural Configurations

The band structure and corresponding projected density of states (PDOS) for various ZnO structural configurations (C-ZnO, W-ZnO and M-ZnO) were calculated in this study to give insights on the Energy band gap as presented in Figures 4.25 and 4.26. The band structure and corresponding PDOS for C-ZnO, W-ZnO, and M-ZnO (Figures 4.25 and 4.26) reveal how different crystal symmetries influence the alignment of valence and conduction bands. In all three configurations, the upper valence band is predominantly derived from O 2p states, while the conduction band originates mainly from Zn 4s states, with some hybridization between Zn 3d and O 2p orbitals. These features underscore the role of structural arrangement in dictating the electronic states near the Fermi level and, consequently, the size of the energy band gap (Muscat et al., 2001). As shown in Table 4.14, the GGA-PBE method systematically underestimates the band gap in each polymorph compared to both experimental results and other DFT-based studies. For instance, W-ZnO is calculated to have a 0.76 eV band gap using GGA-PBE, whereas the experimental gap is about 3.37 eV.

Table 4.14: Energy Band Gap Values in eV of ZnO Calculated with GGA-PBE and GGA+U Approximations

Phase	GGA-PBE	GGA+U	Previous work (DFT)	Previous work (Experiment)
C-ZnO	0.63	3.01	0.65 (Charifi et al., 2007)	-
W-ZnO	0.76	3.19	0.792 (John et al., 2016)	(Dhamodharan et al., 2017)
M-ZnO	1.31	3.38	0.96 (Farooq et al., 2016)	-

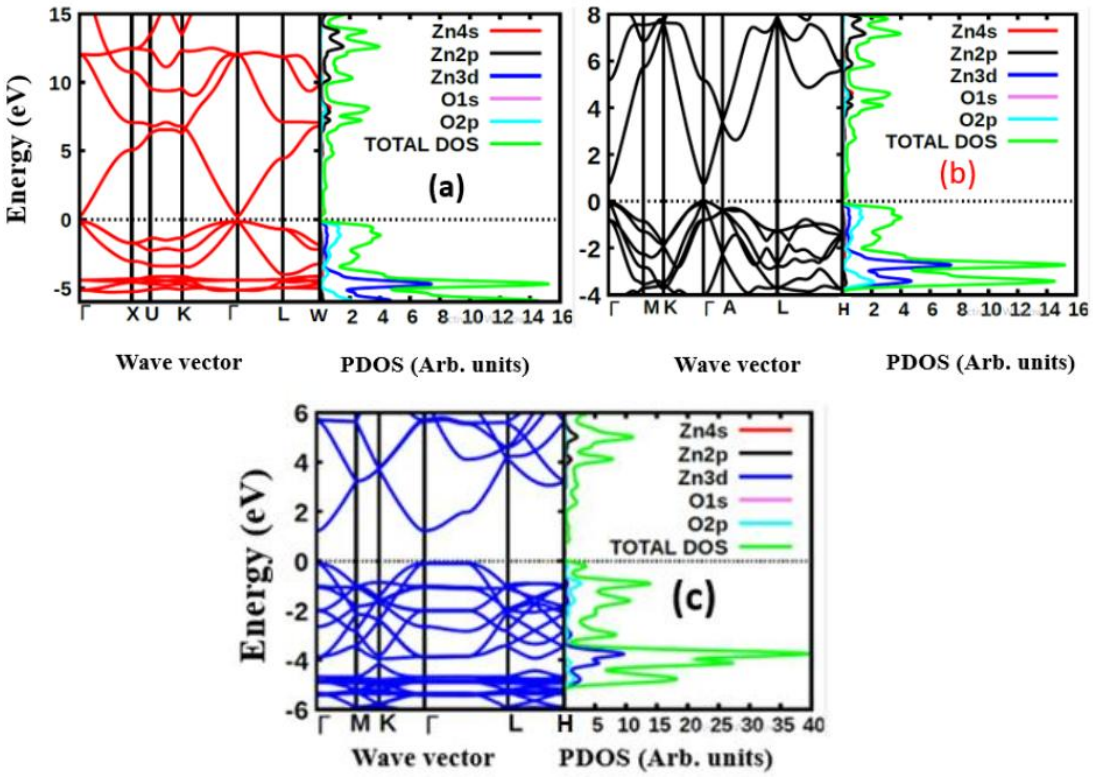

Figure 4.25: The Electronic Band Structure and PDOS of (a) C-ZnO, (b) W-ZnO and (c) M-ZnO Structures using Standard DFT

By introducing a U parameter (GGA+U), the computed gaps increase substantially (e.g., 3.19 eV for W-ZnO), highlighting the importance of including on-site Coulomb corrections to better account for electron-electron interactions in ZnO. Comparing the three phases, M-ZnO shows a larger GGA-PBE gap (1.31 eV) than either the cubic or wurtzite structures, although GGA+U raises all gaps closer to the expected semiconducting range of approximately 3 eV. These results confirm the interplay between crystal symmetry and electronic correlations in determining the band gap of ZnO, as well as the need for beyond-GGA approaches to achieve closer agreement with experiment.

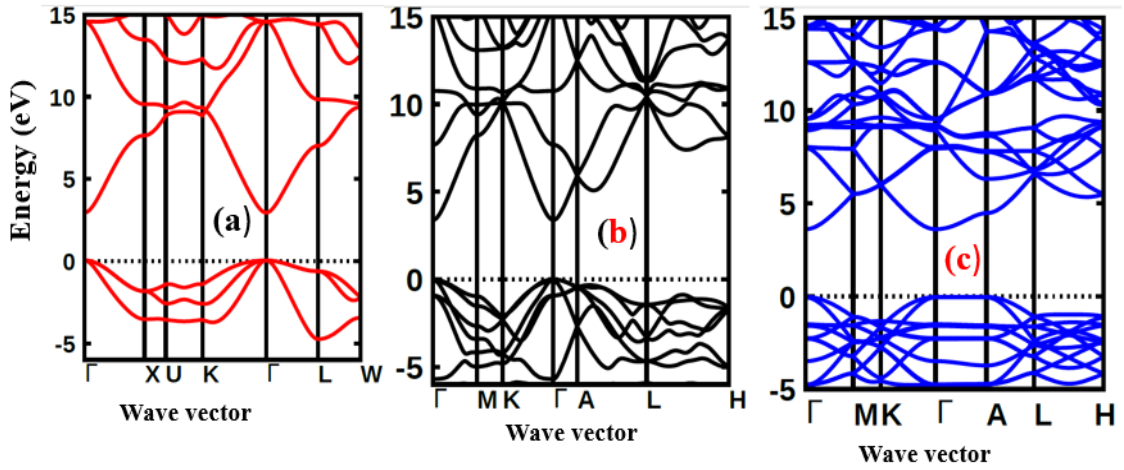

Figure 4.26: The Electronic Band Structure of (a) C-ZnO, (b) W-ZnO and (c) M-ZnO Structures using GGA+U

4.6.4 Electronics Properties of RE (Ce, Dy and Eu) Doped ZnO

Rare-earth (RE) doping in zinc oxide (ZnO) has gained significant attention due to its potential to enhance electronic properties for optoelectronic and photovoltaic applications. In this study, the electronic properties of Ce, Dy, and Eu-doped ZnO were investigated using DFT implemented in QE within the GGA and GGA+U approaches. A 3×3×3 supercell containing 108 atoms was employed to model the doping effects accurately. The introduction of RE elements is expected to modify the electronic band structure, alter bandgap characteristics, and influence the DOS, thereby impacting the material's suitability for applications such as DSSCs. The application of the GGA+U method accounts for strong electron correlations in the RE 4f orbitals, leading to a more accurate description of the electronic structure.

To describe the electronic structure of compounds tested, this study has computed the band structure, the projected as well as the total density of states of the RE (Ce, Dy and Eu) doped W-ZnO. The band gap is a critical parameter in DSSC material since it directly dictates the electrical conductivity and optical properties of a material. To rectify GGA shortcomings, a Hubbard U potential was introduced in the Zn-3d (10 eV) and O-2p (8 eV) and RE-4f (5eV) orbitals in the GGA+ U calculation. Consequently, the band gap was widened to the experimental values of 3.38 eV as illustrated in Figure 4.27(a) for the undoped W-ZnO. When W- ZnO is doped with RE (Ce, Dy, Eu), still the band gap was direct but narrowed down which is an important factor for optical performance in DSSC photoanode. As shown in Figures 4.27 (b-d),

the band structure is more compact indicating great interaction amongst the various atoms in the RE doped W-ZnO.

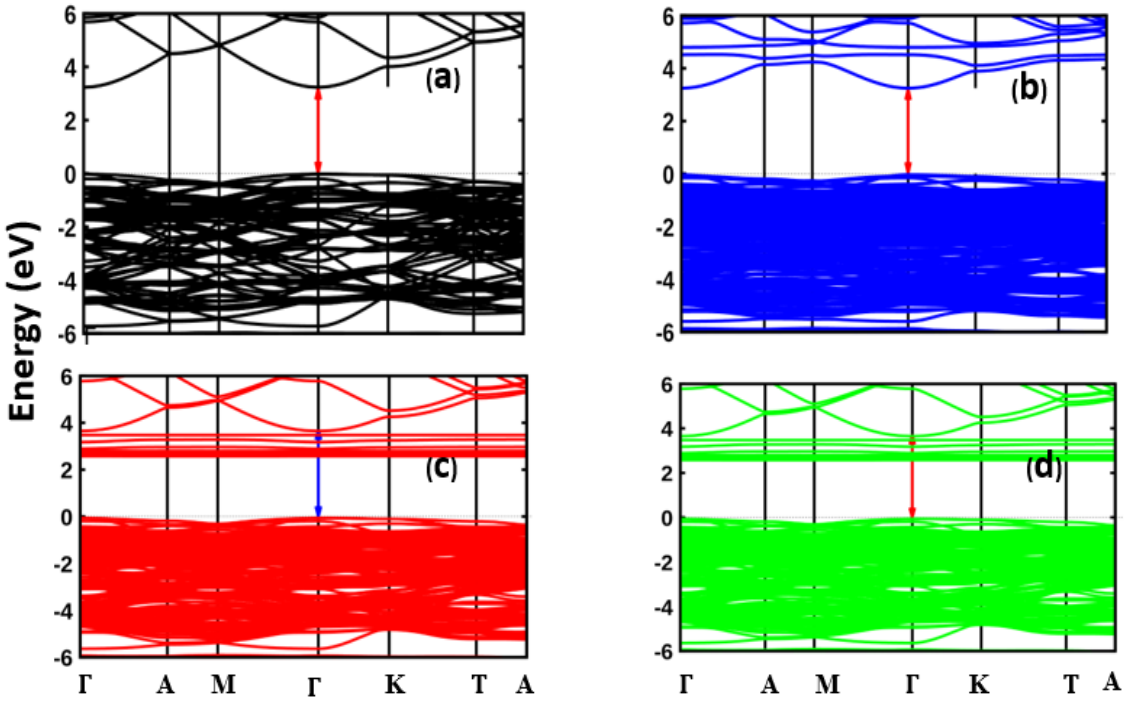

Figure 4.27: The Electronic Band Structures of (a) Pure (b) Ce-Doped, (c) Dy-Doped and (d) Eu-Doped W-ZnO using GGA+U

The fermi level was noted to shift upwards towards the CB reflecting that RE (Ce, Dy, Eu) acts as donor dopant resulting into n-type extrinsic semiconductor due to Burstein-moss effect (Micromachines et al., 2022). From the measurement of band gap the fermi level (set at zero) to the minimum of the CB, the band gap was found to decrease with RE doping. The values obtained were 3.19, 3.14 and 3.24 eV for Ce, Dy and Eu doped M-ZnO respectively. Substituting RE for Zn further generated isolated impurity bands located in the band gap region which was a unique feature in RE (Ce, Dy, Eu) doped W-ZnO. This was attributed to the 4f orbital introduced into the ZnO structure by the RE dopant atoms and is expected to enhance phonon absorption (Rahman et al., 2022). Positioned above the fermi level, these isolated states further act as a trampoline, facilitating the transition of electrons into the CB via thermal and photo-excitation mechanisms. This occurrence diminishes the necessity for photon energy and can promote movement of photogenerated charge carriers in DSSC's (Wu et al., 2023).

The study also performed an analysis of the DOS and PDOS to further interrogate the electronic properties of pure and RE (Ce, Dy and Eu) doped W-ZnO as presented in Figure 4.28. It was found that the O-2s dominated the lower energy region (-18 eV) of the VB. The region near the fermi level was occupied by both the Zn-3d and O-2p orbitals whose hybridization generate a very strong Zn-O bond.

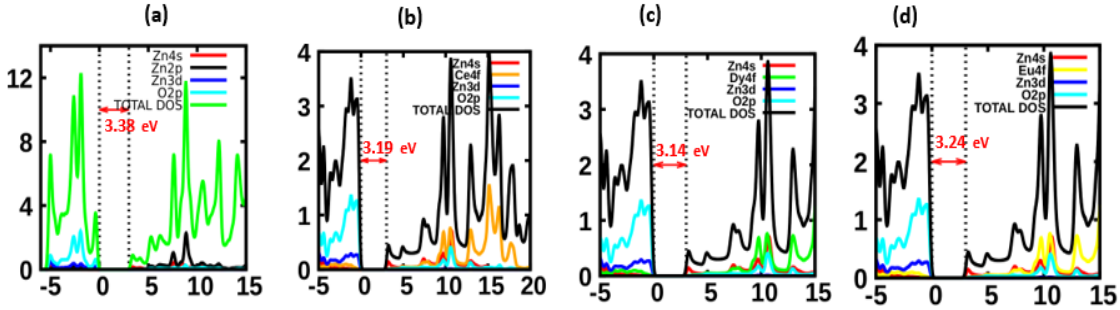

Figure 4.28: The Total DOS and PDOS of (a) Pure (b) Ce, (c) Dy and (d) Eu Doped W-ZnO

The computed total DOS for undoped ZnO using the GGA-PBE reveals that the valence band maximum (VBM) is predominantly composed of O-2p states, while the conduction band minimum (CBM) is primarily derived from Zn-4s states. The Zn-3d states are located well below the VBM, contributing minimally to the electronic states near the Fermi level. The projected density of states (PDOS) further confirms that the introduction of U weakens the Zn-3d–O-2p interaction, leading to a more localized electronic structure and improved bandgap estimation RE doping introduces additional impurity states in the electronic structure of ZnO. The inclusion of RE elements such as Ce, Dy, and Eu leads to the emergence of localized 4f states, which significantly impact the DOS and PDOS characteristics. The total DOS for RE-doped ZnO exhibits a noticeable reduction in the bandgap due to the introduction of RE-4f states within or near the band edges (D. K. Sharma et al., 2016). These impurity states modify the carrier concentration and influence charge transport mechanisms in DSSCs.

4.6.5 Effect of Dopant Concentration Band Gap of W-ZnO

In the case of RE-doped W-ZnO, all three dopants (Ce, Dy, and Eu) exhibit a similar trend: as the dopant concentration increases from 1.85% to 5.56%, the band gap decreases as recorded in Table 4.15. For instance, Ce-doped ZnO shows a reduction in the GGA band gap from 0.74 eV at 1.85% doping to 0.69 eV at 5.56% doping. A comparable trend is observed in the GGA+U results, where the band gap decreases from 3.17 eV to 3.10 eV. Similar narrowing is seen in Dy- and Eu-doped ZnO. This gradual band gap narrowing with increased RE doping can be attributed to the introduction and hybridization of the RE 4f states with the ZnO host states, thereby perturbing the conduction and valence band edges. Such effects have been reported in the literature. Huong et al., (2025) observed a reduction in the band gap of ZnO by approximately 0.1–0.2 eV as the concentration of rare-earth dopants increased, which is in good agreement with findings of this study.

Moreover, the non-linear variation of the band gap with dopant concentration suggests a complex interplay between the dopant-induced localized states and the extended states of the host lattice. noted a similar non-monotonic behavior in RE-doped ZnO, highlighting that the precise effect depends on the dopant's electronic configuration and its interaction with the ZnO lattice. While the absolute band gap values differ between the GGA and GGA+U methods, the overall trend of band gap narrowing with increased dopant concentration remains consistent. These comparative results not only validate DFT computational approach but also emphasize the importance of using advanced methods like GGA+U to accurately capture the electronic properties of doped semiconductors. These theoretical findings show strong agreement with prior experimental reports. The Ce-doped ZnO studies by Meshram et al., 2017 and Khuili et al., 2020 report band gaps above 3.1 eV, in line with the GGA+U results. Notably, for Eu-doped ZnO, previous DFT data is lacking, so the current results provide new insights, especially in showing a mild redshift trend with increasing doping. Overall, the table confirms that RE doping allows for controlled band gap tuning in ZnO, with Ce being the most impactful dopant, making it highly promising for optical and photovoltaic applications. Tailoring the band gap through controlled RE doping is promising for optimizing ZnO's optical and electronic properties for potential applications in optoelectronic and photovoltaic devices. The RE-4f states mainly contribute to conduction band modifications, leading to a slight decrease in the band

gap.

Table 4.15: Effect of Concentration on the Band Gap of RE (Ce, Dy, Eu) Doped ZnO

Dopant	Conc (%)	Current Study (GGA)	Current Study GGA+U	Previous experimental work	Conc (%)	Ref
Ce	0	0.76	3.19	3.35	0	(Meshram et al., 2017)
	1.85	0.74	3.17	3.33	2	
	3.37	0.71	3.14	3.32	4	
	5.56	0.69	3.10	3.31	6	
Dy	0	0.76	3.19	3.2	0	(Huang et al., 2008)
	1.85	0.73	3.16	3.13	1	
	3.37	0.70	3.13	3.09	5	
	5.56	0.68	3.09			
Eu	0	0.76	3.19	3.28	0	Zong et al., 2014
	1.85	0.75	3.18	3.31	1	
	3.37	0.72	3.16	3.29	2	
	5.56	0.70	3.13	3.25	3	

However, at higher concentrations (5.56%), the overlap between RE-4f and O-2p states becomes significant, facilitating the formation of midgap states that have potential to cause undesirable charge recombination (Nguyen et al., 2025). This effect is particularly strong in Eu-doped ZnO, where the 4f states have a higher density near the Fermi level. These findings are consistent with experimental photoluminescence (PL) and absorption studies, which show a redshift in the absorption edge for RE-doped ZnO films at higher concentrations as shown in Table 4.15. The increased presence of dopants levels leads to enhanced sub-bandgap optical transitions, supporting the theoretical predictions from PDOS analysis.

4.6.6 Effects of Oxygen Vacancies

Oxygen vacancy (V_O) in W-ZnO significantly influence the electronic properties of the material, particularly in terms of charge carrier behavior, band structure, and defect states within the material's band gap. The formation of oxygen vacancies creates localized donor states in the conduction band, which contribute to the n-type conductivity of W-ZnO.

Table 4.16: Effects of Oxygen Vacancy on the band gap of W-ZnO

Dopant concentration (%)	**Ce**		**Dy**		**Eu**	
	GGA	GGA+U	GGA	GGA+U	GGA	GGA+U
0	0.74	3.17	0.73	3.16	0.75	3.18
1.85	0.72	3.15	0.71	3.14	0.73	3.16
3.37	0.70	3.12	0.69	3.11	0.71	3.13
5.56	0.68	3.10	0.67	3.09	0.69	3.07

In this study, RE (Ce, Dy, Eu)-doped W-ZnO was investigated at a constant dopant concentration of 1.85%, while the oxygen vacancy concentration was varied over 0, 1.85, 3.70, and 5.56% as shown in Table 4.16. For the case with no oxygen vacancies, the band gap values obtained using GGA are significantly lower than those calculated with the GGA+U approach, as expected. As the oxygen vacancy concentration increases from 0% to 5.56%, a gradual narrowing of the band gap is evident. For instance, in Ce-doped ZnO the GGA band gap decreases from 0.74 eV at 0% vacancy to 0.68 eV at 5.56% vacancy, while the corresponding GGA+U band gap decreases from 3.17 eV to 3.10 eV. Similar trends are observed in Dy- and Eu-doped ZnO. This consistent reduction in the band gap with increasing oxygen vacancies can be attributed to the introduction of localized defect states (Kumar et al., 2021). These states, which are induced by the absence of oxygen, tend to hybridize with the host ZnO states and the RE 4f levels, thereby reducing the energy difference between the conduction and valence bands (Huong et al., 2025).

These defect vacancies -induced states allow electrons to occupy energy levels near the conduction band, thereby reducing the material's band gap. In undoped ZnO, the introduction of oxygen vacancies has been found to shift the Fermi level towards the conduction band, promoting an increase in the electron concentration and improving the material's electrical conductivity. The existence of these localized electronic states influences the optical properties of ZnO, as the material may exhibit diminished band gap absorption. This leads to alterations in its absorption spectrum and could affect its performance as a semiconductor in optoelectronic device.

4.6.7 Charge Density of RE (Ce, Dy Eu) Doped ZnO

The charge density distribution of W-ZnO, both undoped and doped with rare earth elements (Ce, Dy, Eu), is crucial for understanding the electronic structure, bonding characteristics, and potential applications of these materials. Charge density is a key indicator of electron localization, bonding interactions, and charge redistribution due to doping. In order to assess the chemical bonds, present in the compounds, we have mapped their (110) electron density, illustrated in Figure 4.29. In the undoped W-ZnO system, the charge density is primarily localized around the Zn and O atoms, reflecting the ionic bonding nature between Zn^{2+} and O^{2-}. The electron density is concentrated around the oxygen atoms, especially in the oxygen-anion positions, due to their higher electronegativity. The Zn atoms exhibit a more diffuse charge distribution due to their lower electronegativity and higher ionization potential compared to oxygen. The overall charge density distribution is symmetric, and no significant charge redistribution is observed under normal conditions. Upon doping W-ZnO with RE elements, the charge density distribution undergoes notable changes, reflecting the interaction between the dopants and the ZnO matrix.

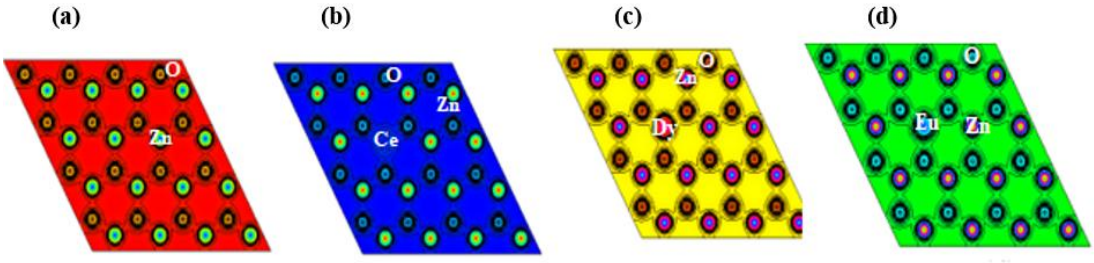

Figure 4.29: The Electron Density for the (a) Pure (b) Ce-Doped, (c) Dy-Doped and (d) Eu-Doped W-ZnO

The charge density is altered primarily in the vicinity of the dopant atoms, with varying effects depending on the type of RE dopant and its concentration. RE (Ce, Dy, Eu) tends to donate electrons to the ZnO lattice, causing a redistribution of charge around the dopant sites. At low dopant concentrations (1.85%), RE (Ce, Dy, Eu) introduces a small perturbation in the charge density, with a slight increase in electron density around the Ce ion. As the dopant concentration increases (3.7% and 5.56%), the charge density around the RE (Ce, Dy, Eu) atom becomes more localized, indicating the increasing influence of Ce on the electronic structure of the material. The redistribution of charge suggests a strong interaction between Ce and the

surrounding ZnO atoms, which may lead to localized states in the band structure.

4.7 Optical Properties

4.7.1 Dielectric Function

ZnO emerged as a promising semiconductor material for DSSC applications due to its wide band gap, high electron mobility, and versatile nanostructured morphologies. Its inherent optical properties play a crucial role in the efficiency of DSSCs, as they directly influenced light absorption, charge separation, and overall device performance. Key optical parameters including the real and imaginary parts of the dielectric function, absorption coefficient, refractive index, reflectivity, energy loss, and exciton energy were calculated to provide deep insights into ZnO's interaction with light. The photon energy range considered in this study spanned from 0 to 20 eV, which allowed for a comprehensive evaluation of the material's response across the relevant spectrum for solar applications. To accurately determine these optical properties, the Thermo_pw code (Sánchez et al., 2018) was integrated with QE, establishing an advanced computational framework for first-principles calculations. This integration enabled precise evaluation of ZnO's complex dielectric behavior and related phenomena at various photon energies. The real and imaginary parts of the dielectric function were computed to analyze the electronic transitions and absorption mechanisms governing the material's optical response. In addition, parameters such as the absorption coefficient, refractive index, reflectivity, energy loss function, and exciton energy were systematically determined, thereby providing a holistic picture of ZnO's optical performance. These detailed insights not only validated the computational approach but also paved the way for optimizing ZnO-based DSSCs for enhanced solar energy conversion.

4.7.2 Effects of Structural Configurations

The structural configuration of a material plays a crucial role in determining its optical properties. Variations in atomic arrangements, bonding, and symmetry can significantly affect the electronic band structure, thereby influencing optical parameters such as the real and imaginary parts of the dielectric function, refractive index, and absorption coefficient. In ZnO, for example, different structural phases for C-ZnO, W-ZnO, and M-ZnO exhibit distinct optical responses, which can be attributed to differences in the spatial distribution of electronic states and the nature

of electron transitions between them. These differences not only impact fundamental optical characteristics but also have practical implications in optimizing ZnO for applications in optoelectronics and photovoltaics, including DSSCs.

Figure 4.30(a) report the electronic findings for the static dielectric function, $\varepsilon_1(0)$, which were determined to be 4.7, 4.5, and 4.89 for the C-ZnO, W-ZnO, and M-ZnO structures, respectively. The refractive indices were then obtained by computing the square roots of these static dielectric values and were presented in Table 4.17. These results indicated that the M-ZnO phase exhibited the highest optical transparency, as evidenced by both its ε_1 (0) value and its corresponding refractive index, n (0). Figure 4.30(b) presented the imaginary dielectric function, $\varepsilon_2(\omega)$, as a function of energy, which defined the connection between the optical and electronic properties of the material. From this spectrum, the critical onset points were identified at 3.0, 3.29, and 3.35 eV for the C-ZnO, W-ZnO, and M-ZnO structures, respectively, as tabulated in Table 4.17. These values were in good agreement with the energy band gaps obtained from the band structure calculations. Moreover, the peaks observed in the imaginary part of the dielectric function are located at 4.2, 6.1, and 5.5 eV for the C-ZnO, W-ZnO, and M-ZnO samples were associated with electron excitations, specifically the transitions between the Zn-3d and O-2p states.

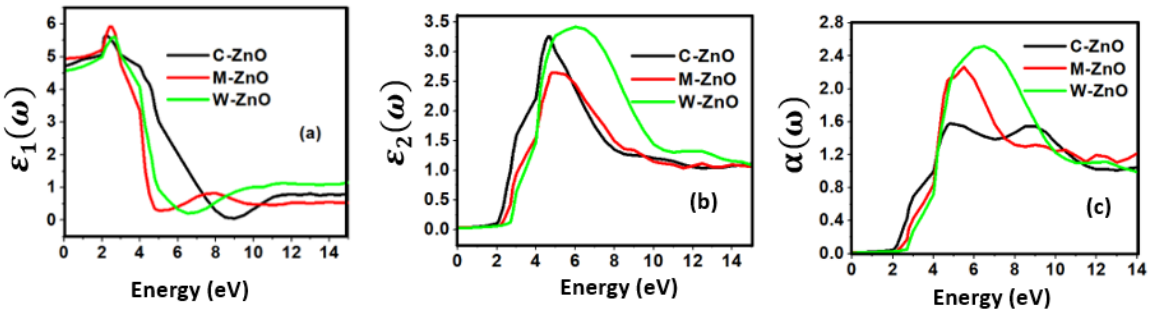

Figure 4.30: The (a) Real Part and (b) Imaginary Part of the Dielectric Constant, (c) Absorption Coefficient of C-ZnO, M-ZnO and W-ZnO Phases

Figure 4.30(c) depicted the absorption coefficient of ZnO, which informed on the decay of light intensity per unit distance in the material medium. The absorption coefficient was significantly affected by the photon frequency, indicating that incident photons would interact with the material electrons, leading to inter-band transitions from the valence band to the conduction band.

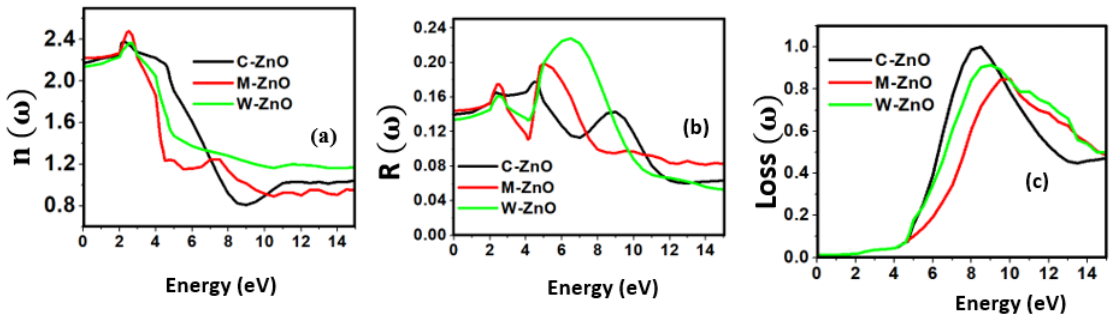

Figure 4.31: The (a) Refractive Index, (b) Reflectivity and (c) Energy Loss as a Function of the Energy in eV of C-ZnO, M-ZnO and W-ZnO Phases

The broad absorption spectrum, ranging from 3.01 eV to 14 eV, demonstrated that ZnO was largely transparent to the majority of solar radiation, a desirable characteristic for the photoanode in DSSCs. Consequently, due to the high transparency of ZnO there is a higher likelihood of the underlying dye to effectively absorb light, thereby facilitating photoemission and current generation (Tan et al., 2016). Materials of refractive index above 1.9 are desirable in DSSC applications for enhanced light trapping (Toghraie & Khodayari, 2020). The calculated refractive indices of ZnO phases are presented in Figure 4.31(a) and the results are analyzed in Table 4.17.

Table 4.17: Real Dielectric Function (ε_1), Refractive Index (n), Absorption Coefficient (α) and Reflectivity (R) at 0 eV

Structure	$\varepsilon_1(0)$	$n\ (0)$	$\alpha(0)$	R (0)
C-ZnO	4.7	2.17	3.00	0.141
W-ZnO	4.5	2.12	3.29	0.139
M-ZnO	4.8	2.21	3.35	0.144

The static refractive indices $n\ (0)$ were located at 2.17, 2.12 and 2.21 for the C-ZnO, M-ZnO and W-ZnO phases respectively. The material tested can therefore effectively bend and slow down light thereby improving the overall photon absorption when used as a DSSC photoanode. A significant decay in the dispersion curve of the refractive index was observed after the first peak indicating that beyond 3.2 eV photon energy, ZnO fails to maintain its transparent nature and instead absorbs such radiations. Reflectivity depicts the surface behavior of a material. Figure 4.31(b) shows a low reflectivity (R_0) of 0.141, 0.139 and 1.42 at zero photon energy for the C-ZnO, W-ZnO and M-ZnO phases respectively as listed in Table 4.17. The least reflectivity

(0.139) was observed in W-ZnO implying its least ability to reflect solar radiation but instead allow it to pass through for dye excitation in DSSC. From the plot, the highest peaks are observed at 5.0, 7.2 and 5.8 eV for the C-ZnO, W-ZnO and M-ZnO phases respectively after which the reflectivity rapidly dropped. Energy loss L (ω) is another vital parameter that characterizes the loss of energy of a fast-moving electron as it transverses a material medium. Figure 4.31(c) shows a near zero energy loss up to 4.0 eV in all the structures. At higher photon energy, the energy loss in ZnO gradually rises to a peak at 9.2 eV. The capability of ZnO within UV-Vis region to retain most of its energy with negligible energy loss to the surrounding as desired in DSSCs photoanode is therefore confirmed.

4.7.3 Effects of Hubbard U on Optical Properties of W-ZnO

The optical properties of Wurtzite ZnO (W-ZnO) are intricately linked to its electronic structure, which is strongly influenced by electron correlation effects. In this context, standard DFT often underestimates band gaps and misrepresents the hybridization between Zn-3d and O-2p states, leading to discrepancies in the predicted optical response. To address these limitations, we employed DFT, DFT+U_d (applying a Hubbard U correction to the Zn d-orbitals), and DFT+U_d+U_p (further correcting the O-2p) to systematically study the impact of these corrections on the optical properties of W-ZnO. These approaches allow for a more accurate representation of the dielectric function, absorption coefficient, and refractive index by properly accounting for on-site Coulomb interactions, thereby offering improved insights into the interband transitions and excitonic effects that are critical for optoelectronic applications.

The graphs depicted in Figure 4.32(a–f) display the relationship between optical properties and energy in eV. In reference to Figure 4.32(a), the electronic portion of the static dielectric function, is 8.52, 6.02 and 5.16 for DFT, DFT + U_d and DFT+U_d +U_p calculations respectively. The calculation of refractive indices is achieved by taking the square roots of the specified values (Namisi et al., 2023) which are summarized in Table 4.18. From this table, the inclusion of Hubbard U term reduces the value of $\varepsilon_1(0)$ as well as the refractive index. Between 5.1 to 5.8 eV, the curve is negative implying that the radiation is at this point fully attenuated and the ZnO compound behaves like a metal. The imaginary spectrum provides a connection between the optical and electronic band structure of a material. From Figure 4.32(b)

of $\varepsilon_2(\omega)$ as a function of energy, the critical onset points are located at 0.78, 1.46and 3.19 eV for DFT, DFT + U_d and DFT+U_d +U_p calculations respectively as tabulated in Table 4.18. The increase in the critical point value from DFT to DFT + U_d to DFT+U_d +U_p is collaborative to the results of computed electronic band gaps. The $\varepsilon_2(\omega)$ plot exhibited three prominent peaks at energies of 5.12, 10.4, and 13.6 eV, which corresponds to the transition of an electron from the valence band to the conduction band. In this context, the transitions of electrons occur between the O-2p and Zn-4s orbitals, the O-2p and Zn-3d orbitals, as well as between the O-2s and Zn-3d orbitals, respectively.

The absorption coefficient describes how light intensity diminishes over a specified distance within a material medium. It is greatly affected by the photon frequency implying that the incident photon interacts with material electrons resulting in inter-band electron transition from the valence to conduction bands. The data presented in Figure 4.32(c) indicates that the absorption edge of W-ZnO occurs at 0.78 eV, 1.44 eV, and 3.19 eV, corresponding to the DFT, DFT + U_d, and DFT + U_d + Up calculations, respectively. Contrast to standard DFT which predicts absorption of low energy photon including infrared, the DFT+U_d +U_p approach reveals that ZnO is transparent to majority of the solar radiation. Consequently, ZnO is able to pass on light to the absorption dye for photoemission and hence current generation (Vettumperumal et al., 2015.) .

The calculated refractive index of W-ZnO is displayed in the plot of Figure 4.32(d) and the results are presented in Table 4.18. Despite the reduction of static refractive indices from DFT to DFT + U_d to DFT+U_d +U_p, the values are high enough for the application of ZnO as a DSSC photoanode. A substantial drop in the dispersion curve related to the refractive index was observed post the initial peak indicating that beyond a certain amount of photon energy, W-ZnO fails to maintain its transparent nature and instead absorbs such radiations. Reflectivity depicts the surface behavior of a material. Figure 4.32 (e) shows a low reflectivity at zero photon energy (R_0). From Table 4.18, DFT+U_d +U_p predicts the least reflectivity of W-ZnO implying the ability of this material to reflect minimum solar radiation but instead allow it to pass through for dye excitation in DSSC.

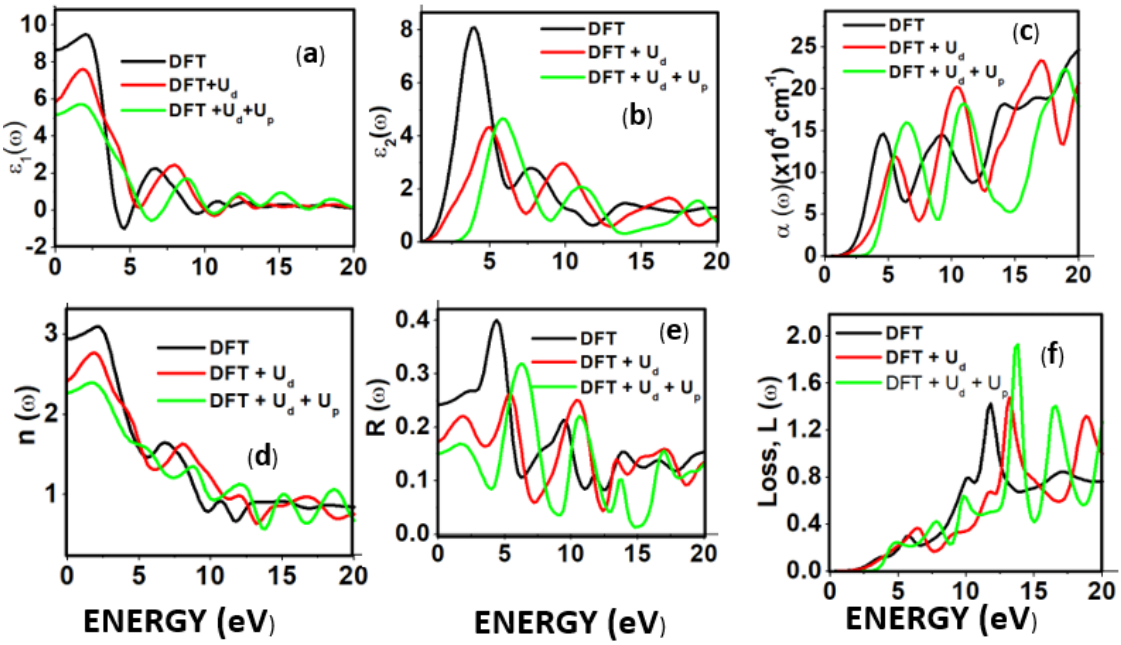

Figure 4.31: The (a) Real (B) Imaginary Part of the Dielectric Constant, (c) Absorption Coefficient, (d) Refractive Index, (e) Reflectivity and (f) Energy Loss as a Function of the Energy in eV of W-ZnO using DFT, DFT + Ud and DFT+Ud +Up

Table 4.18: Real Dielectric Function at 0 eV $\{\varepsilon_1(0)\}$, Refractive Index (n), Absorption Critical Points and Reflectivity at 0 eV (R0)

Formalism	$\varepsilon_1(0)$	Refractive index	Absorption critical points	R (0)
DFT	8.52	2.92	0.78	0.24
DFT + U_d	6.02	2.45	1.44	0.15
DFT+U_d +U_p	5.16	2.27	3.19	0.09

From the plot, the highest peaks are observed at approximately 4.9, 5.1 and 5.8 eV in the DFT, DFT + U_d and DFT+U_d +U_p respectively after which the reflectivity dropped. Energy loss L (ω) is another vital parameter that characterizes the loss of energy of a fast-moving electron as it transverses a material medium. Figure 4.32(f) shows a near zero energy loss up to 4.0 eV all the approximations techniques. At higher photon energy, the energy loss in ZnO gradually rises to a peak at 12.8, 14.2 and 15.4 eV DFT, DFT + U_d and DFT+U_d +U_p respectively. The capability of W-ZnO within UV-Vis region to retain most of its energy with negligible energy loss to the surrounding as desired in DSSCs photoanode is therefore confirmed. However, for high-energy

electrons, the energy loss of W-ZnO is relatively high.

4.7.4 Optical Properties of RE (Ce, Dy, Eu) Doped W-ZnO

In this section and using a 3x3x3 supercell of 108 atoms, one Zn atom was replaced with a RE (Ce, Dy, Eu) to create a RE doped ZnO compound. Thermo_pw in the DFT+U formalism was the employed to evaluate the dielectric coefficients and the rest of optical properties. The Hubbard U was applied to Zn-3d (10 eV), O-2p (8 eV) and RE-4f (5 eV) obtained in earlier optimization. Figure 4.33 and 4.34 represents the optical graphs of as a function of energy in eV as observed in this study. Figure 4.33a shows that doping ZnO with Ce, Dy, or Eu slightly alters the real part of the dielectric constant compared to the pure sample, shifting both the magnitude and spectral shape. This behavior reflects changes in the static dielectric constant, ε_1 (0), which, as Table 4.19 indicates, ranges from 4.98 (Eu-doped) to 5.5 (Dy-doped) versus 5.1 for pure ZnO. The refractive index follows a similar trend, confirming that rare-earth doping increases the polarization response depending on the dopant's effect on the crystal lattice. In Figure 4.33b, the imaginary part of the dielectric constant (linked to absorption and interband transitions) generally shifts to lower energies for doped ZnO, consistent with the lower absorption critical points noted in Table 4.19 (e.g., 3.15 eV for Dy-doped versus 3.38 eV for pure ZnO).

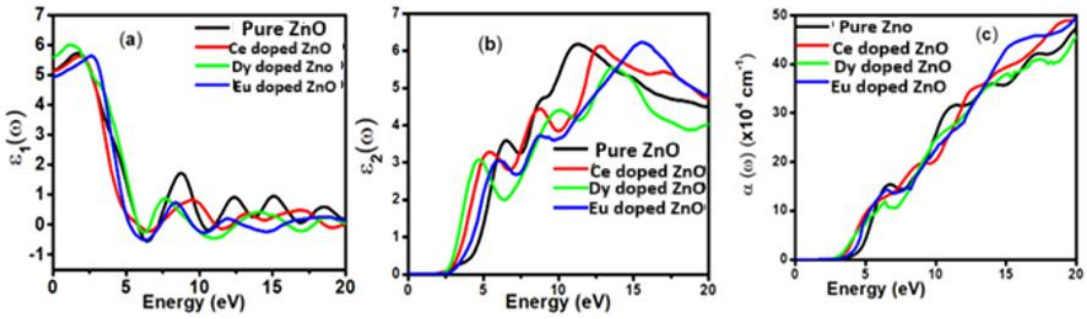

Figure 4.32: The (a) Real Part and (b) Imaginary Part of the Dielectric Constant, (c) Absorption Coefficient of the Pure and RE (Ce, Dy, Eu) Doped W-ZnO

Figure 4.33c highlights the absorption coefficient, whose onset also moves in response to doping, reinforcing the idea that rare-earth elements subtly adjust the band gap and optical transitions of ZnO. These results collectively illustrate that Ce, Dy, and Eu doping modifies key optical parameters such as $\varepsilon_1(0)$, refractive index, and absorption edge in distinct ways. Overall, the interplay of real and imaginary dielectric

components in Figure 4.33 aligns with the numerical values in Table 4.19, showing how rare-earth doping can be used to tailor ZnO's optical performance for specific applications. In Figure 4.34a, the refractive index (n) of pure ZnO and its Ce-, Dy-, and Eu-doped variants exhibits distinct peaks and slopes across the photon energy range, reflecting how rare-earth elements modify the polarization and dispersion behavior. Table 4.19 indicates that RE-doping leads to an increase in the refractive index of W-ZnO, which can be attributed to enhanced polarizability and the introduction of localized 4f electronic states. This suggests that RE doping alters the electronic environment and increases the material's optical density, thereby strengthening its interaction with incident light (Kumar et al., 2020). In the context of DSSC applications, a higher refractive index is beneficial as it enhances light trapping within the photoanode layer, leading to more effective light absorption by the dye.

Table 4.19: Real dielectric function at 0 eV $\{\boldsymbol{\varepsilon_1(0)}\}$, refractive index (n), absorption critical points and reflectivity at 0 eV (R0)

Compound	$\boldsymbol{\varepsilon_1(0)}$	**Refractive index**	**Absorption critical points**	**R (0)**
Pure ZnO	5.1	2.25	3.38	0.150
Ce doped W-ZnO	5.25	2.29	3.185	0.146
Dy doped W-ZnO	5.5	2.38	3.15	0.134
Eu doped W-ZnO	5.15	2.27	3.23	0.148

Figure 4.34 (b) shows the reflectivity (R), where each dopant shifts and reshapes the main peaks, indicative of modified optical transitions and free-carrier responses. The table confirms that the zero-frequency reflectivity R (0) increases to 0.174 for Dy-doped ZnO and decreases slightly to 0.148 for Eu-doped ZnO, relative to the undoped value of 0.150. These variations point to changes in how the surface interacts with incident light, an important factor for solar cell designs, since adjusting reflectivity can help manage the amount of light that enters or leaves the active layer (Touri et al., 2020).

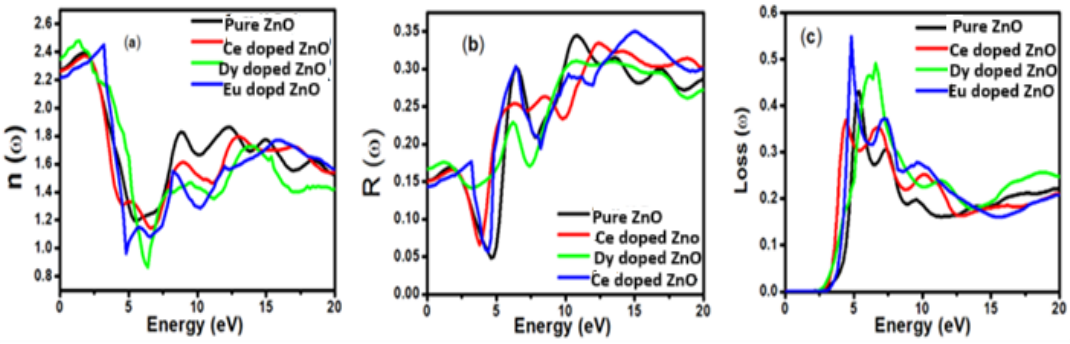

Figure 4.33: The (a) Refractive Index, (b) Reflectivity and (c) Energy Loss as a Function of the Energy in eV for the Pure and RE (Ce, Dy, Eu) Doped W-ZnO

Finally, Figure 4.34(c) presents the energy loss function, which reveals the characteristic plasma resonance peaks that shift according to doping-induced alterations in carrier concentration and electronic structure. Such changes can be leveraged in DSSCs, where optimizing the refractive index, reflectivity, and energy loss peaks can enhance light harvesting and improve charge injection from the dye into the semiconductor. By fine-tuning these optical properties through RE doping, ZnO-based photoanodes may achieve more efficient photon absorption and electron transport, ultimately contributing to higher DSSC performance (Aksoy et al., 2020).

4.7.5 Effects of RE (Ce, Dy, Eu) Concentration

To investigate on this area, Zn atoms in the 108-atoms supercell was substituted with 0, 1, 2 and 3 RE (Ce, Dy, Eu) atoms to generate 0, 1.85, 3.37 and 5.56% dopant concentrations respectively. The results are as shown in Table 4.20. As the dopant concentration of Ce, Dy, or Eu in ZnO increases from 0 to 5.56 mol%, the real part of the dielectric constant at zero frequency ($\varepsilon_1(0)$) rises from around 5.10 to values approaching 5.50–5.55, indicating enhanced polarization. In parallel, the imaginary part's onset (ε_2(onset)) shifts to slightly lower energies. This indicates that, doping introduces new electronic states which modifies existing band edges in ways that alter the material's absorption profile. The refractive index (n) follows a similar upward trend from about 2.30 to as high as 2.43 showing that dopant incorporation systematically changes how light propagates through the lattice. A key observation is the red shift of the absorption critical points from about 3.38 eV (undoped) to the range of 3.18–3.20 eV at higher dopant levels, reflecting a slight narrowing or shifting of the band gap. This change in absorption edge means that the material can absorb photons of lower energy, potentially expanding its usefulness in optoelectronic or

photovoltaic devices.

From Table 4.20, the reflectivity at zero frequency, R (0), increases from 0.15 to as high as 0.18, which implies that dopant atoms modify the free-carrier concentration and surface electronic structure, thereby enhancing reflectance at long wavelengths. From a practical standpoint, these dopant-driven modifications to the dielectric and optical properties can be leveraged in applications such as DSSCs. A lower absorption critical point can capture more photons from the solar spectrum, while a carefully tuned refractive index can improve light coupling into the active layer (Mohammadian-Sarcheshmeh et al., 2020).

Table 4.20: Effects of Dopant Concentration on Optical Properties of RE (Ce, Dy, Eu) Doped W-ZnO

Dopant	**Conc (%)**	$\boldsymbol{\varepsilon_1(0)}$	$\boldsymbol{\varepsilon_2}$ $\boldsymbol{(onset)}$	**Refractive index**	**Absorption critical points**	**R (0)**	**Energy loss peak**
Ce	0	5.10	3.37	2.30	3.38	0.15	16.0
	1.85	5.20	3.28	2.32	3.30	0.158	15.7
	3.37	5.35	3.22	2.36	3.24	0.165	15.5
	5.56	5.50	3.21	2.40	3.20	0.172	15.3
Dy	0	5.10	3.37	2.30	3.38	0.15	16.0
	1.85	5.25	3.27	2.35	3.28	0.16	15.2
	3.37	5.45	3.20	2.38	3.22	0.17	15.1
	5.56	5.55	3.16	2.43	3.18	0.18	14.9
Eu	0	5.10	3.37	2.30	3.38	0.15	16.0
	1.85	5.18	3.25	2.31	3.27	0.152	15.6
	3.37	5.33	3.19	2.35	3.21	0.155	15.2
	5.56	5.47	3.16	2.39	3.17	0.16	15.0

Additionally, adjusting reflectivity can help manage unwanted losses at the device interface. By varying dopant concentration, one can systematically fine-tune ZnO's optical response, thereby optimizing device performance for specific light-harvesting or photoelectronic requirements. Energy loss, typically associated with plasmon resonances at higher energies, shifts when ZnO is doped with rare-earth elements. Increasing dopant concentration often lowers the energy loss peak as shown in Table 4.20, reflecting changes in free-carrier concentration and screening effects within the lattice.

4.7.6 Effects of Oxygen Vacancies

Apart from doping with RE elements, W-ZnO is a wide-band-gap semiconductor whose optical properties can be significantly influenced by the presence of Oxygen vacancies (X. Li et al., 2020). While RE dopants tune the band structure and defect chemistry, oxygen vacancies introduce localized states within the band gap, altering the absorption and emission spectra, Together, these modifications can enhance or suppress particular optical transitions, resulting in notable shifts in photoluminescence, absorption edges, and reflectivity, and making doped W-ZnO with controlled oxygen vacancy concentrations a promising material for optoelectronic applications. To investigate these effects, one Zn atom in the 3x3x3 supercell was replaced with one RE (Ce, Dy, Eu) and simultaneously removing oxygen 0,1,2 and 3 atoms in the structure as shown in Figure 4.11. This creates an oxygen vacancy concentration of 0, 1.85,3.37 and 5.56 % respectively. Optical properties of the modelled compound were then computed and recorded in Table 4.21. At a fixed dopant concentration of 1.85%, varying the oxygen vacancy content in Ce-, Dy-, and Eu-doped W-ZnO shifts each optical parameter between clear minimum and maximum values.

The real part of the dielectric constant ($\varepsilon_1(0)$) reaches its lowest value of 5.18 for Eu doping with no vacancies and its highest of 5.50 for Dy doping at 5.56% vacancies, reflecting how defect states enhance lattice polarization. The imaginary dielectric onset is largest (3.28 eV) when Ce doping has no vacancies and smallest (3.16 eV) for Dy and Eu at 5.56%, suggesting that additional vacancy levels shift absorption to lower energies. The refractive index (n) spans from a low of 2.31 (Eu, 0% vacancies) to a high of 2.45 (Dy, 5.56%), while the absorption critical points drop from about 3.30 eV (Ce, 0%) down to around 3.17 eV (Eu, 5.56%), indicating a subtle narrowing or shifting of the band gap. Reflectivity at zero frequency (R(0)) rises from 0.152 (Eu, 0%) to 0.175 (Dy, 5.56%), highlighting an increase in light reflected at low energies, whereas the energy loss peak decreases from a maximum of 15.7 eV (Ce, 0%) to around 14.6–15.0 eV at high vacancy concentrations, pointing to altered plasmon-like excitations. These trends are significant for DSSC applications because a lower absorption edge and carefully balanced reflectivity can boost photon harvesting, while changes in dielectric properties and energy loss peaks can affect charge-carrier generation and transport, ultimately influencing the cell's overall efficiency (Dutta et

al., 2021).

Table 4.21: Optical Properties of RE-Doped W-ZnO with Oxygen Vacancies

Dopant	Oxygen vacancy Concentration	$\varepsilon_1(0)$	ε_2 $(onset)$	Refractive index	Absorption critical points	R (0)	Energy loss peak
Ce	0	5.20	3.28	2.32	3.30	0.158	15.7
	1.85	5.25	3.24	2.24	3.28	0.160	15.6
	3.37	5.30	3.20	2.36	3.25	0.163	15.4
	5.56	5.35	3.18	2.37	3.22	0.165	15.3
Dy	0	5.25	3.27	2.35	3.28	0.16	15.2
	1.85	5.30	3.23	2.37	3.26	0.163	15.0
	3.37	5.40	3.19	2.40	3.22	0.168	14.8
	5.56	5.50	3.16	2.45	3.20	0.175	14.6
Eu	0	5.18	3.25	2.31	3.27	0.152	15.6
	1.85	5.23	3.22	2.33	3.25	0.155	15.4
	3.37	5.30	3.19	2.35	3.22	0.158	15.2
	5.56	5.40	3.17	2.38	3.19	0.162	15.0

4.8 Transport Properties of ZnO

4.8.1 Electrical conductivity and seebeck coefficients

The transport properties of a compound are a critical factor to consider in the choice of a good DSSC photoanode material. Compared with other metal oxide semiconductors used in DSSC, ZnO has an enhanced electrical conductivity and reduced resistivity (Khuili et al., 2020). In this study, the electrical conductivity of different phases of ZnO as a function of hole concentration is computed and compared. To validate these results, the seebeck coefficients are also reported so as to prove the inverse correlation of electrical conductivity coefficients and Seebeck coefficients (Ahmed et al., 2023). The semi-classical Boltzmann transport equations with constant relaxation time approximation were solved to achieve these transport coefficients as executed in the BoltzTraP code. The investigation was performed at four specific temperatures, that is, at 200K, 400K, 600K and 800K to Investigate the influence of temperature on the transport characteristics of ZnO.

4.8.2 Effects of Structural Configuration

Structural configuration plays a crucial role in determining the transport properties of ZnO. In this study, three distinct phases (cubic, wurtzite, and monolayer) were investigated to elucidate how differences in atomic arrangement impact electrical conductivity, the Seebeck coefficient, and overall thermoelectric performance. The cubic phase, characterized by its high symmetry, generally exhibits isotropic transport properties, resulting in relatively uniform effective masses and carrier mobilities across all crystallographic directions. In contrast, the wurtzite structure, which is the thermodynamically stable phase under ambient conditions, displays significant anisotropy due to its hexagonal symmetry and polar nature. This anisotropy leads to direction-dependent variations in effective mass and carrier mobility (Nakano & Tajima, 2025), factors that can be exploited to enhance thermoelectric performance under specific orientations.

The seebeck coefficients and electrical conductivity coefficients of the n-type phases of ZnO computed in this study are presented in Figures 4.35 and 4.36 respectively, with the calculated values in Table 4.22. It is notable from Figure 4.35 that the Seebeck coefficient increased with temperature, peaking at 251.5, 322.5, and 239.5 μV/K at 800 K for C-ZnO, W-ZnO, and M-ZnO, respectively, as detailed in Table 4.22. Among the three phases tested, W-ZnO exhibited the highest Seebeck coefficient of 322.5 μV/K at 800 K, identifying it as the most promising thermoelectric structure. Previous studies indicated that materials with Seebeck coefficients exceeding 200 μV/K are considered strong candidates for thermoelectric applications (Zhang et al., 2021). The fact that all measured Seebeck values in this study surpass this threshold further confirms ZnO's potential as an effective thermoelectric compound. Moreover, the observed increase in the Seebeck coefficient with temperature suggests enhanced thermal activation of charge carriers, particularly in the W-ZnO phase, where its unique crystalline structure appears to facilitate better thermoelectric performance.

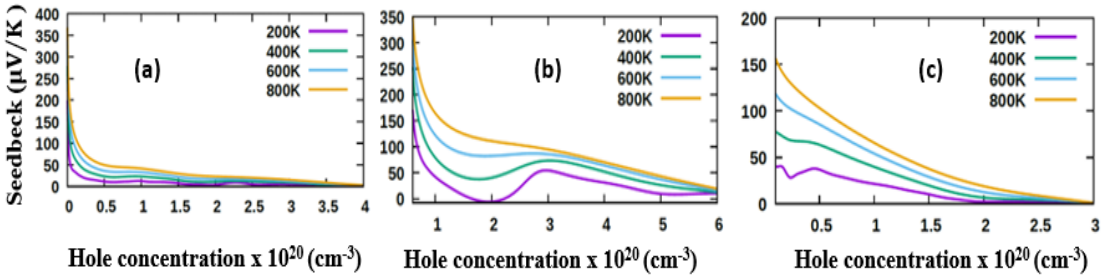

Figure 4.34: Seebeck Coefficient of (a) C-ZnO, (b) W-ZnO and (c) M-ZnO Phases as a Function of Holes Concentration

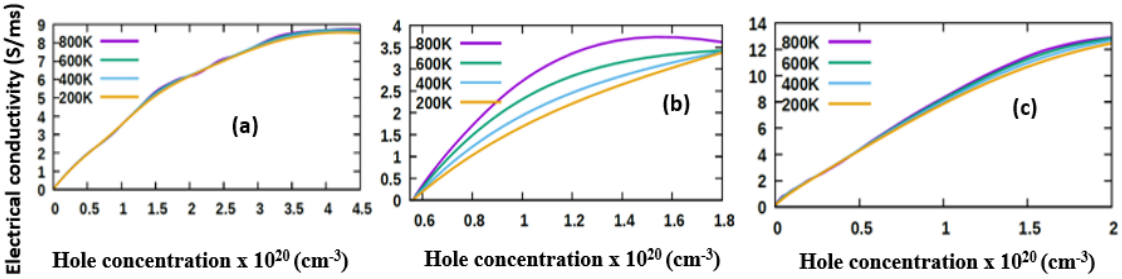

Figure 4.35: Electrical Conductivity of (a) C-ZnO, (b) W-ZnO and (c) M-ZnO Phases as a Function of Hole Concentration

From Figure 4.36, the electrical conductivity of ZnO increases with temperature, which is primarily due to the enhanced thermal activation of charge carriers. As the temperature rises, more holes are generated by overcoming the energy barrier in the semiconductor's band structure, thereby increasing the carrier concentration. Although increased temperature can also lead to enhanced phonon scattering that might reduce carrier mobility, the exponential increase in the number of thermally activated carriers dominates, resulting in a net increase in conductivity.

At 800 K (Table 4.22), all the three ZnO phases exhibit high electrical conductivity with W-ZnO) reaching 13.8 S/m and C-ZnO the lowest at 9.2 S/m. This behavior confirms the inverse relationship between the Seebeck coefficient and electrical conductivity, as higher conductivity is often accompanied by a lower Seebeck coefficient due to the balancing effects of carrier concentration and energy filtering. When applied in DSSC, the high conductivity of W-ZnO is particularly beneficial as it can suppress electron-hole recombination, thereby enhancing solar cell performance.

Table 4.22: Transport coefficients of ZnO at different temperatures

Thermoelectric coefficient	Temperature	C-ZnO	W-ZnO	M-ZnO
S (μV/K)	200K	130.2	156.5	98.5
	400K	156.4	202.9	135.6
	600K	209.1	253.6	197.8
	800K	251.5	322.5	239.5
σ (S/ms)	200K	8.5	12.7	12.2
	400K	8.7	13.1	12.8
	600K	9.0	13.5	13.5
	800K	9.2	13.8	12.2

4.8.3 Transport Properties of RE (Ce, Dy, Eu) Doped ZnO

When doped with RE (Ce, Dy, Eu), the band structure and scattering mechanisms of ZnO are significantly modified, thereby altering carrier concentration and mobility. These changes can improve the electrical conductivity, making RE-doped ZnO an attractive material for applications requiring precise control over transport properties. To affirm the validity of these results, the Seebeck coefficients are also reported, illustrating the inverse correlation between the electrical conductivity coefficients and the Seebeck coefficients. To derive these transport coefficients, the semi-classical Boltzmann transport equations were addressed under the constant relaxation time approximation, utilizing the BoltzTraP code for execution.

Figure 4.37 (a) shows the computed electrical conductivity in relation to changes in temperature. The figure demonstrates that there is a direct correlation between the electrical conductivity of ZnO and temperature across all compounds that were tested. This is attributed to the enhanced concentration of charge carriers in the conduction band that accompanies a rise in temperature. In terms of conductivity, the Ce doped W-ZnO outperformed all other materials evaluated as depicted in Table 4.23. Utilizing this high conductivity within DSSC is projected to diminish the electron-hole recombination, consequently enhancing the PCE of the solar cell. It is notable from Figure 4.37(b) that the seebeck coefficient also increased with temperature. This can be attributed to enhanced scattering effects and more pronounced energy filtering. The seebeck coefficient observed in this study attained peak values at 518, 568.7, 589 and 584 μV/K at 800 K for pure W-ZnO and RE (Ce, Dy, Eu) doped W-ZnO respectively as shown in Table 4.23.

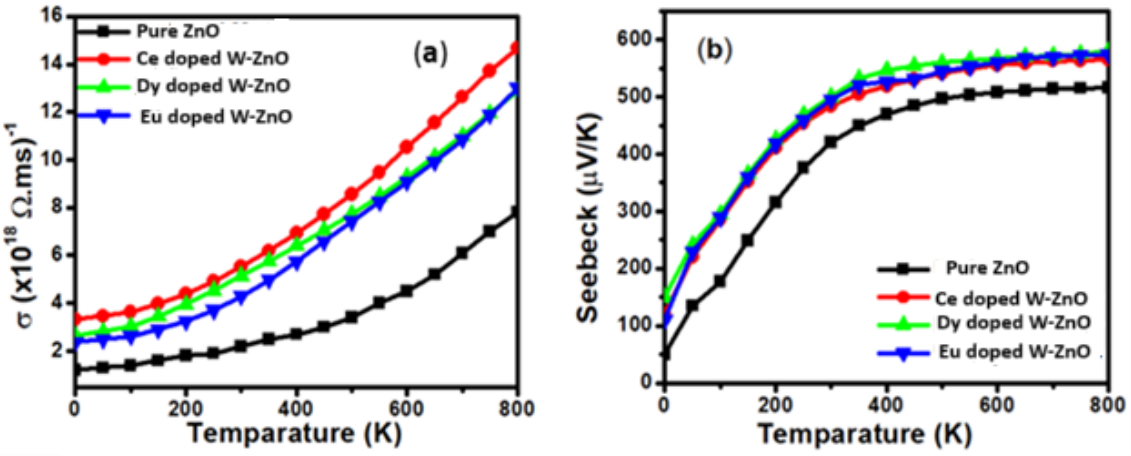

Figure 4.36: The (a) Electrical Conductivity and (b) Seebeck Coefficient of Undoped and RE (Ce, Dy and Eu) Doped W-ZnO

Table 4.23: Transport Coefficients of ZnO at Different Temperatures

Thermoelectric Coefficients	Temperature	Undoped -ZnO	Ce-ZnO	Dy-ZnO	Eu-ZnO
S (μV/K)	200K	315.4	411.6	426	418
	400K	470	518.8	547	527
	600K	508.6	554.4	567	560
	800K	518	568.7	589	584
σ (x 10^{18} S/ms)	200K	1.8	4.4	4.0	3.3
	400K	2.7	6.93	6.39	5.75
	600K	4.5	10.54	9.3	9.07
	800K	7.8	14.7	12.9	13.01

Among the materials tested, Dy doped M-ZnO had the highest seebeck coefficient of 589 μV/K at 800K depicting it as the best thermoelectric structure. Based on reports from previous studies, materials with seebeck coefficient above 200 μV/K are considered good thermoelectric compounds. The seebeck coefficient values obtained in this study were higher than 200 μV/K ascertaining pure and RE (Ce, Dy, Eu) doped M-ZnO as viable thermoelectric compound especially at elevated temperatures. RE-doped W-ZnO show modified electrical conductivity and an enhanced Seebeck coefficient. The introduction of RE ions introduce localized states that facilitate charge carrier movement, improving thermoelectric efficiency. RE doping also improve carrier concentration, consequently reducing the resistivity of W-ZnO, particularly in n-type configurations.

4.8.4 Effects of Dopant Concentration

The doping levels were varied by substituting Zn sites with RE ions at concentrations of 0, 1.85, 3.37, and 5.56%. All properties were evaluated at an elevated temperature (800 K) and fixed carrier concentration (10^{20} cm^{-3}) to simulate conditions relevant for DSSC operation. The results as indicated in Table 4.24 indicate that electrical conductivity increases with doping concentration from 0% to 3.37% for all RE dopants. This increase is attributed to the enhanced thermal activation of carriers; as more RE ions are introduced into the ZnO lattice, additional donor states are generated (often via oxygen vacancies), thereby increasing the carrier concentration. For instance, Ce-doped ZnO exhibits a maximum conductivity of 12.5 S/m at 3.37% doping. However, at 5.56% concentration, a slight decrease in conductivity is observed. This decline is likely due to the onset of significant impurity scattering and defect-induced carrier localization, which counteracts the benefits of increased carrier density. For DSSCs, high electrical conductivity is critical for suppressing electron-hole recombination and ensuring efficient charge collection at the electrodes. Among the three dopants investigated, the trend across all cases indicates that an optimal doping concentration exists (around 3.37%) where the balance between increased carrier density and minimal scattering yields superior transport properties.

While all RE dopants show improved performance compared to undoped ZnO, the specific choice of dopant (Ce, Dy, or Eu) can be further optimized based on the desired balance between conductivity and the Seebeck coefficient. The Seebeck coefficient generally shows an increasing trend with dopant concentration up to 3.37%, indicating that the energy filtering effect is improved as the density of states near the Fermi level becomes more favorable. A higher Seebeck coefficient is beneficial for thermoelectric performance and, in the context of DSSC, can aid in maintaining efficient charge separation. Beyond the optimal doping level, a marginal decline in the Seebeck coefficient is observed (e.g., from 280 to 275 μV/K in Ce-doped ZnO), which again suggests that excessive doping may introduce additional scattering centers that detrimentally affect the energy distribution of the charge carriers.

Table 4.24: Effects of Doping Concentration (%) on the Transport Properties of ZnO

Conc (%)	Ce		Dy		Eu	
	Conductivity σ (x10^{18}S/ms)	Seebeck (μV/K)	Conductivity σ (x10^{18} S/ms)	Seebeck (μV/K)	Conductivity σ (x10^{18}S/ms)	Seebeck (μV/K)
0	4.5	322.5	4.5	322.5	4.5	322.5
1.85	14.7	565.7	12.9	580	13.01	574
3.37	16.4	598	14.8	588	15.1	579
5.56	15.9	599	14.7	587	14.9	578

4.8.5 Effect of Oxygen Vacancies Concentration

Increasing oxygen vacancy concentration from 0 to 5.56% consistently raises both the electrical conductivity and carrier concentration for all three RE (Ce, Dy, Eu) in ZnO, which is a direct result of adding extra free electrons into the conduction band. Oxygen vacancies act as shallow donors, so when more vacancies are introduced, the Fermi level shifts deeper into the conduction band, thereby boosting conductivity (Saxena et al., 2022). Ce-doped ZnO reaches the highest conductivity (16.4×10^{18} S/ms at 5.56% vacancies) and also the highest carrier concentration (4.2×10^{20} cm^{-3}), suggesting that Ce doping plus oxygen vacancies provides a particularly effective means of increasing electron density. Conversely, Dy-doped ZnO starts out with the lowest conductivity (12.9×10^{18} S/ms at 0% vacancies) and has the smallest initial carrier concentration (1.0×10^{20} cm^{-3}), but still follows the same upward trend as vacancy levels grow. Alongside these conductivity gains, the Seebeck coefficient decreases for each dopant as the vacancy content increases as shown in Table 4.25.

Table 4.25: Transport Properties of RE (Ce, Dy, Eu)-Doped ZnO at Different Oxygen Vacancy Concentration

Dopant	Oxygen vacancy concentration (%)	Conductivity σ (x10^{18}S/ms)	Carrier concentration (10^{20}) cm^{-3}	Seebeck (µV/K)
Ce	0	14.7	1.2	565.7
	1.85	15.3	1.8	546.7
	3.37	15.9	3.0	531.2
	5.56	16.4	4.2	498.5
Dy	0	12.9	1.0	580
	1.85	13.25	1.6	571.3
	3.37	14.18	2.7	567.8
	5.56	14.68	3.9	560.2
Eu	0	13.01	1.3	574
	1.85	13.97	2.1	569.7
	3.37	14.29	2.9	550.2
	5.56	15.35	3.8	543.5

This drop occurs because higher electron concentrations push the Fermi level further above the conduction band edge, reducing the difference in energy between occupied and unoccupied states, an effect that directly lowers thermopower (Leiter et al., 2022). Dy-doped ZnO exhibits the highest initial Seebeck coefficient of 580 µV/K, indicating a relatively large voltage generation per temperature gradient at low vacancy concentration, whereas Ce-doped ZnO falls to the lowest Seebeck value of about 498.5 µV/K at 5.56% vacancies. This trade-off between enhanced electrical conductivity and reduced Seebeck coefficient is a hallmark of doping and lattice engineering in semiconductors, highlighting the need to balance electron density (for conductivity) against maintaining an optimal energy distribution of carriers (for thermopower).A favorable Seebeck coefficient indicates efficient separation and diffusion of charge carriers, which can complement light-to-electricity conversion by providing an additional driving force for electron flow (Hébert et al., 2007). In advanced or hybrid solar cells, understanding and optimizing the Seebeck effect can help improve internal electric fields and charge dynamics, especially under temperature gradients (Pingak et al., 2023). Together, these transport properties help assess the photoanode's ability to facilitate efficient charge collection and energy conversion, which are crucial for high DSSC performance.

4.9 Summary

The study investigated the effects of rare earth (RE) doping (Ce, Dy, Eu) on the structural, mechanical, lattice dynamical, electronic, optical, and transport properties of ZnO using Density Functional Theory (DFT), with an aim to improve its suitability for dye-sensitized solar cell (DSSC) applications. Structural analysis revealed that doping with RE elements introduced lattice distortions, manifested by slight increases in lattice constants and cell volume, especially for larger ionic radii dopants like Ce. Bond lengths between Zn–O and RE–O were found to vary with dopant type and concentration, indicating localized strain and possible defect formation

Mechanical property calculations showed that all doped ZnO systems remained mechanically stable as they satisfied Born's mechanical stability criteria. The elastic constants (C_{11}, C_{12}, C_{44}, etc.) were modified upon doping, with Dy-doped ZnO demonstrating increased stiffness, implying better mechanical robustness. The anisotropy indices indicated directional dependence of mechanical behavior, which could influence charge transport under mechanical strain in DSSC architectures. Lattice dynamics studies further revealed the presence of phonon softening in doped systems, with no imaginary frequencies, confirming dynamic stability. This suggests that the materials can withstand vibrational perturbations and retain structural integrity under operational conditions.

Electronic and optical analyses showed that RE doping effectively tailored the band structure of ZnO, leading to bandgap narrowing and the introduction of intermediate states within the bandgap. These features enhance visible light absorption and facilitate charge separation, critical for solar harvesting. Optical properties such as the dielectric function, absorption coefficient, and reflectivity improved with RE doping—especially in the visible range—indicating stronger light-matter interaction. Additionally, transport properties such as Seebeck coefficient and electrical conductivity were significantly enhanced in doped systems, particularly for Dy- and Eu-doped ZnO, suggesting better carrier mobility and energy conversion potential. Collectively, the results support RE-doped ZnO, particularly Eu- and Dy-doped forms, as promising photoanode materials for DSSC applications.

CHAPTER FIVE
CONCLUSION AND RECOMMENDATIONS

5.1 Conclusion

This work has comprehensively examined how RE (Ce, Dy, Eu) doping modifies the structural, mechanical, dynamical, electronic, optical, and transport properties of ZnO, with particular attention to different crystal configurations, namely cubic (C-ZnO), wurtzite (W-ZnO), and monolayer (M-ZnO). Across these phases, the fundamental stability of doped ZnO was confirmed by total energy calculations and phonon dispersion analyses, which showed no imaginary frequencies that would indicate structural or dynamical instabilities. Notably, the inclusion of Hubbard U corrections (GGA+U) proved essential for accurately capturing the electronic structure, especially the band gap and localized f-electron states introduced by lanthanide dopants. While the structural configuration study involved all three polymorphs (cubic, wurtzite, monolayer), the systematic variation of dopant concentration (0 to 5.56 mol%) and oxygen vacancy concentration (0 to 5.56%) was performed only in the wurtzite phase, which is the most experimentally prevalent and technologically relevant form of ZnO.

The DFT-based investigation into the structural properties of lanthanide-doped Wurtzite-ZnO revealed that doping with Ce, Dy, and Eu induces notable changes in the lattice parameters, bond lengths, and unit cell volumes, demonstrating clear structural distortions that influence material functionality in DSSC photoanode applications. For instance, Ce doping at 1.85% increased the lattice constants to a = 3.294 Å, c = 5.289 Å, and volume to 49.68 Å^3, compared to the pristine ZnO values of a = 3.289 Å, c = 5.284 Å, and 49.50 Å^3. A similar trend was observed for Dy- and Eu-doped ZnO at the same concentration, with volumes of 49.59 Å^3 and 49.60 Å^3 respectively. Moreover, increasing dopant concentrations up to 5.56% resulted in further expansion, with Ce-doped ZnO reaching a volume of 52.00 Å^3 and a longer Ce–O bond length of 2.165 Å, compared to the original Zn–O bond length of 1.998 Å. This volumetric expansion is attributed to the larger ionic radii of RE^{3+} ions substituting Zn^{2+} and is further enhanced by the presence of oxygen vacancies, which also cause systematic increases in bond lengths (e.g., Zn–O reaching 2.167 Å at 5.56% O-vacancy). These structural modifications are essential as they alter electronic and optical behavior, which in turn affects light absorption, charge transport, and

recombination dynamics which are key parameters for improving DSSC photoanode efficiency.

The lattice dynamical analysis of ZnO in cubic, wurtzite, and monolayer phases confirmed their structural and dynamical stability, as evidenced by the absence of imaginary frequencies in the phonon dispersion curves. The wurtzite phase exhibited characteristic LO–TO splitting at the Γ point and linear acoustic branches, affirming its mechanical robustness. Upon doping W-ZnO with RE elements (Ce, Dy, and Eu), significant redshifts in the optical phonon modes were observed particularly the LO mode. It decreased from 580 cm^{-1} in pristine ZnO to 570 cm^{-1}, 568 cm^{-1}, and 565 cm^{-1} in Ce-, Dy-, and Eu-doped ZnO, respectively, attributed to the mass effect and induced lattice distortions. The phonon density of states (PDOS) revealed broadening and redistribution in the high-frequency O-dominated region, alongside the emergence of localized vibrational modes due to RE dopants. These changes reflect increased lattice disorder and anharmonicity, which may influence thermal conductivity and electron phonon interactions which are key parameters in optoelectronic and energy device applications.

The elastic properties of W-ZnO and its RE-doped derivatives confirm the mechanical stability and enhanced rigidity induced by doping. The undoped W-ZnO phase, as computed in this work, yielded elastic constants (C_{11} = 195.4 GPa, C_{12} = 104.3 GPa, C_{13} = 110.2 GPa, C_{33} = 190 GPa, C_{44} = 36.4 GPa). Upon doping with Ce, Dy, and Eu, notable increases in elastic constants were observed, particularly C_{44} and C_{66}, suggesting improved resistance to shear deformation. The bulk modulus increased from 136.7 GPa (undoped) to 155.2 GPa (Ce), 157.3 GPa (Dy), and 153.6 GPa (Eu), indicating enhanced incompressibility, in line with experimental trends. Similarly, the Young's modulus showed a significant improvement, rising from 115.0 GPa to 215.6 GPa (Ce), 217.2 GPa (Dy), and 212.0 GPa (Eu), reflecting increased stiffness. Anisotropy indices such as A_Z and A^U remained within acceptable ranges, showing slightly higher isotropy in RE-doped systems. Overall, RE doping improves the elastic performance of W-ZnO, supporting its suitability for high-stress optoelectronic applications.

The study focused on RE doping of W-ZnO and used C-ZnO, W-ZnO, and M-ZnO to

benchmark electronic properties under GGA and GGA+U. The undoped band gaps of C-ZnO, W-ZnO, and M-ZnO were 0.63 eV, 0.76 eV, and 1.31 eV under GGA, and increased to 3.01 eV, 3.19 eV, and 3.38 eV under GGA+U, respectively. These values were in close agreement with previous DFT results and experimental values, particularly for W-ZnO, which had an experimental band gap of 3.37 eV (Dhamodharan et al., 2017). Doping W-ZnO with Ce, Dy, and Eu led to a slight reduction in GGA-calculated band gaps with increasing dopant concentration, from 0.74 eV to 0.68 eV (Ce), 0.73 eV to 0.67 eV (Dy), and 0.75 eV to 0.69 eV (Eu). However, GGA+U values remained relatively stable, ranging from 3.19 eV to 3.10 eV (Ce), 3.19 eV to 3.09 eV (Dy), and 3.19 eV to 3.07 eV (Eu), and were in strong agreement with experimental data. These findings confirm that RE doping fine-tunes the band gap of W-ZnO, and GGA+U provides more accurate predictions for its electronic properties relevant to DSSC applications.

The optical analysis confirms that RE doping enhances the dielectric and refractive behavior of W-ZnO, with slight modifications across increasing dopant concentrations. For the undoped W-ZnO, $\varepsilon_1(0) = 4.5$ and $n(0) = 2.12$, which are comparable to values in literature. Upon doping with Ce, Dy, and Eu, $\varepsilon_1(0)$ increased gradually, reaching 5.50 (Dy) at 5.56%, while the refractive index rose to 2.43 (Dy), indicating increased polarization and optical density. The absorption edge also shifted slightly to lower energies, with absorption critical points decreasing from 3.38 eV (undoped) to 3.17–3.20 eV across dopants, which implies enhanced light absorption in the visible range advantageous for DSSC applications. The reflectivity at 0 eV (R_0) also increased with doping, reaching 0.18 (Dy), consistent with enhanced optical interaction. Moreover, the energy loss function peaks showed a downward trend from 16.0 eV (undoped) to 14.9 eV (Dy), implying reduced inelastic energy loss and improved transparency. These trends were also observed in the presence of oxygen vacancies, suggesting their reinforcing effect on optical responses. Overall, RE doping improves the optical functionality of W-ZnO by increasing dielectric response, refractive index, and visible-light absorption which are key attributes for photoanode performance.

The transport properties analysis reveals that W-ZnO exhibits superior performance compared to C-ZnO and M-ZnO across all temperatures, as evidenced by its higher Seebeck coefficient (S) and electrical conductivity (σ). At 800 K, W-ZnO recorded the highest S of 322.5 μV/K and σ of 13.8 S/ms, attributed to its lower intrinsic hole concentration (1.8×10^{20} cm^{-3}), which enhances thermopower. Upon doping W-ZnO with Ce, Dy, and Eu, transport properties significantly improved. Dy-doped W-ZnO showed the highest S of 589 μV/K at 800 K and σ of 14.7×10^{18} S/ms, with Ce and Eu-doped ZnO closely following. Increasing dopant concentration led to a gradual rise in σ, driven by enhanced carrier density, while S slightly decreased due to the inverse relationship with carrier concentration. For instance, Ce doping at 5.56% yielded $\sigma = 16.4 \times 10^{18}$ S/ms and S = 599 μV/K, outperforming the undoped sample. Oxygen vacancy analysis further affirmed that vacancies boost both carrier concentration and σ, though at the cost of reduced S. Overall, RE doping significantly enhances the thermoelectric efficiency of W-ZnO by optimizing the power factor ($S^2\sigma$), positioning it as a promising material for energy harvesting in thermoelectric applications.

5.2 Recommendations

5.2.1 Recommendations for Policy

Based on the findings of this study, it is recommended that RE doping, particularly with Dy and Ce, be considered a viable strategy for enhancing the performance of W-ZnO for optoelectronic and thermoelectric applications. The study established that RE dopants improve structural stability, elastic strength, and anisotropy tolerance, with Dy-doped W-ZnO exhibiting the highest mechanical and thermoelectric performance. These improvements are attributed to the optimal ionic radius and valence state compatibility of the dopants, which enhance lattice rigidity and carrier transport properties without significantly distorting the ZnO lattice. Therefore, material engineers and device developers are encouraged to adopt Dy and Ce doping in ZnO synthesis to achieve materials with improved functional performance.

Additionally, the optical and electronic property enhancements observed in RE-doped W-ZnO including increased dielectric constants, refractive indices, and tailored band gaps which support its application in photoanodes for DSSCs. The increase in absorption at critical energies and the improved thermoelectric response at elevated temperatures suggest potential for integration in solar energy conversion and waste

heat recovery technologies. Stakeholders in renewable energy and semiconductor device fabrication should prioritize RE-doped W-ZnO as a base material in their development pipelines to exploit its enhanced multifunctional characteristics, which combine mechanical durability, electronic tunability, and energy efficiency.

Among the three studied ZnO phases, W-ZnO consistently outperformed C-ZnO and M-ZnO across most parameters, including mechanical strength, optical absorption, dielectric properties, and thermoelectric efficiency. Its intrinsic hexagonal structure offers a stable and anisotropic framework that responds effectively to RE doping, especially with Dy. Therefore, W-ZnO doped with 3.37% Dy at a moderate oxygen vacancy level is recommended as the most promising configuration for advanced optoelectronic and thermoelectric applications. Researchers and engineers working on ZnO-based devices should prioritize this configuration to achieve optimized performance in real-world applications.

5.2.2 Recommendations for Future Studies

Future work should extend the investigation of rare-earth doping in ZnO beyond the concentrations and specific lanthanides examined here. It would be valuable to explore other dopant species or co-doping strategies (e.g., combining Ce with transition metals) to see if synergistic effects could further enhance mechanical rigidity, electronic conductivity, or optical absorption. Additionally, advanced computational methods such as hybrid functionals or more refined many-body approaches (e.g GW) could be employed to capture subtle electronic and excitonic effects, especially in monolayer and low-dimensional ZnO. Experimental validation of these predictions particularly regarding mechanical stability and carrier transport would also strengthen the link between theoretical insights and practical device fabrication.

Another avenue of research involves optimizing oxygen vacancy engineering by precisely controlling oxygen vacancy concentrations during synthesis, whether through advanced thin-film deposition techniques, ion implantation, or post-growth annealing under carefully tuned atmospheres. Detailed characterization using methods such as X-ray photoelectron spectroscopy (XPS), photoluminescence (PL), and electron paramagnetic resonance (EPR) would help correlate vacancy concentrations with changes in electronic and optical properties. Ultimately, integrating doped ZnO

films into prototype devices such as DSSC or UV photodetectors would offer direct evidence of performance gains, paving the way for large-scale implementation of RE-doped ZnO in next-generation optoelectronic and energy-harvesting technologies.

REFERENCES

Achehboune, M., Khenfouch, M., Boukhoubza, I., Derkaoui, I., Mothudi, B., Zorkani, I., & Jorio, A. (2022). Optimization of the luminescence and structural properties of Er and Dy-doped ZnO nanostructures: Effect of dopant concentration and excitation wavelength. *Journal of Luminescence, 246*, 118843.

Adunka, R., & Orna, M. (2018). Discoveries among the rare earths. In *Discovery and Classification in Chemistry: Philosophical and Educational Perspectives* (pp. 17–34). American Chemical Society.

Agapito, L., Curtarolo, S., & Nardelli, M. (2015). Reformulation of DFT+U as a pseudohybrid Hubbard density functional for accelerated materials discovery. *Physical Review X, 5*(1), 011006.

Agarwal, S., Jangir, L., Kumar, M., Lokesh, J., Jangir, K., Rathore, K., Kumar, M., & Awasthi, K. (2022). Morphology-dependent structural and optical properties of ZnO nanostructures. *Applied Physics A, 125*(8), 553.

Ahmed, H., Abdulwahab, A., El-Feky, M., & Radwan, N. (2023). Impact of Nd doping on electronic, optical, and magnetic properties of ZnO: A GGA+U study. *Molecules, 28*(21), 7416.

Ahmed, M., Zayed, M., & Ali, H. (2021). Structural and transport properties of Nd and Gd-doped ZnO nanomaterials. *Materials Chemistry and Physics, 260*, 124100.

Aksoy, S., Gorgun, K., Caglar, Y., & Caglar, M. (2019). Effect of loading and standby time of the organic dye N719 on the photovoltaic performance of ZnO based DSSC. *Journal of Molecular Structure, 1189*, 181–186.

Aksoy, S., Polat, O., Gorgun, K., Caglar, Y., & Caglar, M. (2020). Li-doped ZnO based DSSC: Characterization and preparation of nanopowders and electrical performance of its DSSC. *Physica E: Low-Dimensional Systems and Nanostructures, 121*, 114127.

Al Boukhari, J., Khalaf, A., & Awad, R. (2020). Structural analysis and dielectric investigations of pure and rare earth elements (Y and Gd) doped NiO nanoparticles. *Journal of Alloys and Compounds, 820*, 153100.

Al-Alwani, M., Mohamad, A., Ludin, N., Kadhum, A., & Sopian, K. (2016). Dye-sensitised solar cells: Development, structure, operation principles, electron kinetics, characterisation, synthesis materials and natural photosensitisers. *Renewable and Sustainable Energy Reviews, 65*, 183–213.

Alhorani, S., Kumar, S., Genwa, M., & Meena, P. (2022). Performance of dye sensitized solar cells extracted dye from wood apple leaves. *Journal of Physics: Communications, 6*, 085012.

Ali, A., Farid, T., Rafiq, M., Zhou, B., & Tang, W. (2022). Evaluating the impact of Hartree–Fock exact exchange on the performance of global hybrid functionals for vertical excited-state energies. *Physical Chemistry Chemical Physics, 24*(35), 20858–20869.

Ali, S., Khan, M., & Ullah, R. (2021). Enhanced transport and optical behavior of RE-doped ZnO thin films for energy applications. Journal of Materials Science: Materials in Electronics, 32(7), 8991–9003.

Allan, L., Mulwa, W., Mwabora, J., Musembi, R., & Mapasha, R. (2023). An ab-initio study of P-type ZrCoY (YSb and Bi) half–Heusler semiconductors. *Heliyon, 9*(8).

Amir Al Zumahi, S., Arobi, N., Rahman, M., Hossain, K., Rozy, M., Bashar, M., Amri, A., Kabir, H., Hossain, M., & Ahmed, F. (2021). Understanding the optical behaviours and power conversion efficiency of novel organic dye and nanostructured TiO_2 based integrated DSSCs. *Solar Energy, 225*, 129–147.

Anitha, A., & Dotter, M. (2023). A review on liquid electrolyte stability issues for commercialization of dye-sensitized solar cells (DSSC). *Energies, 16*(13), 5129.

Anoriyo, K., Ezekoye, B., Ugwuoke, P., Offiah, S., Ezema, F., & Akor, S. (2023). A review of advances on natural dye sensitized solar cells (NDSSCs). *Journal of Engineering Research and Reports, 25*(10), 153–166.

Arbosara, F., Shirini, F., Abedini, M., & Moafi, H. (2015). Introduction of a new high yielding method for the synthesis of 1,8-dioxo-octahydroxanthenes using W-doped ZnO nanocomposite. *Journal of Nanostructure in Chemistry, 5*(1), 55–63.

Assaad, F., Bercx, M., Goth, F., Götz, A., Hofmann, J., Huffman, E., Liu, Z., Parisen Toldin, F., Portela, J., & Schwab, J. (2020). The ALF (Algorithms for Lattice

Fermions) project release 2.4: Documentation for the auxiliary field quantum Monte Carlo code. *arXiv*.

Bai, S., Amirruddin, A., Pandey, A., Samykano, M., Ahmad, M., Sharma, K., & Tyagi, V. (2021). Advancements in the development of various types of dye-sensitized solar cells: A comparative review. *Energy Engineering, 118*(4), 737–759.

Bailie, C., Christoforo, M., Mailoa, J., Bowring, A., Unger, E., Nguyen, W., Burschka, J., Pellet, N., Lee, J., Grätzel, M., Noufi, R., Buonassisi, T., Salleo, A., & McGehee, M. (2015). Semi-transparent perovskite solar cells for tandems with silicon and CIGS. *Energy & Environmental Science, 8*(3), 956–963.

Bartkowiak, A., Korolevych, O., Chiarello, G., Makowska-Janusik, M., & Zalas, M. (2022). Experimental and theoretical insight into DSSCs mechanism influenced by different doping metal ions. *Applied Surface Science, 597*.

Batmunkh, M., Dadkhah, M., Shearer, C., Biggs, M., & Shapter, J. (2016). Tin oxide light-scattering layer for titania photoanodes in dye-sensitized solar cells. *Energy Technology, 4*(8), 959–966.

Baviskar, P., & Sankapal, B. (2021). Morphology-driven design of ZnO nanostructures for efficient dye-sensitized solar cells. *Solar Energy Materials and Solar Cells, 243*, 111811.

Benaissa Cherif, Y., Rouaighia, M., Zaoui, A., & Boukortt, A. (2017). Optoelectronic, elastic and thermal properties of cubic perovskite-type $SrThO_3$. *Acta Physica Polonica A, 131*(3), 406–413.

Bett, K., & Kiprotich, S. (2024). Effects of stirring speed of precursor solution on the structural, optical and morphological properties of ZnO:Al:Ga co-doped nanoparticles synthesized via a facile sol-gel technique. *American Journal of Condensed Matter Physics, 2024*(1), 9–20.

Biswas, R., & Chatterjee, S. (2022). Effect of chenodeoxycholic acid as dye co-adsorbent and ZnO blocking layer in improving the performance of Rose Bengal dye based dye sensitized solar cells. *Optical and Quantum Electronics*, *54*(6).

Bogojeski, M., Vogt-Maranto, L., Tuckerman, M., Müller, K., & Burke, K. (2020). Quantum chemical accuracy from density functional approximations via machine

learning. *Nature Communications, 11*(1), 5223.

Bouhmaidi, S., Marjaoui, A., Talbi, A., Zanouni, M., Nouneh, K., & Setti, L. (2022). A DFT study of electronic, optical and thermoelectric properties of Ge-halide perovskites $CsGeX_3$ (X = F, Cl and Br). *Computational Condensed Matter, 31*.

Brox-Nilsen, C., Jin, J., Luo, Y., & others. (2023). Sputtered ZnO thin-film transistors with carrier mobility over 50. *IEEE Transactions*. Retrieved March 1, 2025, from ieeexplore.ieee.org

Butler, L. (1998). Chemical reaction dynamics beyond the Born-Oppenheimer approximation. *Annual Review of Physical Chemistry, 49*(1), 125–171.

Cangi, A., Dornheim, T., Lokamani, M., Moldabekov, Z., & Vorberger, J. (2022). Plane-wave-based stochastic-deterministic density functional theory for extended systems. *Physical Review B, 106*(12), 125132.

Carella, A., Borbone, F., & Centore, R. (2018). Research progress on photosensitizers for DSSC. *Frontiers in Chemistry, 6*(SEP).

Carey, G., Abdelhady, A., & Ning, Z. (2015). Colloidal quantum dot solar cells. *ACS Publications*.

Carofiglio, M., Barui, S., Cauda, V., & Laurenti, M. (2020). Doped zinc oxide nanoparticles: Synthesis, characterization and potential use in nanomedicine. *Applied Sciences (Switzerland), 10*(15).

Çavaş, M. (2017). Investigation of morphological, electrical, and optical properties of Mn-doped ZnO thin film by sol–gel spin-coating method. *Journal of Theoretical and Applied Physics, 11*(4), 325–331.

Chander, S., & Tripathi, S. (2022). Recent advancement in efficient metal oxide-based flexible perovskite solar cells: A short review. *Materials Advances, 3*(19), 7198–7211.

Charifi, Z. (2007). Ab-initio investigation of structural, electronic and optical properties for three phases of ZnO compound. *Physica Status Solidi (B), 244*(9), 3154–3167.

Chaudhuri, S., Das, K., Das, G., & Dev, B. (2023). Ab initio study of electronic and

lattice dynamical properties of monolayer ZnO under strain. *arXiv*.

Chawla, A., Hothi, N., & Rao, A. (2024). Potential for multi-application advancements from doping zirconium (Zr) for improved optical, electrical, and resistive memory properties of zinc oxide (ZnO) thin films. *IOP Science*.

Chen, J., Lu, Z., Wang, X., Luo, Y., Ma, Y., Lou, G., Chi, D., & Huang, S. (2024). Highly efficient organic/silicon hybrid solar cells with a MoO_3 capping layer. *Nanomaterials, 14*(20), 1630.

Chen, L., Cui, Y., Xiong, Z., Zhou, M., & Gao, Y. (2019). Chemical functionalization of the ZnO monolayer: Structural and electronic properties. *RSC Advances, 9*(38), 21831–21843.

Chen, M., & Xu, F. (2024). Density functional theory methods applied to homogeneous and heterogeneous catalysis: A short review and a practical user guide. *Physical Chemistry Chemical Physics, 26*, 1220–1245.

Chen, S., Yang, J., Gong, X., & Wei, S. (2019). Intrinsic point defects and p-type doping in ZnO. *Journal of Physics D: Applied Physics, 52*(24), 243001.

Chernomordik, B., Marshall, A., Pach, G., Luther, J., & Beard, M. (2016). Quantum dot solar cell fabrication protocols. *ACS Publications, 29*(1), 189–198.

Chibueze, T. (2021). Ab initio study of mechanical, phonon and electronic properties of cubic zinc-blende structure of ZnO. *Nigerian Annals of Pure and Applied Sciences, 4*(1).

Chirchir, G., Mulwa, W., & Adetunji, B. (2022). Structural, electronic and mechanical properties of Re doped $FeMnP_{0.67}A_{0.33}$ (A = Ga and Ge): A DFT study. *International Journal of Physics, 10*(1), 70–78.

Chouchene, B., Chaabane, T., Balan, L., et al. (2016). High performance Ce-doped ZnO nanorods for sunlight-driven photocatalysis. *Beilstein Journal of Nanotechnology, 7*, 1338–1349.

Cococcioni, M., & De Gironcoli, S. (2005). Linear response approach to the calculation of the effective interaction parameters in the LDA+U method. *Physical Review B, 71*(3).

Çolak, H., & Karaköse, E. (2019). Synthesis and structural, electrical, optical properties of Lu^{3+}-doped ZnO nanorods. *Materials Science in Semiconductor Processing, 101*, 230–237.

Cui, Y., Yao, H., Hong, L., Zhang, T., Tang, Y., Lin, B., Xian, K., Gao, B., An, C., Bi, P., Ma, W., & Hou, J. (2020). Organic photovoltaic cell with 17% efficiency and superior processability. *National Science Review, 7*(7), 1239–1246.

Da Silva Lopes, T., Dias, P., Monteiro, R., Vilanova, A., Ivanou, D., & Mendes, A. (2022). A 25 cm^2 solar redox flow cell: Facing the engineering challenges of upscaling. *Advanced Energy Materials, 12*(5), 2102893.

Das, O., Saiduzzaman, M., Hossain, K., Shuvo, I., Rahman, M., Ahmad, S., & Mitro, S. (2023). First-principles calculations to investigate pressure-driven electronic phase transition of lead-free halide perovskites $KMCl_3$ (M = Ge, Sn) for superior optoelectronic performance. *Results in Physics, 44*.

Das, R., Khichar, N., & Chawla, S. (2015). Dual mode luminescence in rare earth (Er^{3+}/Ho^{3+}) doped ZnO nanoparticles fabricated by inclusive co-precipitation technique. *Journal of Materials Science: Materials in Electronics, 26*(9), 7174–7182.

Dash, S., & Padhan, P. (2024). Lattice thermal conductivity of ZnO: Experimental and theoretical studies. *Physical Chemistry Chemical Physics, 26*, 14754–14765.

Debnath, D., Pal, S., Chatterjee, H., & Ghosh, S. (2023). Critical crystallographic transition in violation of Kasha's rule of size-specific ZnO quantum dots. *Crystal Growth and Design, 23*(3), 1941–1950.

Debnath, T., Das, S., & Das, S. (2017). Optical, magnetic and dielectric properties of ZnO:Y nanoparticles synthesized by hydrothermal method. *Elsevier*.

Decremps, F., Pellicer-Porres, J., Datchi, F., Itié, J., Polian, A., Baudelet, F., & Jiang, J. (2003). Trapping of cubic ZnO nanocrystallites at ambient conditions. *Applied Physics Letters, 81*(25), 4820–4822.

Devadiga, D., Selvakumar, M., & Shetty, P. (2021). Recent progress in dye-sensitized solar cell materials and photo-supercapacitors: A review. *Journal of Power Sources, 493*, 229698.

Dhafina, W., Hasiah, S., & Daud, M. (2022). Natural dye-based dye-sensitized solar cells: A review. *Journal of Basic and Applied Research in Biomedicine, 2*(4), 516–521.

Dhamodharan, P., Manoharan, C., Bououdina, M., Venkadachalapathy, R., & Ramalingam, S. (2017). Al-doped ZnO thin films grown onto ITO substrates as photoanode in dye-sensitized solar cell. *Solar Energy*.

Diale, R., Nkomo, D., Ngobe, B., & Phasha, M. (2023). The use of DFT-based ab initio technique to determine the stability difference in B2 Ti PGM compounds. In S. Haider, A. Haider, & S. Khan (Eds.), *Density Functional Theory – New Perspectives and Applications* (pp. 1–X).

Djaja, N., & Saleh, R. (2013). Characteristics and photocatalytic activities of Ce-doped ZnO nanoparticles. *Materials Sciences and Applications, 4*(2), 145–152.

Dovbeshko, G., et al. (2022). Mechanical properties of cold-sintered ZnO investigated by nanoindentation and micropillar testing. *Journal of the European Ceramic Society, 42*, 512–520.

Dubey, D., Singh, D., Kumar, S., Nayak, C., Kumbhakar, P., Jha, S., Bhattacharya, D., Ghosh, A., & Chatterjee, S. (2016). Local structure and photocatalytic properties of sol–gel derived Mn–Li co-doped ZnO diluted magnetic semiconductor nanocrystals. *RSC Advances, 6*(27), 22852–22867.

Dudarev, G., Botton, S., Savrasov, C., Humphreys, C., & Sutton, A. (1998). Electron-energy-loss spectra and the structural stability of nickel oxide: An LSDA+U study. *Physical Review B, 57*, 1505–1509.

Dutta, J. (2021). Upconverting $BiYO_3$ nanophosphors in DSSCs applications. *Elsevier*.

El Amine Monir, M., & Dahou, F. (2020). Structural, thermal, elastic, electronic and magnetic properties of cubic lanthanide-based perovskite-type oxides $PrXO_3$ (X = V, Cr, Mn, Fe): Insights from ab initio study. *SN Applied Sciences, 2*(3).

El Fidha, G., Bitri, N., Chaabouni, F., Acosta, S., Güell, F., Bittencourt, C., Casanova Chafer, J., & Llobet, E. (2021). Physical and photocatalytic properties of sprayed Dy-doped ZnO thin films under sunlight irradiation for degrading methylene

blue. *RSC Advances, 11*(40), 24917–24925.

El Ghoul, M., et al. (2022). *Improvement of Luminescence and Photocatalytic Performance of ZnO:Eu³⁺ Nanocrystals Activated by Na⁺ Ions*. *Applied Sciences, 13*(14), 8448.

Emery, A. A., & Wolverton, C. (2017). High-throughput DFT calculations of formation energy, stability and oxygen vacancy formation energy of ABO3 perovskites. *Scientific Data 2017 4:1*, *4*(1), 1–10.

Eperon, G. E., Leijtens, T., Bush, K. A., Prasanna, R., Green, T., Wang, J. T. W., McMeekin, D. P., Volonakis, G., Milot, R. L., May, R., Palmstrom, A., Slotcavage, D. J., Belisle, R. A., Patel, J. B., Parrott, E. S., Sutton, R. J., Ma, W., Moghadam, F., Conings, B., … Snaith, H. J. (2016). Perovskite-perovskite tandem photovoltaics with optimized band gaps. *Science*, *354*(6314), 861–865.

Farooq, R., Mahmood, T. (2016) First-principles calculation of electronic and optical properties of graphene like ZnO (G-ZnO). *Elsevier*.

Gallegos, M. V., Luna, C. R., Peluso, M. A., Damonte, L. C., Sambeth, J. E., & Jasen, P. V. (2019). Effect of Mn in ZnO using DFT calculations: Magnetic and electronic changes. *Journal of Alloys and Compounds*, *795*, 254–260.

Gao, C., Han, Q., & Wu, M. (2018). Review on transition metal compounds based counter electrode for dye-sensitized solar cells. *Journal of Energy Chemistry*, *27*(3), 703–712.

Gao, J., Fu, L., Jiao, S., Zhang, Z., Chen, S., Zhang, Z., Wu, W., Wan, L., Li, J., Hu, W., & Yang, J. (2025). *PyPWDFT: A lightweight Python software for single-node 10K-atom plane-wave density functional theory calculations*. *Journal of Chemical Theory and Computation*.

Gao, W., Tang, Z., Zhao, J., & Chelikowsky, J. R. (2023). Efficient full-frequency GW calculations using a Lanczos method. *arXiv*.

Garrod, A., & Ghosh, A. (2023). *A review of bifacial solar photovoltaic applications*. Frontiers in Energy, 17, 704–726.

George, A., Sharma, S. K., Chawla, S., Malik, M. M., & Qureshi, M. S. (2011). Detailed of X-ray diffraction and photoluminescence studies of Ce doped ZnO

nanocrystals. *Journal of Alloys and Compounds*, *509*(20), 5942–5946.

Gerosa, M. (2018). Special issue on self-interaction corrected functionals for solids and surfaces. *Journal of Physics: Condensed Matter*, *30*(23), 230301.

Ghali, R., Moussa, R., Djalab, Y., Maache, M., Khenata, R., Bin-Omran, S. A., Iqbal, M. W., Abdiche, A., Ahmed, W., & Manzour, M. (2023). Investigation of electronic, optical, and mechanical behavior of wurtzite $ZnO_{1-x}Te_x$ ternary alloy via DFT. *Current Applied Physics, 55*, 82–92.

Ghosh, S., Sartape, R., & Chakraborty, J. (2020). Role of dye-induced corrosion in determining the efficiency of ZnO-based DSSC: the case of ZnO nanoforest in N719. *Journal of Materials Science: Materials in Electronics*, *31*(3), 2202–2220.

Giannozzi, P., Baroni, S., Bonini, N., Calandra, M., Car, R., Cavazzoni, C., ... & Wentzcovitch, R. M. (2009). QUANTUM ESPRESSO: a modular and open-source software project for quantum simulations of materials. *Journal of Physics: Condensed Matter, 21*(39), 395502.

Giannozzi, P., De Gironcoli, S., Pavone, P., & Baroni, S. (1991). *Ab initio* calculation of phonon dispersions in semiconductors. *Physical Review B*, *43*(9), 7231.

Giustino, F. (2017). Electron-phonon interactions from first principles. *Reviews of Modern Physics*, *89*(1), 015003.

Goh, E. S., Mah, J. W., & Yoon, T. L. (2017). Effects of Hubbard term correction on the structural parameters and electronic properties of wurtzite ZnO. *Computational Materials Science*, *138*, 111-116.

Gorlov, M., Transactions, L.(2008). Ionic liquid electrolytes for dye-sensitized solar cells. *Pubs.Rsc.Org*.

Grätzel, M. (2003). Dye-sensitized solar cells. *Journal of Photochemistry and Photobiology C: Photochemistry Reviews*, *4*(2), 145–153.

Grätzel, M., & Durrant, J. R. (2008). Dye-sensitised mesoscopic solar cells. *Nanostructured And Photoelectrochemical Systems For Solar Photon Conversion*, 503–536.

Guchhait, A., Dewi, H. A., Leow, S. W., Wang, H., Han, G., Suhaimi, F. Bin,

Mhaisalkar, S., Wong, L. H., & Mathews, N. (2017). Over 20% Efficient CIGS-Perovskite Tandem Solar Cells. *ACS Energy Letters*, *2*(4), 807–812.

Guermit, Y., Rached, D., & others. (2020). Structural and electronic properties of ZnO: A first-principles density-functional theory study within LDA (GGA) and LDA (GGA)+U methods. *Computational Materials Science*, 187, 110034.

Gupta, A., & Bhattacharya, S. (2018). On the growth mechanism of ZnO nano structure via aqueous chemical synthesis. *Applied Nanoscience*, *8*, 499-509.

Häcker, A., & Emin, D. (2023). *Advances in CIGS thin film solar cells with emphasis on the alkali element post-deposition treatment*. *Materials Reports: Energy, 3*(3), 100214.

Haider, M. B., Khan, S. B., & Asiri, A. M. (2021). *Structural and mechanical evaluation of RE-doped ZnO thin films for flexible optoelectronic devices*. Applied Physics A, 127, 703.

Harper, A. F., Evans, M. L., Darby, J. P., Karasulu, B., Koçer, C. P., Nelson, J. R., & Morris, A. J. (2020). Ab initio structure prediction methods for battery materials. *Johnson Matthey Technology Review, 64*(2), 103–118.

Harun, K., Mansor, N., Ahmad, Z. A., & Mohamad, A. A. (2016). Electronic Properties of ZnO Nanoparticles Synthesized by Sol-gel Method: A LDA+U Calculation and Experimental Study. *Procedia Chemistry*, *19*, 125–132.

Harun, K., Salleh, N. A., Deghfel, B., Yaakob, M. K., & Mohamad, A. A. (2020). DFT+ U calculations for electronic, structural, and optical properties of ZnO wurtzite structure: A review. *Results in Physics*, *16*, 102829.

He, W., Chow, T. T., Ji, J., Lu, J., Pei, G., & Chan, L. S. (2006). Hybrid photovoltaic and thermal solar-collector designed for natural circulation of water. *Applied Energy*, *83*(3), 199–210.

Hébert, S., Flahaut, D., Martin, C., Lemonnier, S., Noudem, J., Goupil, C., Maignan, A., & Hejtmanek, J. (2007). Thermoelectric properties of perovskites: Sign change of the Seebeck coefficient and high temperature properties. *Progress in Solid State Chemistry*, *35*(2–4), 457–467.

Hermle, M., Feldmann, F., Bivour, M., Goldschmidt, J. C., & Glunz, S. W. (2020).

Passivating contacts and tandem concepts: Approaches for the highest silicon-based solar cell efficiencies. *Applied Physics Reviews*, *7*(2).

Hoffmann, S., Ostlund, F., Michler, J., Fan, H. J., Zacharias, M., Christiansen, S. H., & Ballif, C. (2022). Fracture strength and Young's modulus of ZnO nanowires. *Nanoscale Research Letters, 17*, 352.

Hoppe, H., & Sariciftci, N. S. (2004). Organic solar cells: An overview. *Journal of Materials Research*, *19*(7), 1924–1945.

Hoshikawa, T., Ikebe, T., Kikuchi, R., (2006), undefined. (n.d.). Effects of electrolyte in dye-sensitized solar cells and evaluation by impedance spectroscopy. *Elsevier*. Retrieved February 24, 2025, from

Hou, W., Xiao, Y., Han, G., & Lin, J. Y. (2018). Stable and near-infrared absorption enhanced dye-sensitized solar cell based on silver nanoplates@silica nanocrystals. *Materials Research Bulletin*, *104*, 164–172.

Hou, W., Xiao, Y., Han, G., Zhang, Y., & Chang, Y. (2016). Titanium dioxide/zinc indium sulfide hetero-junction: An efficient photoanode for the dye-sensitized solar cell. *Journal of Power Sources*, *328*, 578–585.

Huang, G. Y., Wang, C. Y., & Wang, J. T. (2012). Detailed check of the LDA + U and GGA + U corrected method for defect calculations in wurtzite ZnO. *Computer Physics Communications*, *183*(8), 1749–1752.

Huang, H., Ou, Y., Xu, S., Fang, G., Li, M., & Zhao, X. Z. (2008). Properties of Dy-doped ZnO nanocrystalline thin films prepared by pulsed laser deposition. *Applied Surface Science*, *254*(7), 2013–2016.

Huo, J., Zheng, M., Tu, Y., Wu, J., Hu, L., & Dai, S. (2015). A high performance cobalt sulfide counter electrode for dye-sensitized solar cells. *Electrochimica Acta*, *159*, 166–173.

Huong, T. T. T., Sa, N. T., Thuy, N. T. M., & Ca, N. X. (2025). *Eu^{3+}-doped ZnO quantum dots: Structure, vibration characteristics, optical properties, and energy transfer process. Nanoscale Advances, 7*, 909–921.

Hwang, K. J., Park, D. W., Jin, S., Kang, S. O., & Cho, D. W. (2015). Influence of dye-concentration on the light-scattering effect in dye-sensitized solar cell.

Materials Chemistry and Physics, *149*, 594–600.

Ibanez, J. G., Rincón, M. E., Gutierrez-Granados, S., Chahma, M., Jaramillo-Quintero, O. A., & Frontana-Uribe, B. A. (2018). Conducting Polymers in the Fields of Energy, Environmental Remediation, and Chemical-Chiral Sensors. *Chemical Reviews*, *118*(9), 4731–4816.

Iftikhar, H., Sonai, G., Hashmi, S., Materials, A. (2019) Progress on electrolytes development in dye-sensitized solar cells. *Mdpi.Com*.

Jafarova, V., Communications, G. (2021). Structural and electronic properties of ZnO: A first-principles density-functional theory study within LDA (GGA) and LDA (GGA)+ U methods. *Elsevier*.

Jayachandraiah, C., Siva Kumar, K., Krishnaiah, G., & Madhusudhana Rao, N. (2015). Influence of Dy dopant on structural and photoluminescence of Dy-doped ZnO nanoparticles. *Journal of Alloys and Compounds*, *623*, 248–254.

Jaysankar, M., Filipič, M., Zielinski, B., Schmager, R., Song, W., Qiu, W., Paetzold, U. W., Aernouts, T., Debucquoy, M., Gehlhaar, R., & Poortmans, J. (2018). Perovskite-silicon tandem solar modules with optimised light harvesting. *Energy and Environmental Science*, *11*(6), 1489–1498.

Jia, S. K., Zou, Y., Xu, J. Y., Wang, J., & Yu, L. (2015). Effect of TiO2 content on properties of Al2O3 thermal barrier coatings by plasma spraying. *Transactions of Nonferrous Metals Society of China*, *25*(1), 175–183.

Jiang, Q., Cao, Z., Chen, J., Qin, X., Hu, W., An, H., & Yang, J. (2024). *PWDFT-SW: Extending the limit of plane-wave DFT calculations to 16 K atoms on the new Sunway supercomputer*. *arXiv*.

John, R., applications, S. P.-C. structure theory and, & 2016, undefined. (n.d.). Ab initio calculations on structural, electronic and optical properties of ZnO in wurtzite phase. *Scirp.OrgR John, S PadmavathiCrystal Structure Theory and Applications, 2016•scirp.Org*.

Jothi Ramalingam, R., Shukla, A. K., Kombaiah, K., Vijaya, J. J., & Tawfeek, A. M. (2017). Synthesis, characterization and optical properties of sulfur and fluorine doped ZnO nanostructures for visible light utilized catalysis. *Optik*, *148*, 325–

331.

Jumabekov, A. N., Siegler, T. D., Cordes, N., Medina, D. D., Böhm, D., Garbus, P., Meroni, S., Peter, L. M., & Bein, T. (2014). Comparison of Solid-State Quantum-Dot-Sensitized Solar Cells with ex Situ and in Situ Grown PbS Quantum Dots. *Journal of Physical Chemistry C*, *118*(45), 25853–25862.

Kafedjiska, I., Farias-Basulto, G. A., Reyes-Figueroa, P., Bertram, T., Al-Ashouri, A., Kaufmann, C. A., Wenisch, R., Albrecht, S., Schlatmann, R., & Lauermann, I. (2023). Integration of rough RTP absorbers into CIGS-perovskite monolithic tandems by NiOx(:Cu)+SAM Hole-transporting Bi-layers: CIGS-perovskie tandems with NiOx:Cu+SAM. *Solar Energy Materials and Solar Cells*, *254*.

Kang, X., Jia, C., Wan, Z., Zhuang, J., & Feng, J. (2015). A novel tri-layered photoanode of hierarchical ZnO microspheres on 1D ZnO nanowire arrays for dye-sensitized solar cells. *RSC Advances*, *5*(22), 16678–16683.

Kasaye, B. B., Shura, M. W., & Dibaba, S. T. (2024). Review of recent progress in the development of electrolytes for Cd/Pb-based quantum dot-sensitized solar cells: performance and stability. *RSC Advances, 14*, 16255–16268.

Kaur, S., Singh, K., & Verma, N. K. (2022). Impact of oxygen vacancy on luminescence properties of dysprosium-doped ZnO thin films. *Journal of Applied Physics, 136*(2), 025302.

Khan, A. A., Abdullah, M. H., Hassan, M. D. A., Osman, M. K., Rahim, A. F. A., Mamat, M. H., Adilah, M. S., & Banu, I. B. S. (2023). Co-active impact of surface hydroxyls on the solvation shell and dye adsorption of Mitragyna Speciosa chlorophyll molecules in dye-sensitised solar cells. *Journal of the Iranian Chemical Society*, *20*(7), 1743–1756.

Khuili, A., Bououdina, M., & Aida, M. S. (2020). Effect of rare-earth doping on ZnO photoanodes for dye-sensitized solar cells. Materials Today: Proceedings, 30, 683–688.

Khuili, M., El Hallani, G., Fazouan, N., Abou El Makarim, H., &Atmani, E. H. (2019). First-principles calculation of (Al, Ga) co-doped ZnO. *Computational Condensed Matter*, *21*, e00426.

Khuili, M., Fazouan, N., Abou El Makarim, H., Atmani, E. H., Rai, D. P., & Houmad, M. (2020). First-principles calculations of rare earth (RE=Tm, Yb, Ce) doped ZnO: Structural, optoelectronic, magnetic, and electrical properties. *Vacuum*, *181*.

Khuili, M., Fazouan, N., El Makarim, H. A., & Atmani, E. H. (2016). Study of properties of (Mg, Al)-codoped ZnO with GGA and mBJ approximations. *Physics Letters, Section A: General, Atomic and Solid State Physics*, *380*(36), 2881–2887.

Kim, H. S., Gibbs, Z. M., Tang, Y., Wang, H., & Snyder, G. J. (2015). Characterization of Lorenz number with Seebeck coefficient measurement. *APL Materials*, *3*(4), 45.

Kim, S., Lebègue, S., Ringe, S., & Kim, H. (2022). GW quasiparticle energies and bandgaps of two-dimensional materials immersed in water. *Journal of Physical Chemistry Letters, 13*(32), 7574–7582.

King, H. M. (2023.). *Production of Rare Earth Elements*. In *Rare Earth Elements and Their Uses*. MediaMan.

Kislov, A. N., & Zatsepin, A. F. (2023). Structural and vibrational properties of wurtzite ZnO with oxygen-deficient defects: *Ab initio* and potential-based calculations. *Physical Chemistry Chemical Physics, 25*(24), 16354–16362.

Kouhestanian, E., Ranjbar, M., Mozaffari, S. A., & Salaramoli, H. (2021). Investigating the Effects of Thickness on the Performance of ZnO-Based DSSC. *Progress in Color, Colorants and Coatings*, *14*(2), 101–112.

Kumar, A., Raizada, P., Khan, A. A. P., Nguyen, V. H., Van Le, Q., Singh, A., Saini, V., Selvasembian, R., Huynh, T. T., & Singh, P. (2021). Phenolic compounds degradation: Insight into the role and evidence of oxygen vacancy defects engineering on nanomaterials. *Science of the Total Environment*, *800*.

Kumar, M., Sharma, A., & Singh, S. (2020). *Effect of rare-earth doping on the optical and electronic properties of ZnO nanostructures*. Journal of Materials Science: Materials in Electronics, 31(10), 8123–8132.

Kumar, R., Sharma, A., & Singh, V. (2023). Upconversion enhancement in Er and Yb

co-doped ZnO for photovoltaic applications. Journal of Luminescence, 256, 119900.

Kumar, V., & Singh, B. P. (2018). Structural and elastic properties of AIBIIIC 2VI semiconductors. *Indian Journal of Physics*, *92*(1), 29–35.

Kumar, V., Singh, P., & Mehta, B. R. (2020). *Charge carrier transport and mobility in ZnO thin films: Dependence on grain boundaries and doping*. Applied Surface Science, 506, 144992.

Kumavat, P. P., Sonar, P., & Dalal, D. S. (2017). An overview on basics of organic and dye sensitized solar cells, their mechanism and recent improvements. *Renewable and Sustainable Energy Reviews*, *78*, 1262–1287.

Kundara, S., Chawla, K., Yadav, D (2024), undefined. (n.d.). Study of Structural, Optical, Electrical and Dielectric Properties of Gd-Doped ZnO Composites Synthesized by Solid State Reaction Method. *Scirp.Org*.

Labazanova, T. N., Bogachev, A. V., Kuznetsova, L. A., & Platonova, O. A. (2021). Enhanced photocatalytic and photoluminescence properties of Ce and Dy co-doped ZnO nanoparticles. *Russian Journal of Physical Chemistry A, 95*(12), 1900–1910.

Laestadius, A., Quantum, M. (2014),. Hohenberg–Kohn theorems in the presence of magnetic field. *Wiley Online Library*.

Lahmer, M. A. (2022). Effect of doping with sulfur atoms on the electronic and photocatalytic properties of the ZnO($10\bar{1}0$) surface: A DFT+U study. *Computational Condensed Matter*, *31*.

Lee, G. M., Kim, T. H., Ham, G., Lee, M. J., Oh, S., Kang, Y., Ahn, H., Cha, H., Chung, S., & Shim, J. W. (2025). Enhancing Dynamic Range in Low-Noise 2D-Integrated Organic Photodiodes by Mitigating Langevin Recombination. *ACS Nano*.

Lee, H., & Kim, J. (2022). *Performance evaluation of flexible CIGS modules based on operational data under outdoor conditions*. *Energy Science & Engineering, 10*(6), 1040.

Lee, J., Park, S., & Chang, Y. H. (2022). First-principles study on mechanical

deformation and elastic constants of Ce-doped ZnO. *Journal of Applied Physics, 132*(8), 085103.

Lee, Y. L., Shanmuganathan, V., Hsu, T. H., Teng, H. (2021). Tandem dye-sensitized solar cells with efficiencies surpassing 33% under dim-light conditions. *Advanced Optical Materials, 9*(22), 2100936.

Li, H., et al. (2022). Deep-learning density functional theory Hamiltonian for efficient ab initio electronic-structure calculation. *Nature Computational Science, 2*, 418–419.

Li, L., Hoyer, S., Pederson, R., Sun, R., Cubuk, E. D., Riley, P., & Burke, K. (2021). Kohn-Sham Equations as Regularizer: Building Prior Knowledge into Machine-Learned Physics. *Physical Review Letters*, *126*(3).

Li, S., Wang, C., Zhao, D., An, Y., Zhao, Y., Zhao, X., & Li, X. (2020). Flexible semitransparent perovskite solar cells with gradient energy levels enable efficient tandems with Cu(In,Ga)Se2. *Nano Energy*, *78*.

Li, Z., Jia, M., Abraham, B., Blake, J. C., Bodine, D., Newberg, J. T., & Gundlach, L. (2018). Synthesis and Characterization of ZnO/CuO Vertically Aligned Hierarchical Tree-like Nanostructure. *Langmuir*, *34*(3), 961–969.

Lysak, A., Przeździecka, E., Wierzbicka, A., Jakiela, R., Khosravizadeh, Z., Szot, M., Adhikari, A., & Kozanecki, A. (2024). *Temperature dependence of the bandgap of Eu-doped {ZnCdO/ZnO}30 multilayer structures*. *arXiv*.

Madathilakath Kurian, C., & Govindarajan, R. (2021). Spectroscopic properties of Dy^{3+}-doped ZnO for white luminescence applications. *Optical Materials, 120*, 111475.

Mahalingam, S., & Abdullah, H. (2016). Electron transport study of indium oxide as photoanode in DSSCs: A review. *Renewable and Sustainable Energy Reviews*, *63*, 245–255.

Mahmood, Q., Hedhili, F., Al-Shomar, S., Chebaaneef, S., Al-Muhimeed, T. I., Al Obaid, A. A., Mera, A., & Alamri, O. A. (2021). Electronic, optical, and transport properties of RbYbX3 (X = Cl, Br) for solar cells and renewable energy: A quantum DFT study. *Physica Scripta*, *96*(9).

Marimuthu, T., & Anandhan, N. (2017). Growth and characterization of ZnO nanostructure on TiO2-ZnO films as a light scattering layer for dye sensitized solar cells. *Materials Research Bulletin*, *95*, 616–624.

Marimuthu, T., Yuvakkumar, R., Kumar, P. S., et al. (2022). Two-dimensional hybrid perovskite solar cells: A review. *Environmental Chemistry Letters, 20*, 189–210.

Mariotti, S., Köhnen, E., Scheler, F., Sveinbjörnsson, K., Zimmermann, L., Piot, M., Yang, F., Li, B., Warby, J., Musiienko, A., Menzel, D., Lang, F., Keßler, S., Levine, I., Mantione, D., Al-Ashouri, A., Härtel, M. S., Xu, K., Cruz, A., Albrecht, S. (2023). Interface engineering for high-performance, triple-halide perovskite–silicon tandem solar cells. *Science*, *381*(6653), 63–69.

Marques Lameirinhas, R. A., Torres, J. P. N., & de Melo Cunha, J. P. (2022). *A photovoltaic technology review: History, fundamentals and applications*. Energies, 15(5), 1823.

Martínez, J. F., Steiner, M., Wiesenfarth, M., Helmers, H., Siefer, G., Glunz, S. W., & Dimroth, F. (2022). Worldwide energy harvesting potential of hybrid CPV/PV technology. *arXiv.*

Materials (2019). Terbium-doped ZnO nanomaterials for DSSC efficiency improvement. Materials, 12(8), 1305.

Materials, L. (2019) The effects of Tb doped ZnO nanorod: An EPR study. *Elsevier*.

Mbilo, M., & Musembi, R. (2022). First-Principle Calculations to Investigate Structural, Electronic, Elastic, Mechanical, and Optical Properties of K2CuX (X=As, Sb) Ternary Compounds. *Advances in Materials Science and Engineering*, *2022*.

Merdan, M., & Banimuslem, H. A. (2024). Synthesis, characterization and LDA+U calculations of zinc oxide nanoparticles. *Physica Scripta*, *99*(6). https://doi.org/10.1088/1402-4896/AD4427

Meshram, S. P., Adhyapak, P. V., Pardeshi, S. K., Mulla, I. S., & Amalnerkar, D. P. (2017). Sonochemically generated cerium doped ZnO nanorods for highly efficient photocatalytic dye degradation. *Powder Technology*, *318*, 120–127.

Micromachines, D. (2022), Engineering of optical and electrical properties of

electrodeposited highly doped Al: ZnO and In: ZnO for cost-effective photovoltaic device technology. *Mdpi.ComDN PapadimitriouMicromachines, 2022•mdpi.Com*.

Mitro, S., Hossain, K., (2021), Effect of the negative chemical pressure on physical properties of doped perovskite molybdates in the framework of DFT method. *ElsevierSK Mitro, KM Hossain, R Majumder, MZ HasanJournal of Alloys and Compounds, 2021•Elsevier*

Mohammadi, I., Zeraatpisheh, F., Ashiri, E., & Abdi, K. (2020). Solvothermal synthesis of g-C3N4 and ZnO nanoparticles on TiO2 nanotube as photoanode in DSSC. *International Journal of Hydrogen Energy*, *45*(38), 18831–18839.

Mohammadian-Sarcheshmeh, H., Arazi, R., & Mazloum-Ardakani, M. (2020). Application of bifunctional photoanode materials in DSSCs: A review. *Renewable and Sustainable Energy Reviews*, *134*.

Moldabekov, Z. A., Lokamani, M., Vorberger, J., Cangi, A., & Dornheim, T. (2022). Assessing the accuracy of hybrid exchange–correlation functionals for the density response of warm dense electrons. *The Journal of Chemical Physics, 158*(9), 094105.

Monkhorst, H. J., & Pack, J. D. (1976). Special points for Brillouin-zone integrations. *Physical Review B*, *13*(12), 5188

Mozaffari, S. A., Ranjbar, M., Kouhestanian, E., Salar Amoli, H., & Armanmehr, M. H. (2015). An investigation on the effect of electrodeposited nanostructured ZnO on the electron transfer process efficiency of TiO2 based DSSC. *Materials Science in Semiconductor Processing*, *40*, 285–292.

Mulwa, M. (2017). Stability and efficiency considerations of rare-earth-doped ZnO for DSSCs. Kenya Journal of Energy Research, 4(1), 22–29.

Mulwa, W. M. (2017). A combined ab initio and experimental study of lanthanides and/or transition metal doped oxides.

Mulwa, W. M., Ouma, C. N. M., Onani, M. O., & Dejene, F. B. (2016). Energetic, electronic and optical properties of lanthanide doped TiO2: An ab initio LDA+U study. *Journal of Solid State Chemistry*, *237*, 129–137.

Murthy, H. (2019). Nanoarchitectures as photoanodes. *Interfacial Engineering in Functional Materials for Dye-Sensitized Solar Cells*, 35–77.

Musembi, R., & Mbilo, M. (2022). Ab Initio Study of Structural, Electronic, Elastic, Mechanical, and Optical Properties of K4XP2 (X = Zn, Cd) Compounds for Optoelectronic Applications. *Materialia*, *26*.

Mwalukuku, J., Gathuru, G., & Macharia, J. (2023). Advanced doping strategies for ZnO nanostructures in DSSC applications. African Journal of Renewable Energy Research, 9(2), 112–121.

Mwalukuku, V. M., Liotier, J., Riquelme, A. J., Kervella, Y., Huaulmé, Q., Haurez, A., Narbey, S., Anta, J. A., & Demadrille, R. (2023). Strategies to Improve the Photochromic Properties and Photovoltaic Performances of Naphthopyran Dyes in Dye-Sensitized Solar Cells. *Advanced Energy Materials*, *13*(8).

Naher, M., Compounds, S. (2020). Structural, elastic, electronic, bonding, and optical properties of topological CaSn3 semimetal. *ElsevierMI Naher, SH NaqibJournal of Alloys and Compounds, 2020•Elsevier*.

Najafi, L., Taheri, B., Martín-García, B., Bellani, S., Di Girolamo, D., Agresti, A., Oropesa-Nunìez, R., Pescetelli, S., Vesce, L., Calabrò, E., Prato, M., Del Rio Castillo, A. E., Di Carlo, A., & Bonaccorso, F. (2018). MoS2 Quantum Dot/Graphene Hybrids for Advanced Interface Engineering of a CH3NH3PbI3 Perovskite Solar Cell with an Efficiency of over 20%. *ACS Nano*, *12*(11), 10736–10754.

Nakano, K., & Tajima, K. (2025). Insights from Planar Heterojunctions: Understanding Charge Carrier Generation in Organic Photovoltaics. *ACS Applied Materials and Interfaces*.

Namisi, M. M., Musembi, R. J., Mulwa, W. M., & Aduda, B. O. (2023). DFT study of cubic, tetragonal and trigonal structures of KGeCl3 perovskites for photovoltaic applications. *Computational Condensed Matter*, *34*, e00772.

Navas, J., Reyes-Pérez, F., Alcántara, R., Fernández-Lorenzo, C., Gallardo Bernal, J. J., & Martín-Calleja, J. (2017). M(Al,Ni)-TiO2-Based Photoanode for Photoelectrochemical Solar Cells. *Zeitschrift Fur Physikalische Chemie*, *232*(4),

559–577

Nguyen, V. H., Vu, N. T., Anders, N., & Hoppe, J. (2025). *Structural and optical properties of Eu-doped ZnO epitaxial thin films grown by pulsed-laser deposition. APL Materials, 12*(11), 111112.

Ning, J., Furness, J. W., & Sun, J. (2021). Reliable lattice dynamics from an efficient density functional. *Chemistry of Materials*, *33*(16), 6289–6298.

Nowsherwan, G. A., Khan, M., Nowsherwan, N., Ikram, S., Hussain, S. S., Naseem, S., & Riaz, S. (2024). Emerging trends in lanthanide-based upconversion and downconversion material for PSCs & DSSCs. *Journal of Materials Science*.

Nowsherwan, G., Khan, M., (2024). Emerging trends in lanthanide-based upconversion and downconversion material for PSCs & DSSCs. *Springer*.

O'Regan, B., & Grätzel, M. (1991). A low-cost, high-efficiency solar cell based on dye-sensitized colloidal TiO_2 films. Nature, 353, 737–740.

Okil, M., Salem, M. S., Abdolkader, T. M., & Shaker, A. (2021). From Crystalline to Low-cost Silicon-based Solar Cells: a Review. *Silicon 2021 14:5*, *14*(5), 1895–1911.

Önen, T., Karakuş, M., Coşkun, R., (2019)., Reaching stability at DSSCs with new type gel electrolytes. *Elsevier*.

Pallikara, I., Kayastha, P., Skelton, J. M., & Whalley, L. D. (2022). The physical significance of imaginary phonon modes in crystals. *Electronic Structure*, *4*(3).

Parhizgar, S. S., & Beheshtian, J. (2018). Effect of nitrogen doping on electronic and optical properties of ZnO sheet: DFT+U study. *Computational Condensed Matter*, *15*, 1–6.

Park, J., Jung, J. H., Jung, K. W., *et al.* (2024). *Ab initio* potential energy surfaces calculation via restricted Hartree–Fock for molecular dynamics simulation: A comprehensive review. *Journal of the Korean Physical Society, 84*, 550–565.

Patel, D., Parmar, R., & Upadhyay, A. (2022). *Enhanced electrical and optical properties of La-doped ZnO for solar cell applications*. Optical Materials, 123, 111896.

Perdew, J. P., Burke, K., & Ernzerhof, M. (1996). Generalized gradient approximation made simple. *Physical Review Letters*, *77*(18), 3865–3868.

Perkins, C. L., Beall, C., Reese, M. O., & Barnes, T. M. (2017). Two-Dimensional Cadmium Chloride Nanosheets in Cadmium Telluride Solar Cells. *ACS Applied Materials and Interfaces*, *9*(24), 20561–20565.

Pingak, R. K., Bouhmaidi, S., Harbi, A., Setti, L., Nitti, F., Moutaabbid, M., Johannes, A. Z., Hauwali, N. U. J., & Ndii, M. Z. (2023). A DFT investigation of lead-free TlSnX 3 (X = Cl, Br, or I) perovskites for potential applications in solar cells and thermoelectric devices. *RSC Advances*, *13*(48), 33875–33886.

Pokluda, J., Černý, M., Šob, M., & Umeno, Y. (2015). Ab initio calculations of mechanical properties: Methods and applications. *Progress in Materials Science*, *73*, 127–158.

Ponnambalam, S., Junluthin, P., Ramaraj, R., & Unpaprom, Y. (2023). A comprehensive review of the evolution of dye-sensitized solar cells from ruthenium dyes to organic pigments with the influence of graphene nanoribbons. *Maejo International Journal of Energy and Environmental Communication, 5*(2), 1–13.

Prabavathy, N. (2017), Enhancement in the photostability of natural dyes for dye-sensitized solar cell (DSSC) applications: a review. *Wiley Online Library*

Prabavathy, N., Shalini, S., Balasundaraprabhu, R., Velauthapillai, D., Prasanna, S., & Muthukumarasamy, N. (2017). Enhancement in the photostability of natural dyes for dye-sensitized solar cell (DSSC) applications: a review. *International Journal of Energy Research*, *41*(10), 1372–1396.

Pugh, S. F. (1954). XCII. Relations between the elastic moduli and the plastic properties of polycrystalline pure metals. *The London, Edinburgh, and Dublin Philosophical Magazine and Journal of Science*, *45*(367), 823–843.

Qi, Q., Deng, S., & Jiang, Y. (2008). A simulation study on a solar heat pump heating system with seasonal latent heat storage. *Solar Energy*, *82*(8), 669–675.

Qiao, B., Zhao, P., Wang, Z., Xiong, J., Hu, Y., Yang, S., Xu, H., & Gu, H. (2020). Adsorption of NO on an Al-doped ZnO monolayer under electric fields: A DFT

study. *Computational and Theoretical Chemistry, 1180*, 112829.

Qing, X., Zhang, C., Gong, J., Vacuum, S. (2021), Ab initio study of photoelectric properties in ZnO transparent conductive oxide. *Elsevier*.

Rafique, M. Y., Iqbal, A., & Ali, R. (2019). *Mechanical behavior of ZnO nanorods for MEMS/NEMS applications: Experimental and simulation studies*. Journal of Nanomaterials, 2019, 1–9.

Raguram, T., & Rajni, K. S. (2022). Synthesis and characterisation of Cu - Doped TiO2 nanoparticles for DSSC and photocatalytic applications. *International Journal of Hydrogen Energy*, *47*(7), 4674–4689.

Rahman, M. H., Rahaman, M. Z., Chowdhury, E. H., Motalab, M., Hossain, A. K. M. A. H., & Roknuzzaman, M. (2022). *Understanding the role of rare-earth metal doping on the electronic structure and optical characteristics of ZnO*.* Molecular Systems Design & Engineering, 7(11), 1516–1528.

Rai, D. P., Laref, A., Khuili, M., Al-Qaisi, S., Vu, T. V., & Vo, D. D. (2020). Electronic, magnetic and optical properties of monolayer (ML) hexagonal ZnSe on vacancy defects at Zn sites from DFT-1/2 approach. *Vacuum*, *182*, 109597.

Raihan, M. F., Wungu, T. K., & Yuliarto, B. (2021). Study of the structure and electronic properties of the ZnO monolayer: Density functional theory. *Computational and Experimental Research in Materials and Renewable Energy, 4*(1), 1–7.

Raihan, M. F., Wungu, T. D. K., & Yuliarto, B. (2021). Study of the structure and electronic properties of the ZnO monolayer: Density functional theory. *Computational and Experimental Research in Materials and Renewable Energy, 4*(1), 1–7.

Raihan, M. F., Wungu, T. D. K., & Yuliarto, B. (2021). Study of the structure and electronic properties of the ZnO monolayer: Density functional theory. *Computational and Experimental Research in Materials and Renewable Energy, 4*(1), 1–7.

Rajeev, P. V., Gnanasekar, S., Gothandapani, K., Sellappan, R., Jacob, G., Raghavan, V., Pitchaimuthu, S., Sonar, P., Chandar, N. K., Jeong, S. K., Ahamed, M.,

Pandiaraj, S., Ramamoorthy, M., & Grace, A. N. (2021). Thermal decomposition derived nano molybdenum nitride for robust counter electrode in dye-sensitized solar cells. *Materials Today Communications*, *26*, 102070.

Rama Krishna, C., & Kang, M. (2017). Improving the photovoltaic conversion efficiency of ZnO based dye sensitized solar cells by indium doping. *Journal of Alloys and Compounds*, *692*, 67–76.

Rangel, T., Del Ben, M., Varsano, D., Antonius, G., Bruneval, F., da Jornada, F. H., Neaton, J. B. (2020). Reproducibility in G₀W₀ calculations for solids. *Computer Physics Communications, 255*, 107242.

Rani, P., & Chauhan, S. (2021). A review on the use of DFT for the prediction of the properties of nanomaterials. *RSC Advances, 11*(27), 16786–16804.

Ravele, T., Kebede, M. A., & Fuku, X. G. (2024). Review of organic–inorganic heterojunction hybrid solar cells with embedded plasmonic nanocrystals: Recent advances and future perspectives. *Energy & Fuels*.

Ravichandran, N. K., & Broido, D. (2020). Phonon-Phonon Interactions in Strongly Bonded Solids: Selection Rules and Higher-Order Processes. *Physical Review X*, *10*(2), 021063.

Rehman, J. U., Rehman, M. A., Usman, M., Tahir, M. B., Hussain, A., Zulfiqar, M., MeshalAlzaid, Ali, A. M., & Shahzad, K. (2023). A DFT study to investigate structural, electronic, optical, mechanical and magnetic properties of NaGeBr3 for photovoltaic and optoelectronic applications. *Emergent Materials*, *6*(2), 699–709.

Richhariya, G., Kumar, A., Shukla, A. K., Shukla, K. N., & Meikap, B. C. (2023). Effect of Different Counter Electrodes on Power Conversion Efficiency of DSSCs. *Journal of Electronic Materials*, *52*(1), 60–71.

Ritacco, I., Sacco, O., Caporaso, L., & Camellone, M. F. (2022). DFT Investigation of Substitutional and Interstitial Nitrogen-Doping Effects on a ZnO(100)-TiO2(101) Heterojunction. *Journal of Physical Chemistry C*, *126*(6), 3180–3193.

Rodriguez, A. J., Gonzalez, L., & Marcos, F. (2022). Mechanical and tribological behavior of Ce-doped ZnO coatings. *Surface & Coatings Technology, 437*,

128303.

Roslan, N., Ya'acob, M. E., Radzi, M. A. M., Hashimoto, Y., Jamaludin, D., & Chen, G. (2018). Dye Sensitized Solar Cell (DSSC) greenhouse shading: New insights for solar radiation manipulation. *Renewable and Sustainable Energy Reviews*, *92*, 171–186.

Rouhi, J., Mamat, M. H., Ooi, C. H. R., Mahmud, S., & Mahmood, M. R. (2015). High-performance dye-sensitized solar cells based on morphology-controllable synthesis of ZnO–ZnS heterostructure nanocone photoanodes. *PLoS ONE*, *10*(4), e0123433.

Rubio, A. (2020). Electronic structure of materials by ab initio methods: Overview. In W. Andreoni & S. Yip (Eds.), *Handbook of Materials Modeling* (pp. 207–212). Springer.

Ruess, R., Scarabino, S., Ringleb, A., Nonomura, K., Vlachopoulos, N., Hagfeldt, A., Wittstock, G., & Schlettwein, D. (2019). Diverging surface reactions at TiO2-or ZnO-based photoanodes in dye-sensitized solar cells. *Physical Chemistry Chemical Physics*, *21*(24), 13047–13057.

Saleem, M., Anwar, M. S., Siddiq, M., Ashiq, M. N., & Amin, N. (2021). Synthesis of Sm/Cu co-doped ZnO nanorod arrays for enhanced photovoltaic performance in dye-sensitized solar cells. *Nanomaterials, 11*(7), 1710.

Salman Khan, M., Gul, B., Khan, G., Salah Mohamed, A., & Abbas, F. (2024). First-principles study of novel CuAgX (X = S, se) semiconductors: Probing electronic, optical, thermodynamic, and thermoelectric properties. *Materials Science in Semiconductor Processing*, *184*.

Samykano, M. (2023). Hybrid photovoltaic–thermal systems: Present and future feasibilities for industrial and building applications. *Buildings, 13*(8), 1950.

Sánchez, E., Bañón Navarro, A., Wilms, F., -, al, Carlsson, J., Khrabrov, A., Kaganovich, I., Motornyi, O., Raynaud, M., Dal Corso, A., & Vast, N. (2018). Simulation of electron energy loss spectra with the turboEELS and thermo_pw codes. *Journal of Physics: Conference Series*, *1136*(1), 012008.

Santra, B., (2019). Perdew-Zunger self-interaction correction: How wrong for uniform

densities and large-Z atoms? *Pubs.Aip.Org*.

Saxena, N., Sharma, R., Hussain, A., Choudhary, R. J., Debnath, A. K., Sinha, O. P., & Krishna, R. (2022). Effect of the triple (Al, Ga, In) doping in ZnO nanostructures on its transmission, conductivity, and stability for TCO applications. *Materials Letters*, *306*.

Scarabino, S., Nonomura, K., Vlachopoulos, N., Hagfeldt, A., & Wittstock, G. (2020). Effect of TiO2 Photoanodes Morphology and Dye Structure on Dye-Regeneration Kinetics Investigated by Scanning Electrochemical Microscopy. *Electrochem*, *1*(3), 329–343.

Shafian, S., Mohd Salehin, F. N., Lee, S., Ismail, A., Mohamed Shuhidan, S., Xie, L., & Kim, K. (2025). Development of Organic Semiconductor Materials for Organic Solar Cells via the Integration of Computational Quantum Chemistry and AI-Powered Machine Learning. *ACS Applied Energy Materials*.

Shahzad, M., Javed, S., & Usman, M. (2021). Zinc oxide nanostructures: Synthesis routes and optoelectronic applications – A review. *Frontiers in Materials, 8*, 613825.

Shahzad, N., Risplendi, F., Pugliese, D., Bianco, S., Sacco, A., Lamberti, A., Gazia, R., Tresso, E., & Cicero, G. (2013). Comparison of hemi-squaraine sensitized TiO2 and ZnO photoanodes for DSSC applications. *Journal of Physical Chemistry C*, *117*(44), 22778–22783.

Sharbatdaran, M., & Janbazi, M. (2024). Mechanical effects of temperature on undoped ZnO nanoparticles: Experimental and DFT study. *RSC Advances, 14*(42), 31153–31164.

Sharma, A., Yadav, R., & Singh, M. (2021). *Phonon dispersion and lattice dynamic study of ZnO nanostructures using first-principles calculations*. Materials Today: Proceedings, 47, 5372–5376.

Sharma, D. K., Sharma, K. K., Kumar, V., & Sharma, A. (2016). Effect of Ce doping on the structural, optical and magnetic properties of ZnO nanoparticles. *Journal of Materials Science: Materials in Electronics*, *27*(10), 10330–10335.

Sharma, Y., Anand, V., & Heera, P. (2023). *Ab initio* study of structural and magnetic

properties of cobalt-doped ZnO. *Journal of Condensed Matter, 1*(2), 48–51.

Sharpe, D. J., Levy, M., & Tozer, D. J. (2018). Approximating the shifted Hartree–exchange–correlation potential in direct-energy Kohn–Sham theory. *Journal of Chemical Theory and Computation, 14*(2), 684–692.

Shi, B. X., Nicholls, R. J., & Yates, J. R. (2022). *Accurate and efficient structure factors in ultrasoft pseudopotential and projector augmented-wave DFT*. *arXiv*.

Shishkin, M., & Sato, H. (2019). DFT+ U in Dudarev's formulation with corrected interactions between the electrons with opposite spins: The form of Hamiltonian, calculation of forces, and bandgap adjustments. *The Journal of Chemical Physics*, *151*(2).

Silvia, F., Rossi, L., Maria, G. R., & Lombardo, S. (2023). Comparative mechanical characterization of ZnO thin films deposited via PVD and CVD. *Thin Solid Films, 756*, 139459.

Sim, E., Song, S., Vuckovic, S., & Burke, K. (2022). Improving results by improving densities: density-corrected density functional theory. *arXiv*, 2203.06863.

Singh Selopal, G., Zhao, H., Rosei, F., Wang, Z. M., Selopal, G. S., Wang, Z. M., Rosei, F., & Zhao, H. (2020). Core/shell quantum dots solar cells. *Wiley Online Library*, *30*(13).

Singh, K., Devi, V., Dhar, R., & Mohan, D. (2015). Structural, optical and electronic properties of Fe doped ZnO thin films. *Superlattices and Microstructures*, *85*, 433–437.

Singh, P., Kumar, R., & Singh, R. K. (2020). Fabrication of Co- and Ce-doped ZnO nanoparticles: a structural, morphological and optical properties investigation. *Applied Nanoscience (Switzerland)*, *10*(4), 1231–1241.

Singh, V., & Patel, R. (2022). *Progress in thin-film photovoltaics: A review of key strategies to enhance the efficiency of CIGS, CdTe, and CZTSSe solar cells*. *Polymers, 9*(3), 143.

Slimani, M. E. A., Amirat, M., Bahria, S., Kurucz, I., Aouli, M., & Sellami, R. (2016). Study and modeling of energy performance of a hybrid photovoltaic/thermal solar collector: Configuration suitable for an indirect solar dryer. *Energy Conversion*

and Management, *125*, 209–221.

Sogabe, T., (2016), Recent progress on quantum dot solar cells: a review. *Spiedigitallibrary.Org*.

Sokolov, P. S., Baranov, A. N., Dobrokhotova, Zh. V., & Solozhenko, V. L. (2011). Synthesis and thermal stability of cubic ZnO in salt nanocomposites. *arXiv*.

Soman, S., Pradhan, S. C., Yoosuf, M., Vinayak, M. V., Lingamoorthy, S., & Gopidas, K. R. (2018). Probing Recombination Mechanism and Realization of Marcus Normal Region Behavior in DSSCs Employing Cobalt Electrolytes and Triphenylamine Dyes. *Journal of Physical Chemistry C*, *122*(25), 14113–14127.

Song, L., Du, P., Xiong, J., Ko, F., & Cui, C. (2015). Efficiency enhancement of dye-sensitized solar cells by optimization of electrospun ZnO nanowire/nanoparticle hybrid photoanode and combined modification. *Electrochimica Acta*, *163*, 330–337.

Su'ait, M. S., Rahman, M. Y. A., & Ahmad, A. (2015). Review on polymer electrolyte in dye-sensitized solar cells (DSSCs). *Solar Energy*, *115*, 452–470.

Szakacs, C. E., Merschrod, E. F. S., & Poduska, K. M. (2013). Structural Features That Stabilize ZnO Clusters: An Electronic Structure Approach. *Computation 2013, Vol. 1, Pages 16-26*, *1*(1), 16–26.

Tahir, A., & Want, B. (2024). Doping effect of Europium (Eu3+) on flower-like ZnO nanostructures: shape variations, optical properties and its applicability in electrochemical sensing of heavy metal (Lead) ion detection. *Applied Physics A: Materials Science and Processing*, *130*(4), 1–15.

Talip, R. A., Yahya, W., Sustainability, M. (2020), Ionic liquids roles and perspectives in electrolyte for dye-sensitized solar cells. *Mdpi.Com*.

Talwar, D. N., & Becla, P. (2025). Systematic simulations of structural stability, phonon dispersions, and thermal expansion in zinc-blende ZnO. *Nanomaterials, 15*(4), 308.

Tan, C. Z., Liu, Z. Q., Peng, Y., & Sang, X. B. (2023). Tunable mechanical and piezoelectric properties of strain-engineered ZnO nanoplates: a first-principles study. *Materials Science and Engineering: B, 292*, 116966.

Tan, C., Sun, D., Xu, D., Tian, X., International, Y. (2016), undefined. (n.d.). Tuning electronic structure and optical properties of ZnO monolayer by Cd doping. *ElsevierC Tan, D Sun, D Xu, X Tian, Y HuangCeramics International, 2016•Elsevier*.

Tan, Y., Fang, Z., Chen, W., Compounds, P (2011), Structural, optical and magnetic properties of Eu-doped ZnO films. *Elsevier*.

Tancogne-Dejean, N., Penz, M., Laestadius, A., Csirik, M. A., Ruggenthaler, M., & Rubio, A. (2022). Exchange energies with forces in density-functional theory. *arXiv*, 2203.16980.

Tancogne-Dejean, N., Penz, M., Laestadius, A., Csirik, M. A., Ruggenthaler, M., & Rubio, A. (2022). Exchange energies with forces in density-functional theory. *arXiv*.

Teimoori, F., Khojier, K., & Dehnavi, N. Z. (2017). Investigation of sensitivity and selectivity of ZnO thin film to volatile organic compounds. *Journal of Theoretical and Applied Physics*, *11*(2), 157–163.

Thanh et al. (2025). Eu^{3+}-doped ZnO quantum dots: structure, vibration and optical properties. *Nanoscale Advances*.

Thomas, A. (2021). High-efficiency dye-sensitized solar cells: A comprehensive review. *Computational and Experimental Research in Materials and Renewable Energy, 5*(1), 1–29.

Thomas, A. (2022). High-efficiency dye-sensitized solar cells: A comprehensive review. *Computational and Experimental Research in Materials and Renewable Energy, 5*(1), 1–29.

Thompson, R., Materials, W. (2018). Predicting whether a material is ductile or brittle. *Elsevier*.

Tindibale, E., Mulwa, W. M., & Adetunji, B. I. (2023). Elastic, anisotropic, lattice dynamics and electronic properties of XNiM and XNi2M (X = Ti, Zr, Hf; M = Sn, Ge, Si): DFT comparison study. *Physica B: Condensed Matter*, *665*.

Todorov, T., Gershon, T., Gunawan, O., Lee, Y. S., Sturdevant, C., Chang, L. Y., & Guha, S. (2015). Monolithic Perovskite-CIGS Tandem Solar Cells via in Situ

Band Gap Engineering. *Advanced Energy Materials*, *5*(23).

Toghraie, P., & Khodayari, M. (2020). *Band-gap Engineering and Relationship with Luminescence in Rare-Earth Elements Doped ZnO: An Overview. Materials Technology, 37*(11), 1–15.

Togo, A., & Tanaka, I. (2015). First principles phonon calculations in materials science. *Scripta Materialia*, *108*, 1–5.

Touri, F., Sahari, A., Zouaoui, A., Deflorian, F., & Guerbous, L. (2020). Optical, Structural, And Morphological Properties Of Undoped and Europium Doped ZnO. *Surface Review And Letters*, *27*(3).

Tran, F., & Blaha, P. (2009). Accurate band gaps of semiconductors and insulators with a semilocal exchange-correlation potential. *Physical review letters*, *102*(22), 226401.

Tse, G. (2021). The optical and elastic properties of strained ZnO by first principle calculations. *Computational Condensed Matter*, *26*.

Tusche, C., Meyerheim, H. L., & Kirschner, J. (2007). Observation of depolarized ZnO (0001) monolayers: Formation of unreconstructed planar sheets. *Physical Review Letters*, *99*(2).

Ulpe, A. C., & Bredow, T. (2020). GW–BSE calculations of electronic band gap and optical spectrum of $ZnFe_2O_4$: Effect of cation distribution and spin configuration. *ChemPhysChem, 21*(6), 546–551.

Ungula, J., & Dejene, B. F. (2016). Effect of solvent medium on the structural, morphological and optical properties of ZnO nanoparticles synthesized by the sol–gel method. *Physica B: Condensed Matter*, *480*, 26–30.

Ungula, J., Dejene, B. F., & Swart, H. C. (2017). Effect of annealing on the structural, morphological and optical properties of Ga-doped ZnO nanoparticles by reflux precipitation method. *Results in Physics*, *7*, 2022–2027.

Ungula, J., Dejene, B. F., & Swart, H. C. (2018). Band gap engineering, enhanced morphology and photoluminescence of un-doped, Ga and/or Al-doped ZnO nanoparticles by reflux precipitation method. *Journal of Luminescence*, *195*, 54–60.

Upadhaya, S., & Purkayastha, D. D. (2020). Enhanced wettability and photocatalytic properties of 1D ZnO nanorods synthesized by hydrothermal method. *Ceramics International, 46*(10), 15831–15839.

Usman, T., Murtaza, G., Luo, H., & Mahmood, A. (2017). GGA and GGA + U Study of Rare Earth-Based Perovskites in Cubic Phase. *Journal of Superconductivity and Novel Magnetism*, *30*(6), 1389–1396.

Varughese, G., Crysty, V. G., Praveen, G., Usha, K. T., & Kumar, A. S. (2015). Characterization and Elastic properties of wurtzite ZnO: Ce Nanocrystallites. *Asian Journal of Research in Chemistry*, *8*(3), 183.

Venkata-Haritha, M., Gopi, C. V. V. M., Thulasi-Varma, C. V., Kim, S. K., & Kim, H. J. (2016). Influence of Mn+2 incorporation in CdSe quantum dots for high performance of CdS-CdSe quantum dot sensitized solar cells. *Journal of Photochemistry and Photobiology A: Chemistry*, *315*, 34–41.

Vettumperumal, R., (2015), undefined. (n.d.). Optical constants and near infrared emission of Er doped ZnO sol–gel thin films. *ElsevierR Vettumperumal, S Kalyanaraman, R ThangavelJournal of Luminescence, 2015•Elsevier*.

Vijayaprasath, G., Murugan, R., Mahalingam, T., Hayakawa, Y., & Ravi, G. (2015). Enhancement of ferromagnetic property in rare earth neodymium doped ZnO nanoparticles. *Ceramics International*, *41*(9), 10607–10615.

Villarreal, D. E. P., Deprez, G., Wang, J., Dufour, I., & Stiens, J. (2022). Young's modulus and hardness of ZnO nanorods assessed by AFM bending tests. *Applied Surface Science, 595*, 153518.

Vincent, O., Mulwa, W. M., & Kirui, M. S. K. (2021). Investigation of magnetic properties of FeMnP1-xAx (A = In, Se and Sn, where x = 0.33) by use of GGA functionals. *Physica B: Condensed Matter*, *613*, 412777.

Vodapally, S. N., & Ali, M. H. (2023). A comprehensive review of solar photovoltaic (PV) technologies, architecture, and its applications to improved efficiency. Energies, 16(1), 319.

Wali, Q., Fakharuddin, A., & Jose, R. (2015). Tin oxide as a photoanode for dye-sensitised solar cells: Current progress and future challenges. *Journal of Power*

Sources, *293*, 1039–1052.

Wang, J., Shen, T., Feng, Y., Matter, H. (2020). A GGA+ U study of electronic structure and the optical properties of different concentrations Tb doped ZnO. *Elsevier*.

Wang, M., Sun, Y., Guo, J., Li, Z., Liu, C., & Guo, W. (2019). Alkali metal salts doped ZnO interfacial layers facilitate charge transport for organic solar cells. *Organic Electronics*, *74*, 258–264.

Wang, R., Huang, T., Xue, J., Tong, J., Zhu, K., & Yang, Y. (2021). Prospects for metal halide perovskite-based tandem solar cells. *Nature Photonics*, *15*(6), 411–425.

Wang, W., Feng, W., Du, J., Xue, W., Zhang, L., Zhao, L., Li, Y., & Zhong, X. (2018). Cosensitized Quantum Dot Solar Cells with Conversion Efficiency over 12%. *Advanced Materials*, *30*(11).

Wang, Y., Laihonen, S. J., Unge, M., & Mostofi, A. A. (2024). *Improving the precision of work-function calculations within plane-wave density-functional theory*. *Electronic Structure, 6*, 037004.

Wang, Y., Laihonen, S. J., Unge, M., & Mostofi, A. A. (2024). *Improving the precision of work-function calculations within plane-wave density-functional theory*. *Electronic Structure, 6*, 037004.

Waqas, M., Ghaffar, R., Irshad, M., Saleem, M., Hanif, M., & Ghaffar, A. (2022). Synergistic effect of morphology on the biocidal response of Ce-doped ZnO nanomaterial synthesized by facile autocombustion method. *Materials Chemistry and Physics*, *282*.

Waqas, M., Shah, S. M. A., & Khan, M. (2022). Cerium-doped ZnO for enhanced photoelectrochemical response. Ceramics International, 48(11), 16142–16149.

Wei, B., Sun, Q., Li, C., & Hong, J. (2021). Phonon anharmonicity: a pertinent review of recent progress and perspective. *arXiv*.

Wen, J. Q., Zhang, J. M., Qiu, Z. G., Yang, X., & Li, Z. Q. (2018). The investigation of Ce doped ZnO crystal: The electronic, optical and magnetic properties. *Physica B: Condensed Matter*, *534*, 44–50.

Wen, Y., Chen, Y., Zhang, J., & Duan, W. (2023). Mechanical stiffness and anisotropy in ZnO single crystals under compression: A high-pressure DFT and experimental study. *Acta Materialia, 245*, 118602.

Wheeler, W. A., Pathak, S., Kleiner, K. G., Yuan, S., Rodrigues, J. N. B., Lorsung, C., … Wagner, L. K. (2023). *PyQMC: An all-Python real-space quantum Monte Carlo module in PySCF*. *The Journal of Chemical Physics, 158*(11), 114801.

Wu, J., Lan, Z., Lin, J., Huang, M., Huang, Y. (2017), Counter electrodes in dye-sensitized solar cells. *Pubs.Rsc.Org*.

Wu, Q., Liu, G., Shi, H., Zhang, B., Ning, J., Shao, T., (2023), Impact of Nd doping on electronic, optical, and magnetic properties of ZnO: a GGA+ U study. *Mdpi.ComQ Wu, G Liu, H Shi, B Zhang, J Ning, T Shao, S Xue, F ZhangMolecules, 2023•mdpi.Com*.

Wu, T.C., Huang, W.M., Meen, T.-H., & Tsai, J.-K. (2023). *Performance Improvement of Dye-Sensitized Solar Cells with Pressed TiO_2 Nanoparticles Layer*. Coatings, 13(5), 907.

Wu, X., Wu, Z., Guo, L., Liu, C., Liu, J., Li, X., Communications, H. X.-S. S., & 2005, undefined. (n.d.). Pressure-induced phase transformation in controlled shape ZnO nanorods. *Elsevier*.

Xiao, H., Lai, W., Chen, A., Lai, S., He, W., Deng, X., … Ren, H. (2024). *Application of photovoltaic and solar thermal technologies in buildings: A mini-review*. Coatings, 14(3), 257.

Xiao, Y., Han, G., Zhou, H., Li, Y., & Lin, J. Y. (2015). Nickel sulfide counter electrodes enhanced by hydrosulphuric acid hydrothermal treatments for use in Pt-free dye-sensitized solar cells. *Electrochimica Acta*, *155*, 103–109.

Xue, Q., Zhao, Y., Zheng, X., & Chen, H. (2024). Mechanical reinforcement of ZnO composites by Ag nanoparticle incorporation. *Composites Part B: Engineering, 259*, 116996.

Xuecheng Shao, W. Mi, & M. Pavanello. (2021). GGA-level subsystem DFT achieves sub-kcal/mol accuracy intermolecular interactions by mimicking nonlocal functionals. *arXiv*.

Yang, J., Falletta, S., & Pasquarello, A. (2023). Range-separated hybrid functionals for accurate prediction of band gaps of extended systems. *npj Computational Materials, 9*(1), 108.

Yang, X., Cai, L., Zhao, L., Li, Z., Wu, C., Sun, J., Liang, Z., & Wang, S. (2021). A triple-functional photoanode for light harvesting enhancement in dye sensitized solar cells. *Materials Science in Semiconductor Processing*, *128*.

Yang, Y., Prokopiou, G., Qiu, T., Schankler, A. M., Rappe, A. M., Kronik, L., & DiStasio, R. A., Jr. (2023). Range-separated hybrid functional pseudopotentials. *Physical Review B, 108*, 165142.

Yang, Z., Liu, Y., & Chen, W. (2024). A brief review of perovskite quantum dot solar cells: synthesis, property and defect passivation. *ChemSusChem*.

Yayapao, O., Thongtem, T., Phuruangrat, A., & Thongtem, S. (2013a). Sonochemical synthesis of Dy-doped ZnO nanostructures and their photocatalytic properties. *Journal of Alloys and Compounds*, *576*, 72–79.

Zhang, G., Zhang, S., & Wang, Q. (2022). Dielectric materials for electrical energy storage. *Journal of Materiomics*, *8*(6), 1287–1289.

Zhang, L., Fan, Y., He, C., Wang, W., Liu, X., & Chen, L. (2021). *Enhanced thermoelectric properties of ZnO: C doping and band gap tuning*. Journal of the European Ceramic Society, 41(6), 3100–3108.

Zhang, M., Ono, S., Nagatsuka, N., & Ohno, K. (2016). All-electron mixed basis G W calculations of TiO 2 and ZnO crystals. *Physical Review B*, *93*(15), 155116

Zhang, R., Cao, W., Xia, Y., -, al, Jones, R. E., Ward, D. K., Gittleson, F. S., Arora Abrol, S., Bhargava, C., & Kumar Sharma, P. (2020). Electrical properties enhancement of Liquid and Polymer Gel based electrolytes used for DSSC applications. *Iopscience.Iop.Org*, *7*, 106202.

Zhang, X. J., Mi, W. B., Wang, X. C., & Bai, H. L. (2014). First-principles prediction of electronic structure and magnetic ordering of rare-earth metals doped ZnO. *Journal of Alloys and Compounds*, *617*, 828–833.

Zhang, Y. H., Peng, M. X., Yue, L. J., Chen, J. L., Gong, F. L., Xie, K. F., & Fang, S. M. (2021). A room-temperature aniline sensor based on Ce doped ZnO porous

nanosheets with abundant oxygen vacancies. *Journal of Alloys and Compounds*, *885*.

Zhang, Y., Ji, Z., & Li, P. (2023). Crystal structure and mechanical properties of ZnO:Ce nano film. *PNAS via PMC*

Zhang, Z., Zhang, D.-B., Sun, T., & Wentzcovitch, R. M. (2021). The phonon quasiparticle approach for anharmonic properties of solids. *arXiv*.

Zhao, J. H., Liu, C. J., & Lv, Z. H. (2016). Photoluminescence of ZnO nanoparticles and nanorods. *Optik*, *127*(3), 1421–1423.

Zhao, X., Dong, T., Ma, H., Li, D., Ying, C., Liu, C., & Wang, F. (2020). Effect of strains on the optical and magnetic properties of Ce-doped ZnO with O or Zn vacancies. *Journal of Materials Science*.

Zheng, W., Cao, J., & Chen, X. (2023). The effect of CuS content on the properties of CuS QDs/Ti3C2 MXene counter-electrodes in QDSCs. *Journal of Materials Science: Materials in Electronics*, *34*(30).

Zong, Y., Li, Z., Wang, X., Ma, J., & Men, Y. (2014). Synthesis and high photocatalytic activity of Eu-doped ZnO nanoparticles. *Ceramics International*, *40*(7), 10375–10382.

APPENDICES

Appendix 1: Approval Letter

MURANG'A UNIVERSITY OF TECHNOLOGY

Office of the Director, Postgraduate Studies

E-mail: bps@mut.ac.ke
Website: www.mut.ac.ke

P.O. Box 75-10200
Murang'a, Kenya

Ref: MUT/ARP/PGS/19/2020 /VOL.1 **Date:** 17th July, 2023

Mr. Irungu Moses Kahura (AS502/5748/2021)
School of Pure, Applied and Health Sciences,
Murang'a University of Technology,
P.O. Box 75-10,200
Murang'a.

Dear Mr. Kahura,

RE: APPROVAL OF RESEARCH PROPOSAL AND SUPERVISORS.

I am pleased to inform you that the Directorate of Postgraduate Studies on 3rd July, 2023 considered and approved your Doctoral research proposal entitled ***"Density Functional Theory Study of Material Properties of Lanthanide-Doped Zinc Oxide for Dye Sensitized Solar Cell Photoanode"*** and appointed the following as supervisors:

1. Dr. Sharon Kiprotich - Murang'a University of Technology
2. Dr. Winfred Mulwa – Egerton University

You may now proceed with your data collection subject to obtaining research permit from NACOSTI, if required. You should also begin consulting your supervisors and submit through them quarterly progress reports to the Director Postgraduate Studies through your CoD and School Dean. Progress Reports forms can be accessed in the Student Portal.

It is the policy and regulations of the University that you observe deadlines. The guidelines on Postgraduate supervision can be accessed in the post graduate Handbook.

Your responsibilities as a student will include, among others;

i. Maintain regular consultation with your supervisor(s), at least once a month
ii. Submit quarterly reports on time, through your supervisors, CoD, Dean and to the Director of Postgraduate Studies;
iii. Ensure quality work all through;

iv. Present your research findings at 2-3 seminars/conferences prior to thesis examination.

v. Publish two articles from your research findings in a refereed journal prior to thesis examination.

For any further clarification please contact the undersigned.

Yours Sincerely,

Prof. Geoffrey Muchiri, PhD
Director, Postgraduate Studies
GM/PIM

DIRECTORATE OF POSTGRADUATE STUDIES
MURANG'A UNIVERSITY OF TECHNOLOGY
17 JUL 2023
P. O. Box 75 - 10200, MURANG'A
Tel: 0771463515, Email: info@mut.ac.ke

Copy to:
1. Registrar – Academics and Students Affairs
2. Dean, School of Pure, Applied and Health Sciences

Appendix 2: Publications

This thesis has produced the following publications:

Irungu, M. K., Kiprotich, S., & Mulwa, W. M. (2024). A DFT investigation of RE (Ce, Dy, Eu) doped monolayer ZnO for potential application in dye-sensitized solar cells. Nanoscience and Nanotechnology, 13(2), 17–27.

Irungu, M. K., Kiprotich, S., & Mulwa, W. M. (2024, November). An ab initio GGA+U study of the wurtzite structure of ZnO for dye-sensitized solar cells application. International Journal of Theoretical and Mathematical Physics.

Irungu, M. K., Kiprotich, S., & Mulwa, W. M. (2024, November). Energy band-gap engineering for ZnO as a photoanode of dye-sensitized solar cells: An ab initio study. American Journal of Materials Science.

This thesis is supported by the following conferences:

Irungu, M. K. (2022, November 16–18). DFT study of lanthanide-doped zinc oxide for photovoltaic application [Conference presentation]. 2022 MSSEESA Materials Science Conference, University of Eldoret, Eldoret, Kenya.

Irungu, M. K. (2023, June 14–16). An ab initio study of the wurtzite structure of Ce and Yb doped ZnO for dye-sensitized solar cells application [Conference presentation]. 5th Annual International Conference, Machakos University, Machakos, Kenya.

Irungu, M. K. (2024, July 10-11). A comparison investigation of an ab initio GGA+U and experimental study of the wurtzite structure of ZnO for dye-sensitized solar cells application [Conference presentation]. 15th International Research Conference for School of Science, Engineering & Technology, Kabarak University, Nakuru, Kenya.